Università
degli Studi
di Padova

Università Degli Studi Di Padova

Dipartimento di Ingegneria Industriale

Scuola di Dottorato di Ricerca in Ingegneria Industriale

Curriculum in Ingegneria dell'Energia Elettrica

Ciclo XXXII

Design Advances in Synchronous Reluctance and Permanent Magnet Assisted Synchronous Reluctance Machines

Direttore della Scuola:
Ch.mo Prof. Paolo Colombo

Coordinatore d'Indirizzo:
Prof. Roberto Turri

Supervisore:
Ch.mo Prof. Nicola Bianchi

Dottorando: Ing. Cristian Babetto

02 Dicembre 2019

Contents

Preface

This Preface describes the background and motivation of the thesis. The contents of each Part are briefly summarized. Finally, a list of publications during the Ph.D. period is reported.

Background

The synchronous reluctance (SyR) machine is an electromechanical converter whose energy conversion is entirely based on the rotor magnetic saliency. Such a principle was already known in the early 1900s when the salient pole synchronous machines without field excitation, derived from the more popular synchronous alternator, was the unique design concept. Due to its intrinsic poor performance and absence of a valid contemporary technology for its control, the first ancestor of SyR machine didn't have a chance to show its potential. Only with the advances on the solid state inverter technology, carried out between the 1960s and 1970s, grow the interest for the SyR machine drives inducing many researchers to study new design solutions aimed to improve the rotor saliency. However, only in the last three decades the SyR technology has reached its maturity both in design and control. Concerning the design aspect, remarkable progresses have been made on the rotor geometry which, nowadays, allows to achieve good torque density with a low torque ripple. Nevertheless, the rotor structure continues to be literally a *piece of iron* with all relative benefits: cheap and robust rotor structure, high overload capability and high reliability. Thanks to these features, the SyR machine has been proposed as a valid alternative to the widely used machine topologies, such as induction machine and permanent magnet (PM) machine, in many fields: home appliance, pumping or fan. On the other hand, the low power factor and limited power capability are the main drawbacks and make the SyR machine not suitable for applications, e.g. automotive, in which a high drive compactness and a wide constant power speed range are required.

The SyR machine performance can be improved by adding a proper amount of rotor PMs with the aim of saturating the rotor ribs, increasing the power factor and extending the machine power capability. What distinguishes a PMASyR machine from a typical interior PM (IPM) machine is the ratio between the cylindrical and reluctance torque components. In the first case, most of the torque is due to the rotor anisotropy (up to 70%) and only a minor contribute is given by the PMs. In the second case, the cylindrical torque is predominant and most of the flux is given by the PMs, typically rare-earth materials. Since the PM flux plays a secondary role in the PMASyR torque production, it is sufficient to create a low PM flux. To preserve the rare-earth free feature of the SyR machine, cheaper sintered ferrite PMs with low magnetic energy are usually adopted. Unfortunately, the PMs presence involves additional machine cost and compromises the overload capability.

Aim of the research

Despite a large number of studies have investigated the SyR machine suitability for different industry applications, a very poor documentation dealt with its potential applicability in the field of high-speed (HS) and fault-tolerant (FT) applications.

The main advantage to work at HS is the possibility to reduce the overall electric drive size hence its cost and weight. Such an advantages are even more evident in the direct-drives systems

in which the motor is directly coupled to the load without any gear box often subject to failure. On the other hand, the high operating speeds need an accurate mechanical design and losses management which often determine an overall deterioration of the initial machine performance. The fault-tolerant capability of a drive system is a mandatory requirement in those applications where the failure could cause economic costs or, more important, injure the human safety as in the automotive, aerospace and military applications.

The main aims of this research is to investigate the SyR machine suitability for high-speed and fault-tolerant applications. Being these two topics quite independent from each other they are tackled in two different parts of the thesis:

Part I deals with the design of SyR machine for HS applications. The study starts from the development of an analytical procedure to design the radial ribs of the rotor in order to ensure the structural integrity against the centrifugal stress. Then, the SyR machine power capability is estimated analytically for different mechanical speed limits taking into account both magnetic and mechanical aspects. At first, a simple analytical models is developed to have an overall idea of the main aspects that rule the HS-SyR machine design. Then, a more complex reluctance network is proposed to estimate the HS-SyR machine performance with more accuracy. After that, two alternative complete design procedures are proposed. The first one is supported by both analytical and finite element (FE) computation while the second one is entirely based on a FE-based multi-objective differential evolution algorithm. The most suitable procedure is then employed for the design of rotor geometries at different mechanical speed limits in order to evaluate the behavior of the optimal rotor parameters versus the rated speed. Finally, a comparison between a surface mounted PM machine and a SyR machine, properly design for HS applications, is carried out highlighting pros and cons of the two topologies;

Part II investigates different design solutions to improve the FT reliability of a dual three-phase SyR machine drive. The study meanly focuses on the performance evaluation when both the three-phase windings are fed (full winding mode, FWM) or when one is disconnected and the other is normally fed (open circuit half winding mode, OC-HWM). The three phase short circuit of one of the two windings is considered only in the final analyses. The impact of different dual three-phase winding arrangements on the SyR machine performance in FWM and OC-HWM is initially investigated by means of FE analysis. In particular, two alternative dual three-phase winding arrangements with three magnetic axes and an actual six-phase winding are proposed. The evaluated performance are the average torque, the torque ripple, the unbalanced radial force on the rotor and the mutual magnetic coupling between the two windings. Once the most suitable winding arrangement is found, several FE-based optimization strategies of the machine geometry are proposed with the aim of improving the average torque and torque ripple in both FWM and OC-HWM. Finally, an optimal motor geometry is manufactured and tested in laboratory to verify the reliability of the proposed design procedure.

After these parts the thesis deals with the PMASyR machine focusing on its design for an automotive application and the possibility to use bonded magnets (BMs) to improve its performance. Their contents are organized as follows:

Part III proposes an automatic FE-based multi-objective procedure for the design of a PMASyR machine for a low-voltage electric scooter application. The first parts describes in detail each step of the objectives evaluation algorithm carried out during the optimization. Then, the optimization results are reported and commented. Finally, a prototype of the most promising individual is manufactured to test the actual performance of the motor and the design procedure effectiveness;

Part IV evaluates the impact of two different BMs production technologies on the performance of a PMASyR machine. In particular, the compression and injection moulding process are considered. The study starts with the description of the BMs production procedures from

raw materials to final product. Then, a SyR rotor geometry is properly optimized and three prototypes are manufactured: one SyR machine and two PMASyR machines (one for each BMs type). The prototypes performance are finally evaluated by means of experimental tests highlighting the performance improvement due to different BM typologies.

After the presentation of the research activities, the main tools developed and used during the doctoral period are presented in the final part:

Part V consists of three main topics. The first one describes a novel and computationally efficient technique to compute the efficiency map of synchronous machines. The second topic presents the open-source FE solver used for the structural analyses carried out on the HS-SyR rotor geometries. The third one reports the automatic procedures adopted to design the SyR rotors in all the thesis works.

List of publications

Several parts of this Ph.D. thesis have been presented by the author during his Ph.D. period in international conferences and journals. Hereafter the publications are listed in a chronological order:

Journals

- C. Babetto, G. Bacco, and N. Bianchi. "Analytical Power Limits Curves of High-Speed Synchronous Reluctance Machines". In: *IEEE Transactions on Industry Applications* (2018), p. 1. ISSN: 0093-9994
- C. Babetto, G. Bacco, and N. Bianchi. "Synchronous Reluctance Machine Optimization for High Speed Applications". In: *IEEE Transactions on Energy Conversion* 8969.c (2018), pp. 1–1. ISSN: 0885-8969
- C. Babetto, G. Bacco, and N. Bianchi. "Design methodology for high-speed synchronous reluctance machines". In: *IET Electric Power Applications* 12.8 (2018), pp. 1110–1116. ISSN: 1751-8660

Conferences

Published

- C. Babetto, G. Bacco, and N. Bianchi. "Analytical approach to determine the power limit of high-speed synchronous reluctance machines". In: *2017 IEEE International Electric Machines and Drives Conference, IEMDC 2017*. 2017. ISBN: 9781509042814
- C. Babetto et al. "High speed motors: A comparison between synchronous PM and reluctance machines". In: *2017 IEEE Energy Conversion Congress and Exposition (ECCE)*. Cincinnati, 2017, pp. 3927–3934
- C. Babetto and N. Bianchi. "Synchronous Reluctance Motor with Dual Three-Phase Winding for Fault-Tolerant Applications". In: *2018 XIII International Conference on Electrical Machines (ICEM)*. 2018, pp. 2297–2303
- E. Poskovic et al. "The study of permanent magnet assisted reluctance machine with the adoption of NdFeB bonded magnets". In: *2018 International Symposium on Power Electronics, Electrical Drives, Automation and Motion (SPEEDAM)*. 2018, pp. 274–279
- C. Babetto et al. "High-Speed Synchronous Reluctance Motors: Computation of the Power Limits by Means of Reluctance Networks". In: *2018 IEEE 18th International Power Electronics and Motion Control Conference (PEMC)*. 2018, pp. 556–561

- C. Babetto et al. “Design Optimization and Analysis of a Synchronous Reluctance Machine for Fault-Tolerant Applications”. In: *2019 IEEE International Electric Machines Drives Conference (IEMDC)*. 2019, pp. 1784–1791
- C. Babetto, N. Bianchi, and G. Benedetti. “Design and Optimization of a PMASR Motor for Low-Voltage E-Scooter Applications”. In: *2019 IEEE International Electric Machines Drives Conference (IEMDC)*. May 2019, pp. 1016–1023
- E. Pošković et al. “Bonded Magnets in PM-Assisted Synchronous Reluctance Machines: Performance Dependence on the Production Technology”. In: *2019 IEEE International Electric Machines Drives Conference (IEMDC)*. 2019, pp. 442–448
- J. Park, C. Babetto, and N. Bianchi. “Fault Analysis for Dual Three-Phase Synchronous Reluctance Motor”. In: *2019 IEEE International Electric Machines Drives Conference (IEMDC)*. 2019, pp. 1–6
- A. Bellini et al. “Stator fault diagnosis by reactive power in dual three-phase reluctance motors”. In: *12th IEEE International Symposium on Diagnostics for Electric Machines, Power Electronics and Drives, 2019. SDEMPED 2019.* 2019

Submitted

- C. Babetto et al. “Design and Optimization of Synchronous Motors for Low-Voltage Electric Vehicles”. In: *2019 IEEE Energy Conversion Congress and Exposition (ECCE)*. Baltimore, 2019
- G. Bacco et al. “Efficiency Maps Computation and Comparison Including Thermal Limits”. In: *2019 IEEE Energy Conversion Congress and Exposition (ECCE)*. Baltimore, 2019
- C. Babetto et al. “Optimal Design and Experimental Validation of a Synchronous Reluctance Machine for Fault-Tolerant Applications”. In: *2019 IEEE Energy Conversion Congress and Exposition (ECCE)*. Baltimore, 2019
- J. Park et al. “Comparison of Fault Characteristics for Dual Three-Phase Synchronous Reluctance Motor”. In: *2019 IEEE Energy Conversion Congress and Exposition (ECCE)*. Baltimore, 2019

Part I

High-Speed Synchronous Reluctance Machines

Chapter 1

High-Speed SyR Machine: Introduction

In the last few decades, the interest for high-speed (HS) electrical machines such as vacuum pumps, turbo-compressors, and machining spindles, arose from the requirement of compact and efficient drive systems [18]. In addition, the lack of gearbox, in the direct-drives systems, involves some important advantages such as high reliability, low cost and weight. The advances in new power electronic components, materials and control methodologies contributed to the HS drive systems success [19–27].

During the years, different electrical machine typologies have been proposed for HS applications [28, 29]. Despite the universal motor was widely diffused in many civil and industrial applications in the past, the presence of the brushes strongly limited its diffusion in HS applications. The induction machine (IM) has been proposed for its intrinsic robustness and mature technology with several design solutions aimed to increase the rotor strength (i.e. solid rotor) and to reduce its inertia (i.e. solid cage, coated conducting sheet) [30–35]. However, its low power factor and efficiency limited its suitability for HS applications.

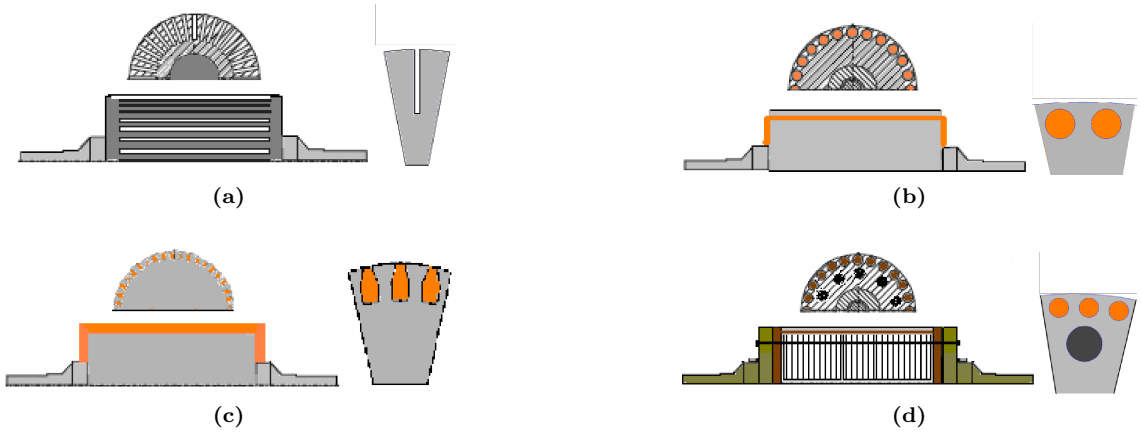

Figure 1.1: Different IM rotor design for HS applications: slitted solid rotor (*a*), solid rotor with embedded squirrel cage (*b*), solid rotor with squirrel cage (*c*) and laminated rotor with embedded squirrel cage (*d*) [35].

The interest to find a more efficient alternative to IM, increased the attention for the permanent magnets synchronous machine (PMSM) well known for its high torque/power density and efficiency mainly due to the high-energy magnets which, on the other hand, have a strong impact on the machine total cost.

In general, the magnetic and thermal aspects are taken into account in the PMSM design to avoid any PM demagnetization and dangerous winding overheating [36, 37]. In HS applications, the mechanical aspect represents an additional design key point to satisfy in order to ensure the

machine structural integrity against the high centrifugal force that acts on the rotating parts. Moreover, the PMs demagnetization risk is amplified by the higher PM eddy current that can arise on their surface. Also the thermal limit has to be reduced because of the higher harmonic core and joule losses [38–40]. The overall effect of these aspects worsen the PMSM performance in terms of efficiency and reliability so that, the total losses limitation represent the most important challenge in the HS PM machine design. Typically, as shown in Figure 1.2(a), the PMs are glued on the rotor surface and the structural integrity is ensured by a retaining sleeve, which is often made of carbon fiber, for its high tensile strength. However, the low thermal conductivity of such a solution prevents the rotor heat exchange and increases the PMs thermal demagnetization risk [41]. Some HS PMSM design guidelines are presented in [42] where the use of soft magnetic composite, as alternative to the lamination core, and of a slotless stator are proposed as effective solution to reduce the total machine losses. In [43] a non-magnetic conductive rotor sleeve is proposed as a valid solution capable of ensuring both structural integrity and reducing eddy-current PM losses. Alternatively, a non-conductive sleeve with a solid rotor core and a particular winding arrangement is proposed in [44] to reduce the rotor losses of a PM generator.

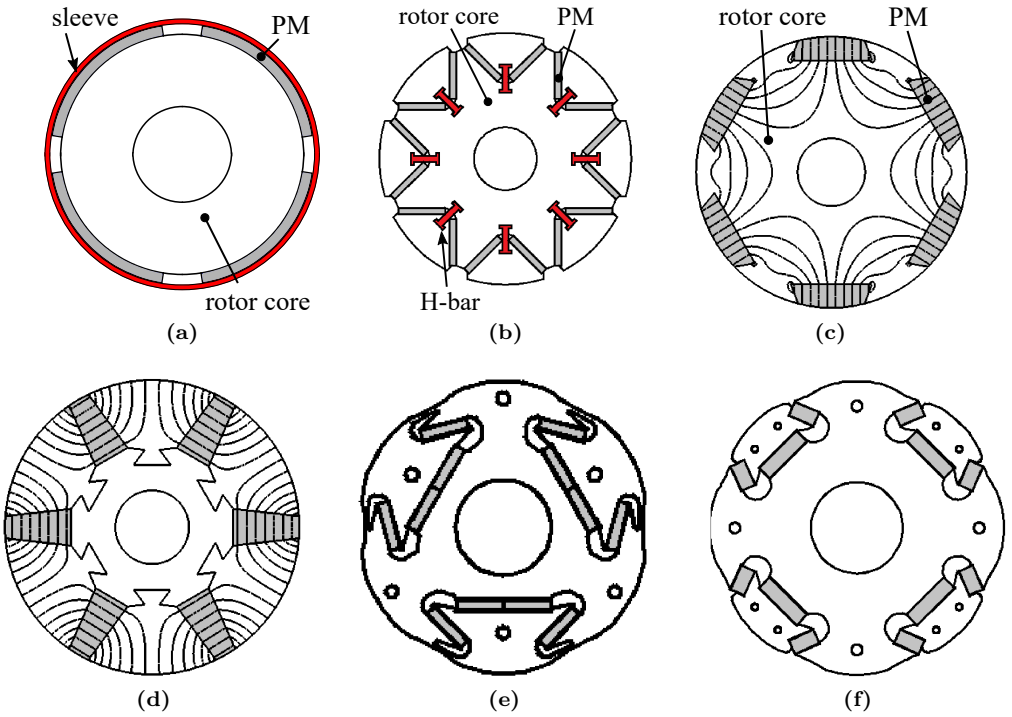

Figure 1.2: PM synchronous rotor for HS applications: SPM (*a*), H-shaped bars (*b*) [45], dovetail magnet (*c*) and (*d*) [46, 47], dovetail poles (*e*) and (*f*) [48].

Instead of placing the PMs on the rotor surface, they can be *buried* in the rotor core so that the structural integrity is entirely ensured by the rotor iron and no additional sleeve and cost are needed. This also involves a reduction of the total amount of PM material [38] (lower air-gap length) but, on the other hand, higher Joule losses [49]. In [45], the rotor integrity is increased by means of H-shaped bars in the bottoms of the V-shaped poles as reported in Figure 1.2(b). The rotor sketches in Figure 1.2(c) and Figure 1.2(d) show the *dovetail* shapes used to keep the PMs locked to the rotor [46, 47]. Finally, Figure 1.2(e) and Figure 1.2(f), report the rotor sketches of two dovetail poles rotors [48]. Even though rare earth PMs involves high machine performance, their high cost fluctuations during the past years induced many researchers and PM machine manufacturers to find alternative solutions which yield a good compromise in terms of performance but less dependent on the PMs.

Among the PM-less machine scenario, the switched reluctance (SWR) and synchronous reluc-

tance (SyR) machine are the most promising suitable candidates in HS applications. The SWR machine main advantages are intrinsic fault tolerance, low cost, robust design and low rotor inertia [50]. Unlike PMSM or IM, there are no additional components which add complexity to the mechanical or electrical design process but, conversely, it presents a simple rotor structure that allows to reduce the manufacturing cost as well. Despite these advantages, the adoption of SWR machine in industry is still compromised by its high torque ripple, low torque density, high noise and high vibration [51]. Moreover, the SWR rotor structure contributes to a higher drag coefficient (i.e. higher air friction losses) even thought some design solutions have been investigated to overcome such an aspect [52].

Similarly to SWR machine, the SyR one presents all the advantages due to the lack of rotor PMs but it has been barely proposed for HS applications. However, thanks to its success in other industry applications, it has been receiving great attention in the recent years. The solid salient pole and transversely laminated rotor are the two main SyR rotor topologies. The HS SyR salient pole machine, shown in Figure 1.3(a), presents the simplest and cheapest rotor geometry but it is well known for its intrinsic low rotor anisotropy [53] and high torque ripple even thought a proper winding chording and rotor skewing allow to mitigate such a drawback [54]. As already point out for SWR machine, also the salient pole suffers of significant aerodynamic losses at high speed so that a cylindrical rotor jacket could be required at the cost of increasing the air-gap length and reducing the torque density. The anisotropic solid rotor configurations in Figure 1.3(b) allows to obtain a rotor saliency higher than the salient pole with lower air-friction losses thanks to the cylindrical rotor shape [55]. An exotic HS SyR rotor topology is presented in [56]. As shown in Figure 1.3(c), the rotor consists of a round iron rod array holding a number of rods evenly spaced from each other. The goal of such a solution is to achieve low magnetic reluctance along d-axis direction by means of the iron rods and high q-axis reluctance with the nonmagnetic rods holder material (e.g. Cu-Al alloy). The quite simple rotor construction and robustness are the main advantages of this design however it can easily manufactured with two poles only.

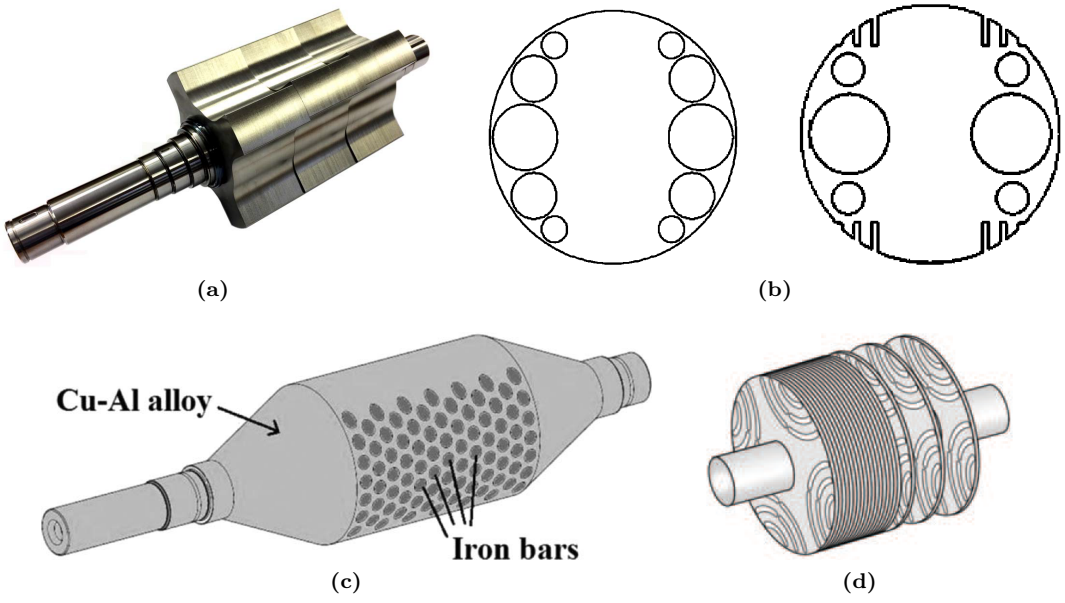

Figure 1.3: HS SyR solid rotor geometries: salient pole (a) [54], drilled and drilled/slitted [55], iron rods (c) [56], transversally laminated (d) [57].

In normal applications, the transversally laminated SyR rotor, shown in Figure 1.3(d), is designed to maximize the rotor anisotropy and to minimize the torque ripple giving to the mechanical design aspect a secondary role. In particular, the structural integrity of such a machine is ensured by thin iron bridges which size is kept small as much as possible (i.e. lamination width) to limit their negative effect on the rotor anisotropy. However, in HS applications, the iron bridges has

to be accurately designed and their effect on the machine performance have to be taken into account. In fact, as the mechanical speed limit increases, their size have to be increased as well to limit the centrifugal mechanical stress but at the same time they have to limit the q-axis flux that compromises the rotor anisotropy.

In [58], Cupertino et. al introduced this topic providing some design guidelines for multi flux-barriers SyR rotor without any retaining sleeve for an HS aerospace application. In particular, the work mainly focuses on the lamination material selection and the analytical radial ribs design. A comparative study of two FE-based optimization strategies for HS-SyR is carried out in [59, 60] where it is found that a physically decoupled electromagnetic and mechanical optimization is more suitable than the coupled approach in which both electromagnetic and structural analysis are performed for objective evaluation. Figure 1.4 reports a comparison between two SyR rotor geometries designed for common and HS application where it is evident the larger radial rib sizes of the second one.

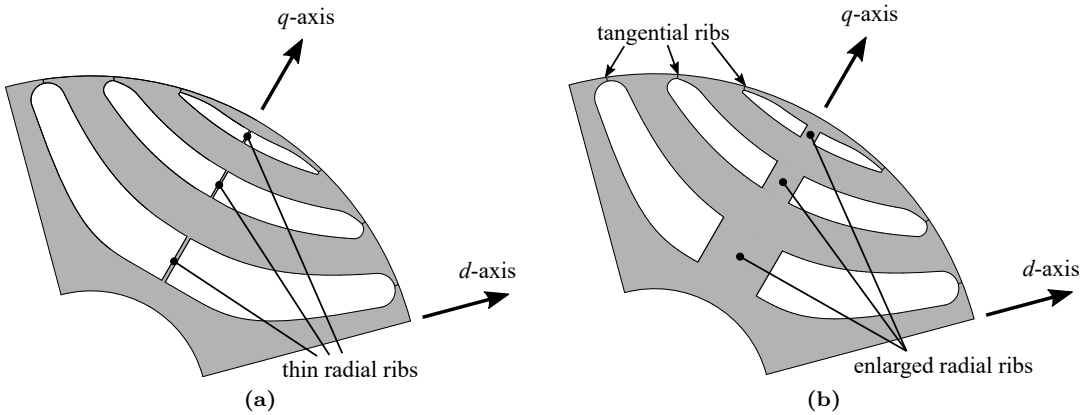

Figure 1.4: SyR rotor sketches with three flux-barriers per pole designed for common (a) and HS application (b).

The main goals of this part of the thesis are: (i) to describe the HS-SyR machine behavior by means of analytical models, (ii) to propose some multi-physics design methodologies for HS-SyR machine, (ii) to observe how the rotor geometry changes with the mechanical speed limit and its impact on the machine performance and (iv) to make a comparison with a HS SPM machine in terms of performance and cost.

The topics are organized as follows:

chapter 2 presents the criteria used to mechanically design the HS-SyR radial ribs, describes the HS-SyR machine behavior by means of an analytical model taking into account both mechanical and electromagnetic aspects, evaluates the analytical results reliability by means of FE analyses and makes a performance comparison between a flux-barriers rotor and a salient pole one on the basis of their torque and power limit curves;

chapter 3 proposes an improved analytical model which takes into account the radial ribs contribution on the rotor saturation and the cross coupling between d-and q-axis, finally the results are validated by means of FE analysis;

chapter 4 describes two alternative procedures to design a HS SyR machine. In particular, a semi-analytical and a FE-based optimization are described. Finally, a thorough FE analysis of one optimal solution is performed focusing on the iron losses and mechanical stress distribution;

chapter 5 deals with the FE optimization of HS SyR machine at different mechanical speed limits focusing on the optimization results sensitivity and the rotor geometry flux-barrier shape changes. The suitability of a retaining sleeve in addition to the radial ribs is also investigated;

chapter 6 makes a comparison in terms of performance and cost between a SyR machine and a SPM machine designed for HS applications.

Chapter 2

Analytical Power Limits Curves of HS-SyR Machines

2.1 Introduction

The main goals of this chapter are: (i) to present the criteria used to mechanically design the HS-SyR radial ribs (ii) to develop an analytical model which allow to couple magnetic and mechanical design and (iii) to describe the HS-SyR power limit curve versus the mechanical speed limit [2, 4, 5]. Some solutions are investigated by means of FE analysis so as to validate the results obtained by means of the proposed analytical approach. Finally, a comparison between the flux-barriers rotor and a salient pole rotor is carried out on the basis of their torque and power limit curves with the aim of find out a mechanical speed limit in which the two rotor typologies present the best performance in terms of torque and power density.

2.2 Radial iron ribs computation

The radial iron ribs are designed considering the stress due to the centrifugal force. The mechanical contribution of the tangential iron ribs is neglected and their thicknesses are set equal to the minimum manufacturing length (e.g. the lamination width) [58]. The main idea used to design the j-th radial rib consists of three main steps. With reference to Figure 2.1, firstly, the j-th iron cross section, $A_{\mathrm{Fe}j}$, delimited by the j-th flux-barrier outer edge and rotor periphery. Then, the associated centrifugal force is:

$$F_{cj} = \omega_{\mathrm{m}}^2 R_{\mathrm{G}j}\, \gamma_{\mathrm{Lam}} A_{\mathrm{Fe}j} L_{\mathrm{stk}} \tag{2.1}$$

where ω_{m} is the machine maximum speed, $R_{\mathrm{G}j}$ is the iron cross section center of gravity radius, γ_{Lam} is the lamination mass density and L_{stk} is the machine stack length. Finally, assuming that the j-th radial rib reaction, $F_{\mathrm{rib}j}$, has to compensate such a centrifugal force, its thickness is given by:

$$t_{\mathrm{rib}j} = \nu_\sigma \frac{F_{\mathrm{c}j}}{\sigma_{\mathrm{r}} L_{\mathrm{stk}}} \qquad\qquad |F_{\mathrm{c}j}| = |F_{\mathrm{rib}j}| \tag{2.2}$$

where σ_{r} is the tensile strength of the lamination while ν_σ is a safety factor, typically set in the range between 2 and 3 [61], which takes into account the fatigue effect. The two methods proposed in the following differs from each other only for the computation of the j-th iron cross section area.

2.2.1 Simplified method

The method proposed in this section allows to compute analytically both the rotor iron channel masses and radial ribs size. Such a method refers to the simplified rotor geometry reported in Figure 2.2 in which the j-th iron channel cross section can be easily computed from the circular segment delimited by the j-th flux-barrier [1].

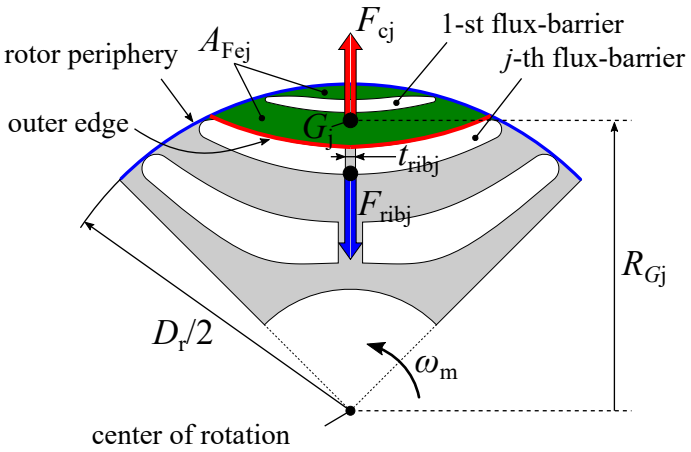

Figure 2.1: Dimensions for the computation of the j-th radial rib thickness in a SyR rotor. The radial rib reaction $F_{\mathrm{rib}j}$ has to compensate the centrifugal force $F_{\mathrm{c}j}$ of the j-th iron mass whose is supposed to be concentrated on its center of gravity, G_j, distance $R_{\mathrm{G}j}$ from the axis rotation.

Figure 2.2(a) shows that the first iron channel cross section is twice the circular segment, A_{cs1}, defined by the first flux-barrier, $2\vartheta_{\mathrm{b1}}$, so that it can be computed as follows:

$$A_{\mathrm{Fe1}} = 2A_{\mathrm{cs1}} = \frac{D_{\mathrm{r}}^2}{4}\left(2\vartheta_{\mathrm{b1}} - \sin 2\vartheta_{\mathrm{b1}}\right) \tag{2.3}$$

where D_{r} is the rotor diameter. The radius of the center of gravity, G_1, is:

$$R_{\mathrm{G1}} = \frac{D_{\mathrm{r}}}{2}\cos\vartheta_{\mathrm{b1}} \tag{2.4}$$

and the centrifugal force is given by:

$$F_{\mathrm{c1}} = \gamma_{\mathrm{Lam}}\omega_{\mathrm{m}}^2 R_{\mathrm{G1}} A_{\mathrm{Fe},1} L_{\mathrm{stk}} = \gamma_{\mathrm{Lam}}\omega_{\mathrm{m}}^2 \frac{D_{\mathrm{r}}}{2} A_{\mathrm{Fe},1} L_{\mathrm{stk}} \cos\vartheta_{\mathrm{b1}} \tag{2.5}$$

with the (2.2), the iron rib thickness results:

$$t_{\mathrm{rib1}} = \nu_\sigma \frac{F_{\mathrm{c1}}}{\sigma_{\mathrm{r}} L_{\mathrm{stk}}} = \nu_\sigma \frac{\gamma_{\mathrm{Lam}}\omega_{\mathrm{m}}^2 D_{\mathrm{r}}^3 \left(2\vartheta_{\mathrm{b1}} - \sin 2\vartheta_{\mathrm{b1}}\right)\cos(\vartheta_{\mathrm{b1}})}{8\sigma_{\mathrm{r}}} \tag{2.6}$$

The red shaded area highlighted in Figure 2.2(b) is the total iron area used to design the second radial rib. In this case, the cross section area of the first flux-barrier, A_{b1}, has to be subtracted by the total area delimited by the rotor periphery and the second flux-barrier (i.e. $2A_{\mathrm{cs2}}$). To do that, it is convenient to define the following ratio:

$$k_2 = \frac{A_{\mathrm{b1}}}{2A_{\mathrm{cs2}}} = \frac{4t_{\mathrm{b1}}\vartheta_{\mathrm{b1}}}{D_{\mathrm{r}}^2\left[2\vartheta_{\mathrm{b2}} - \sin(2\vartheta_{\mathrm{b2}})\right]} \tag{2.7}$$

from which it is possible to compute the actual iron cross section area:

$$A_{\mathrm{Fe2}} = (1-k_2)\frac{D_{\mathrm{r}}^2}{4}\left[2\vartheta_{\mathrm{b2}} - \sin(2\vartheta_{\mathrm{b2}})\right] \tag{2.8}$$

the relative centrifugal force and radial rib thickness can be computed, with the proper substitutions, by means of (2.1) and (2.2), respectively. In general, the computation of the j-th iron cross section area can be extended as follows:

$$A_{\mathrm{Fe}j} = (1-k_j)\frac{D_{\mathrm{r}}^2}{4}\left[2\vartheta_{\mathrm{b}j} - \sin(2\vartheta_{\mathrm{b}j})\right] \tag{2.9}$$

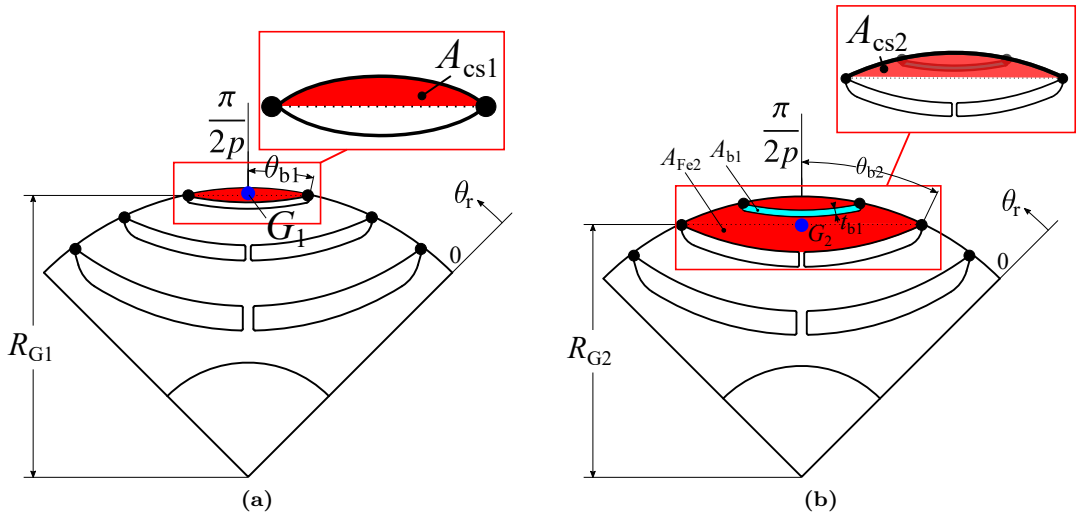

Figure 2.2: Computation of iron channel cross sections in simplified method.

where k_j is:

$$k_j = \frac{4\sum_{i=1}^{j-1} t_{bi}\vartheta_{bi}}{D_r^2\left[2\vartheta_{bj} - \sin(2\vartheta_{bj})\right]} \tag{2.10}$$

Assuming an uniform distribution of the magnetic insulation, for a preliminary design it is possible to substitute k_j with the magnetic insulation ratio k_{air}, defined in section 15.3.

2.2.2 Accurate method

The method proposed in this section is more general than the previous one since it does not refer to a specific rotor geometry. Its accuracy is related to the fact that the iron cross sections areas, referred to as iron channels, and centers of gravity are computed on the basis of the FE mesh. In particular, the j-th iron channel cross section area is given by:

$$A_{Fej} = \sum_{i=1}^{n} a_{ij} \tag{2.11}$$

where a_{ij} is the i-th mesh element of the j-th iron channel and n is its mesh element number. The relative center of gravity, R_{Gj}, is

$$R_{Gj} = \frac{\sum_{i=1}^{n} a_{ij} R_{Gij}}{\sum_{i=1}^{n} a_{ij}} \tag{2.12}$$

where R_{Gij} is the center of radius of the element a_{ij}. Finally, the centrifugal force and radial rib thickness are computed by means of (2.1) and (2.2), respectively.

2.3 Computation of the sleeve thickness

The formulation to design a retaining sleeve comes from the membrane theory since its thickness, t_{sleeve}, is much smaller than the rotor radius. Hence, the relationship between the centrifugal force and the radial pressure is the following:

$$F_{c,sleeve} = \int_{-\pi/2}^{\pi/2} P\cos\vartheta \frac{DL_{stk}}{2} d\vartheta = PDL_{stk} \tag{2.13}$$

where P is the pressure at the air-gap (i.e. contact pressure) and ϑ is the angular coordinate. As reported in Figure 2.3, the pressure is assumed to be uniformly distributed along the rotor periphery so as to link the centrifugal force and the sleeve thickness through:

$$t_{\text{sleeve}} = \nu_{\text{sleeve}} \frac{F_{\text{c,sleeve}}}{2\sigma_{\text{sleeve}} L_{\text{stk}}} \tag{2.14}$$

where ν_{sleeve} and σ_{sleeve} are the sleeve material safety factor and tensile strength, respectively.

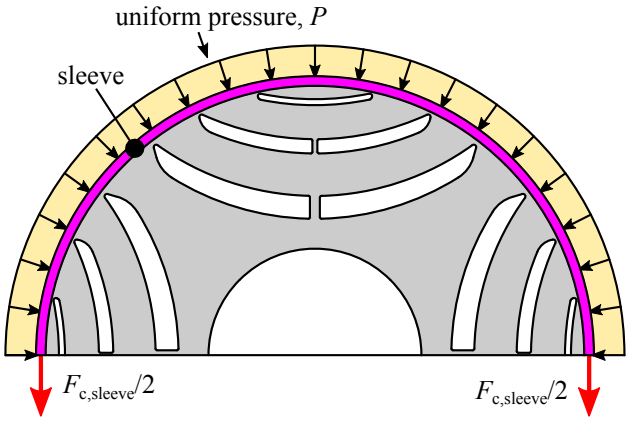

Figure 2.3: Computation of the sleeve thickness.

2.4 Analytical model of the SyR motor

In this section the analytical model of the SyR machine is developed. Only the fundamental magnetomotive force (MMF) is considered. This leads to a simple computation of the d- and q-axis inductances, through which the average electromagnetic torque is derived.

Only the radial ribs are taken into account while the tangential ones are neglected.

2.4.1 d-axis inductance computation

The fundamental harmonic amplitude of the electric loading along the d-axis is:

$$\hat{K}_{\text{sd}} = \frac{3 k_{\text{w}} N_{\text{s}} \hat{I}_{\text{d}}}{\pi D_{\text{s}}} \tag{2.15}$$

where k_{w} is the winding factor, N_{s} is the number of series conductors per phase, D_{s} is the stator inner diameter and I_{d} is the d-axis current.

Figure 2.4(a) sketches the flux lines through the rotor with d-axis electric loading. Usually, in SyR machines, the magnetic reluctance along the d-axis is mainly due to the air-gap reluctance. However, as will be proved in section 2.6, in HS applications, the rotor saturation is higher and greatly affected by the radial rib sizes so that it has to be considered to obtain reliable results from the analytical model. In the present model, the rotor saturation is taken into account multiplying the actual air-gap length by the saturation factor, k_{sat}, that is greater than one [62].

The fundamental of the scalar magnetic potential, $\hat{U}_{\text{sd}}$, along the stator inner diameter can be computed integrating the electric loading yielding:

$$\hat{U}_{\text{sd}} = \frac{\hat{K}_{\text{sd}} D_{\text{s}}}{2p} \tag{2.16}$$

the fundamental harmonic amplitude of the d-axis air-gap flux density, $\hat{B}_{\text{gd}}$, can be computed by means of the Ampère's law as follows:

$$\hat{B}_{\text{gd}} = \mu_0 \frac{\hat{U}_{\text{sd}}}{g\, k_{\text{carter}}\, k_{\text{sat}}} \tag{2.17}$$

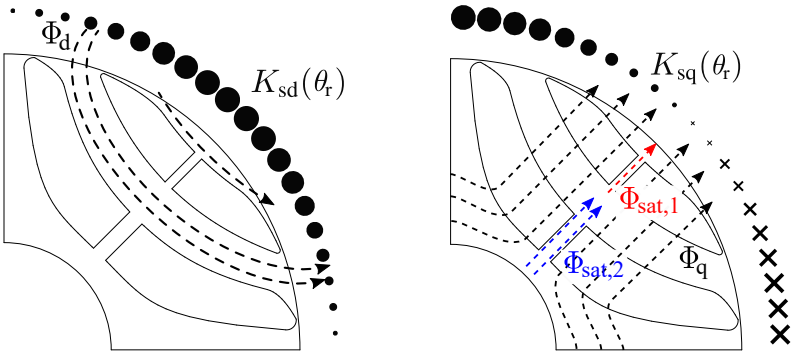

(a) *d*-axis exitation. **(b)** *q*-axis exitation.

Figure 2.4: Qualitative flux lines for a rotor with 2 flux-barriers per pole.

where p is the number of pole pairs and k_{carter} is the Carter coefficient that considers the slot opening effect. The d-axis flux linkage is:

$$\hat{\Lambda}_{\text{d}} = \mu_0 \frac{k_{\text{w}} N_{\text{s}}}{(2p)^2} \frac{D_{\text{s}}^2 L_{\text{stk}} \hat{K}_{\text{sd}}}{g\, k_{\text{carter}}\, k_{\text{sat}}} \tag{2.18}$$

the iron saturation and the slot openings reduce the value of d-axis flux, since these factors decrease the maximum anisotropy of the rotor and have negative effect on the average torque.

2.4.2 q-axis inductance computation

Along the q-axis the flux flows through the rotor flux-barriers and the air-gap as reported qualitatively in Figure 2.4(b).

The q-axis magnetic circuit of a three flux-barriers per pole rotor and its schematic representation are shown in Figure 2.5.

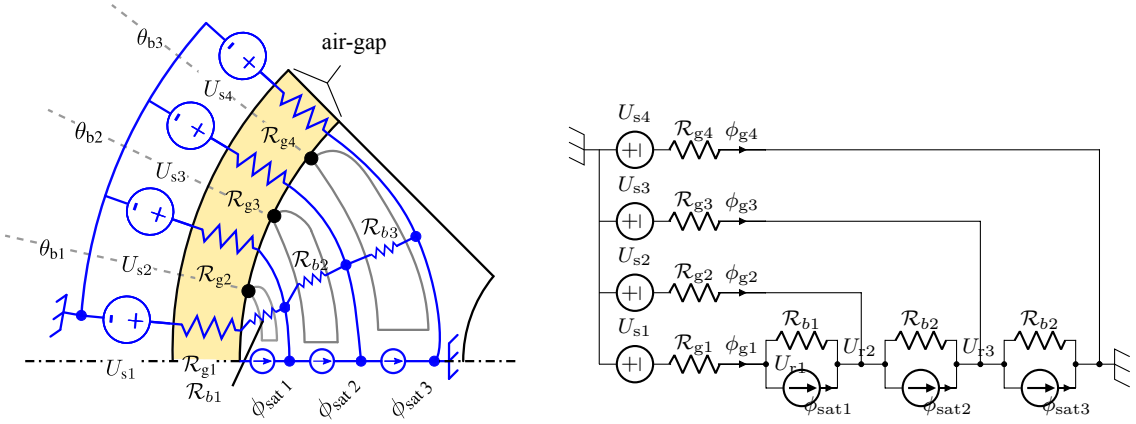

(a) *Schematic representation of the magnetic circuit.* **(b)** *Magnetic circuit.*

Figure 2.5: Magnetic circuit of rotor with 3 flux-barriers per pole.

The fundamental harmonic amplitude of the electric loading along the q-axis is:

$$\hat{K}_{\text{sq}} = \frac{3 k_{\text{w}} N_{\text{s}} \hat{I}_{\text{q}}}{\pi D_{\text{s}}} \tag{2.19}$$

where I_q is the q-axis current. The relative q-axis scalar magnetic potential amplitude is:

$$\hat{U}_\mathrm{sq} = \frac{\hat{K}_\mathrm{sq} D_\mathrm{s}}{2p} \tag{2.20}$$

Its waveform is split in parts according to the rotor geometry. The j-th generator, U_sj (with $j = 1, 2, 3$ in case of 3 flux-barriers per pole), represents the average value of the stator scalar magnetic potential computed between two flux-barrier angles. It is given by integrating the stator scalar magnetic potential as follows:

$$U_\mathrm{sj} = \frac{1}{\vartheta_{\mathrm{b}j} - \vartheta_{\mathrm{b}(j-1)}} \cdot \int_{\vartheta_{\mathrm{b}(j-1)}}^{\vartheta_{\mathrm{b}j}} \hat{U}_\mathrm{sq} \sin\left(p\vartheta_\mathrm{r}\right) d\vartheta_\mathrm{r} \tag{2.21}$$

The equivalent air-gap magnetic reluctance in front of the j-th flux-barrier, already considering the parallel of the two reluctances in symmetrical position with respect to the q-axis, is proportional to the air-gap region delimited by the flux-barrier angles $\vartheta_{\mathrm{b}j}$ and $\vartheta_{\mathrm{b}(j-1)}$, computed as:

$$\mathcal{R}_{\mathrm{g}j} = \frac{g''}{\mu_0 L_\mathrm{stk} D_\mathrm{s} [\vartheta_{\mathrm{b}j} - \vartheta_{\mathrm{b}(j-1)}]} \tag{2.22}$$

where $\vartheta_{\mathrm{b}0} = 0$ and $\vartheta_{\mathrm{b}(N_\mathrm{b}+1)} = \frac{\pi}{2}$. Each flux-barrier is modeled by a magnetic reluctance in parallel to a flux generator. The magnetic reluctance of j-th flux-barrier is a function of the geometrical parameters as:

$$\mathcal{R}_{\mathrm{b}j} = \frac{t_{\mathrm{b}j}}{\mu_0 L_\mathrm{stk} l_{\mathrm{b}j}} \tag{2.23}$$

where $t_{\mathrm{b}j}$ and $l_{\mathrm{b}j}$ are the equivalent thickness and length of the j-th flux-barrier, respectively. The magnetic flux generator, $\phi_{\mathrm{sat}j}$, represents the flux flowing through the iron ribs, computed as:

$$\phi_{\mathrm{sat}j} = B_\mathrm{sat} t_{\mathrm{rib}j} L_\mathrm{stk} \tag{2.24}$$

where $t_{\mathrm{rib}j}$ is the thickness of the j-th iron rib and B_sat is the iron saturation flux density (usually set in the range between 1.8 T and 2 T). Let us note that the t_rib thickness affects the rotor anisotropy and it must be kept as thin as possible, according to the centrifugal force stress.

The scalar magnetic potentials of the iron ribs are computed by means of Thévenin's theorem multiplying the flux flowing through the iron rib by the magnetic reluctances:

$$U_{\mathrm{sat}j} = \mathcal{R}_{\mathrm{b}j} \phi_{\mathrm{sat}j} = \mathcal{R}_{\mathrm{b}j} B_\mathrm{sat} t_{\mathrm{rib}j} L_\mathrm{stk} \tag{2.25}$$

the transformation is explained in Figure 2.6(a) and Figure 2.6(b). The first one shows the initial bipole with the j-th flux generator in parallel with the j-th flux-barrier reluctance. The second one, shows the equivalent circuit composed by a potential generator $U_{\mathrm{sat}j}$ connected in series with the flux-barrier reluctance $\mathcal{R}_{\mathrm{b}j}$.

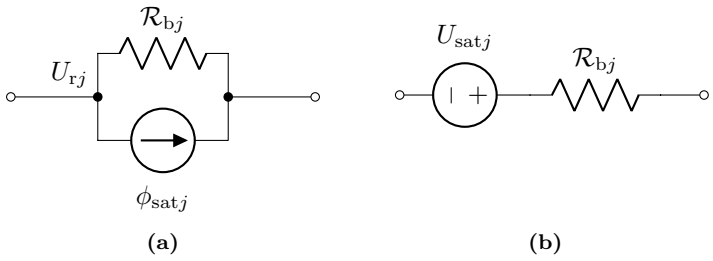

Figure 2.6: (a) Bipole of a flux-barrier with a radial rib and (b) equivalent circuit with Thévenin's theorem.

Solving the magnetic circuit, the three islands potentials $U_{\mathrm{r}1}$, $U_{\mathrm{r}2}$ and $U_{\mathrm{r}3}$ are found. They are respectively:

$$\begin{aligned} U_{\mathrm{r}1} &= \mathcal{R}_{\mathrm{b}1}\phi_{\mathrm{g}1} + U_{\mathrm{r}2} - U_{\mathrm{sat}1} \\ &= -\frac{t_{\mathrm{b}1}}{\mu_0 L_{\mathrm{stk}} l_{\mathrm{b}1}} \int_{\frac{\pi}{2p}-\vartheta_{b1}}^{\frac{\pi}{2p}+\vartheta_{b1}} B_{\mathrm{g}}(\vartheta_r)\frac{D_{\mathrm{s}}}{2} L_{\mathrm{stk}} d\vartheta_r + U_{\mathrm{r}2} - U_{\mathrm{sat},1} \end{aligned} \tag{2.26}$$

$$\begin{aligned} U_{\mathrm{r}2} &= \mathcal{R}_{\mathrm{b}2}(\phi_{\mathrm{g}1} + \phi_{\mathrm{g}2}) + U_{\mathrm{r}3} - U_{\mathrm{sat}2} \\ &= \mathcal{R}_{\mathrm{b}2}\left[\phi_{\mathrm{g}1} - 2\int_{\frac{\pi}{2p}+\theta_{b1}}^{\frac{\pi}{2p}+\theta_{b2}} B_{\mathrm{g}}(\theta_r)\frac{L_{\mathrm{stk}} D_{\mathrm{s}}}{2} d\theta_r\right] + U_{\mathrm{r}3} - U_{\mathrm{sat}2} \end{aligned} \tag{2.27}$$

$$\begin{aligned} U_{\mathrm{r}3} &= \mathcal{R}_{\mathrm{b}3}(\phi_{\mathrm{g}1} + \phi_{\mathrm{g}2} + \phi_{\mathrm{g}3}) - U_{\mathrm{sat}3} \\ &= \mathcal{R}_{\mathrm{b}3}\left[(\phi_{\mathrm{g}1} + \phi_{\mathrm{g}2}) - 2\int_{\frac{\pi}{2p}+\vartheta_{b3}}^{\frac{\pi}{2p}+\vartheta_{b2}} B_{\mathrm{g}}(\theta_r)\frac{L_{\mathrm{stk}} D_{\mathrm{s}}}{2} d\theta_r\right] - U_{\mathrm{sat}3} \end{aligned} \tag{2.28}$$

The rotor island potentials can be finally written as:

$$\begin{aligned} U_{\mathrm{r}1} &= -\frac{\hat{K}_{\mathrm{sq}}}{p^2} D_{\mathrm{s}}\rho_1 + f_{\mathrm{r}1} \\ U_{\mathrm{r}2} &= -\frac{\hat{K}_{\mathrm{sq}}}{p^2} D_{\mathrm{s}}\rho_2 + f_{\mathrm{r}2} \\ U_{\mathrm{r}3} &= -\frac{\hat{K}_{\mathrm{sq}}}{p^2} D_{\mathrm{s}}\rho_3 + f_{\mathrm{r}3} \end{aligned} \tag{2.29}$$

where the three terms $f_{\mathrm{r}j}$ (with $j = 1, 2, 3$) are functions of the scalar magnetic potentials $U_{\mathrm{sat}1}$, $U_{\mathrm{sat}2}$ and $U_{\mathrm{sat}3}$ of the rotor ribs, that is $f_{\mathrm{r}j} = f_{\mathrm{r}j}(U_{\mathrm{sat}1}, U_{\mathrm{sat}2}, U_{\mathrm{sat}3})$. They depend on the rotor geometry and can be obtained solving the magnetic model presented above.

Eq. (2.29) highlights the impact of the rotor ribs. In SyR machines designed for low mechanical speed, the impact of the rotor ribs is negligible [63, 64], so that the terms $f_{\mathrm{r}j}$ are often omitted in (2.29).

In HS applications, the radial rib thicknesses are so big that their impact on the machine performance cannot be neglected. Therefore, it is mandatory to consider the scalar magnetic potentials $U_{\mathrm{sat}1}$, $U_{\mathrm{sat}2}$ and $U_{\mathrm{sat}3}$ in the model.

As for the *d*-axis, the flux along the quadrature axis is computed integrating the air-gap flux density in a pole pitch:

$$\phi_{\mathrm{q}} = \int_0^{\frac{\pi}{p}} \mu_0 \frac{-U_s(\theta_r) + U_r(\theta_r)}{g''} \frac{D_{\mathrm{s}}}{2} L_{\mathrm{stk}}\, d\vartheta_r \tag{2.30}$$

finally, the flux linkage Λ_{q}, is:

$$\Lambda_{\mathrm{q}} = \mu_0 \frac{k_{\mathrm{w}} N_{\mathrm{s}}}{(2p)^2} \frac{D_{\mathrm{s}}^2 L_{\mathrm{stk}} \hat{K}_{\mathrm{sq}}}{g''} \left[1 - 4\sum_{j=1}^{3}(\rho_j - \rho_{j-1})(\vartheta_{\mathrm{b}j} - \vartheta_{\mathrm{b}(j-1)})\right] \tag{2.31}$$

where the terms ρ_j are detailed reported in [65]. The first term of (2.31) does not consider neither the flux-barriers nor the iron ribs. For this reason, its expression is the same as for the *d*-axis flux linkage (2.18) and can be considered constant. The terms with ρ_j (with $j = 1, 2, 3$) depend on the geometry of the rotor flux-barriers. They are negative, in the sense that they tend to decrease the flux along the *q*-axis for given current, increasing the rotor anisotropy. Therefore, their effect is beneficial as far as the electromagnetic torque is concerned.

2.4.3 Torque and Power equations

Substituting (2.25) in (2.31), after some computations, the electromagnetic torque results as a function of the rotor geometry, the two axis currents, and the rotor mechanical speed limit. It can be expressed as:

$$T = X - Y\omega_{\mathrm{m}}^2 \tag{2.32}$$

where the variables $X = X(I_{\mathrm{d}}, I_{\mathrm{q}})$ and $Y = Y(I_{\mathrm{d}})$, reported in Appendix 15.3.5, contain geometrical and winding parameters.

Let us remark that (2.32) indicates the torque exhibited by a motor designed for reaching the mechanical speed limit ω_{m}. It is worth noticing that the first term is independent on the rotor mechanical speed limit, i.e. it is constant, while the second one is a square function of the mechanical speed limit. Multiplying (2.32) by ω_{m}, the output power is:

$$P = X\omega_{\mathrm{m}} - Y\omega_{\mathrm{m}}^3 \tag{2.33}$$

The critical speed limit at which the output power (2.33) is maximum is obtained posing to zero the derivative of the power with respect to ω_{m}. The critical speed limit then results:

$$\omega_{\mathrm{m,cr}} = \sqrt{\frac{X}{3Y}} \tag{2.34}$$

Figure 2.7 shows the qualitative behavior of the torque and the power versus the mechanical speed limit. In the shaded region, the torque is constant since all the rib thicknesses, equal to the lamination width (t_{Lam}), do not vary because they are sufficient to counteract the low centrifugal stress. Thus the power increases linearly with the mechanical speed limit. The speed limit, $\tilde{\omega}_{\mathrm{m}}$, after which the radial ribs have to be modified, can be computed setting, for each flux-barrier, $t_{\mathrm{rib}} = t_{\mathrm{Lam}}$ in (2.2).

For $\omega_{\mathrm{m}} > \tilde{\omega}_{\mathrm{m}}$ the thickness of the iron ribs increases with the square of the mechanical speed limit as shown in (2.2). The torque decreases monotonically because of (2.32) while the power increases until the critical speed limit, $\omega_{\mathrm{m,cr}}$ computed by (2.34). After this point the power decreases: this means than the anisotropy of the machine is compromised by the high iron ribs thickness.

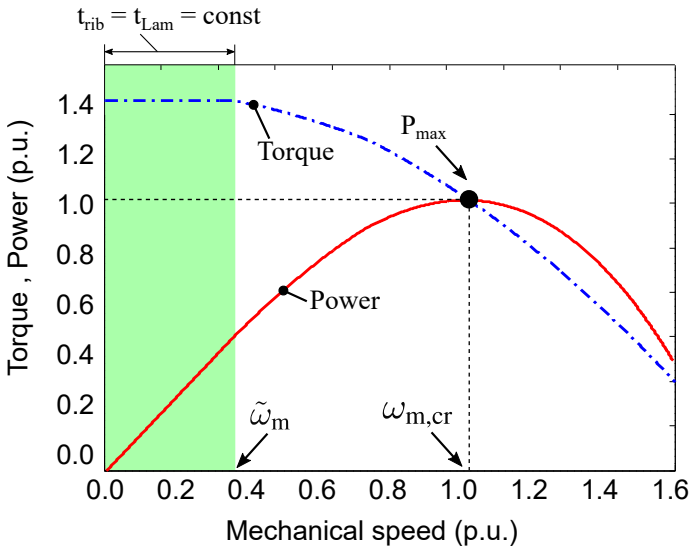

Figure 2.7: Torque and power versus mechanical speed limit. Each point of the curves refers to a different rotor geometry designed for a specific speed.

2.5 Case study results

The analytical model has been applied to a case study machine. The main motor parameters are reported in Table 2.1. A NO20 lamination has been adopted to limit the iron losses, due to the high operating frequencies. All the working points have been evaluated in maximum torque per ampere (MTPA) condition. The saturation factor has been computed for some rotor geometries by means of FE analysis. In particular, it has been computed as the ratio between the d-axis flux linkage obtained with linear and nonlinear magnetic parts with d-axis current only. In the linear problems, the iron bridges regions material has been set as air to avoid magnetic short circuits and wrong results. All the other points have been computed by means of interpolation.

Table 2.1: Main data of the machine under analysis.

Motor part	Symbol	Value
Outer diameter	D_e	240 mm
Inner diameter	D_s	140 mm
Stack length	L_stk	140 mm
Pole number	$2p$	4
Slot number	Q	48
Slot height	h_s	25 mm
Tooth width	w_t	5 mm
Air-gap	g	1 mm
Current	$\hat{I}$	90 A
Iron lamination		NO20

Figure 2.8(a) shows both torque and power behaviors versus the mechanical speed limit obtained with three different safety factors: 1.5, 2 and 2.5. The constant torque region is limited because of thin lamination thickness. It is evident that the torque decreases as the safety factor increases. In fact, with a larger rib thickness, the q-axis flux increases and the rotor anisotropy decreases. The higher the mechanical speed limit, the higher the torque reduction. In particular, at 20 krpm the torque ranges from about 75 N m to 80 N m, depending on the safety factor adopted. At 60 krpm only the motor with the lowest safety factor is still capable of producing power.

Figure 2.8(b) shows the d- and q-axis inductances versus the mechanical speed limit. The d-axis inductance does not depend directly on the mechanical speed limit, i.e. on the radial ribs thickness. Conversely, the q-axis inductance is greatly affected by the mechanical speed limit since the iron rib thickness is a square function of the mechanical speed limit, as indicated in (2.2). Furthermore, as observed from the torque behavior, the increment depends on the safety factor because it implies a larger leakage-flux. The anisotropy ratio, ξ, is also reported in Figure 2.8(b) and it decreases with the rotor speed limit as expected. The power factor, computed with a fixed current angle equal to $\pi/4$ as in [63], versus the mechanical speed limit is reported in Figure 2.8(c). It can be noted that for low mechanical speed limits the power factor is about 0.65 that is quite usual for a SyR machine. As the mechanical speed limit increases, the power factor decreases because of the rapid increase of the q-axis inductance. In particular, it is lower than 0.5 for mechanical speed limits higher than 24 krpm, for $\nu_\sigma = 2.5$ and 30.5 krpm, for $\nu_\sigma = 1.5$.

2.6 Finite Element validation

2.6.1 Flux-barriers rotor

In order to confirm the power and torque values obtained by means of the analytical model, some FE analyses have been carried out.

Figure 2.9 shows the flux density plots of three different motors whose radial ribs have been designed according to the procedure described above (See chapter 4 for more details about the rotor flux-barriers design). In particular, Figure 2.9(a) refers to the motor designed for a speed

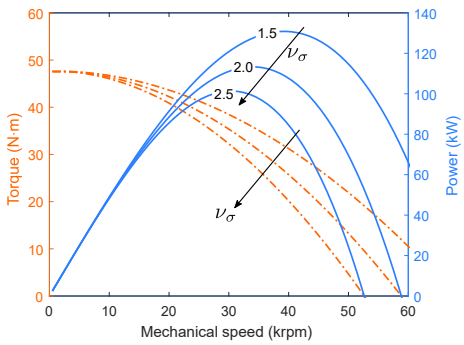

(a) *Power (solid line) and torque (dash-dotted line).*

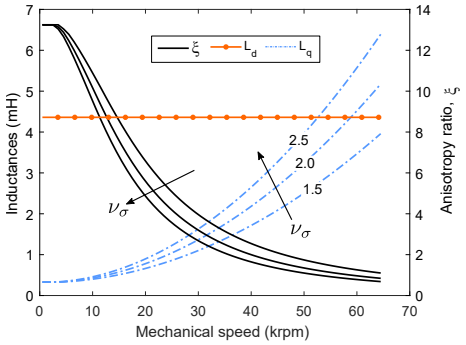

(b) *d- and q-axis inductances and anisotropy ratio.*

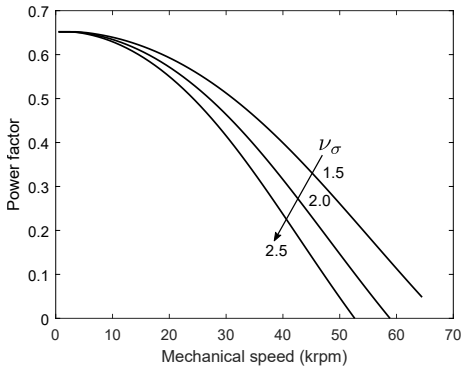

(c) *Power factor.*

Figure 2.8: HS-SyR output versus the mechanical speed limit with different safety factors ν_σ.

limit lower than $\tilde{\omega}_{\mathrm{m}}$ while the motors in Figure 2.9(b) and Figure 2.9(c) are designed for the same speed limit of 35 krpm but with safety factors equal to $\nu_\sigma = 1.5$ and $\nu_\sigma = 2.5$, respectively. It can be observed that, in the first motor, the radial ribs are heavily saturated because of their small size as in the common applications. In the other two motors the magnetic situation is quite different since the radial ribs saturation is lower than the iron channel one. This aspect is amplified by the safety factor adopted. This is essentially due to the higher q-axis flux effect that arises as the speed limit increases.

Figure 2.10 shows the torque behavior versus the rotor position of the two motors reported in Figure 2.9(b) and Figure 2.9(c). As already observed, the motor with the higher safety factor reaches a lower average torque of about 20 %. Comparing the results of Figure 2.8(a) and Figure 2.10 it can be noted that the analytical model, once the saturation factor is known, is able to correctly predict the torque values with different safety factors in a specific speed limit. Furthermore, Figure 2.10 shows that the torque ripple is almost the same, even with different safety factors, thanks to the choice of the flux-barrier end angles to minimize the torque oscillations.

2.6.2 Salient pole rotor

The salient pole rotor, shown in Figure 2.11(a), is characterized by an intrinsic structural robustness so that it does not need to be mechanically designed for each mechanical speed. For this reason, the rotor anisotropy and the maximum average torque do not depend on the mechanical speed limit. This implies that the power limit curve is a straight line whose slope is equal to the maximum average torque.

In most of the common applications, the flux-barriers rotor is preferred to the salient pole one for its high magnetic anisotropy and low torque ripple. In HS applications, the effect of the large radial ribs on the rotor anisotropy could make the salient pole rotor a valid alternative to the flux-

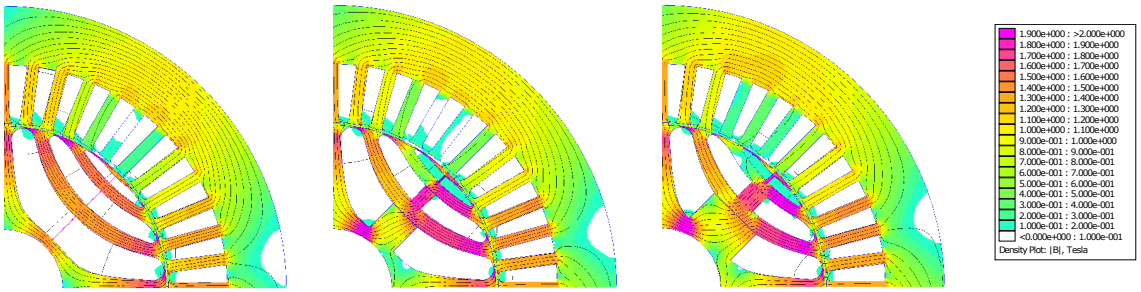

(a) $\omega_{\mathrm{m}} < \tilde{\omega}_{\mathrm{m}}$. **(b)** $\omega_{\mathrm{m}} = 35\,\mathrm{krpm}$ with $\nu_\sigma = 1.5$. **(c)** $\omega_{\mathrm{m}} = 35\,\mathrm{krpm}$ with $\nu_\sigma = 2.5$. **(d)** Legend.

Figure 2.9: Flux density plots of three different HS SyR machines. The first one is designed for a speed limit lower that the critical one. The second and third one are designed for the same speed limit but different safety factors.

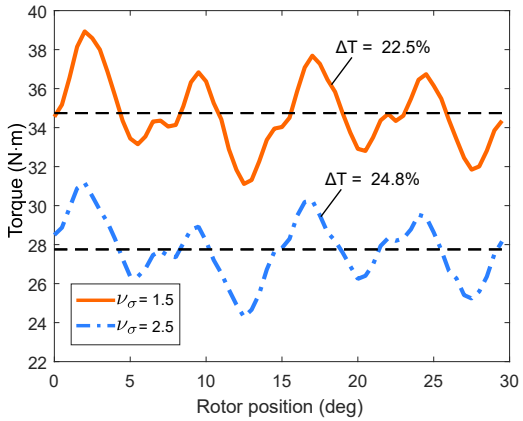

Figure 2.10: Torque versus rotor position of the motors in Figure 2.9(b) and Figure 2.9(c).

barrier one beyond a determined mechanical speed limit. The aim of this section is to determine a mechanical speed limit above which the salient pole rotor exhibits a torque and a power higher than the flux-barriers ones.

The rotor geometry is reported in Figure 2.11(a). The polar shoe spans an angle of $\pi/4$ electrical degrees and the air-gap is $g = 1\,\mathrm{mm}$.

2.6.3 Rated radius

Figure 2.11(b) shows the torque behavior versus the rotor position of the salient pole rotor (dashed line). The average torque is 37.85 N m (20% lower than the flux-barriers rotor designed for low speed limit) with a ripple of about 70%. However, the torque ripple can be greatly reduced skewing the rotor by the slot angle, $\alpha_{\mathrm{s}} = 7.5°$. With this solution the torque ripple reduces down to 4.06% without compromise too much the average torque (continuous line in Figure 2.11(b)).

Figure 2.12(a) and Figure 2.12(b) compare the torque and the power limit curves of the salient pole rotor with the flux-barriers ones. It is possible to observe that the mechanical speed limit in which the torque and power density of the salient pole rotor are higher than the flux-barriers one depends on the safety factor. In particular, with $\nu_\sigma = 2.5$, the salient pole rotor achieves a higher torque density than the flux-barriers one for mechanical speed limits over 24 krpm. The mechanical speed limit is about 31 krpm with a safety factor equal to 1.5.

In conclusion, for the given stator geometry, the salient pole rotor should be preferred to the flux-barriers one for mechanical speed limits higher than 24 krpm (with the highest safety factor) or 31 krpm (with the lowest safety factor).

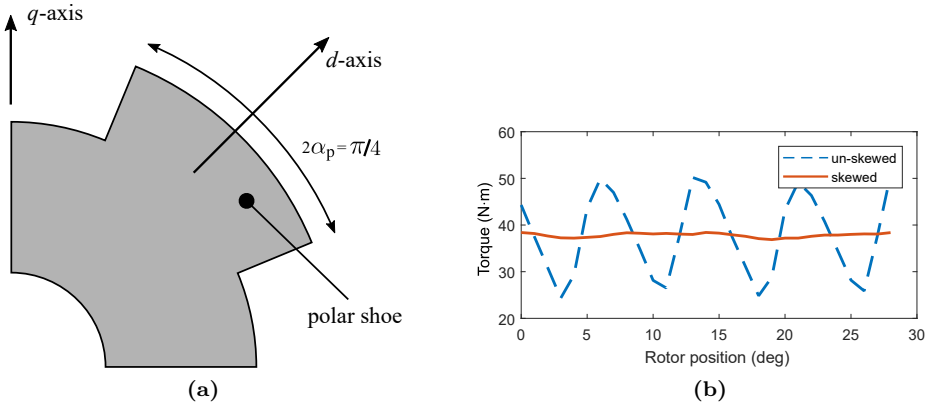

Figure 2.11: Salient pole rotor sketch (a) and torque versus rotor position with and without skewing (b).

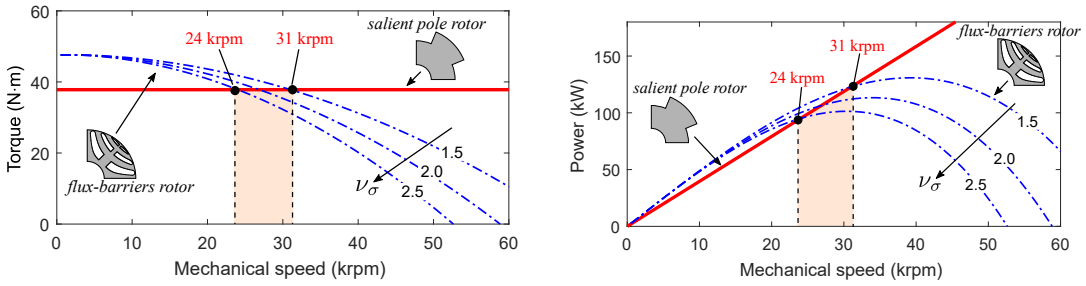

(a) Torque versus mechanical speed limit. **(b)** Power versus mechanical speed limit.

Figure 2.12: Power and torque versus mechanical speed limit with different safety factors ν_σ: comparison between flux-barriers rotor and salient pole rotor.

2.6.4 Different radial dimensions

The same study has been carried out on two similar machines whose transversal dimensions have been reduced of 20% and 40% with respect to the original size. The resulting torque and power limit curves, obtained with different safety factors, are reported in Figure 2.13(a) and Figure 2.13(b).

It the first case the mechanical speed limit range in which the flux-barrier rotor exhibits higher torque than the salient pole one is between 32 krpm and 42 krpm depending on the safety factor. Such speed shifting is due to the fact that the total iron mass of the rotor is lower than the original case, hence the radial ribs presents lower thickness with beneficial effect on the rotor anisotropy. Moreover, the maximum torque of the flux-barrier rotor achieved at the lowest mechanical speed limit is 42% higher than the salient pole one.

In the second case, the maximum torque of the flux-barrier rotor is about 12% higher than the salient pole one so that the two rotor topologies appear to be more and more comparable as the radial size reduces. This because the contribute of the iron bridges (tangential and radial ones) is higher since their dimensions cannot be rescaled proportionally below the manufacturing limit but are kept fixed. On the contrary, the salient pole rotor is not affected by this aspect and it becomes a possible alternative to the flux-barrier rotor in such conditions. The speed range in which the flux-barrier rotor yields higher torque is between 22 krpm and 29 krpm which results to be lower than the previous case.

2.7 Conclusion

An analytical model has been developed dealing with a SyR machine designed for high mechanical speeds. The presence of the iron ribs is fundamental to guarantee the rotor structural integrity under centrifugal load. However, they also increase the q-axis flux causing a significant reduction

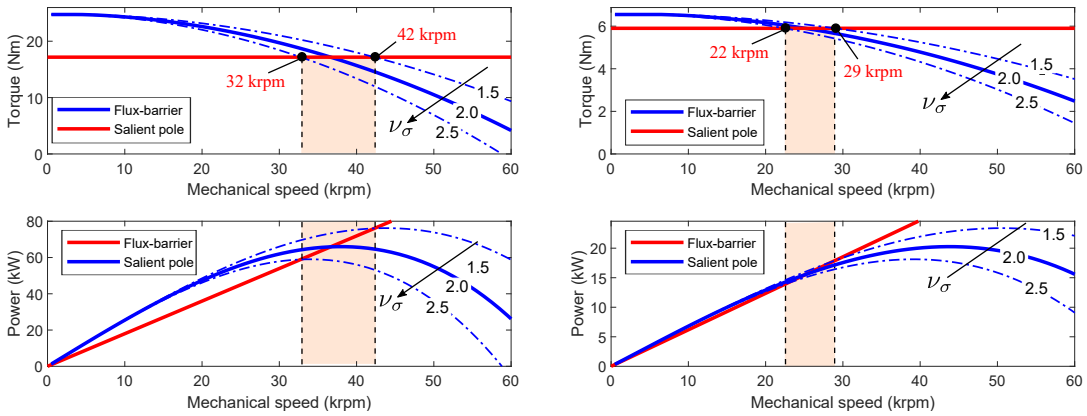

(a) 80% of the original size. **(b)** 60% og the original size.

Figure 2.13: Power and torque versus mechanical speed limit with different safety factors and radial dimensions: comparison between flux-barriers rotor and salient pole rotor.

of the output torque. Through the analytical model it is possible to quickly evaluate their impact on the motor performance. In particular, it has been shown that a theoretical maximum output power exists for a given machine geometry and a given critical speed limit.

Finally, a comparison between several flux-barriers rotors, designed for different speed limits, and a salient pole rotor performances has been carried out in order to determine the mechanical speed limit in which each rotor has the best performance in terms of torque and power density. From the FE analysis it has been observed that, for the given stator geometry, the salient pole rotor becomes a valid alternative to the flux-barriers one for mechanical speed limits higher than 24 krpm and 31 krpm with a safety factor equal to 2.5 and 1.5, respectively.

Chapter 3

Power Limits Curves of HS-SyR Machine by means of Reluctance Networks

In chapter 2 an analytical model to describe the HS-SyR power limit versus mechanical speed limit has been developed. Despite its relative simplicity, the method, referred to as simplified reluctance network (SRN), needs almost one FE evaluations to estimate the machine saturation properly for a specific rated mechanical speed limit. More FE evaluations are needed to estimate the machine behavior in a wide mechanical speed limit range.

The aim of the present chapter is to better describe the magnetic behavior of the HS-SyR rotor by means of an improved reluctance network (IRN) [66, 67] that takes into account the radial ribs contribution on the rotor saturation and the cross coupling between d- and q-axis by means of nonlinear reluctances [8].

To prove the effectiveness of the proposed method some rotors are designed for different mechanical speed limits. For simplicity, only the radial rib thickness are mechanically designed, following the procedure discussed in section 2.2, while the rotor flux-barrier angles and insulation ratio are kept fixed to the values reported in Table 3.1. The stator geometry is given and its main data are reported in Table 3.1. All the motors performance are evaluated in MTPA condition.

All the motors are analyzed by means of FE magnetostatic simulations and the results are compared with the IRN ones providing the relative conclusion.

3.1 Improved reluctance network

As previously mentioned, the nonlinear magnetic behavior of the iron parts (i.e iron channels and radial ribs) and the cross-coupling effect, due to the higher q-axis flux, have to be taken into account in order to better describe the rotor saturation. To this purpose, a magnetic model based on an improved reluctance network (IRN) is adopted [67].

In such approach, all the motor parts are modeled by a magnetic reluctance or a MMF generator. In particular, nonlinear and linear magnetic reluctances are used to model the iron and the air regions, respectively. Therefore, the proposed IRN is solved in a iterative process in which the unknowns are the flux density values in each reluctance [67, 68]. In this context, there is a seed value for each magnetic flux density, then the equation system is solved and the new values of magnetic fluxes are obtained. Then, if these values are different from the seed values, the process will start again using the solutions as seed values.

The aim of this IRN is to model the iron saturation locally with particular care of the rotor radial ribs and channels. This allows to take into account the unusual flux-density distribution in the rotor that cannot be described accurately with the SRN.

Table 3.1: Main data of the motors.

Motor part	Symbol	Value
Outer stator diameter	D_e	300 mm
Inner stator diameter	D_s	190 mm
Stack length	L_stk	100 mm
Pole number	$2p$	4
Slot number	Q	48
Slot height	h_s	25 mm
Tooth width	w_t	6.76 mm
Air-gap	g	1 mm
Flux-barrier angles	$\vartheta_\mathrm{b1}, \vartheta_\mathrm{b2}, \vartheta_\mathrm{b3}$	14.8°, 26.7°, 38.7°
Magnetic insulation ratio	k_air	0.4
Series conductor per slot	n_ncs	1
Phase Current	I	572 A peak
Iron lamination		N020
Ultimate tensile strength	σ_r	500 MPa

3.1.1 Stator and air-gap magnetic network

A sketch of the stator magnetic network is shown in Figure 3.1(a). Each stator slot is modeled by two magnetic reluctances (the tooth and the yoke one) and a MMF generator. The reluctances are given by:

$$\mathcal{R} = \frac{l}{\mu_\mathrm{steel}(H)\, S} \tag{3.1}$$

where $\mu_\mathrm{steel}(H)$, function of the magnetic field, is the absolute magnetic permeability of the lamination, l is the length in the flux direction and S is the surface normal to flux direction.

The value of each MMF generator depends on the winding distribution and on the time instant [66]. The direct MMF is obtained with:

$$I_a = n_\mathrm{cs} I \qquad \text{and} \qquad I_b = I_c = -n_\mathrm{cs} I/2 \tag{3.2}$$

while the q-axis MMF is obtained with:

$$I_a = 0 \qquad \text{and} \qquad I_b = -I_c = \sqrt{3}/2\, n_\mathrm{cs} I \tag{3.3}$$

in general, for a generic current vector amplitude, $\hat{I}$, and angle, $\alpha_\mathrm{i}^\mathrm{e}$, the phase currents I_a, I_b and I_c are computed by means of the Park's anti-transformation and used to determine the stator MMF generator values. The air-gap in front of each tooth is modeled with a magnetic reluctance computed as follows:

$$\mathcal{R}_\mathrm{g} = \frac{g\, k_\mathrm{carter} Q}{\mu_0 \pi D_\mathrm{si}} \tag{3.4}$$

the slotting effect is taken into account with the Carter's coefficient as for the SRN. Conversely, the saturation factor is not necessary since the reluctance network is nonlinear.

3.1.2 Rotor magnetic network

The rotor reluctance networks of one pole is shown in Figure 3.1(b). The iron channels and the iron bridges (i.e. radials and tangentials) are modeled by nonlinear magnetic reluctances in order to take into account the saturation while the flux-barrier regions are modeled by linear magnetic reluctances. It is worth noticing that the proposed network is not unique but it is trade-off between the magnetic accuracy and the solving time consumption. Regarding the latter aspect, it has been observed that the IRN allows to reduce the computational time up to 75% with respect to the commercial software Flux [66].

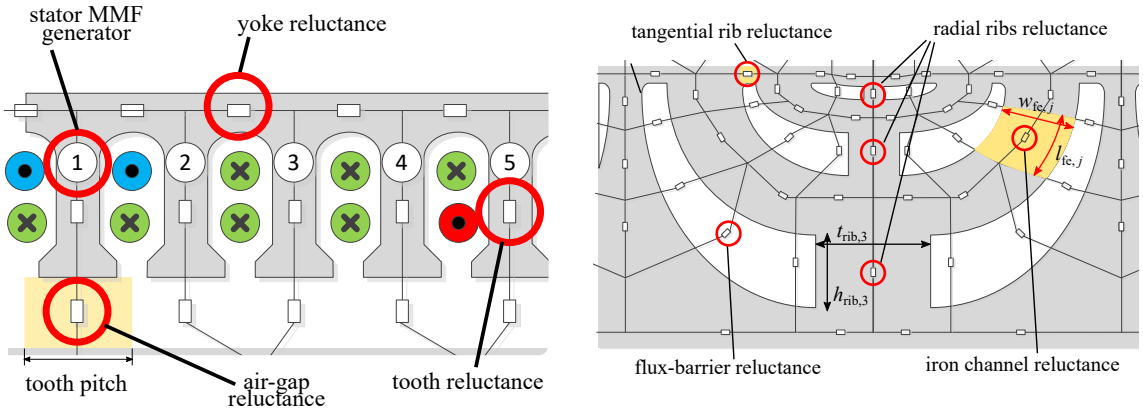

(a) *Stator network.* **(b)** *Rotor network.*

Figure 3.1: Improved magnetic reluctance magnetic network of a HS-SyR machine with three flux-barriers per pole.

3.2 Finite element analysis results

Figure 3.2 reports the flux density plots of the four different rotors designed for 500 rpm, 10 krpm, 20 krpm and 25 krpm with a safety factor $\nu_\sigma = 2.5$. It is quite evident the high influence of the radial rib thicknesses on the rotor saturation. In particular, when the radial ribs are saturated the flux density levels in the iron channels are lower than 1.64 T, as usual. This condition is achieved for mechanical speed limits lower than 10 krpm. As the mechanical speed limit increases (i.e. near 20 krpm), the radial rib thickness of the third flux-barrier is such that the flux density level, in the same rib, is lower than the iron channel one. The saturation of the other radial ribs is higher with respect to the third one. At the highest mechanical speed limits (i.e. 25 krpm), the saturation of the rotor parts is reversed: the iron channels flux density levels are about 1.9 T while, within the radial ribs, the flux density is lower than 1.7 T.

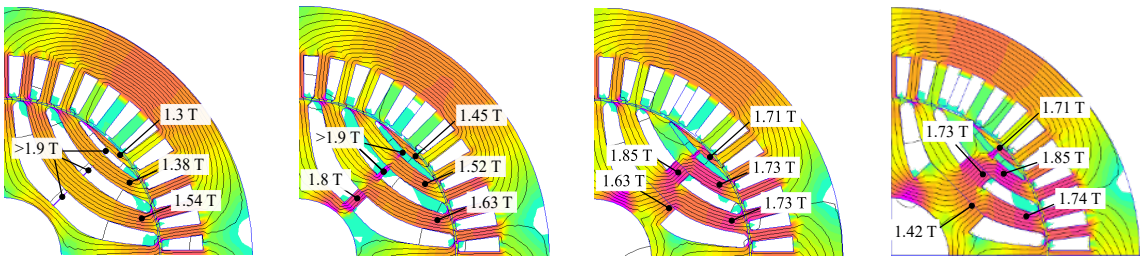

(a) 500 rpm. **(b)** 10 krpm. **(c)** 20 krpm. **(d)** 25 krpm.

Figure 3.2: Flux density plots of different HS-SyR rotor designe for different mechanical speed limits.

The FE inductances and the saliency ratio behaviors versus the mechanical speed limit are reported in Figure 3.3. It is evident that both the inductances depend on the mechanical speed limit unlike the analytical model seen in chapter 2. The d-axis inductance decreases as the mechanical speed limit increases because of the iron channels saturation. The q-axis inductance increases with the mechanical speed limit because of the higher flux linkage that flows through the iron ribs.

3.3 Results comparison

This section reports the comparison between the FE and the proposed reluctance networks results in terms of torque and power limit curves.

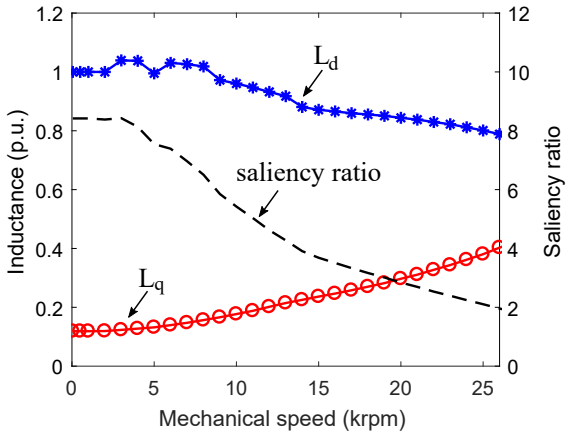

Figure 3.3: FEA results: inductances and saliency ratio versus mechanical speed limit. The base value is the d-axis inductance at 0 rpm.

3.3.1 Simplified reluctance network results

Figure 3.4(a) and Figure 3.4(b) show the torque and the mechanical power behaviors versus the rotor mechanical speed limit obtained with SRN and FE analysis. For mechanical speed limits lower than 10 krpm, there is a good agreement between the curves resulting from the two methods. This is because the analytical model hypotheses, discussed in chapter 2 (i.e. radial ribs saturated and low iron channel saturation), are met. For higher mechanical speed limits, the larger radial rib thicknesses affect the flux density distribution in the rotor channels so that the analytical model overestimates the electromagnetic torque with respect to the FE analysis results. In particular, at the highest mechanical speed limit (25 krpm), the torque computed analytically is 36% higher than the FE one.

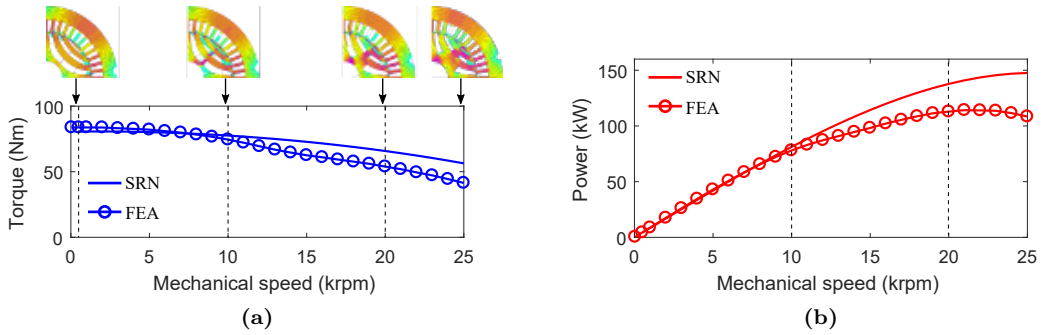

Figure 3.4: Torque (a) and Power (b) versus mechanical speed limit: comparison between the simplified reluctance network and FE analysis results.

3.3.2 Improved reluctance network results

The torque and the power versus the mechanical speed limit curves, obtained with IRN and FE analysis, are reported in Figure 3.5(a) and Figure 3.5(b), respectively. There is a good agreement between the results in the whole mechanical speed limit range. However, at the highest mechanical speed limit, the IRN torque is 11% higher than FE analysis one. The same observation is valid for the power curves. This is due to the fact that, as reported in Figure 3.6(a), the IRN underestimates the q-axis inductance and so the relative flux linkage. Conversely, along the d-axis, there is a good agreement between FE analysis and IRN curves. The underestimation of the q-axis flux linkage is related to the not uniform flux density distribution within the radial rib regions as can be observed

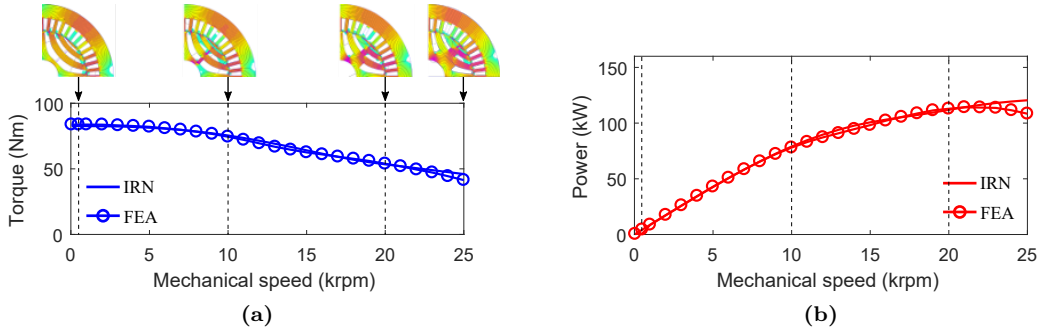

Figure 3.5: Torque (a) and Power (b) versus mechanical speed limit: comparison between IRN and FE results.

in Figure 3.2(d). A better estimation of the flux linkage that flows through the radial ribs can be achieved increasing the number of magnetic reluctances associated.

From the same curves, it can be noted that near 5000 rpm and 15 000 rpm the d-axis inductance presents some discontinuities. In the first case, the flux linkage drop is due to the saturation of the inner iron channel as showed on top of Figure 3.6(b) and the variation of the MTPA current angle that passes from 57.5° to 60°. The second flux linkage drop is caused by the change of the saturation level in the third radial rib and iron channel. In fact, as the mechanical speed limit steps over 13 000 rpm, the radial rib flux density decreases below the knee point causing an increase of the flux linkage which pass through it. This determines, in turns, an higher saturation of the third iron channel, as reported on bottom of Figure 3.6(b), which motivates the reduction of d-axis flux linkage.

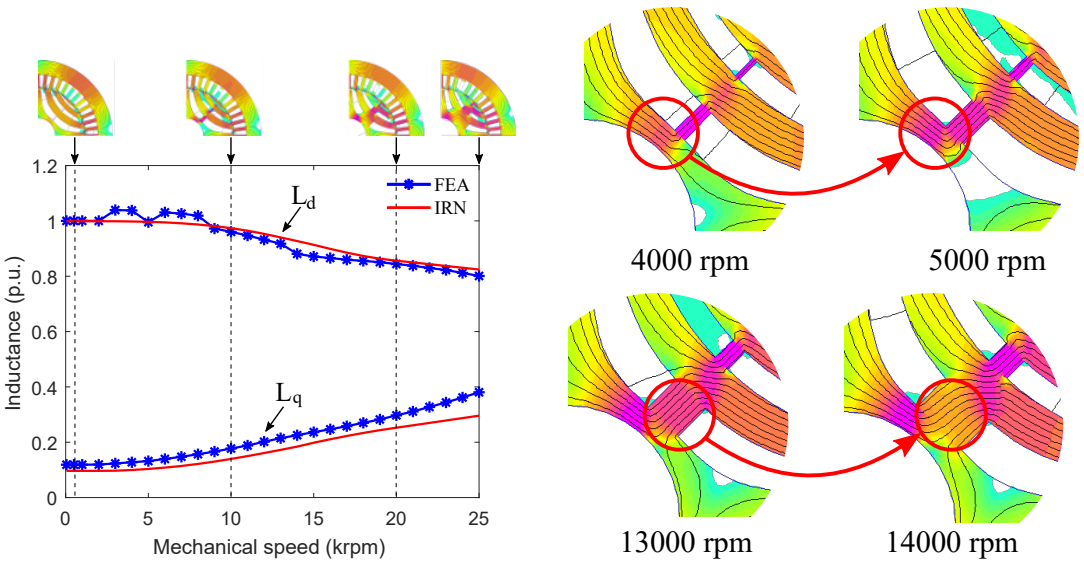

(b) *Flux density plot at different mechanical speed limits.*

Figure 3.6: Inductances versus mechanical speed limit: comparison between FE analysis and IRN results. The base value is the FE analysis d-axis inductance at 0 rpm.

3.4 Conclusion

This chapter dealt with the analysis of HS-SyR by means of two different reluctance networks: the simplified one and improved one. Some motors have been designed for different mechanical

speed limits taking into account both magnetic (flux-barriers shape) and structural aspects (radial rib thicknesses) to prove the suitability of the proposed methods for the analysis and design of HS-SyR. From a comparison with the FE analysis results it has been observed that the simplified reluctance network does not allow to describe the motors performance with accuracy in a wide mechanical speed limit range since the rotor saturation in the radial ribs and in the iron channels is not modeled properly. This is because the simplified model does not describe locally the iron channels saturation and considers the radial ribs to be saturated with a constant flux density regardless of the radial rib thicknesses. These simplifications are reasonable with the common SyR motors but are not met as the radial rib thicknesses and the saturation of the iron channels increase with the mechanical speed limit as in the considered case study.

Conversely, a good agreement has been found between the FE and the improved reluctance network results in the whole considered mechanical speed limit range. This because the improved reluctance network takes into account the saturation of stator and rotor locally since all the motor regions are modeled by magnetic reluctances, which are nonlinear for the iron parts, and magnetomotive force generators.

Chapter 4

Design Methodology for HS-SyR Machines

4.1 Introduction

In this chapter two alternative guidelines to design HS-SyR machines are presented [3]. The main target of these guidelines is the accurate design of the rotor geometry to obtain a robust mechanical structure, a high torque density and a low torque ripple. The stator geometry is fixed and its main data are reported in Table 4.1. A typical RMS value of 6 A/mm^2 is set for the current density.

In the first one, referred to as semi-analytical design approach (SADA), the flux-barrier angles are selected so as to minimize the torque oscillation [69–72] while the magnetic insulation ratio, which yields the highest torque density, is determined by means of a FE parametric analysis according to a fixed mechanical speed limit. The radial ribs are designed with the method, described in subsection 2.2.1, since the exact iron channel cross section areas are not known in the preliminary design.

In the second one, referred to as FE-based optimization (FEO), a multi-objective optimization of the rotor geometry is carried out selecting the flux-barrier angles and magnetic insulation ratio as parameters and the average torque and torque ripple as cost functions. The radial ribs are accurately designed during the optimization by means of the method presented in subsection 2.2.2.

Finally, after a comparison of the two approaches, a thorough analysis of the optimal solution is carried out. In particular, a detailed FE electromagnetic analysis is performed to verify the actual machine performance focusing also on the accurate iron losses estimation. Moreover, a FE mechanical analysis is also carried out, by means of the procedure reported in chapter 14, to verify the rotor structure integrity and the effectiveness of the analytical iron ribs design method.

4.2 Semi-analytical design approach

In this section the main steps of the SADA approach are described. At first, a brief resume of the analytical model used for the flux-barrier angle choice is presented [69]. For simplicity, only one and two flux-barriers per poles are considered. Then, the optimal magnetic insulation ratio is selected by means of a FE parametric study. For this reason, such a design a approach is called *semi-analytical*.

4.2.1 Flux-barrier angles selection

The assumptions of the considered analytical model are:

(i) to neglect the saturation of the ferromagnetic material;

(ii) to neglect the stator slotting effect;

Table 4.1: Main motor data.

MOTOR OUTPUT			
Rated voltage (RMS)	V_{N}	400	V
Number of poles	$2p$	4	-
Mechanical speed	n	30 000	rpm
GEOMETRICAL DATA			
Outer diameter	D_{e}	152	mm
Inner diameter	D_{i}	90	mm
Stack length	L_{stk}	100	mm
Number of poles	$2p$	4	-
Number of slots	Q	36	-
Slot height	h_{s}	16.3	mm
Tooth width	w_{t}	4.14	mm
Air-gap	g	0.7	mm
WINDING			
Conductors in slot	n_{c}	6	-
Number of parallel paths	n_{pp}	2	-
Coil pitch	y_{q}	8	-
LAMINATION PROPERTIES			
Name			N020
Tensile strength	σ_{r}	500	MPa
Mass density	γ_{Fe}	7650	kg/m^3
Safety factor	ν_σ	2.5	-

(iii) to neglect the rotor iron ribs;

(iv) to consider rotor magnetic scalar potentials constants and with constant steps.

Through this model it is possible to predict the combinations of flux-barrier angles which lead to the lower torque ripples.

One flux-barrier rotor

Torque harmonics are produced by a couple of electric loading harmonics. In fact, the torque ripple of order h is due to the electric loading harmonics $\nu_1 = (1-h)$ and $\nu_2 = (1+h)$, where $h = 6n\,,\ n \in \mathbb{N}$.

The hypothesis of constant current angle, $\alpha_{\mathrm{i}}^{\mathrm{e}} = 45°$, is considered throughout the following derivation as it represents the worst case scenario in practical applications ($\alpha_{\mathrm{i}}^{\mathrm{e}} \geq 45°$). Then, the torque ripple expression for the two harmonics becomes [69]

$$\left[\Delta T_{\mathrm{m}}^{(h)}\right]^2 \propto \left[\frac{\sin \nu_1 \vartheta_{\mathrm{b}}^{\mathrm{e}}}{\nu_1}\right]^2 + \left[\frac{\sin \nu_2 \vartheta_{\mathrm{b}}^{\mathrm{e}}}{\nu_2}\right]^2 \tag{4.1}$$

imposing to zero the derivative of the torque ripple with respect to $\vartheta_{\mathrm{b}}^{\mathrm{e}}$, it results

$$\nu_2 \sin(2\nu_1 \vartheta_{\mathrm{b}}^{\mathrm{e}}) + \nu_1 \sin(2\nu_2 \vartheta_{\mathrm{b}}^{\mathrm{e}}) = 0 \tag{4.2}$$

This equation can be solved numerically for the barrier angle $\vartheta_{\mathrm{b}}^{\mathrm{e}}$. The solutions found are the minima and maxima of the torque ripple.

Figure 4.1 reports the torque behavior due to the first two slot harmonics as a function of the electrical barrier angle, $\vartheta_{\mathrm{b}}^{\mathrm{e}}$. According to a 4-pole machine ($2p = 4$), they are the 17$^{\mathrm{th}}$ and 19$^{\mathrm{th}}$ for

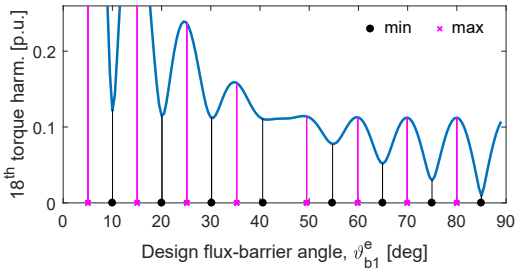

Figure 4.1: One flux-barrier machine. The vertical lines represent the positions of the torque ripple minima and maxima found by means of (4.2).

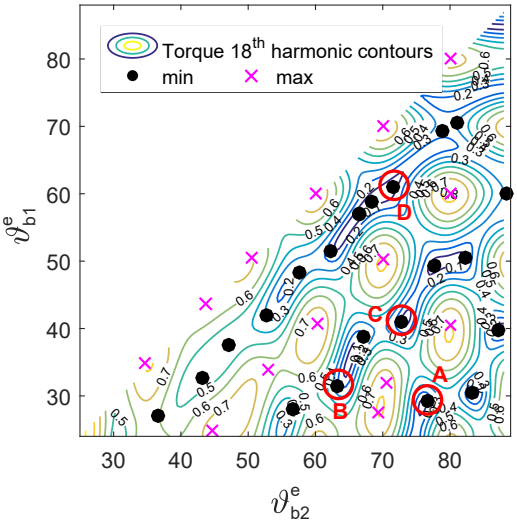

Figure 4.2: Analytical torque maps of the first slot harmonic in a two flux-barriers machine. The black dots show the minima found through (4.3).

the machine with $Q = 36$. These waveforms are obtained through the complete model of the SyR machine [65, 70]. This figure shows how much the choice of the flux-barrier angle affects the torque ripple resulting from the harmonic under study. In addition, the vertical lines identify the barrier angles found by the simple formulation derived in (4.2). It can be noted that the prediction of the torque minima and maxima by (4.2) perfectly corresponds to the minima computed by means of the complete analytical magnetic model of the machine. As an example, a proper choice of the flux-barrier angle would be about 75° and not 70°.

Two flux-barriers rotor

The equation describing the ripple due to the slot harmonics for a two-flux-barriers motor becomes:

$$\left[\Delta T_{\mathrm{m}}^{(h)}\right]^2 \propto \left[\frac{\sin \nu_1 \vartheta^{\mathrm{e}}_{\mathrm{b1}}}{\nu_1} + \frac{\sin \nu_1 \vartheta^{\mathrm{e}}_{\mathrm{b2}}}{\nu_1}\right]^2 + \\ + \left[\frac{\sin \nu_2 \vartheta^{\mathrm{e}}_{\mathrm{b1}}}{\nu_2} + \frac{\sin \nu_2 \vartheta^{\mathrm{e}}_{\mathrm{b2}}}{\nu_2}\right]^2 \tag{4.3}$$

In order to get the minima, (4.3) is derived first by the first barrier angle, $\vartheta^{\mathrm{e}}_{\mathrm{b1}}$, and then by the second one, $\vartheta^{\mathrm{e}}_{\mathrm{b2}}$. This represents a system of two equations in two variables, $(\vartheta^{\mathrm{e}}_{\mathrm{b1}}, \vartheta^{\mathrm{e}}_{\mathrm{b2}})$, and it is solved numerically, both searching for minima and maxima.

Figure 4.2 reports the torque behaviors due to the first two slot harmonics in the plane of the two electrical barrier angles $\vartheta^{\mathrm{e}}_{\mathrm{b1}}$ and $\vartheta^{\mathrm{e}}_{\mathrm{b2}}$. These harmonics are of the same order of the previous ones. The two-dimensional maps are again obtained through a complete model of the two flux-barrier SyR machine in [70]. Then the points marked by black dots and magenta crosses are found by means of the model proposed in (4.3). They identify the barrier angles which correspond to the torque ripple minima and maxima, respectively. Once again this model is able to predict these points with satisfactory precision, despite additional assumptions.

Table 4.2 reports some flux-barrier angle combinations, which exhibit the lowest torque ripple, obtained from the map in Figure 4.2.

4.2.2 Magnetic insulation ratio selection

A common guideline to choose the proper insulation ratio is to let the rotor saturate more than the stator teeth, in order to reduce teeth iron losses [73]. The coefficient k_{air} can be preliminary

Table 4.2: Flux-barrier angles combinations that exhibit the lowest torque ripple found through Figure 4.2.

Rotor -	ϑ^{e}_{b1} (deg)	ϑ^{e}_{b2} (deg)	ϑ_{b1} (deg)	ϑ_{b2} (deg)
A	29.25	76.63	14.63	38.32
B	31.49	63.25	15.75	31.63
C	40.96	72.73	20.48	36.37
D	61.02	71.61	30.51	35.81

estimated through the following equation:

$$k_{air} = 1 - \frac{B_g}{B_r} \cdot \frac{D_r}{p(D_r - D_{sh})} \tag{4.4}$$

where B_g is the peak air-gap flux density, B_r is the desired rotor flux density, D_r the rotor diameter, D_{sh} the shaft diameter and p the number of pole pairs. Its value typically ranges between 0.4 and 0.6. In the present case study, it results a value around 0.55.

However, in this case a more accurate parametric FE analysis is performed to select the optimal k_{air}. The flux-barrier thicknesses and iron channel widths are computed on the basis of the selected flux-barrier angles magnetic and k_{air} as described in section 15.3. The radial rib size is computed with the simplified method in subsection 2.2.1.

The resulting parametric curves of the average torque versus the k_{air}, for the four different flux-barrier combinations in Table 4.2, are shown in Figure 4.3. Some rotor geometry sketches are also reported in the figure. It is evident that k_{air} strongly affects the flux-barrier shape and the radial rib thicknesses. In fact, as this coefficient increases, the amount of rotor iron is lower and so, the radial ribs become thinner. It can be noted that, in current case study, the maximum average torque is achieved with a k_{air} between 0.4 and 0.55. The motor C exhibits the highest average torque among the selected ones. The main motor outputs, in MTPA condition, are reported in Table 4.3. It is worth noticing that these observations are not general but are valid only for the considered case study.

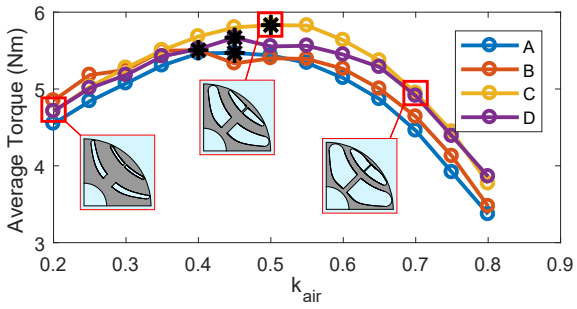

Figure 4.3: Average torque versus magnetic insulation for different flux-barrier angles.

4.3 FE optimization approach

A multi-objective differential evolution optimization algorithms has been adopted in this study since it usually guarantees good performance and convergence in a reasonable amount of time. Typical objectives for HS machines include the maximization of average torque (or power), of the saliency, of the power factor, the minimization of the torque ripple, of the losses or of the cost. The solutions found should also exhibit a proper robustness against slight variations of the design parameters. In this case study, the selected objectives are to maximize the average torque and to minimize the torque ripple in MTPA condition. The radial ribs are designed with the accurate method described in subsection 2.2.2. The optimization parameters are the flux-barrier angles,

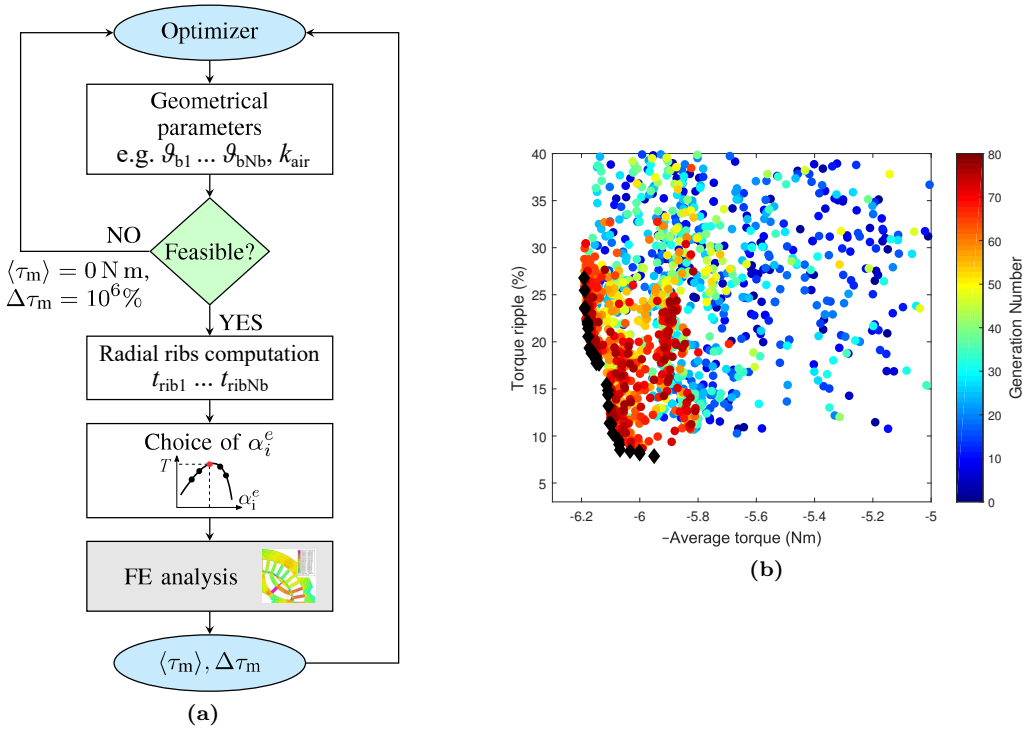

Figure 4.4: Optimization objectives evaluation flowchart (a) and objectives plane (b).

(ϑ_{b1} and ϑ_{b2}) and k_{air}. The dimensions of the flux-barriers and iron channels are computed as in section 15.3. The number of generations has been set to 80 with 25 individuals each.

Figure 4.4(a) shows the flowchart of the evaluation procedure performed for each individual. At first, the geometrical feasibility is evaluated considering the optimizer input parameters. The unfeasible individuals are discarded setting zero average torque and a high torque ripple (e.g. $10^6\%$). Otherwise, the algorithm computes the radial rib thicknesses, finds the MTPA current angle and evaluates the average torque and its oscillation in a sixth of electrical period. The research of the MTPA condition can be omitted if the current angle is set as additional parameter in the optimization as described in [74]. The optimization required two full days to be completed.

The final objectives plane is shown in Figure 4.4(b). The black diamonds represent the Pareto front. For HS applications it is mandatory to limit the torque oscillation that causes dangerous mechanical vibrations and acoustic noise. For this reason, the individual with the lowest torque ripple has been selected. The average torque is about 6 N m while the torque ripple is about 9 % with respect to the average torque. The related barrier angles are $\vartheta_{b1} = 20.70°$ and $\vartheta_{b2} = 31.81°$ while the insulation ratio is 0.43. With respect to the flux-barrier angles analytically predicted, the first one is practically the same while the second one is 9.12° (electrical) lower.

4.4 Optimal individuals comparison

The performance of the two optimal rotor geometries found by the SADA and FEO approaches have been detailed analyzed in this section. The main simulation results are reported in Table 4.3. It is possible to see that the two individuals exhibit about the same average torque but the SADA one presents a torque ripple of 17.6% that is almost two times the FEO one. This is mainly due to the different flux-barrier angles selected for the two individuals. Both the design solutions exhibits a very low power factor of about 0.4. Since the FEO individual exhibits the lowest torque ripple, it has been selected for the core losses estimation and for a FE structural analysis.

Table 4.3: Main results obtained through finite element analysis of the machines designed with SADA and FEO.

Design Method	α_i^e (deg)	$\langle T_m \rangle$ (Nm)	ΔT_m (%)	L_d (mH)	L_q (mH)	$\cos\varphi$ -
SADA	52.5	5.83	17.6	0.896	0.344	0.43
FEO	47.5	5.91	9.16	0.910	0.367	0.40

4.5 Further FE analyses

4.5.1 Electromagnetic

The flux density plot of the FEO motor is shown in Figure 4.5(a). It can be noted that the iron saturation within the tangential ribs covers a larger area and the iron saturation of channels is not negligible. These aspects highly affect the analytical model hypothesis and explains the different torque ripple predicted by the approaches.

The HS of rotation involves high frequency for the current supply. Even though thin lamination sheets have been considered, iron losses may play an important role in the overall machine performance. So, to accurately estimate the losses, the flux density for every mesh element has been recorded in both x and y directions for a complete electrical rotation. This allows to split the flux density fluctuations in Fourier series and, thus, to find the losses for all the harmonics involved. The harmonic losses are caused by the staircase MMF waveform and by the effect of stator slots. Current distortion may introduce additional losses, but it is not considered in this study.

The loss density map is reported Figure 4.5(b). It can be noted that the maximum loss density appears near the rotor periphery and near sharp corners. However the volumes involved are rather small. On the other hand, stator teeth and back-iron see lower loss densities but they are diffused, filling almost the entire volume. In fact, the stator iron is subjected also to the fundamental harmonic of the flux density, which is obviously the highest harmonic.

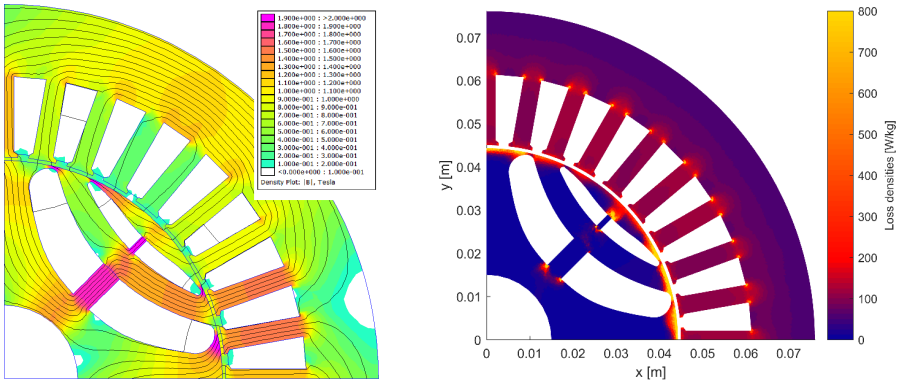

(a) **(b)**

Figure 4.5: Flux density (a) and core losses density (b) plots of the FEO rotor in MTPA condition.

The numerical comparison among the losses is reported in Table 4.4. The majority of losses is due to the iron losses in the stator caused by the fundamental of the flux density. Joule losses in the stator winding are the second main cause. Then it can also be seen that the additional losses introduced by the harmonics are not negligible at this speed, as they represent almost 30 % of the total electromagnetic losses.

4.5.2 Structural Analysis

To prove the effectiveness of the radial ribs design a FE structural analysis is carried out by means of the procedure reported in section 14.6. The rotor sharp corners, near the radial ribs, have been

Table 4.4: Motor losses in different parts.

Part	Losses (W)		
	Fundamental	Space Harmonics	Total
Copper	194	0	194
Stator iron	479	100	579
Rotor iron	0	159	159
Total	673	259	932

smoothed out in order to avoid dangerous stress concentrations. The von Mises stress and the displacement plots are shown in Figure 4.6. The scale of the Von Mises stress has been set to the desired stress value, which is 200 MPa for this study. It can be observed that the target stress value is never reached within the radial iron ribs. Stress concentration is present near corners, but it will lead only to some yielding.

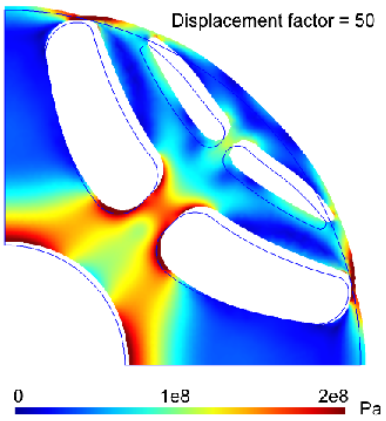

Figure 4.6: Von Mises stress of the FEO rotor at 30 000 rpm.

4.6 Conclusion

In this chapter two alternative design procedures for HS-SyR machines have been investigated: the semi-analytical and FE optimization approach.

The first one is faster and finds suitable flux-barrier angles by means of a simple analytical model while the magnetic insulation ratio is found on the basis of a FE parametric study. The second one is more accurate since it considers the iron saturation but requires more time because of the optimization algorithm.

The comparison between the two methods revealed that the non-localized saturation of the tangential ribs and the radial rib thicknesses strongly affect the torque ripple estimation of the analytical model. For this reason, the torque oscillation obtained by means of the FE optimization is about 52% of that resulting from the semi-analytical approach.

The losses computation has shown that rotor losses have to be taken into account for an accurate efficiency prediction. In fact, the rotor losses represent about 30 % of the total.

The structural analysis confirmed the validity of the radial ribs design method giving a suitable stress distribution within the rotor.

In conclusion, the semi-analytical method is a quick procedure that allows to obtain a good initial design of a HS-SyR rotor. However a multi-objective optimization algorithm should be employed to get more performing designs.

Chapter 5

HS-SyR Machine Optimizations at Different Speed limits

5.1 Introduction

In chapter 4, it has been observed that a FE optimization is the best way to design an HS-SyR machine since it yields higher torque density and low torque ripple.

In this chapter, the same methodology is applied to design HS-SyR rotors for different mechanical speed limits including also a sensitivity analysis of the results [2].

The stator geometry is fixed and its main data are reported in Table 5.1, a current density of $7\,\mathrm{A/mm^2}$ is set for the winding. Such a value has been selected taking as reference a surface PM motor with the same stator geometry and winding. A rotor geometry with three fluid flux-barriers per pole is selected for the optimizations.

The parameters set for the optimization are the three flux-barrier angles and magnetic insulation ratio while all the flux-barriers and iron channel dimensions are computed as reported in section 15.3. The optimization objectives are to maximize the average torque and to minimize the torque ripple.

In addition to the mechanical radial ribs design solution seen in the previous chapters, the adoption of a retaining sleeve is also investigated with the aim of limiting the radial ribs size and improve the rotor saliency even thought it requires a larger air-gap length.

A NO20 lamination is adopted for both stator and rotor to limit the specific core losses at high frequency. The carbon fiber has been selected for the rotor sleeve for its high tensile strength (i.e. 2000 MPa).

Finally, some considerations are carried out on the basis of the overall machines design.

5.1.1 Optimization at 20 krpm without sleeve

The first optimization is performed with an air-gap length of 1 mm without sleeve for a rated mechanical speed limit of 20 krpm. The optimization is carried out with 80 generations constituted by 40 individuals. The results of the whole optimization is reported in the objectives plane in Figure 5.1(a), together with the Pareto front. On the x-axis there is the opposite of the average torque, while on the y-axis the torque ripple is reported. It can be observed that the solutions converges to the optimal ones, located near the bottom left corner of the plot. The resulting Pareto front is steep, since the torque ripple has high variations around similar average torque values. Nonetheless the results show that the rotor with three flux-barriers is able to reach a proper average torque with many combinations of the input parameters.

In order to highlight the dependence of the torque ripple on the barrier angles, Figure 5.1(b) shows the barrier angles sorted by the relative torque ripple. The points lying on the Pareto front are highlighted by black dots. Many of them are near the angles $(\vartheta_{\mathrm{b1}}, \vartheta_{\mathrm{b2}}, \vartheta_{\mathrm{b3}}) = (17°, 29°, 34°)$. The value of the fourth parameter, k_{air}, is close to 0.42. The Pareto points are all close to the

Table 5.1: Main data of the machines under optimization.

Motor part	Symbol	Value	Unit
Outer diameter	D_e	240	mm
Inner diameter	D_i	140	mm
Stack length	L_{stk}	140	mm
Pole number	$2p$	4	-
Slot number	Q	48	-
Slot height	h_s	25	mm
Tooth width	w_t	5	mm
Air-gap	g	1	mm
Lamination properties			
Iron lamination		N020	
Tensile strength	σ_r	500	MPa
Safety factor	ν_σ	2.5	-
Carbon fiber properties			
Tensile strength	σ_{CF}	2000	MPa
Safety factor	ν_{CF}	2	-

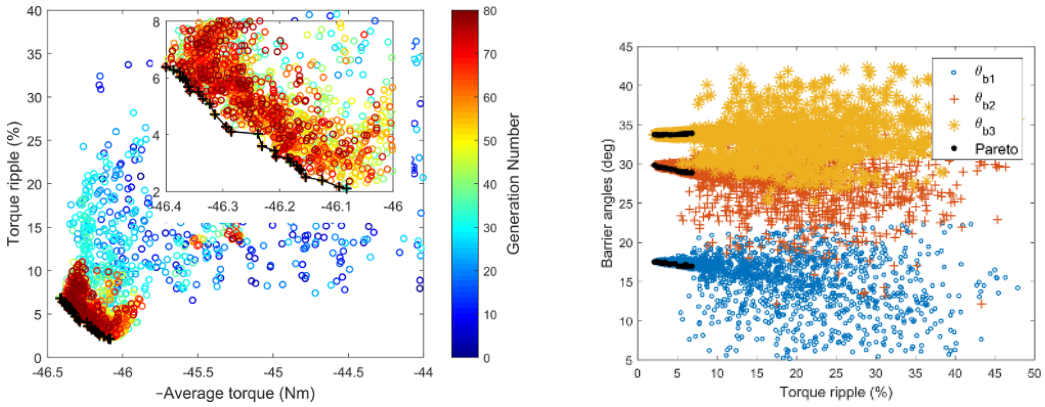

(a) (b)

Figure 5.1: Simulated individuals in the objectives plane (a) and flux-barrier angles versus torque ripple (b). Optimization at 20 krpm.

aforementioned angles, slight deviations from these values cause an increase in the torque ripple and/or the leaving of the front.

Moreover, Figure 5.1(b) shows that the flux-barrier angles are not evenly spaced since the third barrier angle is close to the second one. In fact, the third angle is directly related to the average torque so, generally, the greater the third barrier angle the higher the torque. However, the decrease of such an angle permits to reduce the respective island mass and, as a consequence, the rib thickness. It is clear that a compromise solution has been found by the optimizer.

5.1.2 Sensitivity analysis of the results

To estimate the robustness of good candidates (high average torque and low torque ripple), a sensitivity analysis on the results has been carried out [75]. The dimensions of the parameter space is equal to the number of parameters, four in the considered optimization. Furthermore all the parameters are normalized within the interval 0 and 1.

It is useful to consider a 3-dimensional space first. In the case study, the parameters can be the

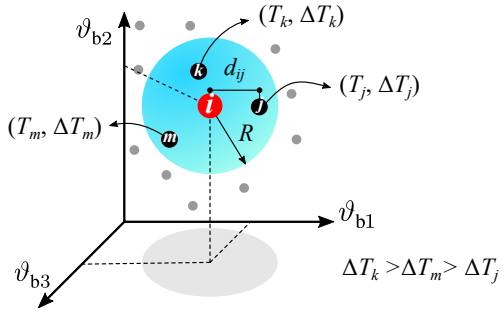

(a) *T_k and ΔT_k are the average torque and the torque ripple of the k-th individual.*

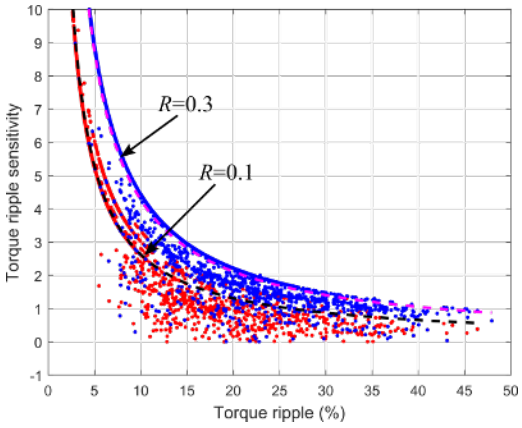

(b) *For mechanical speed limit* 20 krpm.

Figure 5.2: Meaning of the hypersphere and distance d_{ij} between the points i and j in the space parameters (a) and torque ripple sensitivity versus the torque ripple percentage for different radius.

flux-barrier end angles as shown qualitatively in Figure 5.2(a). Each dot in the space corresponds to an individual with an associated average torque and a torque ripple. For example, the point j in Figure 5.2(a) is characterized by the objectives $(T_j, \Delta T_j)$.

The sensitivity analysis is carried out for each point in the parameter space. The distance between two points is computed with the euclidean norm. It is verified that $d_{ij} = d_{ji}$ since the distance is a symmetric property. The matrix of the distances, $\mathbf{D}$, is symmetric and its order is the number of the individuals N. The element in the i-th row and in the j-th column is the distance d_{ij} defined above. Obviously the matrix has all the diagonal elements equal to zero.

$$\mathbf{D} = \begin{bmatrix} 0 & d_{12} & \dots & d_{1N} \\ & \ddots & & \\ d_{i1} & \dots & 0 & d_{iN} \\ d_{N1} & \dots & \dots & 0 \end{bmatrix} \tag{5.1}$$

To the purpose of analyzing a restricted volume around each single point, it is useful to define a radius R of an hypersphere. The sensitivity can be computed locally in each point. In the normalized research space, the maximum normalized radius of the hypersphere, that includes all the individuals from each one of them, is equal to $\sqrt{N_{\text{par}}}$ where N_{par} is the number of parameters.

Referring to Figure 5.2(a), the hypersphere around the individual i includes only the points j, k and m. The other ones are not considered. This means that a restricted number of elements of the i-th row of the matrix $\mathbf{D}$ are useful. Among these remaining individuals the maximum and the minimum torque ripple are researched. The figure reports that the maximum and the minimum torque ripple correspond to the individual k and j respectively.

The sensitivity of the i-th individual is finally given by:

$$s_i = \frac{\max(\Delta T)\big|_i - \min(\Delta T)\big|_i}{\Delta T_i} \tag{5.2}$$

where the subscripts at the numerator indicates the maximum and the minimum torque ripple among the individuals inside the hypersphere centered in the individual i. The result of (5.2) is obviously a function of the hypersphere radius.

Figure 5.2(b) shows the sensitivity of the optimization results for two different radii, $R_1 = 0.1$ and $R_2 = 0.3$. The radius has to be sufficiently small to correctly evaluate the sensitivity of each point, but also sufficiently large to find other points around each one. Figure 5.2(b) also reports the tendency lines of the sensitivity, which would otherwise be very scattered. These lines clearly

point out how the lower torque ripple values are more sensible to geometric variations of the chosen parameters. Additionally the larger the variation—so the larger R—the higher the torque ripple change. This fact highlights the importance of good manufacture of the rotor, which therefore needs small tolerances.

5.1.3 Structural analysis

The structural integrity of one optimal individual at 20 krpm has been verified with the method presented in section 14.6. The Von Mises stress is shown in Figure 5.3. The full-scale value is set to 200 MPa which represents the acceptable lamination limit. It can be noted that the iron rib stress is always lower than the maximum limit according to the preliminary design. Higher stress values are concentrated in the proximity of the edges.

The tangential iron ribs of the first flux-barrier (the outer one) are not stressed while the other ones presents values of about 200 MPa.

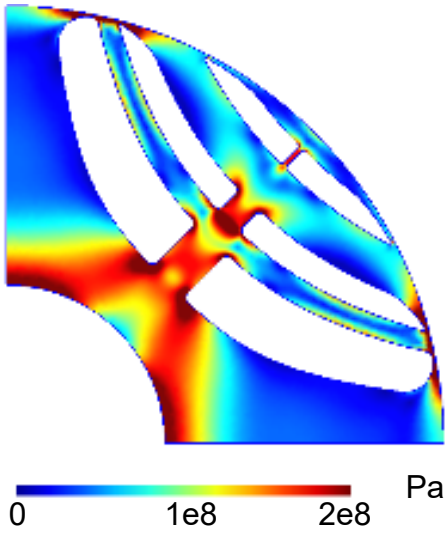

Figure 5.3: Von Mises stress of the optimized rotor at 20 krpm.

The maximum displacement is about 83 µm which has been observed in the third island while close to the air-gap the value is about 70 µm. This results in a 7 % variation of the air-gap thickness.

5.2 Optimizations at 20 krpm with sleeve

Two similar optimizations have been carried out with a sleeve thicknesses of 0.25 mm and 0.5 mm. Since the carbon fiber is a nonmagnetic material, the effective air-gap lengths are 1.25 mm and 1.5 mm, respectively. The corresponding sleeve reaction, taking into account the carbon fiber safety factor, ν_{CF}, can be computed with the (2.14). The total force that the radial ribs have to sustain is decreased by $F_{\mathrm{c,sleeve}}$. For negative values, radial rib thickness is set equal to the lamination width. Finally, the radial iron ribs are computed with the (2.2) neglecting the tangential rib contribution as usual.

The optimization results, reported in Table 5.2, show that the adoption of the sleeve greatly reduces the available torque because of the larger air-gap length and, consequently, lower flux linkage. This aspect has been verified with the optimistic assumption of no sleeve precompression. In fact, the rotor iron ribs should be designed according to the precompression stress at zero speed, otherwise lateral deflection of radial ribs might occur. This requires thicker radial ribs, decreasing the machine anisotropy hence the average torque. Therefore, a rotor with a precompressed sleeve would exhibit worst performance.

Table 5.2: Average torque for different thicknesses of the sleeve for a mechanical speed limit of 20 krpm.

t_{sleeve}	(mm)	0	0.25	0.5
$\langle T_{\text{m}} \rangle$	(Nm)	46.3	43.9	42.1

5.3 Optimization at higher mechanical speed limits

Further optimizations at different mechanical speed limits are presented hereafter. The aim of these investigations is to determine the influence of the mechanical speed limit on the overall performance and on the rotor flux-barriers shape.

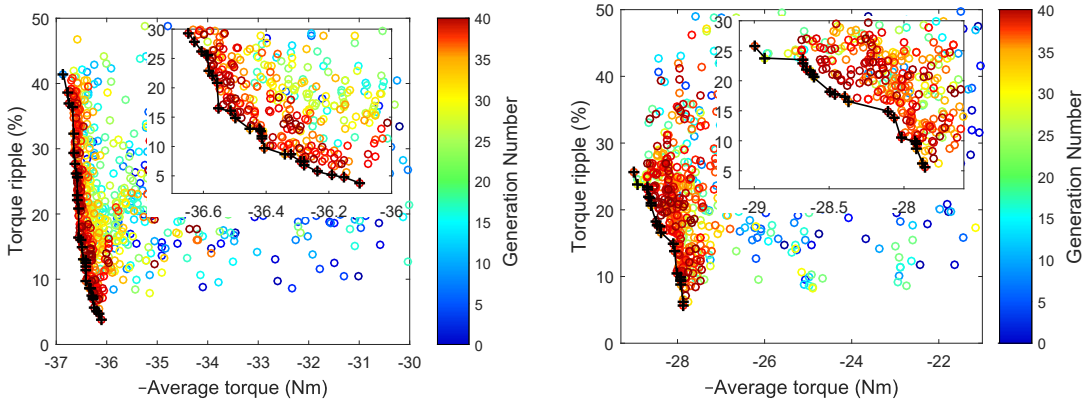

(a) 30 000 rpm. **(b)** 40 000 rpm.

Figure 5.4: Simulated individuals in the objectives plane and Pareto front at different mechanical speed limits.

The objectives plane of the optimization for the mechanical speed limit of 30 krpm is reported in Figure 5.4(a). It can be noted that the average torque is lower than before and it is around 36 Nm. In addition the minimum torque ripple achievable is slightly higher than the one at 20 krpm. The Pareto front is very steep and different from the front obtained in Figure 5.1(a).

The optimization has been repeated for a mechanical speed limit of 40 krpm and its objective plane is reported in Figure 5.4(b). As expected, the average torque, which is about 26 Nm, is lower than the previous optimizations because of the larger radial ribs size.

5.4 Optimization results comparison

Figure 5.5 shows the flux density plots of the HS-SyR motors optimized for 20 krpm, 30 krpm and 40 krpm. It is worth noticing that the radial iron ribs increase as the mechanical speed limit increases because of the higher centrifugal load. Furthermore, the magnetic insulation ratio, k_{air}, increases too. This because the optimizer finds the compromise between wider ribs and lighter islands. It can also be noted that the saturation of the radial iron ribs decreases as the mechanical speed limit increases. On the contrary, the iron paths between the flux-barriers becomes more and more saturated.

The torque behaviors versus rotor position of the three motors are reported in Figure 5.6. For each plot, the average torque and the ripple are also reported. It can be noted that the average torque of the motor designed for 20 krpm is higher than the other ones. In particular, the average torque of the motor designed for 30 krpm and 40 krpm are about 21 % and 43 % lower, respectively. Furthermore it can be observed that the torque ripple tends to increase with the mechanical speed limit. In fact, at the lowest mechanical speed limit it is 4.77 % while at 40 krpm it is 12.88 %.

Table 5.3 reports the d- and q-axis inductances, the saliency ratio, the inductances difference and the power factor of the designed machines.

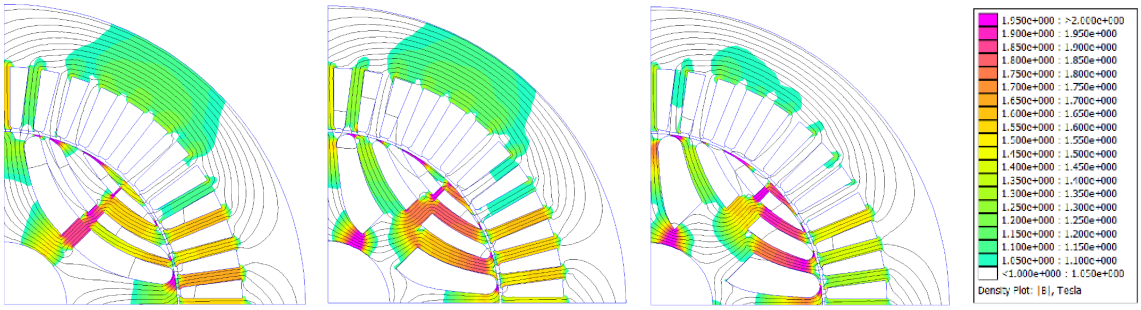

(a) 20 krpm. **(b)** 30 krpm. **(c)** 40 krpm. **(d)** *Legend.*

Figure 5.5: Flux density plot of HS-SyR machines design for different mechanical speed limits at $\vartheta_{\mathrm{m}} = 0°$.

All values are expressed in per unit, referring to the d-axis inductance obtained with the lowest radial rib thicknesses, i.e. for motor running at 1500 rpm. It is possible to observe that at the highest mechanical speed limit the d-axis inductance is 30% lower than the reference one. The q-axis inductance increases of about 120%, this is essentially due to the larger radial ribs thicknesses. The reduction of rotor anistropy related to the mechanical speed limit is evident considering both the saliency ratio and, mainly, the difference between d- and q-axis inductances. With respect to the reference one, the former parameter decreases of about 68% while the latter of 57%. The power factor worsens with the mechanical speed limit decreasing from 0.652 to 0.339.

This aspect can be explained considering the flux density plots at different mechanical speed limits reported in Figure 5.5. It is evident that, for low mechanical speed limits, the radial ribs are saturated and so the iron islands can be considered magnetically isolated from each other. Conversely, as the mechanical speed limit increases, the radial ribs are no more saturated and so the islands are far from being magnetically isolated.

Table 5.3: Per-unit d- and q-axes inductances and saliency ratios for different mechanical speed limits. The d-axis inductance at 1500 rpm is the reference value.

n (rpm)	L_{d} (p.u.)	L_{q} (p.u.)	ξ (-)	$L_{\mathrm{d}} - L_{\mathrm{q}}$ (p.u.)	PF (-)
1500	1	0.157	6.38	0.843	0.652
20 000	0.937	0.267	3.50	0.670	0.542
30 000	0.810	0.313	2.59	0.497	0.427
40 000	0.708	0.348	2.03	0.359	0.339

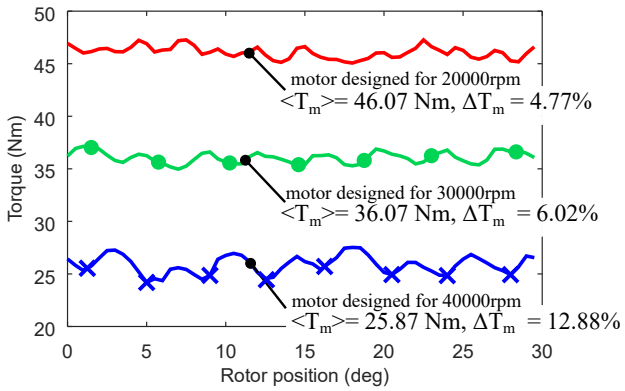

Figure 5.6: Torque versus rotor position at different mechanical speed limits.

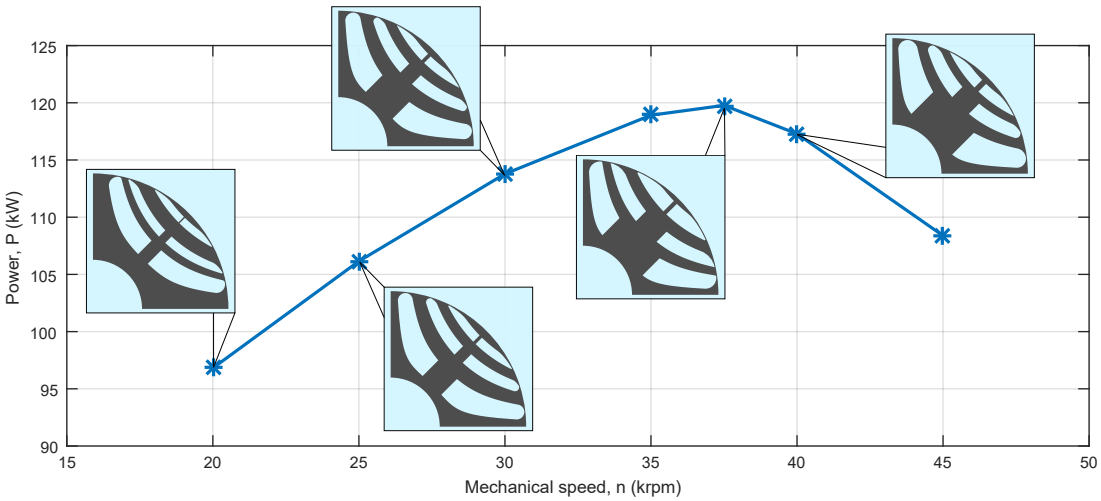

Figure 5.7: Maximum output power versus mechanical speed limit. For each mechanical speed limit the rotor geometry is different, as obtained by a specific optimization.

The rated powers of the HS-SyR motors designed for different mechanical speed limits are reported in Figure 5.7. It can be noted that the power increases up to the mechanical speed limit of 37 500 rpm, then it decreases. This aspect represents a limit of the transverse-laminated reluctance machines for the geometry under investigation.

Despite the fixed stator geometry, the magnetic insulation ratio increases with the mechanical speed limit since it involves a decrease of the overall iron mass and, consequently, a decrease of the rib thicknesses with beneficial effect on the rotor anisotropy.

5.5 Conclusions

In this chapter several HS-SyR rotors have been optimized for different mechanical speed limits. The optimization was focused on the rotor geometrical parameters, such as flux-barrier angles and insulation ratio. The goals were high torque density and low torque ripple.

It has been verified that, for the mechanical speed limit of 20 krpm, the rotor flux-barrier geometry, with a proper radial ribs design, is the most suitable solution with respect to the adoption of a retaining sleeve. This is due to the fact that the higher air-gap length determined by the retaining sleeve involves a rotor anisotropy reduction higher that the one achieved by the large radial ribs only. For this reason, the retaining sleeve does not represent a valid design solution for HS-SyR machines.

A sensitivity analysis on the optimization results has also been carried out. It has been observed that low-ripple solutions have a high sensitivity and thus require a high manufacturing precision. The optimizations carried out for higher mechanical speed limits suggested that the magnetic insulation ratio, has to be increases with the mechanical speed limit in order to reduce the total rotor iron mass and so, the radial ribs size. Moreover, for this case study, the maximum rated power of 120 kW was achieved for the mechanical speed limit of about 37.5 krpm.

Chapter 6

Comparison between SPM and SyR Machine for HS Applications

6.1 Introduction

In this chapter a performance comparison between a SyR machine and a SPM machine designed for HS application is carried out [5]. In particular, the required power and speed are 120 kW and 20 krpm, respectively. The same stator geometry and winding arrangement are used for both motors, their main data are reported in Table 6.1. A NO20 lamination is adopted to limit the core losses at high frequency. A natural cooling system is considered for both the motor typologies.

The comparison mainly takes into account the total motor costs and the losses due to current time harmonics, MMF space harmonics and slot openings [40]. The first one are produced by the inverter and their amplitude depends on the inverter switching frequency, i.e. 10 kHz, and machine impedance. The method to estimate their spectrum is described in [76]. The MMF space harmonics are caused by the non sinusoidal MMF distribution produced by the winding. The simplest solution to reduce their amplitude is to select a proper winding chording. A more complex solution is to adopt a dual three-phase winding system as in [77]. The slot opening losses are due to the air-gap flux density variations near the slot openings. They can be effectively reduced by increasing the air-gap length or by reducing the slot opening width at the cost of a lower torque density and higher slot leakage flux.

Regarding the SPM motor, some design aspects are firstly discussed and a complete procedure to design the rotor sleeve is presented. Then, a detailed analysis of the rotor losses is performed.

For the SyR machine, the FE optimization procedure, seen in chapter 4, is adopted for its design. After that, a computation of the different rotor losses is carried out on the optimal geometry.

Finally, the results of the two motor analyses are compared and discussed.

6.2 HS-SPM motor design and analysis

The HS-SPM motor geometry is sketched in Figure 6.1(a) and the main materials properties are reported in Table 6.2. The rated current density has been set to 5.2 A/mm^2 according to [76].

A NdFeB magnet UH grade has been chosen for the PM since high rotor temperature is expected because of the absence of a cooling system. To reduce eddy-current rotor losses they have been segmented in both radial and axial direction and insulated one from the others [76]. Moreover, a solid rotor core made of steel C45 is adopted to further reduce the PM demagnetization risk due the eddy-currents. In fact, in such a design solution, most of the eddy-currents arise in the rotor core [41].

A retaining sleeve has been adopted to ensure the rotor structural integrity to keep PMs on the rotor. The chosen sleeve material is carbon fiber for the advantages reported in chapter 5. The main drawbacks of such a material is the low thermal conductivity and negative coefficient

Table 6.1: Main motor data.

MOTOR OUTPUT			
Rated line to line voltage	$\hat{V}$	520	V
Rated power	P_{N}	120	kW
Frequency	f	667	Hz
Mechanical speed	n	20 000	rpm
GEOMETRICAL DATA			
Outer diameter	D_{e}	240	mm
Inner diameter	D_{i}	140	mm
Stack length	L_{stk}	140	mm
Number of poles	$2p$	4	-
Number of slots	Q	48	-
Slot height	h_{s}	25	mm
Tooth width	w_{t}	5	mm
Mechanical Air-gap	g	1	mm
WINDING			
Conductors in slot	n_{c}	6	-
Number of parallel paths	n_{pp}	4	-
Number of conductors per phase	N_{s}	24	-
Coil pitch	y_{q}	10	-
MATERIALS			
Iron Lamination			N020
Solid Steel (SPM rotor)			C45
Permanent Magnet			N38UH
Sleeve			Carbon Fiber

Table 6.2: SPM motor material properties.

Carbon fiber Young's Modulus	E_{sleeve}	132	GPa
PMs coefficient of thermal expansion	$\lambda_{T,\mathrm{PM}}$	10×10^{-6}	K^{-1}
Iron coefficient of thermal expansion	$\lambda_{T,\mathrm{fe}}$	12×10^{-6}	K^{-1}
Carbon fiber bandage thickness	t_{sleeve}	2.5	mm
Magnet thickness	t_{PM}	8	mm

of thermal expansion (CTE). The first one makes the rotor cooling more difficult since the rotor sleeve act as thermal insulator and the heat mainly flows in axial direction. The second one involves additional stress in the sleeve at the operating temperature. On the basis of these considerations, a detailed procedure to design the sleeve thickness is reported in the following.

6.2.1 Sleeve design

The sleeve thickness is designed according to the total mechanical stress at the highest speed and maximum temperature.

At the operating speed, the sleeve and PMs pressures due to the centrifugal effect are:

$$p_{\mathrm{sleeve}} = \rho_{\mathrm{sleeve}} \omega_{\mathrm{m}}^2 t_{\mathrm{sleeve}} R_{\mathrm{sleeve}} \tag{6.1}$$

$$p_{\mathrm{PM}} = \rho_{\mathrm{PM}} \omega_{\mathrm{m}}^2 t_{\mathrm{PM}} R_{\mathrm{PM}} \tag{6.2}$$

where ρ_{sleeve}, ρ_{PM}, R_{PM} and R_{sleeve} are the mass density and the radius of the sleeve and PM, respectively.

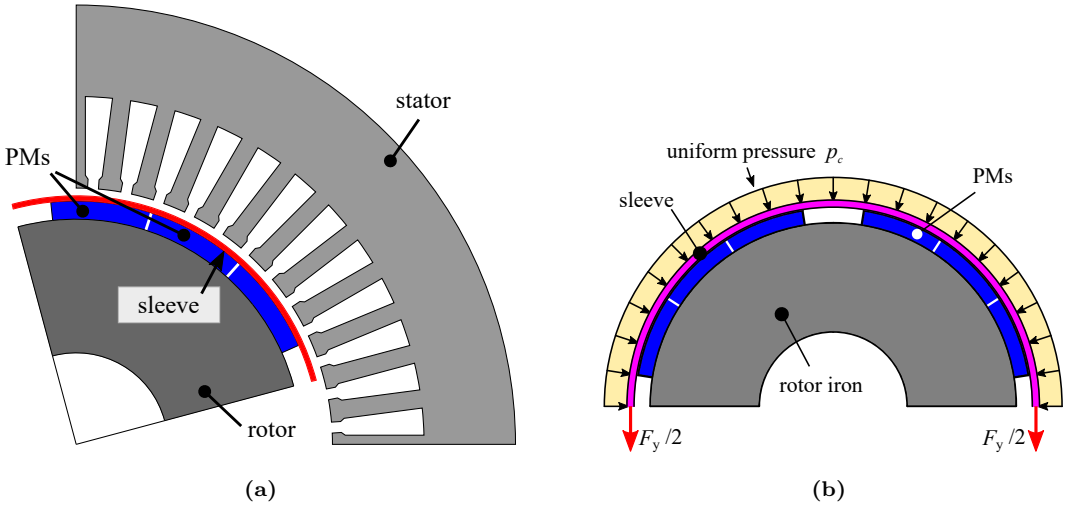

Figure 6.1: Sketch of SPM motor with discretized magnets and retaining sleeve (*a*) and Computation of the SPM sleeve thickness (*b*).

As a design choice, the sleeve has to ensure a zero residual contact pressure p_c between magnets and rotor iron at 20 % over-speed, without exceeding the maximum allowable tangential stress. This is possible imposing a pre-stress pressure p_{pre} during manufacture, thus the total contact pressure is:

$$p_c = p_{pre} - p_{PM} - p_{sleeve} \tag{6.3}$$

the corresponding pre-stress results to be:

$$\sigma_{pre} = \frac{p_{pre} R_{sleeve}}{t_{sleeve}} \tag{6.4}$$

An additional stress has to be considered in order to take into account the radial expansion of the rotor iron and PMs due to the temperature rise. In fact, their CTE is higher than the carbon fiber one.

The radial expansion of the rotor iron and PMs is:

$$\Delta R_{th.exp} = R_{20}\, \lambda_T\, \Delta T \tag{6.5}$$

where R_{20} is the rotor radius with no sleeve at 20 °C, λ_T is the material rotor CTE (reported in Table 6.2) and ΔT is the temperature increase. The corresponding stress can be computed as follows:

$$\sigma_{th.exp} = E_{sleeve} \frac{\Delta R_{th.exp}}{R_{sleeve}} \tag{6.6}$$

where E_{sleeve} is the Young's modulus of the sleeve material. Finally, the total stress in the sleeve is:

$$\sigma_{tot} = \sigma_{pre} + \sigma_{th.exp} \tag{6.7}$$

For the rotor under analysis the sleeve thickness results to be $t_{sleeve} = 2.5$ mm. Thus, assuming a mechanical air-gap of 1 mm, the total magnetic air-gap results 3.5 mm.

6.2.2 SPM rotor losses computation

This section reports the losses computation carried out on the SPM machine by means of FE analyses.

Time harmonic losses

The order and amplitude of the highest current time harmonics produced by the inverter are reported in the first and second columns of Table 6.3, respectively. A FE time harmonic simulation has been carried out for each current harmonic component. In these analyses, the PMs segmentation has been considered imposing the total net current flowing through each magnet to be zero.

The resulting losses in the solid iron and PMs are reported in Table 6.3. It can be noted that most of the losses are in the rotor iron rather than in the PMs as expected.

Table 6.3: Time harmonic rotor losses of SPM motor.

h	I (A)	P_{Fe} (W)	P_{PM} (W)	P_{tot} (W)
13	12.32	121	68	189
17	9.24	87	43	130
29	7.7	77	37	114
31	7.5	73	35	108

Space harmonic losses

The effect of MMF harmonics is taken into account replacing the stator with a uniform current sheet [40]. The stator electric loading is split in its Fourier series. The amplitude of each harmonic and the corresponding frequency are reported in Table 6.4. The total losses in the rotor iron and PMs are also reported. It can be seen that the higher losses occur for multiples of slot harmonics, which are of order $Q/p \pm 1$. Anyway, comparing the losses in Table 6.3 and Table 6.4, it is evident that space harmonic losses are quite lower than time harmonic ones. The eddy-current density plots due to 5-th an 23-rd current harmonic are reported in Figure 6.2. As expected, the higher the harmonic order, the lower the skin depth.

Table 6.4: Losses produced by the MMF space harmonics in the SPM motor.

h	K_{s} (A/m)	f_{h} (kHz)	Losses (W)
5	2.86	4	5.96
7	2.18	4	1.04
11	6.42	8	3.88
13	6.35	8	1.57
17	2.07	12	0.07
23	44.57	16	7.23
25	43.63	16	3.57
29	2.39	20	0.00
31	1.78	20	0.00
35	5	24	0.00
37	4.83	24	0.00
41	1.5	28	0.00
43	1.87	28	0.00
47	29.62	32	0.01
49	28.12	32	0.01

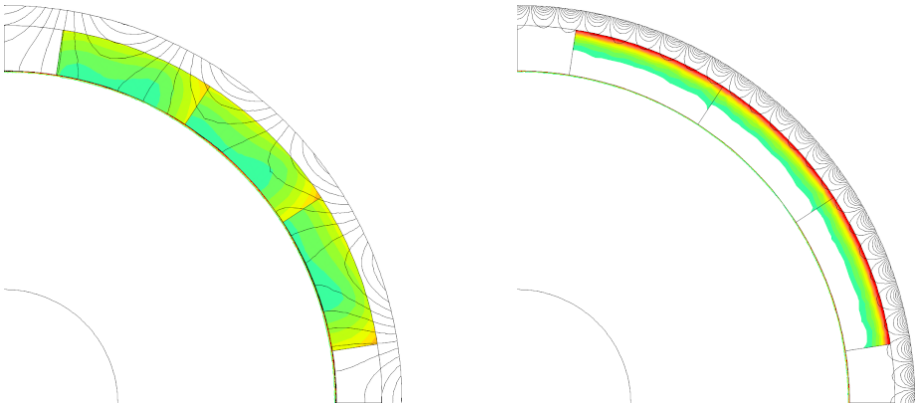

(a) $h = 5$ **(b)** $h = 23$

Figure 6.2: Eddy-current density plots of different time harmonic simulations with SPM rotor.

Slot opening harmonic losses

The slot openings effect has been simulated by adopting a slotless stator and by imposing a linear current density along the inner stator circumference as in [40]. In the actual case study, the high air-gap, determined a total losses of about 50 W.

6.3 HS-SyR motor design and analysis

In this section the HS-SyR machine geometry is firstly designed by means of a FE-based optimization and then a detailed rotor losses computation is carried out. The optimization procedure described in chapter 4 is adopted in the following.

6.3.1 Optimization

On the basis of the torque density values obtained in chapter 5, a current density of 7.5 A/mm^2 has been selected for this case study in order to produce about the same torque of the SPM motor. A rotor geometry with three fluid shaped flux-barriers per pole has been selected. The optimization parameters are the three flux-barriers angles, $(\vartheta_{b1}, \vartheta_{b2}, \vartheta_{b3})$, and the magnetic insulation ratio k_{air}. The objectives are to maximize the average torque and to minimize the torque ripple. The optimization has been performed with 60 generations consisting of 30 individuals each.

The optimization results are reported in the objectives plane in Figure 6.3(a), together with the Pareto front (black markers). It can be observed that the Pareto front is steep, since the torque ripple has high variations around similar average torque values. In fact, the torque ripple varies from 2% to 12% while the average torque is always between 57.7 N m and 58 N m. In this case study, the motor geometry with the lowest torque ripple has been selected.

Figure 6.3(b) shows the flux-barrier angles versus the torque ripple plane. It shows also the values of k_{air} through the marker size (the larger the point, the smaller k_{air}) and the age of the individual through the color. The black markers belong to the Pareto front. The flux-barrier angles corresponding to the lowest torque ripple are quite defined close to the values $(\vartheta_{b1}, \vartheta_{b2}, \vartheta_{b3}) = (16.9°, 29.4°, 33.5°)$, the magnetic insulation ratio, k_{air}, approaches 0.41.

The optimized geometry is shown in Figure 6.3(c). It can be noted that the flux-barrier angles are not evenly distributed along the rotor periphery as already observed in chapter 5. In particular, the second and the third flux-barriers are quite close to each other and so the second iron island is wider than the third one.

The structural integrity of the rotor geometry at the operating speed of 20 krpm has been finally verified by means of FE analysis as reported in section 14.6. The resulting Von Mises plot

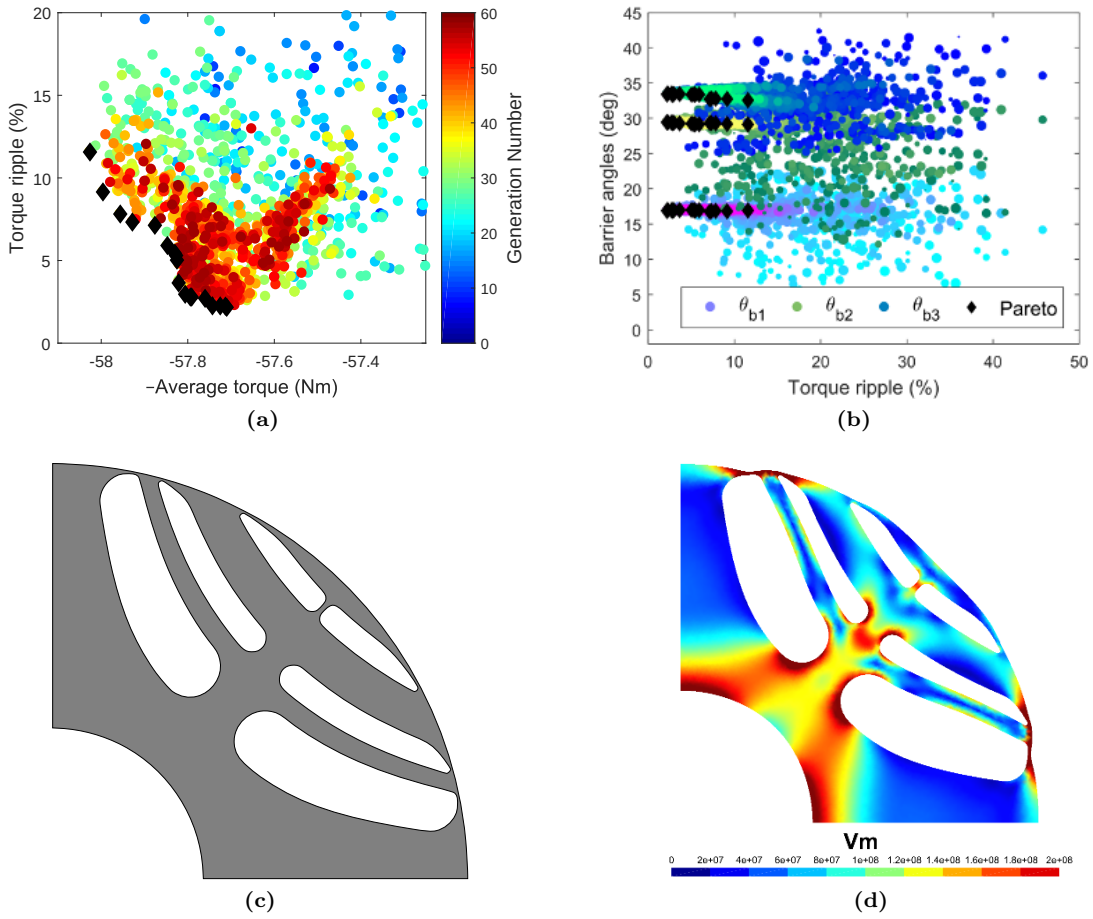

Figure 6.3: HS-SyR motor optimization: objectives plane (a), flux-barrier angles versus torque ripple (b), optimal rotor geometry (c) and Von Mises stress plot (d).

is reported in Figure 6.3(d) where the it is possible to see that the maximum stress are below the maximum limit.

6.3.2 HS-SyR rotor losses computation

Time harmonic losses

The current harmonics have been computed with the procedure discussed in section 6.2.2. The first and second column of Table 6.5 report the order and amplitude of the highest current time harmonics, respectively. It is worth noticing that the current ripple of the SyR motor is about 50% of the SPM one since the SyR inductances are higher (i.e. lower air-gap length). The iron losses produced by the highest current harmonics are reported in Table 6.5.

Space and slot opening harmonic losses

The computation of the losses produced by the space harmonics and the slotting effect have been carried out as reported in subsection 6.2.2. The numerical results are not reported since their magnitude is negligible.

Figure 6.4 shows the results of time harmonic simulations for $h = 5$ and $h = 23$. The flux lines in Figure 6.4(a) flow through the inner part of the rotor while with the higher harmonic, in Figure 6.4(b), the flux lines are confined near the rotor periphery.

Table 6.5: Time Harmonic rotor losses of SyR motor.

h -	I (A)	P_{tot} (W)
13	9.1	183
17	6.6	185
29	5.6	276
31	5.6	276

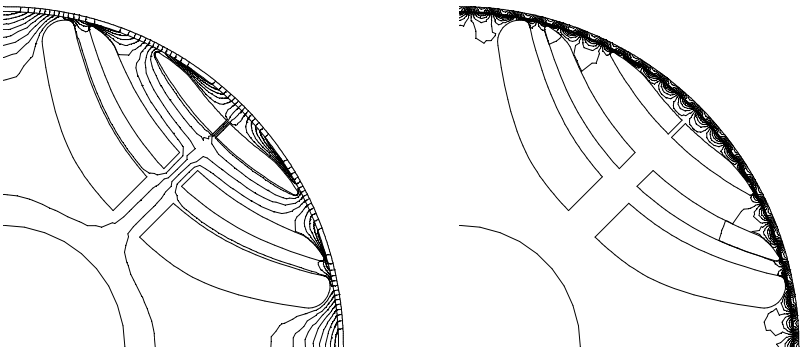

(a) $h = 5$. **(b)** $h = 23$.

Figure 6.4: Time harmonic simulations of space MMF harmonics with SyR rotor.

6.4 Final comparison

A final comparison between the SPM and SyR motor is reported in Table 6.6. The same winding temperature of 150 °C has been selected for both the machine neglecting the thermal aspect. An accurate estimation of the winding temperature on the base of the actual operating condition can be found in [78–80]. At first, it is possible to see that the current density required by the SyR machine is 44% higher than the SPM one, as expected. This because both torque and magnetizing current have to be supplied in the case of SyR machine. Obviously, this involves higher stator Joule losses in the winding, which result 140 % higher for the SyR motor.

From the tooth and yoke flux density values it is evident that the SPM machine magnetic loading is lower than the SyR one because of the wider air-gap length. This is also visible in the flux density plots, obtained in MTPA condition, in Figure 6.5.

The SyR machine exhibit a very low power factor, i.e. 0.55, due to the large radial ribs. This aspect could represents a strong limitation since it requires a higher inverter Volt-Ampere rating. Conversely, an optimal value of 0.87, is achieved by the SPM machine.

Despite the higher SyR inductances are beneficial for the current ripple, which results to be quite lower, the overall SyR rotor losses, essentially due to current time harmonics, are higher compared to the SPM ones. This is due to the lower SyR machine air-gap length which does not limit the magnetic field caused by the current harmonics. Nonetheless, the electric efficiency is not heavily compromised, being 96.5 % for the SyR and 97.6 % for the SPM motor.

The material weights are also reported in Table 6.6. The lamination weight is computed considering the total machine volume occupied by the lamination material. This allows to take into account both the active and waste parts and explains why the two motors present the same lamination weight. Also the winding cost is the same since the motors have the same winding. In the SPM machine, the PMs, the rotor steel and the carbon fiber weights increase the total material weight as well as the total cost. In terms of total material weight the SPM machine results to be 25% heavier. From the cost point of view, the difference is much more evident since the SPM machine cost is about three times the SyR one. This is essentially due to high PMs cost which represents about the 41% of the total one. It is worth noticing that actual SPM machine cost could

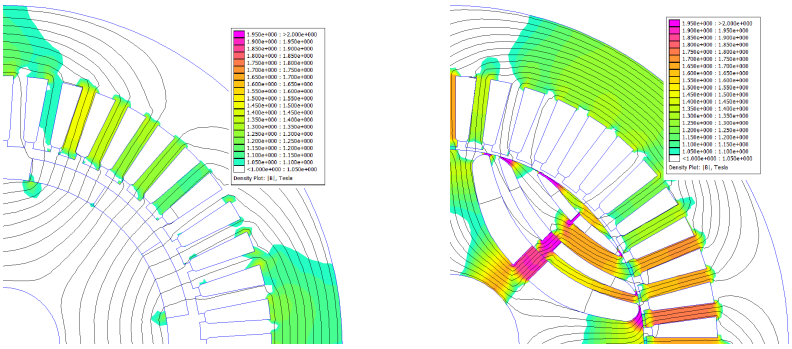

(a) *SPM motor.* **(b)** *SyR motor.*

Figure 6.5: Flux density plots of the analyzed HS motors in MTPA condition.

results much more higher than the one presented here if the manufacturing processes to assemble the PMs, to produce the retaining sleeve and the rotor sleeve are taken into account. Regarding the whole drive system cost, the SyR machine one is surely higher than the SPM one since a larger inverter overrating is required.

6.5 Conclusions

This chapter dealt with the performance comparison between a SyR and a SPM machine designed for HS applications. Both electromagnetic and mechanical aspects have been taken into account in the machines design.

The final comparison showed that the SyR machine yields and efficiency that is 1% lower than the SPM one despite the higher Joule and iron losses determined by the higher magnetic and electric loadings. The SyR machine total cost results to be one third of the SPM one thanks to the lack of rotor PMs, additional rotor steel and carbon fiber sleeve. On the other hand, the SyR machine exhibits a very poor power factor, i.e. 0.55, with respect to the SPM one (about 0.87).

In conclusion, even thought the SyR machine yields a good efficiency at very low cost, its poor power factor compromises its suitability for HS applications.

Table 6.6: Comparison between the SPM and SyR motors.

Output	Unit	Motor	
		SPM	SyR
Conductor current density	A/mm^2	5.2	7.5
Minimum inductance	µH	230	500
Power factor	-	0.87	0.55
Tooth flux density	T	1.49	1.8
Back-iron flux density	T	1.16	1.3
Losses			
Stator Joule losses	W	513	1070
Stator iron losses	W	1875	2360
Rotor losses	W	630	920
Total losses	W	**3018**	**4350**
Efficiency	-	97.5	96.5
Material weights			
Lamination	kg	48.5	48.5
Copper	kg	6.7	6.7
Permanent Magnets	kg	1.76	0
Rotor steel	kg	11.8	0
Carbon Fiber	kg	0.27	0
Total weight	kg	**69**	**55.2**
Material costs			
Lamination	€	73	73
Copper	€	47	47
Permanent Magnets	€	140	0
Rotor steel	€	7	0
Carbon Fiber	€	73	0
Total cost	€	**340**	**120**

Part II

Fault-Tolerant Synchronous Reluctance Machines

Chapter 7

Fault-Tolerant SyR machine: Introduction

The fault-tolerant (FT) reliability of an electric drive system is a mandatory requirement in those applications where the failure could cause economic costs or, more important, injure the human safety as in the automotive, aerospace and military applications [81–83].

The fault-tolerance of a drive system is defined as the ability to ensure proper speed or torque reference tracking in the event of fault. In other words, more the fault-tolerance is high, more the drive system performance in fault condition approach the rated one. Faults can be firstly classified on the basis of their nature: mechanical and electrical. The most common mechanical faults are due to eccentricity problems [84] and misalignment of bearings [85]. From the electric point of view, the faults mainly occur in the power converter and electric machine [82, 84, 86]. In AC drives, a failure of the inverter switches can cause short-circuit (SC) of the DC bus or a disconnection of one or more phases. In electrical machines, the winding is typically subject to faults due to insulation failures (caused by thermal stress, abrasion or voltage surge), unbalanced supply conditions, a bad connection at the motor terminal, or high resistance contact.

In recent years, several solutions have been adopted to improve the FT reliability of different drive systems focusing on advanced control strategies and dedicated machine design aimed to increase their redundancy [87].

The IM is definitely one of the most used electric machines in the world thanks to its robustness, reliability and mature technology. Most of the proposed solution to increase the FT of IM drive are based on the principle of systems redundancy. Some examples are to adopt multi-phase (greater than three) windings [88–90], to make the winding neutral connection available, or to use inverters with a redundant number of controlled power switches. On the other hand, very poor solutions deals with the IM design itself. A typical IM drive system is shown in Figure 7.1(a). In the event of one phase disconnection the IM can be controlled in single phase operation mode obtaining as result a very high torque ripple component. To overcome such a problem, a two-phase operation mode has been proposed in [91, 92] where the IM neutral point is connected to the middle point of the DC source capacitor bank, as in Figure 7.1(b), and the shifting angle between the healthy phases is set to $\pi/3$. Alternatively, in [93] the IM neutral point is connected to a converter fourth leg as reported in Figure 7.1(c). In this way, the FT reliability is increased, however additional components, i.e. costs, are necessary. In addition, in faulty condition the current amplitudes are $\sqrt{3}$ times higher than the healthy ones so that a high inverter overrating is required. A further solution proposed in [94] is to connect the IM phase terminals to the middle point of the DC bus link as in Figure 7.1(d). With this reconfiguration mode, the available voltages at the IM terminals are $\sqrt{3}$ times lower than the healthy ones. To overcome such a problem it is possible to increases DC bus voltage or the stator winding has to be changed from star connection to delta connection. This involves higher faulty current amplitudes hence, an inverter overrating is still required. Otherwise, the IM may continue to operate in faulty condition yielding only a 50% of the rated torque. Instead of changing the IM drive system connections or adding additional components, it is possible to

mitigate the characteristic low-frequency pulsating torque by injecting odd harmonic voltages at appropriate phase angles [95].

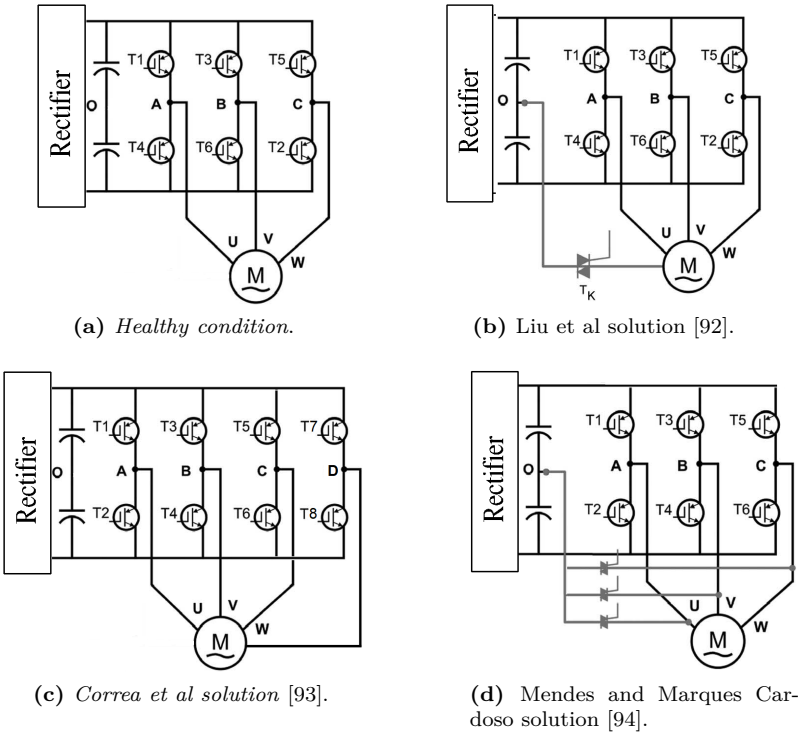

(a) *Healthy condition.*

(b) Liu et al solution [92].

(c) *Correa et al solution* [93].

(d) Mendes and Marques Cardoso solution [94].

Figure 7.1: IM drive system arrangements: typical and custom solutions for maintaining the machine under balanced operation in the event of one inverter leg fault.

A more advanced solution is the adoption of a dual three-phase system as reported in [96]. A sketch of such a drive system is illustrated in Figure 7.2(a). It consist of two separate standard three-phase inverters and a IM with two independent three-phase windings. Each inverter supplies one of the two IM windings. In healthy conditions both windings are fed and the IM produces the rated performance. In the event of fault of one of the two three-phase windings, only the healthy one is supplied while the faulty one is disconnected by means of a dedicated power switch. In this condition, the IM performance are reduced unless a proper power converter overrating is adopted. Despite the high FT reliability of this drive system, it still represents a cheaper solution with respect to the fully redundant systems, composed by two inverters and two motors, or the multi-phase machines that need dedicated power converters and switches [97–99].

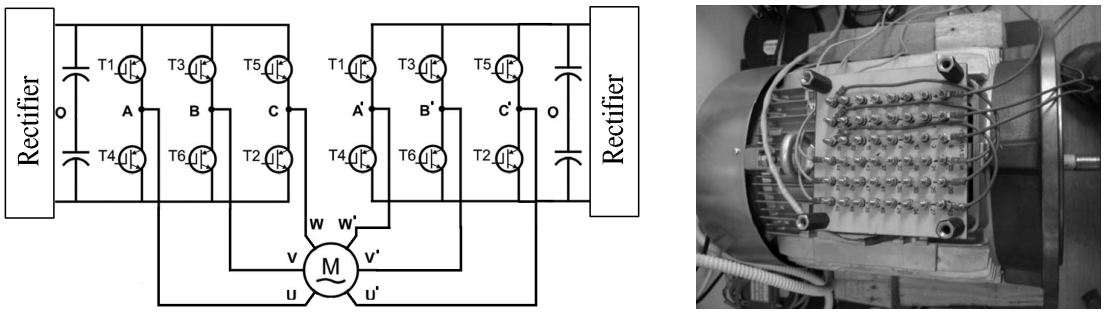

(a)

(b)

Figure 7.2: IM dual-three phase: drive system and prototype [96, 100].

Thanks to its working principle and robust structure, the SWR machine received great attention in FT applications. In addition to the wide variety of control techniques, some solutions which focus on the machine design can be found in literature. The simplest solution to improve its torque ripple is to increase the number of teeth [83] as shows the sketch in Figure 7.3(a). In [101], the modular SWR stator design, illustrated in Figure 7.3(b), is proposed. It consists of a certain number of modules isolated from each other by nonmagnetic spacers [101], the rotor has a classical geometry instead. The magnetic insulators between the stator modules force the magnetic flux lines to flow in the energized module and the corresponding rotor poles only, as highlighted in Figure 7.3(b). Since the coils of each phase are fed independently and one stator slot is not shared by coils from different phases, such a solution exhibit high reliability in case of SCs or overheating. An other interesting solution, patented by Hassan and shown in Figure 7.3(c), consists of adding an additional winding in a typical SWR salient pole rotor to compensate the unbalanced magnetic radial forces that arise in the event of stator winding fault [102]. In healthy condition, the rotor flux paths are symmetrically distributed in all rotor poles so that the resultant electromotive force and induced current in the compensating winding is zero. In faulty condition, the flux is non-symmetrical and an electromotive force different from zero is induced in the rotor winding. Hence, a rotor current arise and its reaction flux tends to compensate the unbalanced radial force.

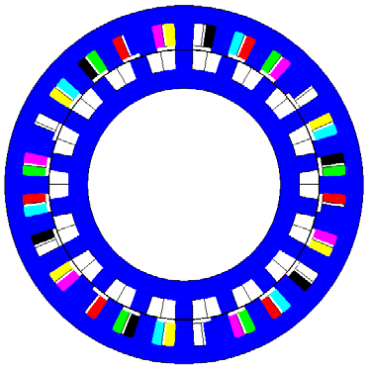

(a) *High number of teeth.*

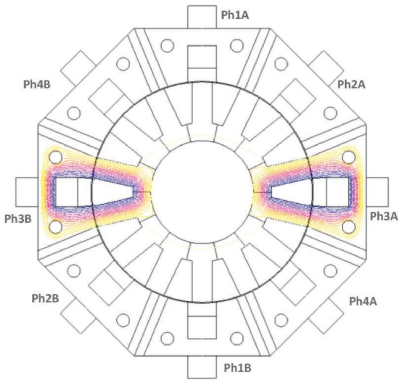

(b) *Modular stator.*

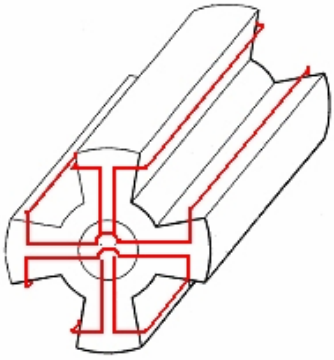

(c) *Active rotor.*

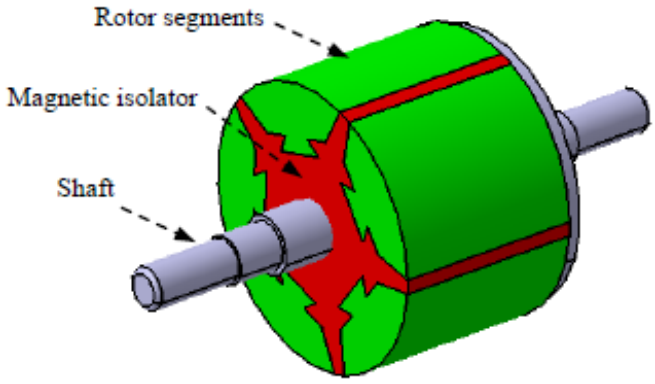

(d) *Segmental rotor.*

Figure 7.3: SWR machine design solutions to improve the FT reliability.

Despite all the proposed solutions allows to effectively increase the SWR machine FT reliability, they have no effect on the well known low power factor and torque density. To overcome such a drawbacks the segmental rotor topology, in Figure 7.3(d), can be adopted. In fact, it has been proven that it yields about a 40% increase in torque for the same copper loss with respect to the usual toothed rotor topology [103, 104]. Its rotor is constructed from a series of discrete magnetic segments insulated from each other by nonmagnetic material.

The PMSM is usually the first choice in the applications where high torque density and effi-

ciency are required even though it presents the highest cost among the electric machines scenario. However, unlike IM and SWR machine, it does not shows an intrinsic FT capability. For example, in the event of a winding SC, the faulty current is continuously fed by the rotor bemf and its amplitude may exceed of several times the rated one with a consequent risk for the PMs magnetization and winding insulation [105, 106]. In case of a open circuit (OC) fault, dangerous high voltages are induced in the faulty phases. Several research activities have been proposed in literature to solve or mitigate these aspects. The risk of SC fault can be reduced with a complete electrical insulation between the phases driving each of them with a dedicated single-phase bridge [107]. Concerning the SC fault reliability, two alternative design solutions can be adopted. The aim of the first one is to minimize the per unit inductance in order to have SC current amplitudes high enough to determine a rapid deterioration of the failure parts and, consequently, to lead to a OC condition. Conversely, in the second and more FT reliable solution, the d-axis inductance is maximized to limit the SC current amplitude below the rated one and therefore to increase the tolerance of the drive system to such a fault even for a long time. Because of its large air-gap length, the PMSM exhibits a very low inductance so that fractional slot windings are usually adopted for their high slot leakage inductance [108]. In such winding arrangements the phase coils are wound around single teeth, as shown in Figure 7.4(a), so that the contact among the phases is reduced as well as the SC risk and overheating propagation. In addition, the fractional slot winding could be arranged to minimize the mutual magnetic coupling too [109]. On the other hand, the main drawbacks of the fractional–slot configurations are a slightly lower winding factor, a high harmonic contents in the MMF distribution and, consequently, higher core and rotor losses [86, 108, 109].

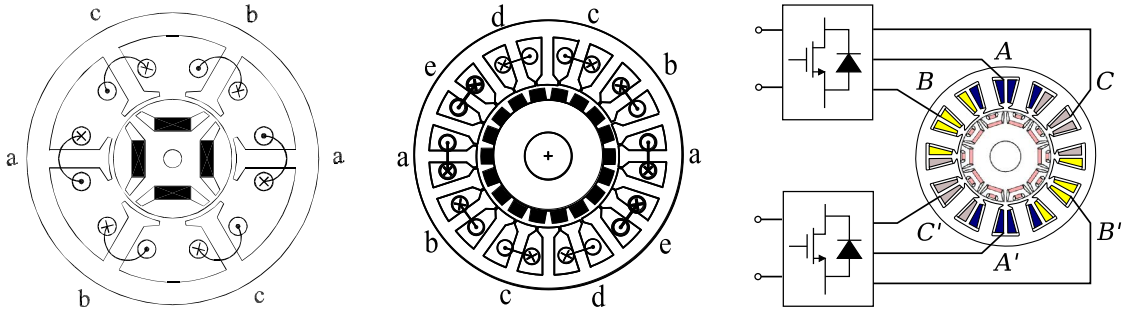

(a) *6-slot 4-pole machine.* **(b)** *Five-phase machine.* **(c)** *Dual three-phase machine.*

Figure 7.4: PMSM for FT applications: utilization of the fractional slot windings and multi-phase systems.

As usual, more than three phases can be adopted to increase the drive system redundancy. The good FT reliability of a five–phase PMSM has been demonstrated in [99, 110] while current control strategies and detailed thermal analyses for an analogous motor, sketched in Figure 7.4(b), have been presented in [111, 112] obtaining good results in terms of FT reliability. In [113, 114], the impact of different dual thee-phase winding arragements in a 12-slot 10-pole PMSM machine, shown in Figure 7.4(c), is investigated in several operating conditions focusing on many aspects such as average torque, torque ripple, unbalanced radial force and thermal limits.

Despite the well known peculiarities of the SyR machine and its potential FT capability due to the lack of rotor PMs, its use in FT applications has been barely proposed during the last years in literature. As for the IM, there is an appreciable electrical, magnetic and thermal interactions among the winding phases. The adoption of fractional slot windings with non overlapped coil to improve the physical and magnetic coupling is not suitable for SyR machine since the high harmonic content of the stator MMF. In [115] a control strategy for a SyR machine supplied by a three-phase full bridge inverter with neutral point accessible is proposed to mitigate the dangerous effect of one phase winding SC failure. Likewise, the behavior of SyR machine supplied by a multi-level inverter with neutral point clamped is analyzed in [116] for different single power switches short-circuit faults. No study noteworthy investigated the SyR machine design for FT application and focused on the impact of different winding arrangements on its FT capability.

This part of the thesis deals with the design of SyR machines with dual three-phase winding

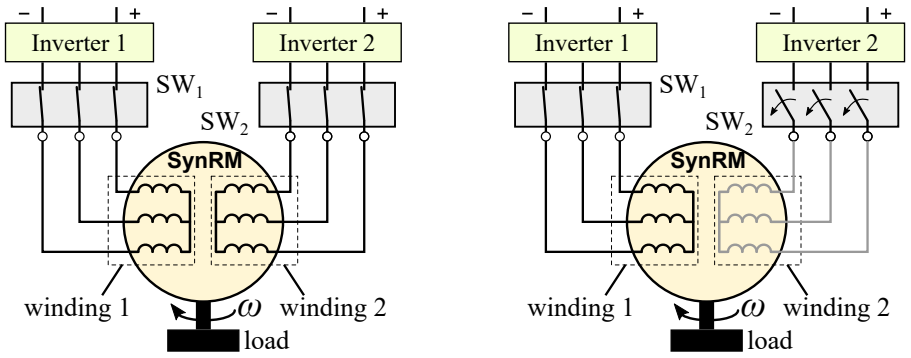

(a) *FWM.* **(b)** *HWM.*

Figure 7.5: Dual three-phase drive system layout in full winding mode (FWM) and open circuit half winding mode (OC-HWM).

with the aim of improving its FT reliability. The dual three-phase winding solution is selected on the basis of the good performance exhibited in the IM and PMSM applications mentioned before. The main operating conditions investigated to evaluate the SyR machine FT reliability are the *full winding mode* (FWM) and *open circuit half winding mode* (OC-HWM). In the first one, reported in Figure 7.5(a), both the three-phase windings are normally supplied by two independent inverters and the SyR machine produces the rated outputs. In the second case, reported in Figure 7.5(b), one of the two windings (i.e. winding 2) is disconnected while the other one is normally supplied.

This thesis part tackles the arguments as follows:

chapter 8 introduces the study of the FT-SyR machine investigating the impact of different dual three-phase winding arrangements on the machine performance by means of FE analysis;

chapter 9 firstly investigates two alternative SyR rotor geometry optimization strategies and secondly carries out a detailed FE analysis on the optimal geometry found;

chapter 10 focuses on both stator and rotor SyR machine geometry optimization and then verifies the FE analyses prediction by means of experimental results carried out on a prototype specifically designed on the basis of the optimization results.

Chapter 8

Impact of winding arrangement in dual three-phase SyR machine

8.1 Introduction

This chapter introduces the study of the FT-SyR machine investigating the impact of different dual three-phase winding arrangements on the machine performance by means of FE analysis [6].

The machine performance under investigation are: average torque, torque ripple, unbalanced radial force on the rotor and mutual magnetic coupling between the two three-winding phases. The first three items are evaluated in FWM and OC-HWM.

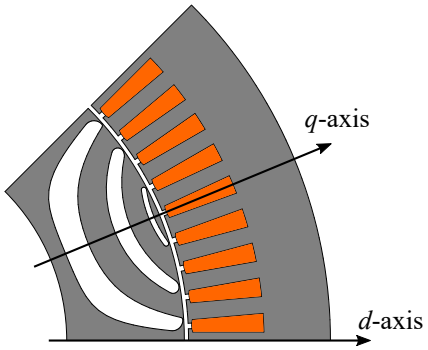

Figure 8.1: Sketch of portion of an eight–pole synchronous reluctance motor with three flux–barriers per pole.

The FE analyses are performed on the SyR motor sketched in Figure 8.1 whose main data are reported in Table 8.1. The stator geometry is standard while the rotor one has been optimized accordingly following the procedure reported in section 4.3. A single layer three-phase winding was initially adopted to have only one phase coils per slot. The parameters used for the optimization were the magnetic insulation ratio and the three flux-barrier angles, the other rotor parameters have been computed as reported in section 15.3. The optimization cost functions were the maximum average torque and the minimum torque ripple in MTPA condition. The optimal rotor parameters are reported in Table 8.1. The objective evaluation procedure reported in section 4.3 has been adopted in the optimization. Initially, a rated current density of $6\,\mathrm{A/mm^2}$ has been selected according to the typical operating condition and thermal limits. However, the results of such optimization were characterized by high flux density values in the stator yoke (e.g. 1.8 T) and teeth (e.g. 1.9 T). For this reason, the current density has been decreased to $5\,\mathrm{A/mm^2}$ obtaining optimal flux density values as will be described later on.

The first part of the chapter describes the dual three-phase winding arrangements under analysis. Then, the motor performance, in FWM and OC-HWM, are evaluated for each winding

configuration. Finally, a comparison between the different winding arrangements is carried out highlighting their pros and cons.

Table 8.1: Main data of the motor.

Motor part	Symbol	Value	Unit
Outer diameter	D_e	535	mm
Inner diameter	D_s	375	mm
Stack length	L_stk	100	mm
Pole number	$2p$	8	-
Slot number	Q_s	72	-
Slot height	h_s	42.5	mm
Tooth width	w_t	9.6	mm
Air-gap	g	0.5	mm
Flux-barrier angles	$\vartheta_\mathrm{b1}, \vartheta_\mathrm{b2}, \vartheta_\mathrm{b3}$	$\{20.6, 51.9, 75.3\}$	deg
Magnetic insulation ratio	k_air	0.4	-
Winding layers	N_Lay	1	-
Series conductor per slot	n_ncs	1	-
Phase current density	J	5 rms	$\mathrm{A/mm^2}$
Iron lamination			M530-50A

8.2 Dual three-phase winding arrangements

In the following, the phases of the two windings are labeled as A_1, B_1, C_1 and A_2, B_2, C_2, respectively. The latter phases are open-circuited in OC-HWM condition. In all the analyses, the root mean square current density is kept fixed to $5\,\mathrm{A/mm^2}$.

8.2.1 Configurations with three winding axes

The distribution of the phase coils and relative phase axes, A, B, C (indicated with arrows) in a conventional single layer three-phase winding with 72-slot and 8-pole, labeled W-3ph, are reported in Figure 8.2(a). It presents 3 slots per pole per phase, a coil throw equal to 9 slots, a winding factor $k_\mathrm{w} \approx 0.96$ and a periodicity equal to 4 (i.e. the winding can be split in four equal parts).

From such a coil distribution, it is possible to arrange two different dual three-phase windings arrangements. In the first configuration, referred to as W-11-22, the stator is split in two separate parts, each of them containing one of the two three-phase windings. In the second one, referred to as W-12-12, the stator is split in four parts and the dual winding coils are alternated for each pole pair. The two configurations are shown in Figure 8.2(b) and Figure 8.2(c), respectively. The background colors highlight the regions that belong to the three-phase winding 1 and 2. Even though the number of electrical phases is six, the actual number of winding axes is still three. For example, the A_1- and A_2-axis coincide with the A-axis of the standard three-phase winding, the same for the left phases. This implies that, in both cases, the dual three-phase windings has to be supplied with an equal number of three-phase current systems *in phase* as reported in Figure 8.2(d). Moreover, it is worth noticing that, in FWM, all the windings in Figure 8.2 are equivalent by definition while, as will be explained in section 8.3 and section 8.5, they exhibit different characteristics in OC-HWM.

8.2.2 Configuration with six winding axes

With the adopted slot-pole configuration, the unique coil distribution which allows to obtain six different winding axes is reported in Figure 8.3(a) and labeled as W-6ph. It can be noted that the phases of the two three-phase windings are distributed along the whole stator periphery so that it is not possible to distinguish areas which belongs to only one winding as in Figure 8.2(b) or

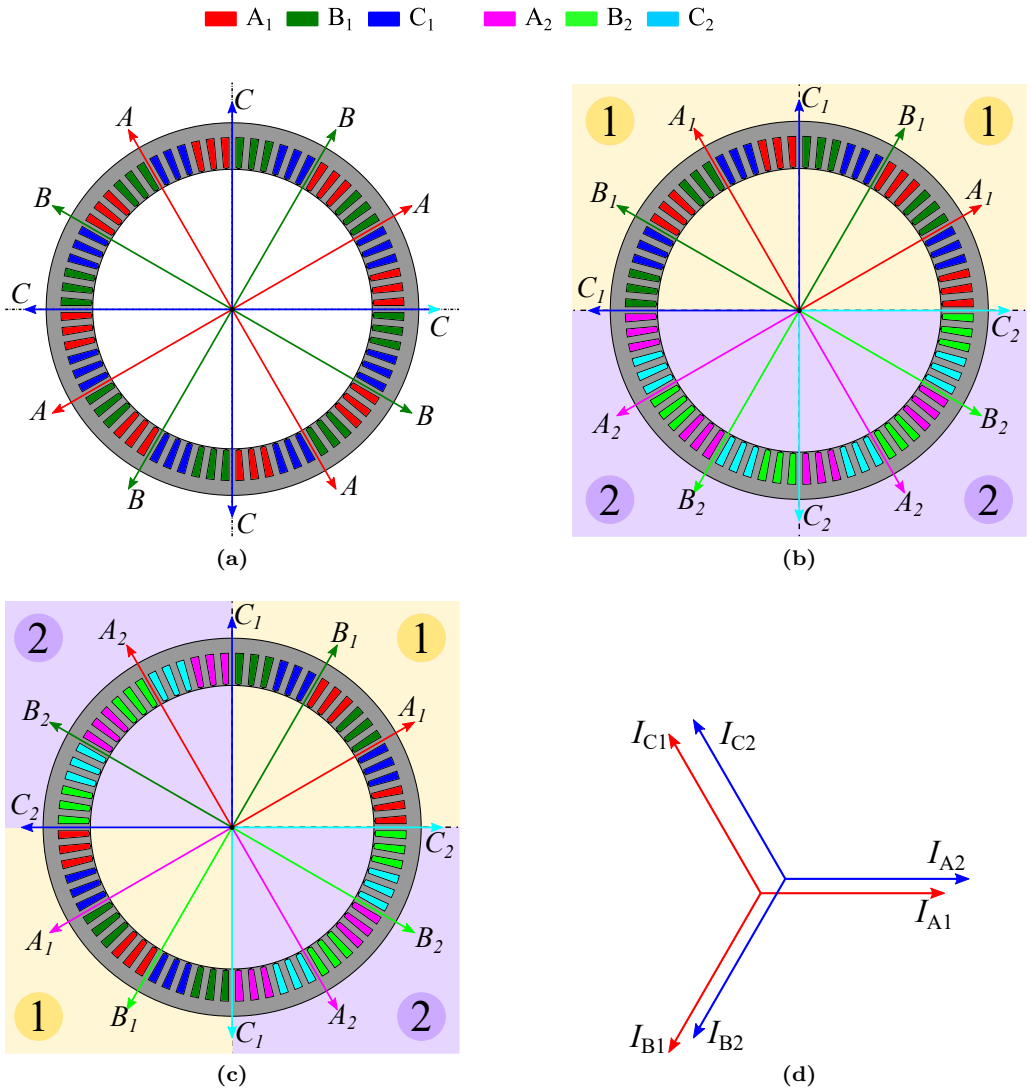

Figure 8.2: Phase coils distribution in standard three-phase (*a*) and dual three-phase winding arrangements W-11-22 (*b*), W-12-12 (*c*) with relative *in phase* currents supply condition.

Figure 8.2(c). The winding is characterized by a periodicity of 2 and a winding factor equal to 0.986. From the vector diagram in Figure 8.3(b) the electrical displacement between the phases A_1 and A_2 [117, 118] results to be:

$$\beta = 2\left[\frac{\pi}{9} - \arctan\left(\frac{\sin(\pi/9)}{2+\cos(\pi/9)}\right)\right] = 0.466\,\text{rad} = 26.7° \tag{8.1}$$

that differs from the classical 30° of the six phase windings.

In addition to the *in phase* current supply condition, in Figure 8.2(d), this winding can be also supplied by currents *out of phase*, as reported in Figure 8.3(c). In the first case, the winding FWM behavior in the same of the standard three-phase one in Figure 8.2(a). In the second case, the winding behaves as an actual six-phase winding yielding higher winding factor (i.e. 0.986) and lower MMF harmonics. In particular, in this operating condition, the temporal displacement of the the two three phase system is equal to the spatial one.

Hereafter, only this current supply condition will be considered for the considered winding. In OC-HWM, the winding exhibits completely different characteristics from the other ones as will be described later on.

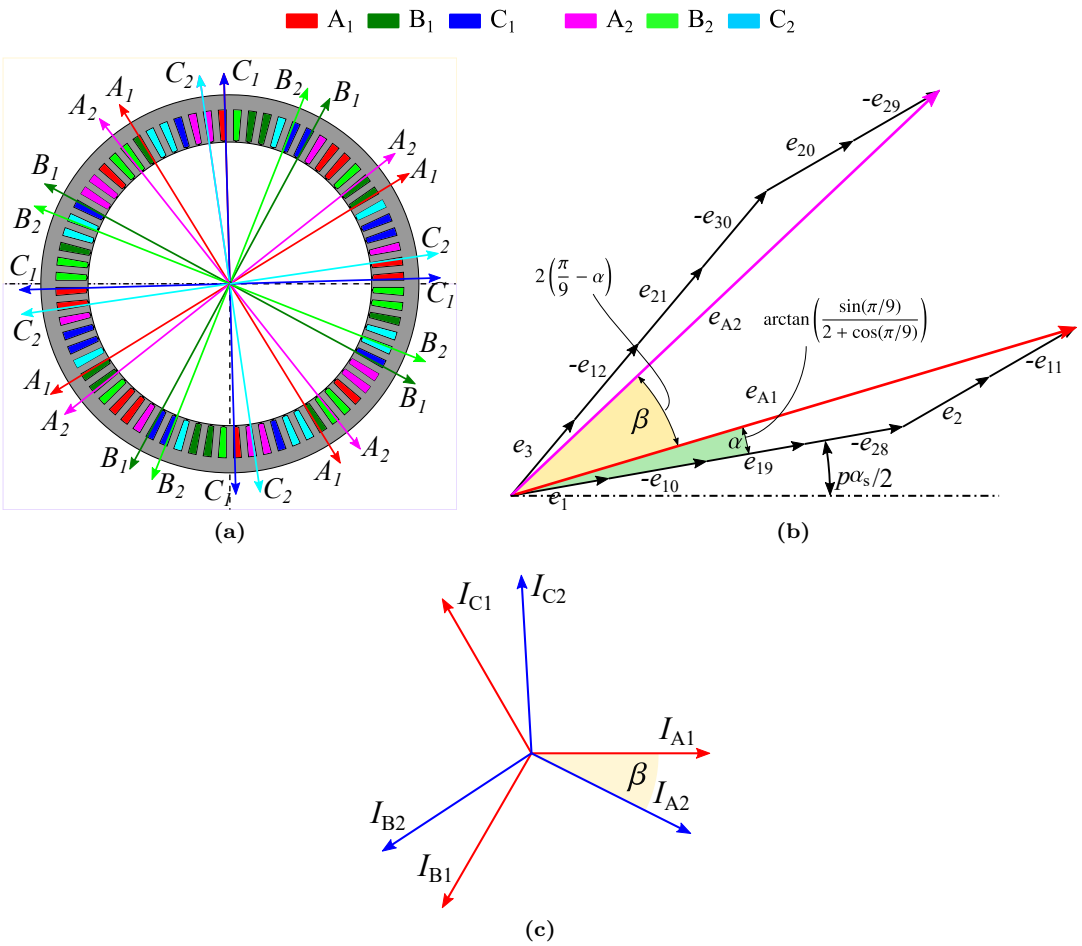

Figure 8.3: Phase coils distribution in the dual three-phase winding arrangement with six different winding axes (*a*), phases displacement computation (*b*) and relative *out of phase* current supply condition (*c*).

8.3 Torque comparison

This section shows the FE results about the torque behavior of the different winding configurations in FWM and OC-HWM. Table 8.2 summarizes the numerical results in terms of average torque, torque ripple and maximum unbalanced force on the rotor.

8.3.1 FWM torque

From Table 8.2 it can be noted that the average torque of the winding W-3ph is slightly lower than the W-6ph one while the torque ripple is about 3% higher. The better performance of the winding W-6ph are mainly due to the higher winding factor and the lower MMF harmonic content. The flux density plots obtained with the two different windings are reported in Figure 8.4(a) and Figure 8.4(b), respectively. From the comparison it can be observed that the maximum flux density in teeth is about the same while in the stator yoke the flux density increases of about 6.2% from W-3ph to W-6ph.

8.3.2 OC-HWM

Winding W-11-22

Figure 8.5(a) reports the torque behavior obtained with the winding configuration W-11-22 in OC-HWM. It is possible to see that the average torque is about 44% of the FWM one so that the

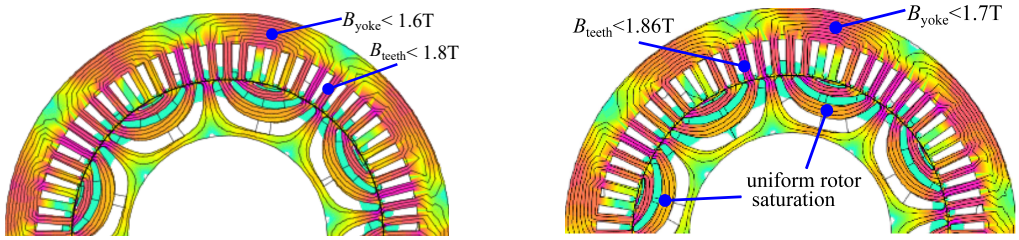

(a) W-3ph. **(b)** W-6ph.

Figure 8.4: FWM flux density plots with in phase (a) and out of phase (b) current supply conditions. The first one refers to the winding arrangements in Figure 8.2 while the second one to Figure 8.3(a).

torque ripple results to be more than double (i.e. 37.5%).

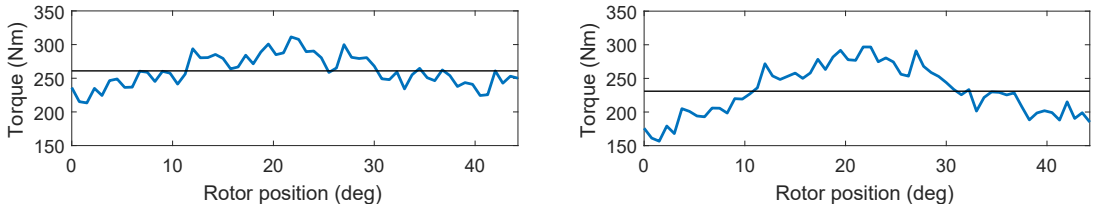

(a) W-11-22. **(b)** W-12-12.

Figure 8.5: Torque versus rotor position of winding W-11-22 and W-12-12 in OC-HWM.

The torque waveform has a period of 180 electrical degrees. Figure 8.6(a) and Figure 8.6(b) show the flux density plots obtained when the torque is minimum, $\vartheta_{\mathrm{m}} = 0°$, and maximum, $\vartheta_{\mathrm{m}} = 22.5°$, respectively. The shaded area highlights the region of the supplied winding (i.e. winding 1). The horizontal dashed line that splits the two winding regions is called boundary axis $\overline{xx'}$. The continuous line which surround a rotor pole indicates its position during the rotation.

It is possible to see that the flux-barriers position, with respect to the axis $\overline{xx'}$, greatly affects the flux density distribution. In particular, when the flux-barriers do not cross the axis $\overline{xx'}$, as in Figure 8.6(a), most of the flux lines flow in the region of the winding 1. The flux lines flowing in the stator yoke of the winding 2 (open-circuited) are due to the sub-harmonic of the stator MMF. With respect to the FWM, the flux density in the stator yoke and in the teeth increase up to 1.69 T and 1.88 T, respectively. As the flux-barriers cross the axis $\overline{xx'}$, as in Figure 8.6(b), a large number of flux lines, surrounded by red dashed line, flow in the stator area of the winding 2 causing a reduction of useful flux, a higher saturation near the boundary axis and, consecutively, the torque reduction.

Winding W-12-12

Figure 8.5(b) shows the torque waveform of the winding configuration W-12-12 in OC-HWM. The average torque is 38% of FWM one while the absolute torque ripple is 50% higher. The two boundary axes $\overline{xx'}$ and $\overline{yy'}$ (dashed lines) delimit the winding 1 and 2 regions. The torque period is 180 electrical degrees but in this case the difference between maximum and minimum torque is higher than the previous one.

The flux density plots, corresponding to the minimum and the maximum torque of the winding W-12-12, are reported in Figure 8.7(a) and Figure 8.7(b), respectively. Similarly to the winding configuration W-11-22, the maximum torque is achieved when the flux-barriers are within the winding 1 regions (dashed areas in Figure 8.7(a)). Conversely, when the flux-barriers cross the axes $\overline{xx'}$ and $\overline{yy'}$, as in Figure 8.7(b), a part of the main flux flows in the winding 2 regions. The wider boundary regions of such a winding arrangement with respect to W-11-22 explains the lower average torque and higher oscillation.

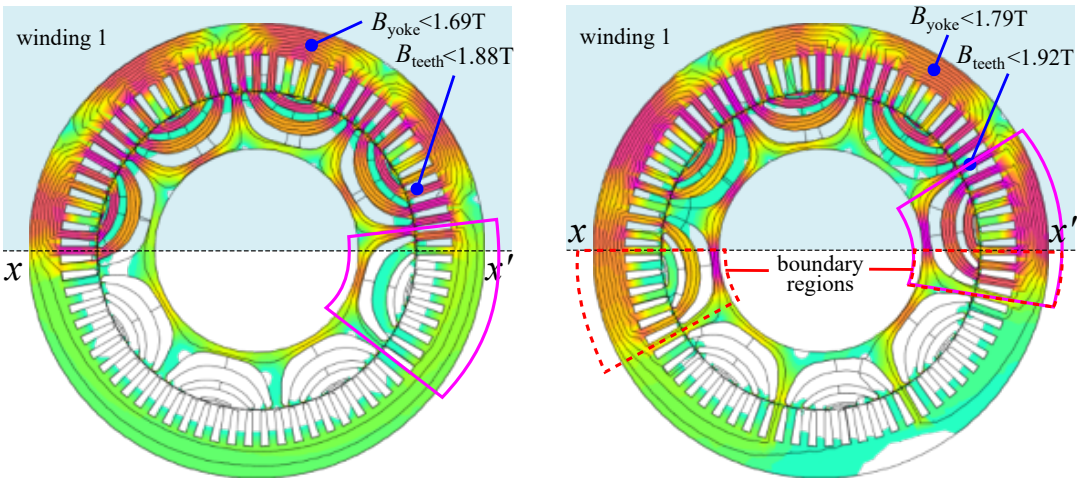

(a) $\vartheta_m = 22.5°$, *maximum torque.* **(b)** $\vartheta_m = 0°$, *minimum torque.*

Figure 8.6: Flux density plots of the winding W-11-22 in OC-HWM for different rotor positions.

Winding W-6ph

The torque waveform of the winding W-6ph in OC-HWM is shown in Figure 8.8(a). The motor achieves an average torque that is 41% of the FWM one while the torque ripple is about four times higher. The lower average torque with respect to the dual three-phase arrangements (W-11-22 or W-12-12) is due to the fact that, in the current case, the whole air-gap motor has to be magnetized. The higher torque ripple is justified by the worst harmonic content of the stator MMF due to the lower number of effective slots.

From the flux density plot in Figure 8.8(b), it can be noted that the magnetic loading is not uniform in the motor. In particular, the stator yoke flux density in the left area is higher than the right one since the number of slots occupied by the winding 1 is higher in the right machine quarter.

8.4 Radial force

The radial force on the rotor has been computed for each winding configuration. From Table 8.2, it results that in OC-HWM only the winding configuration W-11-22 exhibits a non negligible radial force (i.e. 12 kN). This is expected since, in such configuration, the winding 1 covers only a part of the stator periphery. On the contrary, in all other arrangements, a balanced force remains even in OC-HWM since a mechanical winding symmetry remains.

8.5 Magnetic coupling between winding 1 and 2

This section deals with the evaluation of the magnetic coupling between winding1 and winding 2 phases for different winding configurations. The self and mutual inductances between the phases are computed setting a constant current in the phase A_1 and considering the other phases disconnected. The current density is still $5\,\mathrm{A/mm^2}$.

Figure 8.9 shows the waveform of self and mutual inductances versus rotor position for different winding configurations. The self inductance of the phase A_1 is labeled as L_{A1} while the mutual inductance with phase B_1 and C_1 are labeled as M_{A1B1} and M_{A1C1}, respectively. The mutual inductances between phase A_1 and the winding 2 phases are labeled as M_{A1A2}, M_{A1B2} and M_{A1C2}.

All self and mutual inductances of the winding 1 phases exhibit about the same maximum value (i.e. 0.077 mH). Only W-6ph inductance curves, shown in Figure 8.9(c), are symmetric with respect to the A_1-axis for symmetry reason. The magnetic coupling of each winding configuration

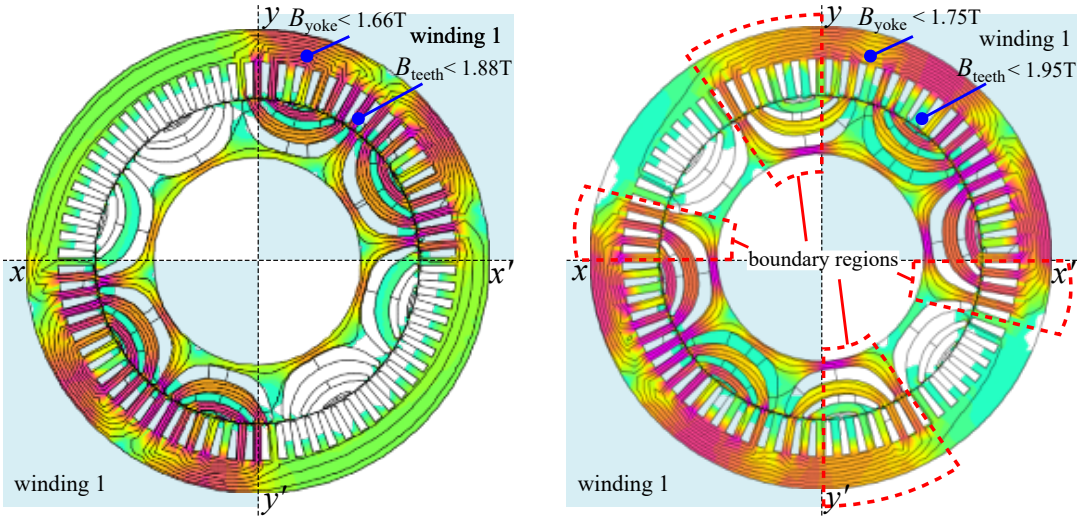

(a) $\vartheta_m = 22.5°$, *maximum torque.* **(b)** $\vartheta_m = 0°$, *minimum torque.*

Figure 8.7: Flux density plots of the winding W-12-12 in OC-HWM for different rotor positions.

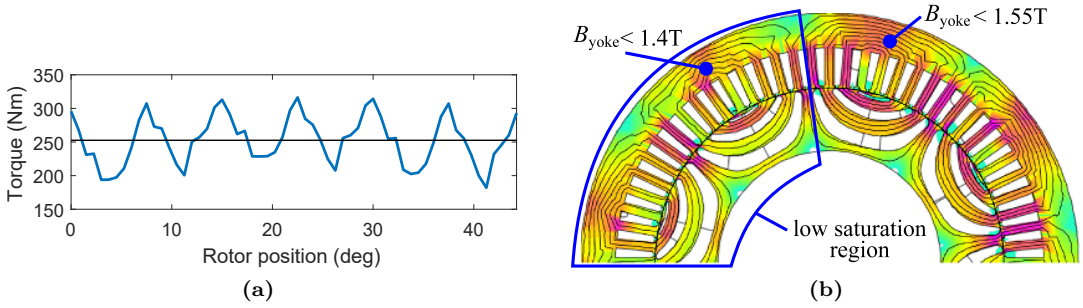

(a) **(b)**

Figure 8.8: Torque waveform (a) and flux density plot (b) obtained with the winding W-6ph in OC-HWM.

is determined by the amplitude of the mutual inductance between phase A_1 and the winding 2 phases. In particular, the maximum value of the ratio between L_{A1} and the mutual inductances M_{A1A2}, M_{A1B2} and M_{A1C2}, indicated as r_{mc}, gives the grade of coupling and allows to compare the different winding configurations. The behaviors of the mutual inductance are reported in Figure 8.9(d), Figure 8.9(e) and Figure 8.9(f). It is possible to observe that the winding W-11-22 achieves the lowest magnetic coupling ($r_{mc} = 0.37$) while the six-phase winding achieves the highest one ($r_{mc} = 0.95$). The magnetic coupling ratio of the winding W-12-12 is 60% higher than the W-11-22 one ($r_{mc} = 0.59$). The high magnetic coupling of the winding W-6ph is due to the fact that the coils of different phases are distributed along the whole stator diameter. Conversely, the windings W-11-22 and W-12-12 exhibit a lower magnetic coupling since, as can be observed in Figure 8.6(b) and Figure 8.7(b), only a small part of the flux flows through the winding 2 regions.

8.6 Conclusions

In this chapter the open circuit fault suitability of three different dual three-phase winding arrangements has been investigated by means of FE analysis on a SyR machine. Various aspects are taken into account: average torque, torque ripple, unbalanced radial force on the rotor and magnetic coupling. The analyses have shown that when one of the two three-phase system is disconnected (OC-HWM) all the winding arrangements exhibit an average torque that ranges between 38% and 44% of the rated one (FWM). The torque ripple in OC-HWM is always higher than the FWM

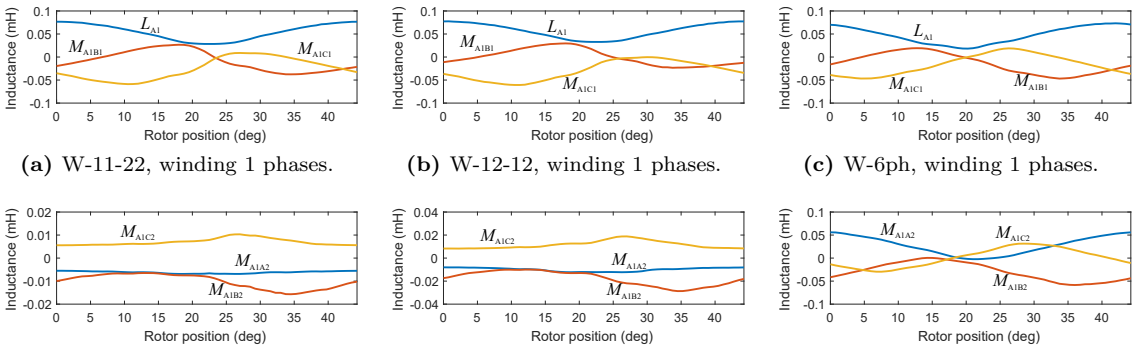

(a) W-11-22, winding 1 phases. **(b)** W-12-12, winding 1 phases. **(c)** W-6ph, winding 1 phases.

(d) W-11-22, winding 2 phases. **(e)** W-12-12, winding 2 phases. **(f)** W-6ph, winding 2 phases.

Figure 8.9: Self and mutual inductances versus rotor position for different winding configurations. The columns refer to the winding W-11-22, W-12-12 and W-6ph, respectively.

Table 8.2: Comparison of simulated motor performance with various winding arrangements in different operating conditions.

Operating condition	Winding arrangement	Average Torque (Nm)	Torque Ripple (%)	Unbalanced Radial Force (kN)
FWM	W-3ph	595	16.4	≈ 0
	W-6ph	611	13.3	≈ 0
OC-HWM	W-11-22	261	37.5	$\approx 12\,\text{kN}$
	W-12-12	231	60.7	≈ 0
	W-6ph	253	53.2	≈ 0

one and ranges between 37% and 61%. These aspects suggest that, during the design of this SyR motor, the reduction of torque ripple in OC-HWM, has to be an objective.

Furthermore, concerning the radial force, the configuration W-11-22 is the worst among the analyzed solutions achieving 12 kN. This is due to the asymmetric distribution of the stator winding. For this reason, the considered configuration cannot be applied in OC-HWM even if it exhibits the highest average torque and minimum ripple. The radial force of the other solutions is negligible for symmetry reasons.

The magnetic coupling of the different windings has been evaluated to estimate the amplitude of the maximum induced voltages in OC-HWM. The analyses showed that configurations W-11-22 and W-12-12 present the lowest magnetic coupling (i.e. $r_{\text{mc}} < 0.6$) while winding W-6ph reaches the maximum one (i.e. $r_{\text{mc}} \approx 0.95$). Hence, the latter winding is not reliable in OC-HWM since the induced voltages in the disconnected phases reach about the nominal value.

In conclusion, the winding W-12-12 represents a good compromise in terms of radial force and magnetic coupling but further investigations has to be carried out to limit its high torque ripple in OC-HWM.

Chapter 9

Optimization and Analysis of a SyR machine for FT Applications

9.1 Introduction

In chapter 8 it has been shown that the SyR machine with the dual three-phase winding arrangement W-12-12 exhibits, in general, good performance in both FWM and OC-FWM except for the torque ripple that is quite high in the second operating condition.

The aim of the this chapter is to improve the torque waveform of such a drive system focusing on the SyR rotor design. In particular, a standard geometry, whose main data are reported in Table 9.1, is selected for the stator lamination, while two alternative FE-based optimization approaches are proposed for the rotor design. On the basis of the optimization results, the most promising individual is selected and analyzed in detail by means of FE analysis in FWM and OC-HWM.

Table 9.1: Main motor data.

Dimension	Value	Unit
Stator outer diameter	170	mm
Stator inner diameter	115	mm
Number of slots	36	-
Pole pairs	4	-
Air-gap	0.4	mm
Slot height	17.5	mm
Tooth width	5.3	mm
Stack length	85	mm
Winding layers	2	-
Current density RMS	6	A/mm^2
Rated current	8	A
Voltage DC bus	350	V

9.2 Rotor optimization strategies

Two different optimization strategies are proposed in the following. In the first one, referred to as FWM optimization (FWM-OPT), the objectives are to maximize the average torque and to minimize the ripple in FWM only (FWM objectives). In the second one, referred to as Full-Half winding mode optimization (FHWM-OPT), the average torque and ripple in OC-HWM are additional objectives of the optimization (OC-HWM objectives).

The rotor parameters are the flux-barrier angles, ϑ_{b1}, ϑ_{b2}, ϑ_{b3}, and magnetic insulation ratio k_{air}. The flux-barrier and iron channel thicknesses are computed as described in section 15.3. A rated current density of $6\,A/mm^2$ has been set for the performance evaluation in FWM and OC-HWM. The torque ripple is computed as the relative standard deviation percentage of the FE torque waveform.

9.2.1 FWM-OPT strategy

Following the procedure described in section 4.3, this optimization has been carried out in 80 generations with a population of 30 individuals each. The resulting objectives plane is reported in Figure 9.1. The horizontal and the vertical axes report the average torque and torque ripple, respectively. The circle markers indicate the Pareto front individuals. It can be noted that the average torque of the Pareto front ranges between 13.4 Nm and 13.7 Nm while the ripple presents a high variation between 1% and 10%. Some rotor sketches are reported in the plot to highlight how the geometry varies as the ripple decreases. It is possible to see that the shape of the flux-barriers near the air-gap tends to be sharper as the ripple decreases. This is because the shape of the flux-barrier strongly affects the flux density distribution within the tangential iron ribs. The individual with the lowest torque ripple (1%) and an average torque of 13.5 Nm has been selected. The corresponding flux-barrier angles are $\vartheta_{b1} = 34.8°$, $\vartheta_{b2} = 55.1°$ and $\vartheta_{b3} = 71°$ while the magnetic insulation ratio is $k_{air} = 0.44$. The same rotor geometry has been analyzed in OC-HWM yielding an average torque of 6.5 Nm (50% of the FWM value) and a torque ripple of 11.7 %, 11 times higher than the FWM one. The results are summarized in Table 9.2.

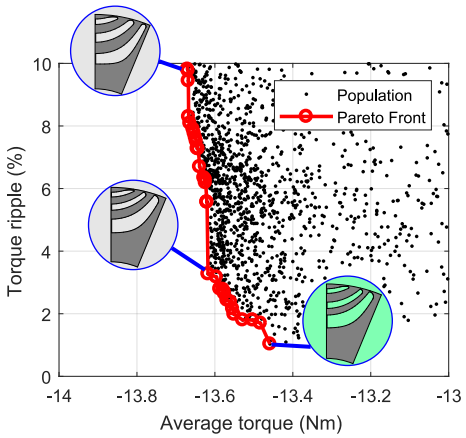

Figure 9.1: Objectives planes of the optimization strategy FWM-OPT: torque ripple versus average torque.

9.2.2 FHWM-OPT strategy

Figure 9.2 reports the flowchart of the objectives evaluation procedure performed for each individual of the optimization strategy FHWM-OPT. At first, the geometry feasibility of the motor is evaluated. The unfeasible individuals are rejected and their average torque and ripple values are set to 0 and 10^6, respectively. Otherwise, the radial ribs of the feasible individuals are computed according to the maximum speed. Next, the MTPA current angle in FWM is estimated in an iterative way by means of single step FE simulations. The resulting current vector is then used to evaluate the average torque and torque ripple in FWM. After that, the MTPA current angle in OC-HWM is found like before and then used to get the OC-HWM cost functions.

The objectives planes of the FWM and OC-HWM cost functions are reported in Figure 9.3(a) and Figure 9.3(b), respectively. The green diamond markers in the two figures are the non-dominated individuals in the FWM objectives plane (FWM Pareto front). Similarly, the red circle markers represent the non-dominated individuals in the OC-HWM objectives plane (OC-HWM Pareto front). It can be noted from the first plot that the average torque of the FWM Pareto

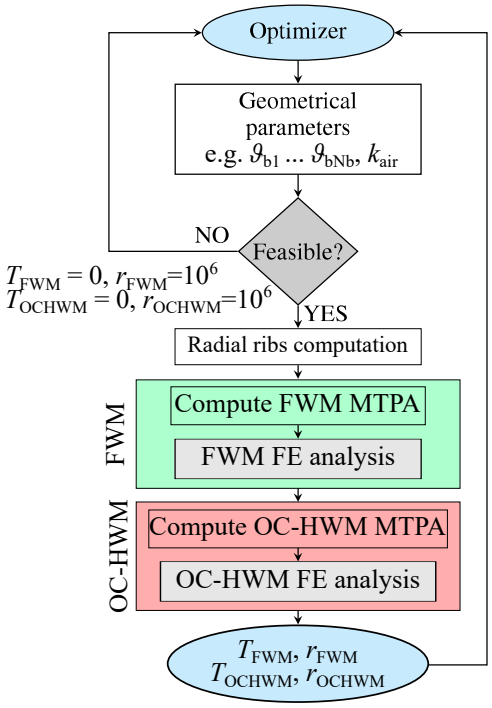

Figure 9.2: Flowchart of the FHWM-OPT strategy.

front ranges between 13.5 Nm and 13.8 Nm while the ripple is always lower than 4%. Conversely, the OC-HWM Pareto individuals, in the same plot, are distributed in a wide average torque range (from 13 Nm to 13.7 Nm) with a limited torque ripple variation (between 2% and 4%). The OC-HWM objectives plane, in Figure 9.3(b), shows that the average torque of the OC-HWM Pareto individuals ranges between 5 Nm and 5.7 Nm with a limited torque ripple variation (i.e. between 4.3% and 6.6%). On the contrary, the FWM Pareto individuals, in the OC-HWM plane, are characterized by a high torque ripple variation with a limited average torque variation (shaded area in Figure 9.3(b)). The rotor sketches reported in the plot show the rotor geometry variation along the OC-HWM Pareto front. It should be noted that the outer flux-barrier angle tends to increase as the torque ripple decreases while the inner flux-barrier angle moves away from the d-axis.

In this case, due to the higher number of cost functions, the selection of the optimal individual is less oblivious than in the previous case. For the present case study, the individual C, sketched in Figure 9.4(b), has been selected having chosen the OC-HWM torque ripple as the main objective to minimize. Such an individual has also been selected on the basis of the flux-barriers geometry feasibility. In fact, many geometries among the alternative solutions were actually unfeasible because of the very small iron channel thickness or the sharp flux-barrier fillets near the air-gap.

Table 9.2: Average torque and ripple of the optimal individuals in FWM and OC-HWM.

Optimization strategy	Operating condition	Torque (Nm)	Ripple (%)
FWM-OPT	FWM	13.5	1.1
	OC-HWM	6.5	11.7
FHWM-OPT	FWM	13.3	2.6
	OC-HWM	5.6	5

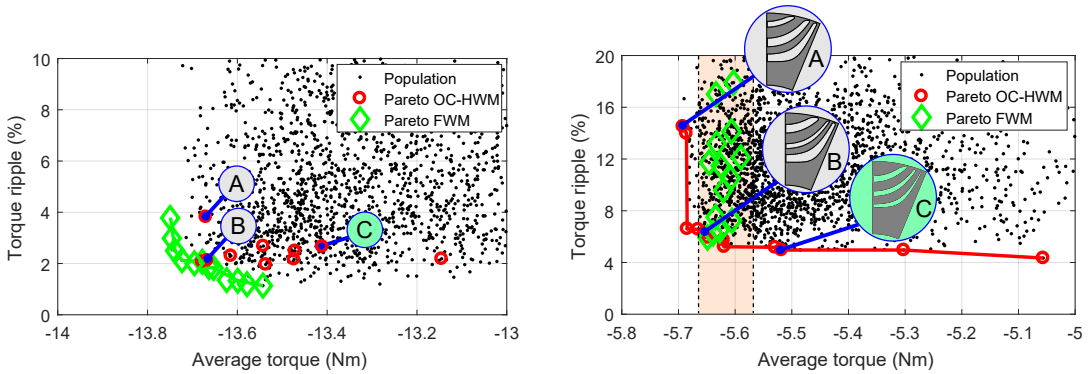

(a) *FWM objective plane.* **(b)** *OC-HWM objective plane.*

Figure 9.3: Objectives planes of the optimization strategy FHWM-OPT: torque ripple versus average torque.

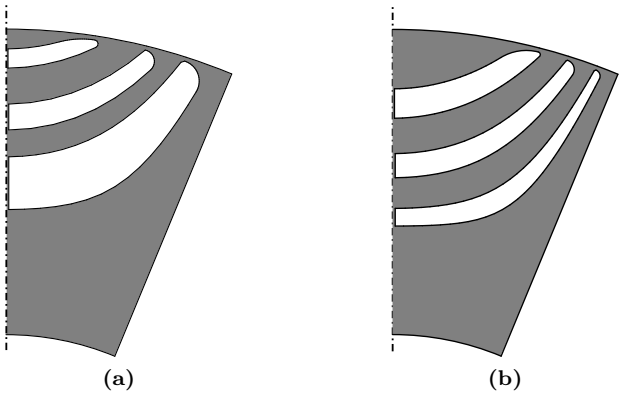

(a) **(b)**

Figure 9.4: Rotor sketches of the optimal individuals obtained from FWM-OPT (*a*) and FHWM-OPT (*b*).

9.3 Mutual magnetic coupling

This section deals with the analysis of the mutual inductances among the two three phase windings. The simulations are carried out imposing constant currents in the winding 1 and considering the other one open-circuited. The winding 1 phases are fed with the following constant currents: $I_{\mathrm{A1}} = 8\,\mathrm{A}$ and $I_{\mathrm{B1}} = I_{\mathrm{C1}} = -4\,\mathrm{A}$.

Figure 9.5(a) shows the flux linkage behavior of the supplied phases. The flux linkage of each phase follows the behavior of the rotor permanence. In fact, it is maximum (minimum) when the rotor d-axis (q-axis) is aligned to the phase axis. Figure 9.5(b). report the flux linkage amplitude (i.e. without sign) behaviors of the winding 2 phases. It can be noted that the maximum induced flux linkage is about 76 mVs that is about 25% of the maximum flux linkage in the winding 1 phases. This confirms the low magnetic coupling between the two windings.

9.4 Magnetic model of the machine

From the control point of view, it is particularly important to know the magnetic characteristics of the machine and its behavior in FWM and OC-HWM. This section reports the most important curves used to determine the control of a machine. In particular they are: the constant torque loci and the magnetizing curves along the d- and q-axis described by:

$$\begin{cases} \Lambda_{\mathrm{d}} = \Lambda_{\mathrm{d}}(I_{\mathrm{d}}, I_{\mathrm{q}}) \\ \Lambda_{\mathrm{q}} = \Lambda_{\mathrm{q}}(I_{\mathrm{d}}, I_{\mathrm{q}}) \end{cases} \tag{9.1}$$

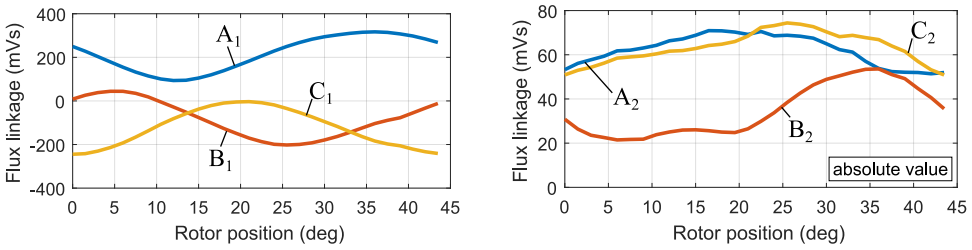

(a) *Winding 1 phases.* **(b)** *Winding 2 phases.*

Figure 9.5: Flux linkages versus rotor position of the FWM and disconnected phases. The curves are obtained feeding only one of the two windings with constant currents whose amplitudes are: $I_{\mathrm{A1}} = 8\,\mathrm{A}$ and $I_{\mathrm{B1}} = I_{\mathrm{C1}} = -4\,\mathrm{A}$.

where Λ_{d} (Λ_{q}) and I_{d} (I_{q}) are the flux linkage and current along the d-axis (q-axis), respectively.

9.4.1 Magnetizing characteristics

d-axis

The d-axis magnetizing curves obtained in FWM and OC-HWM are reported in Figure 9.6(a) and Figure 9.6(b). The thicker black lines are obtained without cross-saturation, i.e. $I_{\mathrm{q}} = 0$. It is possible to see that, in general, the flux linkage obtained in OC-HWM is tends to be higher than in FWM. In particular, the maximum FWM flux linkage is about 0.36 Vs while in OC-HWM is 10% higher. Likely, for the same d-axis current $I_{\mathrm{d}} = 8\,\mathrm{A}$, the maximum flux linkage in the two cases is 0.31 Vs (point D_F) and 0.35 Vs (point D_H), respectively. This aspect can be explained with the flux density plots in Figure 9.6(c) and Figure 9.6(d) obtained in the point D_F and D_H, respectively. From the comparison it is evident that in FWM the magnetic loading is higher than in the other operating condition. In particular, the maximum flux density in the teeth is about 1.8 T in the first case while is 1.7 T in the second one. The cross-saturation impact is also different in the two operating conditions. With respect to a fixed d-axis current, i.e. 8 A, in FWM the flux linkage reduces of 12% (point D'_F) while in OC-HWM the reduction is about 15.5% (point D'_H). The higher flux linkage drop in the latter case can be explained with the flux density plots in Figure 9.6(e) and Figure 9.6(f). In fact, in the second one it is possible to note a higher stator yoke flux density and a higher number of flux leakage lines that flow in the winding 2 region (left machine portion). This "deviation" of the flux lines is more evident for low current levels in which the stator yoke saturation does not limit such a flux leakage.

q-axis

The q-axis magnetizing curves in FWM and OC-HWM are reported in Figure 9.7(a) and Figure 9.7(b), respectively. The thicker black lines are obtained with $I_{\mathrm{d}} = 0$ that means without cross-saturation. In such a supply condition, the difference between FWM and OC-HWM is evident only for very high currents, i.e. $I_{\mathrm{q}} = 16\,\mathrm{A}$, while is not meaningful for $I_{\mathrm{q}} = 8\,\mathrm{A}$. As I_{d} increases, the variation of the q-axis flux is more evident than along the d-axis. More precisely, the flux linkage in the point Q'_H is 0.092 Vs (increment of 42% with respect Q_F) while in the point Q'_F is 0.112 Vs (increment of 72% with respect Q_H). From the flux density plots in Figure 9.7(c) and Figure 9.7(d), corresponding to the points Q'_F and Q'_H, it can be noted that the teeth flux density in the winding 1 region is similar in the two cases while the yoke flux density is higher in OC-HWM. The more evident effect of the cross-saturation on the q-axis flux linkage is due to the fact that the flux lines can easily bypass the flux-barriers and flow through the winding 2 region.

9.4.2 Constant-torque loci map

Figure 9.8 sketches the constant torque loci of the machine in FWM and OC-HWM. The shaded circle represents the current limit. The MTPA and MTPV loci are also plotted. It can be observed

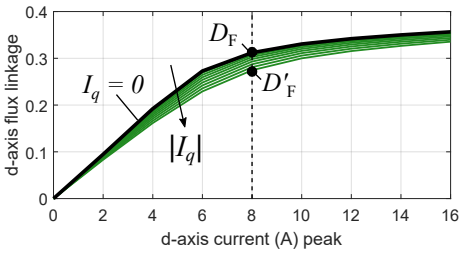

(a)

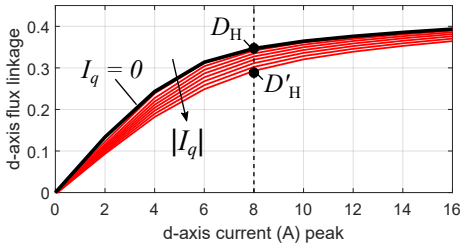

(b)

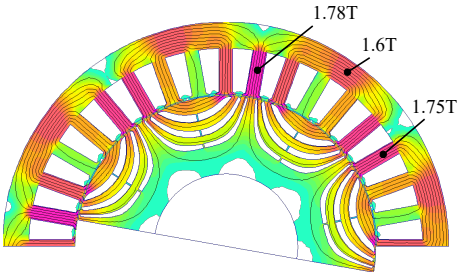

(c) Point D_F.

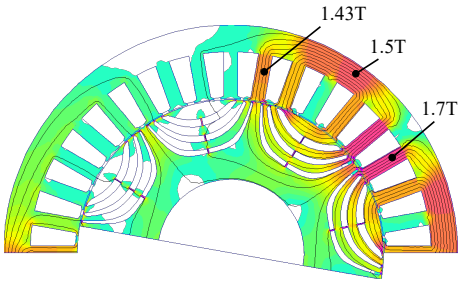

(d) Point D_H

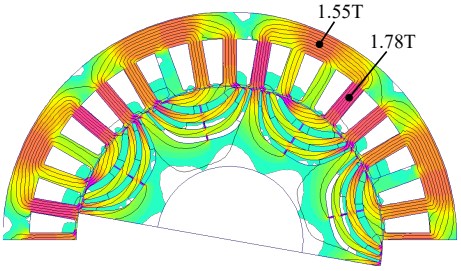

(e) Point D'_F.

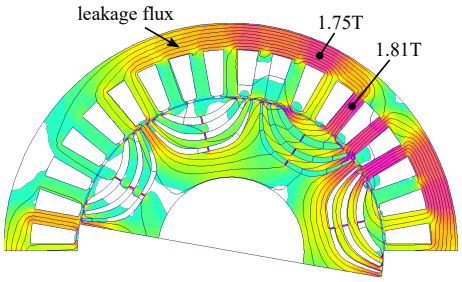

(f) Point D'_H.

Figure 9.6: *d*-axis magnetizing curves in FWM and OC-HWM and relatives flux density plots.

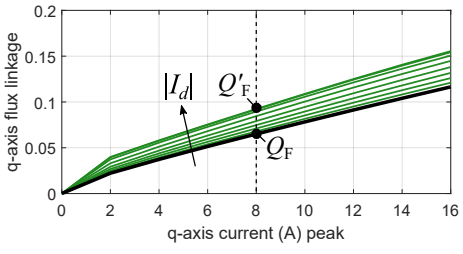

(a)

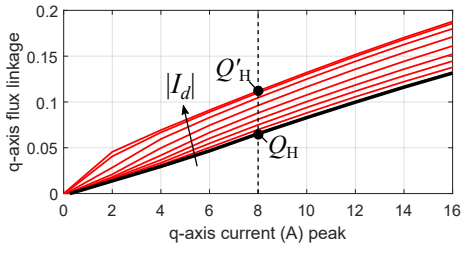

(b)

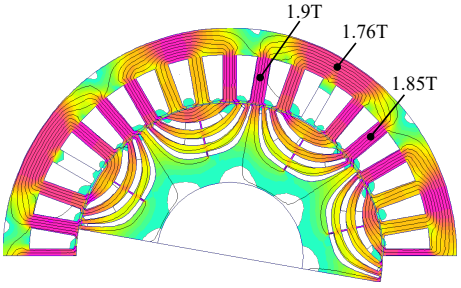

(c) Point Q'_F.

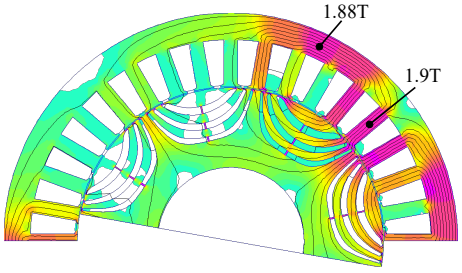

(d) Point Q'_H.

Figure 9.7: *q*-axis magnetizing curves in FWM and OC-HWM and relatives flux density plots.

that the same trajectories are valid both in FWM and OC-HWM. The working points A, B and C have been selected for the computation of torque ripple and power factor. In particular, A is the base point while B and C are flux-weakening points. The speed of each point is computed according to the machine flux linkage and voltage supply. The results are reported in Table 9.3. It can be noted that in FWM the torque ripple is always lower than 4% and is maximum at the highest speed because of the lower average torque. Moreover, the base power factor is quite low, i.e. 0.6, and increases up to 0.66 at the maximum speed. It can be noted that the per-unit torque ripple in OC-HWM increases by 100% or more in all cases. This because, as point out before, the anisotropy is mainly compromised by the higher q-axis flux that bypasses the flux-barriers. Consequently, also the OC-HWM torque ripple is higher than 50% but in any case its value is not higher than 10%. The reduction of rotor anisotropy also involves a very poor OC-HWM power factor which ranges between 0.4, in the base point, and 0.45, at the highest speed.

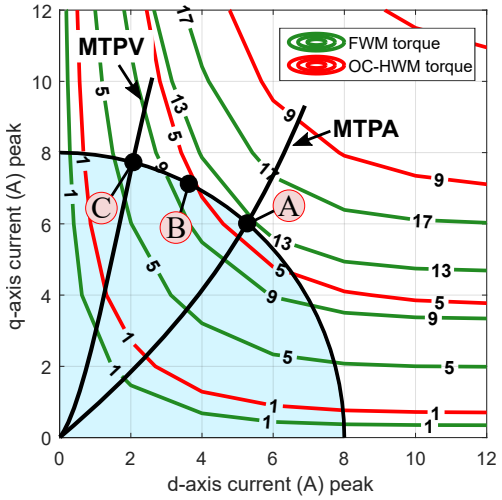

Figure 9.8: Iso-torque locus in the I_d-I_q plane in FWM and OC-HWM.

Table 9.3: Simulated working points in FWM and OC-HWM.

Working point	I	α_i^e	n	FWM			OC-HWM		
				T	$r_{\%}$	PF	T	$r_{\%}$	PF
	(A)	(deg)	(rpm)	(Nm)	(%)	-	(Nm)	(%)	-
A	8	138	800	12.7	2.8	0.60	5.7	5.5	0.45
B	8	148	900	11.9	3.2	0.64	5.3	7.4	0.47
C	8	158	1000	9.3	4.0	0.66	4.2	9.6	0.49

9.5 Conclusion

In this chapter two alternative optimization procedures have been investigated to improve the torque quality of a dual three-phase SyR drive in FWM and OC-HWM. In the first one, the FWM average torque and torque ripple were optimized only. In the second one, both the FWM and OC-HWM average torque and ripple have been set as cost functions. The results have shown the better effectiveness of the second approach yielding good average torque and torque ripple both in FWM and HWM. On the basis of the optimization results, an optimal motor geometry has been selected and then analyzed in details, by means of FE analysis. The analyses have shown that the proposed winding arrangement exhibits a low mutual magnetic coupling between the two three-phase windings. A high sensitivity of the magnetic characteristics to the operating conditions and

to cross-coupling phenomenon has been observed. In particular, in OC-HWM the rotor saliency is lower than in FWM essentially because of the higher q-axis flux that can bypass the flux-barriers flowing through the region of the disconnected winding. This aspect, together with the high number of poles, also compromises the power factor. In fact, despite the rotor optimization, the power factor is always lower than 0.7 in FWM and reaches even lower values in OC-HWM, e.g. 0.45.

Chapter 10

Optimal Design and Experimental Validation of a SyR machine for FT Applications

10.1 Introduction

This chapter continues the investigation of the SyR machine design for FT applications optimizing both stator and rotor geometry [16]. In order to permit a single layer winding, a 48-slot 8-pole configuration is adopted. Two alternative stator geometries are proposed. The first one is a classical stator with slots all equal and evenly spaced along the stator periphery. The second one still presents all the slots of the same shape but their displacement is not uniformly distributed along the stator periphery. The rotor presents three fluid flux-barriers per pole. In both the optimization the strategy FHWM-OPT, described in chapter 9, is adopted. On the basis of the optimization results, an optimal individual is selected and manufactured. Such a prototype is tested in laboratory to verify the reliability of the proposed design procedure and the machine suitability for FT applications.

10.2 Dual three-phase winding arrangement

The coils distribution of the adopted winding W-12-12 is shown in Figure 10.1(a). The winding connection scheme of an half machine is reported in Figure 10.1(b). As can be observed, the frontal connections of phases B and C (or Y and Z) have the same length and are 20% shorter with respect to the one of phase A (or X). This has also been verified by the winding phase resistance measurement which has provided the following results:

$$R_A = R_X = 1.1\,\Omega \qquad R_B = R_C = R_Y = R_Z = 1.2\,\Omega$$

10.3 Motor geometry

Two stator geometries are proposed: *standard stator optimization* (SS-OPT) and *custom stator optimization* (CS-OPT). The geometry parameters selected for the stator and rotor geometry optimization are described in the following. In both optimizations the outer stator diameter is fixed to 170 mm while the stack length is 85 mm. Other motor data are reported in Table 10.1.

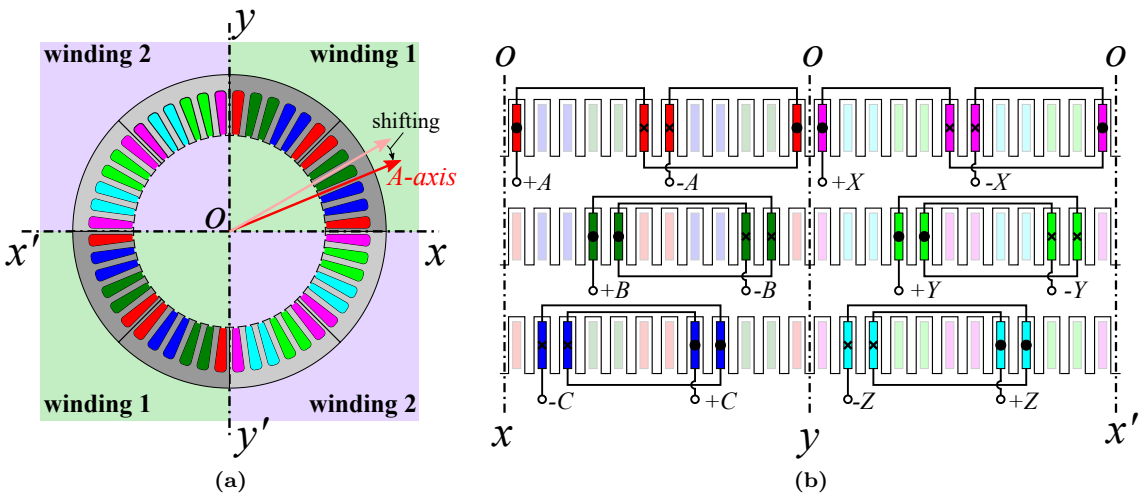

Figure 10.1: Dual three-phase winding arrangement W-12-12 shifted: phase coils distribution (a) and connections scheme of two pole pairs (b).

Table 10.1: Main motor data.

Dimension	Value	Unit
Voltage DC bus	350	V
Stator outer diameter	170	mm
Rotor shaft diameter	38	mm
Air-gap length	0.4	mm
Number of slots	48	-
Pole pairs	4	-
Stack length	85	mm
Winding layers	1	-
Current density RMS	6	A/mm^2
Materials		
Lamination		M330-35A
Winding		Copper

10.3.1 Stator parameters

Standard stator

The SS-OPT refers to a stator in which the slots are all equal and evenly spaced along the stator circumference of a mechanical angle equal to $360/Q_s$, where Q_s is the slot number. This involves that all the teeth present the same rectangular cross section area as in the typical stator geometries. In such an optimization the stator parameters are the inner diameter, D_s, the tooth width, w_t, and the slot height h_s, as indicated in Figure 10.2(a). The total number of stator parameters is 3.

Custom stator

In the CS-OPT, all the slots have the same shape and are symmetric (to easy the winding insertion) but the angle between the slot axes is not constant. This means that the slot distribution is not uniform along the stator periphery and the tooth cross section is trapezoidal instead of rectangular. Figure 10.2(b) shows the parameters used for the stator optimization. This solution has been considered on the basis of the observations made in section 8.3 regarding the torque oscillations due to the flux linkage that "escapes" from the fed winding region. The aim of this geometry solution is to find a particular slot distribution capable of limiting the amount of flux leakage near

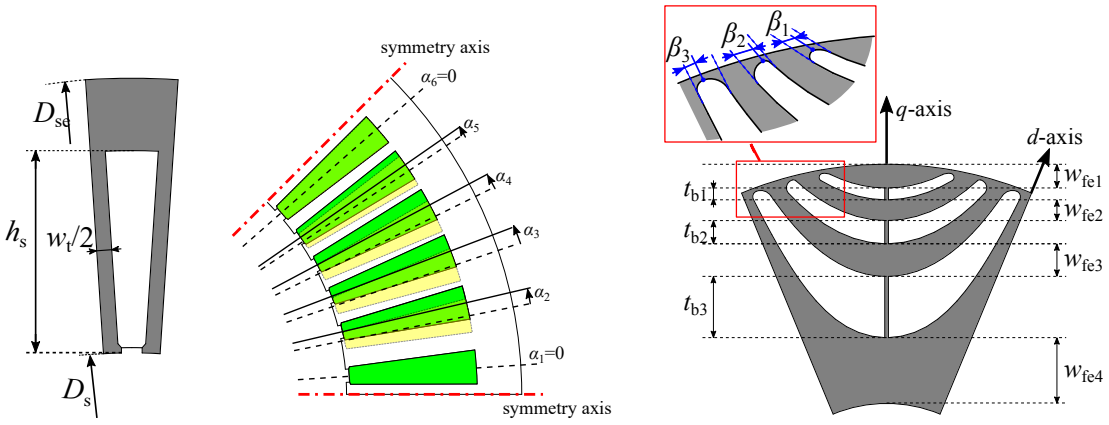

(a) *Standard stator geometry.* **(b)** *Custom stator geometry.* **(c)** *Rotor geometry.*

Figure 10.2: Geometrical parameters used for the stator and rotor optimization.

the boundary regions in OC-HWM.

The dashed lines represent the angular positions of the fictitious evenly spaced slots (the yellow ones). The continuous lines are the axes of the shifted slots whose angles are computed with respect to the original axes. For example, the shifting angle of the first slot is $\alpha_1 = 0$ which means that there is no angular displacement between the original position. The second slot is shifted of an angle α_2 and so on. In order to reduce the total number of parameters, the slot distribution is assumed to be symmetric with respect to the symmetry axis (dash dotted lines in Figure 10.2(b)) and all the pole pairs present the same slot distribution. Considering, D_s, h_s, w_t and the six slot angles, the total number of stator parameters is 9.

10.3.2 Rotor parameters

The fluid flux-barriers geometry, described in section 15.1, is selected for the rotor design. The parameters used for the rotor optimization are reported in Figure 10.2(c). In particular, they are the iron channel widths, $w_{fe1}, \ldots, w_{fe4}$, flux-barrier thicknesses, $t_{b1}, \ldots, t_{b3}$, and flux-barrier angles, $\beta_1, \ldots, \beta_3$. Note that the j-th angle, β_j, is actually computed as a certain percentage of the angle delimited by the outer and inner edge of the j-th flux-barrier. The inner rotor diameter is fixed an equal to 38 mm according to the test bench requirement. The total number of rotor parameters is 10.

10.4 Optimization results

This section reports the optimization results obtained from the two approaches. In both the optimizations a fixed current density of 6 A/mm^2 has been selected. The adopted objectives evaluation is described in subsection 9.2.2. For the individual selection, a maximum torque ripple of 16.5% has been preliminary set. In this section the OC-HWM will be indicated shortly as HWM for more clarity since no other operating conditions are evaluated during the optimization.

10.4.1 Standard stator optimization results

The optimization has been carried out with 300 generations of 65 individuals each. The two objective planes of the SS-OPT are reported in Figure 10.3(a). The first one, labeled as FWM-plane, plots the torque ripple versus average torque in FWM while the second one, labeled as HWM-plane, plots the same cost functions in HWM. The continuous line in the FWM-plane represents the Pareto front in FWM. The red circle markers indicate the individual of the Pareto

front that exhibit a HWM torque ripple lower than 16.5%. The HWM performance of these survived individuals are also plotted in the HWM-plane with the same markers style. The dot markers are the whole individuals of the optimization.

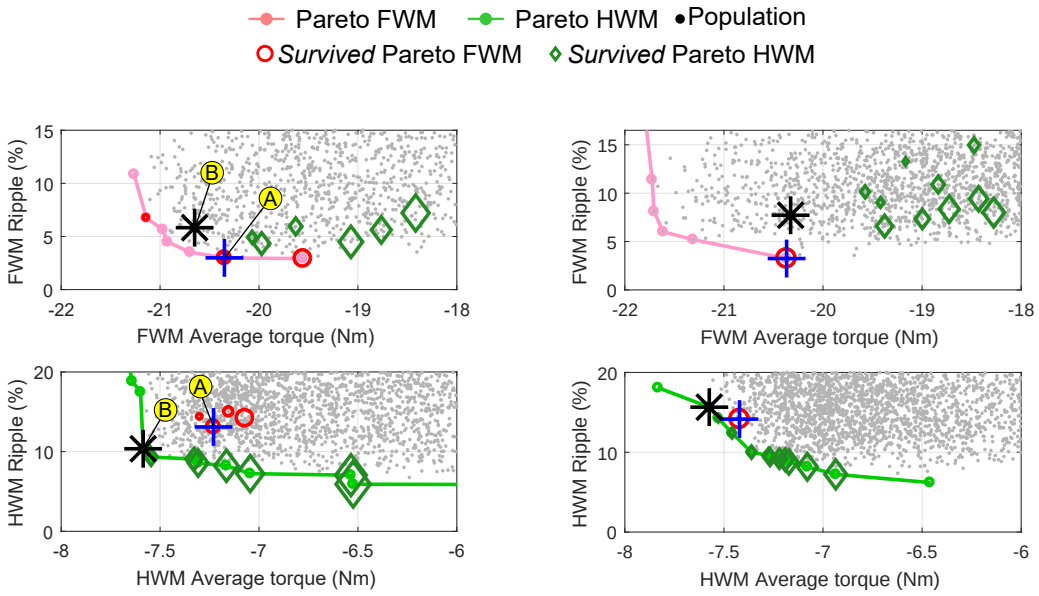

(a) *Objective planes of the SS-OPT.* **(b)** *Objective planes of the CS-OPT.*

Figure 10.3: Objective planes of the *standard* and *custom* optimization.

Likely, the continuous line in the HWM-plane is the Pareto front and the diamond markers represent the front individuals that present a torque ripple lower than 16.5%, they are plotted in the FWM-plane as well. The markers size of the Pareto front individuals increases as the torque ripple decreases. The distribution of the two Pareto fronts in the FWM-plane is quite different. In particular, the individuals of the FWM Pareto front exhibit an average torque that range between 19.5 Nm and 21.6 Nm with a torque ripple between 3% and 11%. The average torque of the survived HWM Pareto front individuals ranges between 12 Nm and 20.6 Nm but their torque ripple is always lower than 10%. In the HWM-plane, the individuals of the HWM Pareto front exhibit an average torque between 5.6 Nm and 7.7 Nm and, except for two individuals, all of them yield a torque ripple lower than 10%. Conversely, the average torque of the FWM Pareto front individuals is bounded between 7 Nm and 7.5 Nm with a torque ripple that ranges between 14.5% and 16.5%.

The individuals marked with cross (labeled as A) and star (labeled as B) yield good performance both in FMW and HWM. In particular, the individual A exhibits the lowest torque ripple in FWM but its average torque is 1.5% lower than B. In HWM, the average torque of the individual B is 4.8% higher than B while the torque ripple is 2% lower.

10.4.2 Custom stator optimization results

The optimization has been carried out with 500 generations of 95 individuals each. Computationally speaking such an optimization is mo

The objectives planes of the CS-OPT are reported in Figure 10.3(b). The same graphical convention described before is valid. As can be seen in the figure, only one individual of the FWM Pareto front yields an HWM average torque lower than 16.5%. In HWM, the same individual exhibits an average torque of about 7.4 Nm with a ripple of 14%. Conversely, many individuals of the HWM Pareto are present but their torque ripple is higher than 6.2%. In the HWM-plane, the survived individuals of the HWM Pareto front yield an average torque between 6.5 Nm and 7.8 Nm while the torque ripple is between 6.2% and 18%.

It can be noted that the individual of the HWM Pareto front that yields the highest FWM average torque (marked with a star) has a HWM torque ripple of about 16.5% that is higher than

A and B in the SS-OPT. On the other hand, the FWM Pareto individual that exhibits the lowest FWM torque ripple (marked with a cross) achieves an average torque similar to B but with a HWM torque ripple of 14.5% that is higher than the one achieved by A and B.

In conclusion, the higher time consumption of such an optimization, due to the higher number of parameters, does not provide any design solution better than the SS-OPT. For this reason it is not suitable for this application.

10.5 Prototype

The individual A of the SS-OPT has been selected for the prototype manufacturing. The main machine data are reported in Table 10.2. A view of the prototype is shown in Figure 10.4(a). The 24 terminals of the dual three-phase winding are all accessible by means of the terminal boards in Figure 10.4(b). The terminals on the left and right belong to the winding 1 and 2, respectively. In the considered picture, the winding 2 is short circuited by means of the short circuit bridges to perform the test discussed in section 10.8. The rotor prototype is visible in Figure 10.4(c). A three-step-skew rotor is adopted to further reduce the torque ripple. The slot pitch angle (i.e. 7.5°) is selected as skewing angle, so that the rotor steps are displaced of 2.5° each others. In Figure 10.2(c) it is possible to see a rotor pole and the three rotor steps used for the skewing.

Table 10.2: Prototype main data.

Definition	Value	Unit
Rated current (peak)	8	A
Inner diameter	104	mm
Slot height	24.3	mm
Tooth width	3.6	mm
Conductors in slot	46	-
Flux-barrier angles	$\{9.86, 14.51, 20.28\}$	deg
Flux-barrier thicknesses	$\{1.61, 3.17, 8.34\}$	mm
Iron channel width	$\{3.22, 2.81, 4.43, 8.98\}$	mm
Rotor skewing (3 steps)	7.5	deg

10.6 Torque behaviors

Figure 10.5(a) reports the FE and experimental torque behaviors obtained with different current amplitudes in MTPA condition. The test setup is similar to the one described in Figure 10.13. For this target, the test is carried out at very low speed (e.g. 10 rpm), the motor under test (MUT) is connected to the master motor with mechanical joints and a torquemeter is used to measure the torque. The MUT is fed by the current vector set by the user with a host PC. In particular, in the current case, for each current amplitude, different current angles are tested in order to find the MTPA condition.

It can be noted that for low currents (i.e. 4 A and 8 A), the FE average torque is higher than the experimental one. This is mainly due the manufacturing tolerance of the air-gap and the different magnetic properties of the lamination with respect to the FE model. Conversely, for higher current amplitudes, there is a good agreement between the FE and experimental curves. It can be observed that the torque ripple in FWM condition is always lower than 3%.

Figure 10.5(b) reports the torque behaviors obtained in HWM for different current amplitudes. In this case, there is a good agreement in terms of average torque for current amplitudes higher than 8 A. The FE torque ripple is always higher than the experimental one and ranges between 8% and 20% except for the lowest current amplitude.

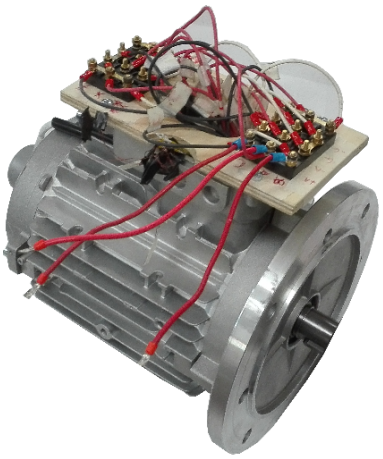

(a) Prototype view.

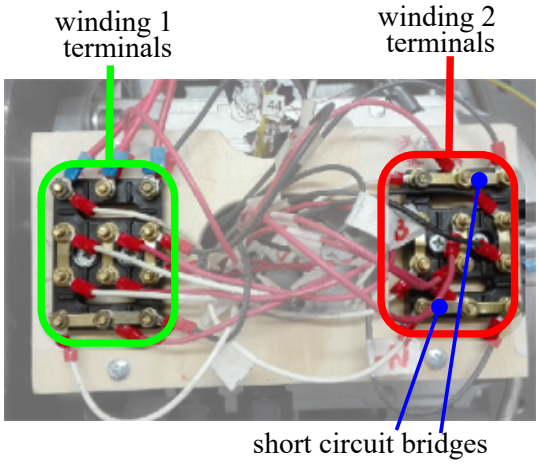

(b) Terminals board and connections.

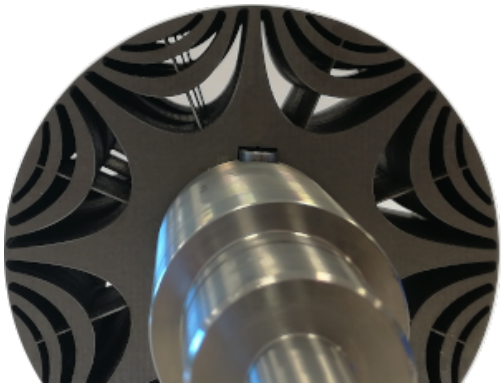

(c) Rotor prototype.

(d) Rotor skewing zoom.

Figure 10.4: Views of the manufactured prototype parts.

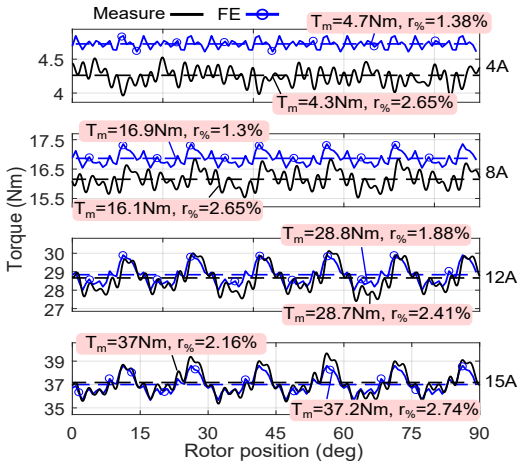

(a) *FWM.*

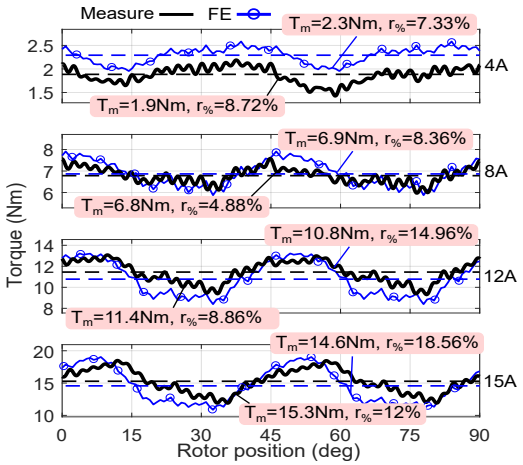

(b) *HWM.*

Figure 10.5: Torque versus rotor position: comparison between FE and experimental results for different current amplitudes and operating conditions.

10.7 Magnetic coupling

In this section the mutual coupling between the winding 1 and 2 is evaluated by means of FE analyses and experimental tests.

10.7.1 FE analysis results

The simulations are carried out feeding only the A_1-phase with the rated current (i.e. 8 A), in MTPA condition ($\alpha_i^e = 55\,°C$), and with all the left phases open circuited. The flux linkage of each phase is evaluated in an half electric period. Figure 10.6(a) and Figure 10.6(b) show the winding 1 and winding 2 flux linkages behaviors versus the rotor position. The maximum of the A_1-phase flux linkage is reached when the rotor d-axis is aligned to the A_1-phase magnetic axis. The flux density plot corresponding to such a condition is shown in Figure 10.8(a). It can be noted that the stator region occupied by the winding 2 (left region) is interested by a higher magnetic loading. Conversely, when the rotor q-axis is aligned to the A_1-axis, the relative flux linkage is minimum as well as the winding 2 flux linkages. This is also confirmed by the flux density plot in Figure 10.8(b) in which it is evident the low magnetic loading of the the winding 2 stator region and the low number of flux lines that flow thought the stator yoke. In general, the ratio between the flux linkage of A_1-phase and the others ranges between 10 and 70, depending on the rotor position. The phase voltage waveforms of the winding 1 and 2 are reported in Figure 10.7(a) and Figure 10.7(b); the dashed lines represent the fundamental of the voltages e_A and e_X, respectively. Concerning the fundamental amplitude, it can be noted that e_X is about 20% of e_A while e_Y and e_Z are about 10% of e_A. Regarding the instantaneous values, the phase voltages e_Y and e_Z reach about 24 V that is 50% of the phase A voltage.

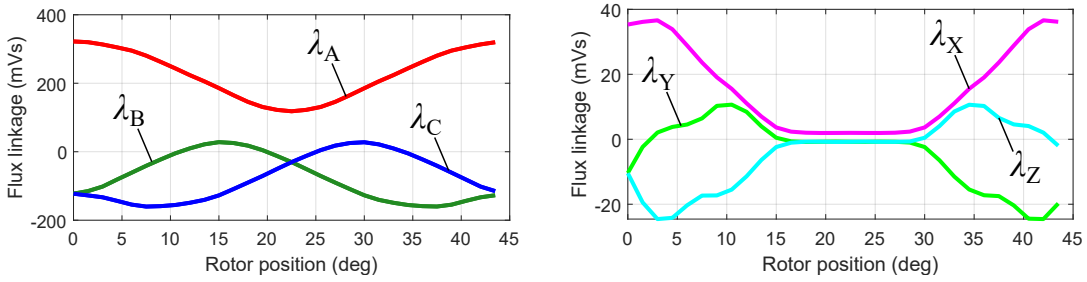

(a) Winding 1 phases. **(b)** Winding 2 phases.

Figure 10.6: Winding 1 and winding 2 flux linkages versus rotor position when only A_1-phase is supplied.

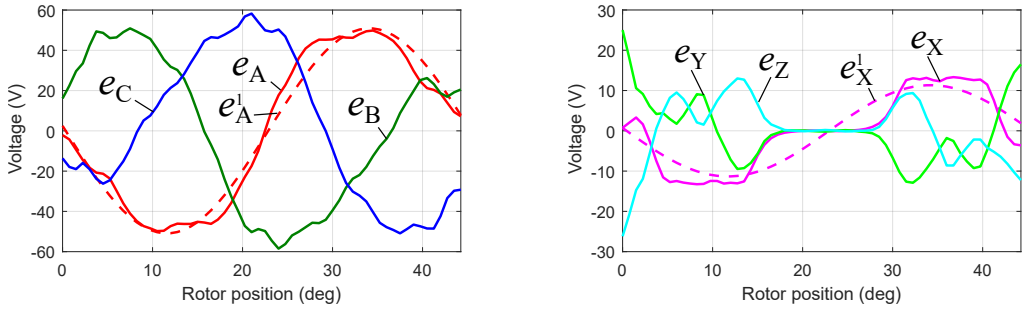

(a) Winding 1 phases. **(b)** Winding 2 phases.

Figure 10.7: Winding 1 and winding 2 phase voltages versus rotor position when only A_1-phase is supplied.

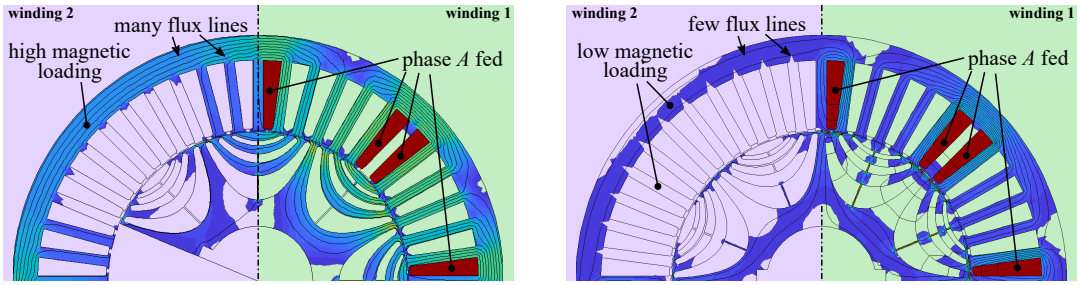

(a) *Maximum magnetic coupling.* **(b)** *Minimum magnetic coupling.*

Figure 10.8: Flux density plot for different rotor positions when only the A_1-phase is supplied.

10.7.2 Experimental results

The mutual magnetic coupling between the winding 1 and 2 has been verified experimentally by means of the test bench setup reported in Figure 10.9. In such an experiment the rotor of the MUT is kept in rotation by a prime mover at a constant speed (i.e. 37.5 rpm) while only one phase (i.e. A) is fed by AC voltage supply with an electric frequency much greater than the motor electric one (i.e. 50 Hz). Then, the voltages of the disconnected phases and the current of the supplied phase are measured by means of voltage and current probes.

Their waveforms are finally displayed on the oscilloscope and are reported in Figure 10.10. The first plot shows the current behavior of the supplied phase. Its oscillation is due to the change of the motor inductance during the rotation. Its value is maximum when the rotor d-axis is aligned to the phase axis and is minimum after 90 electric degrees. The voltage of the supplied phase is reported in the second plot, its amplitude is constant since it is imposed by the power supply. The second and third plots show the voltage of the phase B and C, respectively. It can be observed that the relative position of their waveforms reflects the FE results in Figure 10.7. Moreover, their maximum amplitude is about half of V_A since in the three-phase winding system the mutual inductance is an half of the self inductance. The last three plots show the phase voltages of winding 2. Their maximum amplitude is about 10% of the supplied phase which confirms the low magnetic coupling between the winding 1 and 2.

10.8 Three-phase short circuit test

This section reports the machine performance when the winding 1 is regularly supplied and a three-phase short circuit is applied to the winding 2 (SC-HWM). The aim of such an analysis is evaluating the maximum amplitude of the short circuit currents and their effect on the average torque. The effect on the torque ripple has not been verified experimentally because of the test bench limitation.

10.8.1 FE analysis results

The simulations are carried out feeding the winding 1 with a given current vector and short circuiting the terminals of the winding 2. The results obtained at rated current in MTPA condition are reported in the following.

Figure 10.11 reports the torque waveforms in OC-HWM and SC-HWM. This analysis is carried out neglecting the skewing effect for simplicity. It can be noted that the short circuit condition involves a lower torque oscillation and slightly increases the average torque.

These results can be explained considering the flux density plots in Figure 10.12(a) (winding 2 open circuited) and Figure 10.12(b) (winding 2 short-circuited). It is evident that the magnetic loading in short circuit condition is lower as well as the flux leakage that flow in the winding 2 region. This is due to the demagnetization effect of the short circuit currents.

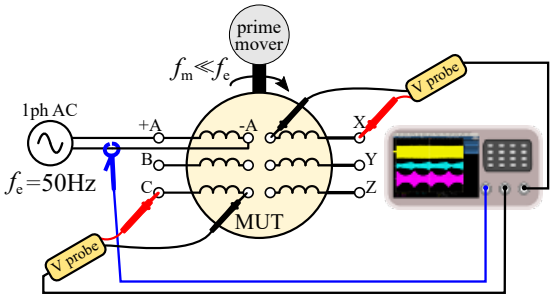

Figure 10.9: Test bench setup when only the phase A is fed.

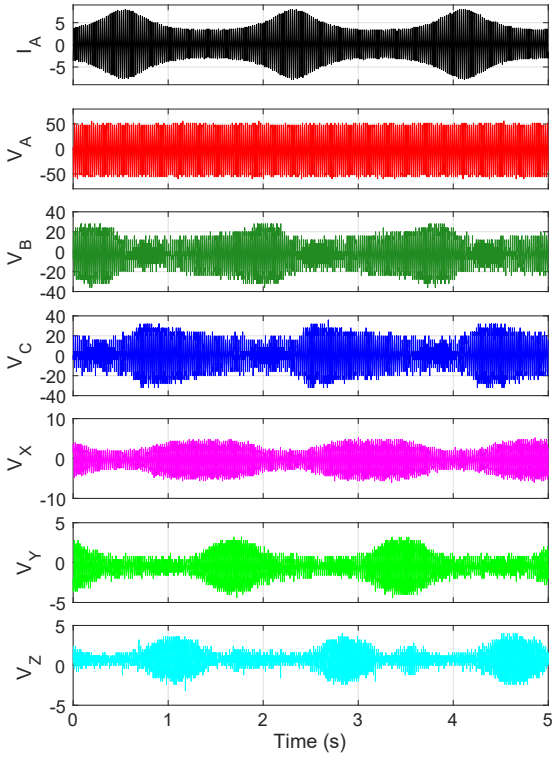

Figure 10.10: Voltages and current behaviors of the mutual coupling test. The voltage V_A is imposed by the power supply while the other voltages are induced. The maximum current amplitude is equal to the rated one (i.e. 8 A).

The short circuit current behaviors have been simulated with rated and overload conditions (i.e. 16 A) at the mechanical speed of 500 rpm, the results are plotted in Figure 10.13(b) and Figure 10.13(c), respectively. The maximum amplitude is always lower than 4 A, this means that such an operating condition does not represent a risk for the inverter and the machine itself. Of course, the presence of the short circuit currents affects the efficiency of the machine since additional Joule losses are present.

10.8.2 Experimental results

The test bench setup is shown in Figure 10.13(a). The winding 1 of the MUT is regularly fed with the current vector imposed by the user by means of the Host PC, the mechanical speed is set by the user as well. The MUT is connected to the prime mover with a torquemeter, its signal is then visualized by the torque display. The short circuit currents are measured by means of three different current probes and then visualized on the oscilloscope screen.

The short circuit currents waveform measured at different speed and current supply conditions are shown in Figure 10.13(d) and Figure 10.13(e). It can be observed that their behavior and maximum amplitude are in good agreement with the FE results discussed before. The small difference between the waveform is due to the skewing effect of the experimental test.

Different working conditions have been tested varying the mechanical speed and the current amplitude of the winding 1, the results are reported in Table 10.3. In general, the average torque in SC-HWM is higher than the OC-HWM, this confirms the observations made on the FE results. In particular, this increment is amplified by the mechanical speed. For example, with the rated current at 100 rpm, the torque increment is about 2.6% while, at 500 rpm, the increment is about 4.6%. In overload condition the torque increment, in the same mechanical speeds, pass from 4.2% to 7.5%.

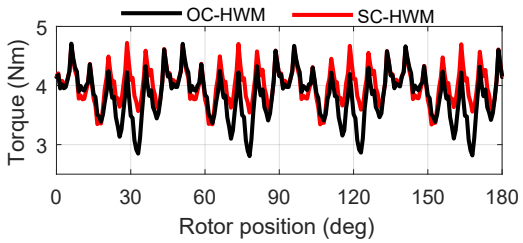

Figure 10.11: Torque vs. rotor position in OC-HWM and SC-HWM in MTPA condition.

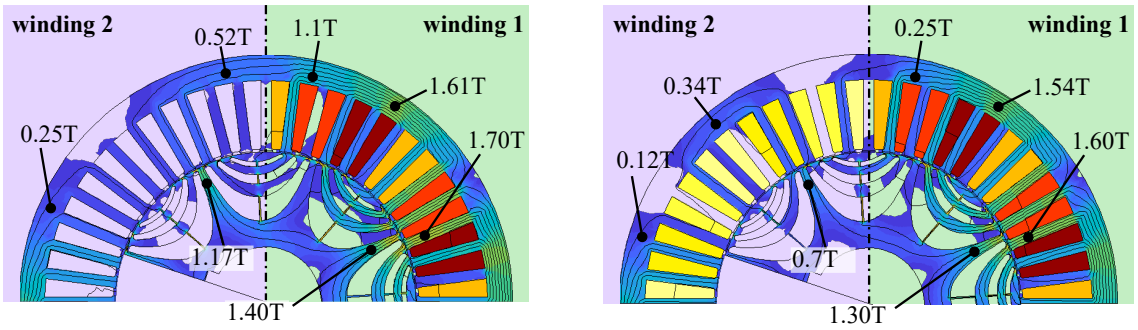

(a) OC-HWM. **(b)** SC-HWM.

Figure 10.12: Flux density and current density plots in OC-HWM and SC-HWM. The winding 1 is normally fed with the rated current in MTPA condition.

Table 10.3: Average torque at different mechanical speed in OC-HWM and SC-HWM.

I (A)	HWM	Mechanical Speed (rpm)				
		100	200	300	400	500
8	OC	6.96	6.91	6.88	6.84	6.8
	SC	7.14	7.15	7.15	7.12	7.11
12	OC	11.49	11.45	11.4	11.36	11.34
	SC	11.94	12.08	12.1	12.11	12.1
16	OC	15.29	15.24	15.21	15.16	15.12
	SC	15.93	16.15	16.22	16.24	16.25

10.9 Conclusion

This chapter dealt with the optimization and analysis of a synchronous reluctance motor with dual three-phase winding for fault-tolerant applications.

The stator and rotor have been optimized by means of a multi-objective differential evolution algorithm in order to obtain good performance both in full winding and half winding mode. Two stator geometries have been investigated: the standard one and the custom one. The optimization results revealed that only the first one is suitable both in terms of time consumption and results.

A prototype of the most promising individual provided by the optimization has been manufactured and tested to prove the finite element results. The torque waveform provided good results in terms of average torque and torque ripple both in full winding mode and half winding mode. The mutual magnetic coupling between the phases of the dual three-phase winding has been tested in order to verify the amplitude of the induced voltages in the disconnected phases in half winding mode. The experimental results confirmed the finite element predictions since very low induced voltages have been observed. A three-phase short circuit of one of the two three-phase winding has been finally tested to verify the amplitude of the short circuit currents and their effect on the motor performance. From the measurements and finite element analysis as well, it has been observed

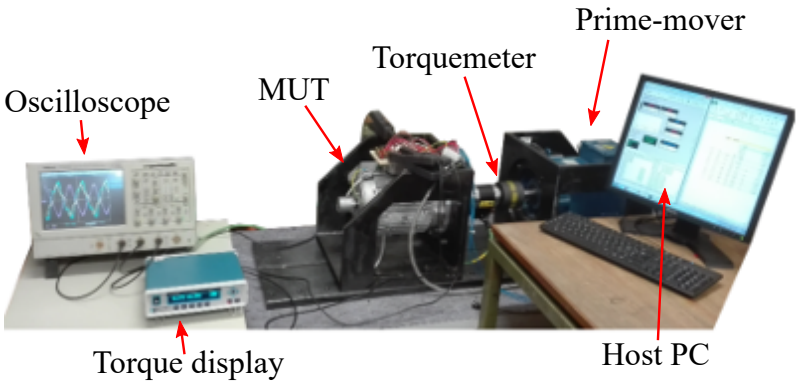

(a) Test bench setup.

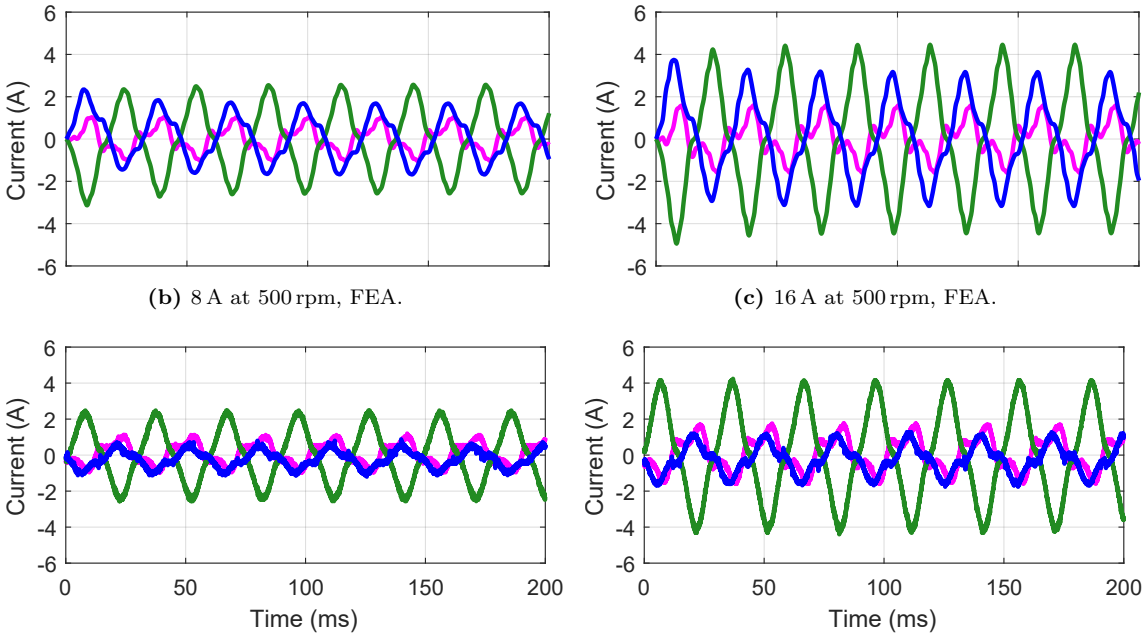

(b) 8 A at 500 rpm, FEA.

(c) 16 A at 500 rpm, FEA.

(d) 8 A at 500 rpm, Measure.

(e) 16 A at 500 rpm, Measure.

Figure 10.13: Short circuit current behaviors for different current amplitude in the winding 1.

that the maximum short circuit current is always lower than the rated one and, in addition, the demagnetizing effect of the short circuit currents has a beneficial effect on the average torque and torque ripple.

Part III

PMASyR motor design for automotive applications

Chapter 11

Design and Optimization of a PMASyR motor for Low-Voltage E-Scooter Applications

11.1 Introduction

Nowadays, the increasingly evident effects of the transportation pollution on the climate change and human healthy [119–121] are inducing many countries to employ policies to encourage the diffusion of the electric vehicles [122]. All these aspects and the technological advances of the automotive industry in the recent years stimulated the market of the electric vehicles with promising results in China, United States and Europe [123, 124].

Among the automotive products, the electric motorcycle is one of the most effective solution for the mobility and its market is anticipated to grow in the next years. The main benefits are the high efficiency, low weight, compactness, ease of use and relative low cost with respect to an electric car.

The brushless DC motor and IPM motor have been proposed in the past with different geometry layouts (i.e. outer or inner rotor) and transmissions (i.e. belt or direct) [125–129]. The main advantages of these machines are the high torque density and efficiency due to use of rare-earth PMs with high remanence flux. However, the sharply fluctuations of the rare-earth PMs price in the last years and their non negligible environmental impact encouraged the research activities to find alternative solutions with cheaper PMs (e.g. ferrite) or, more drastically, without any PM. The SWR motor has been proposed for its design simplicity, low cost and fault-tolerant reliability but, to date, is still no attractive for the automotive application due to its high noise and vibrations [130].

In the last years, the SyR motor has been proposed in several applications for its good torque density, low cost, robustness and overload capability [63, 131]. The main drawbacks of such a machine are the torque ripple, the low power factor and the limited constant power speed range (CPSR). The first point can be reduced effectively with a proper design of the rotor geometry [74, 132] while the other two items are intrinsic properties of the machine and are hard to improve with the motor geometry design only. Regarding the last two aspects, the PM assisted synchronous reluctance (PMASyR) machine represents a valid solution [133–135]. In such a machine, PMs with poor magnetic properties (e.g. ferrite) or a small amount of rare-earth PMs are inset in the rotor flux-barriers to saturate the iron ribs, improve the power factor and extend the CPSR. The rotor PMs addition represents an additional cost of the motor but allows to limit the Volt-Ampere ratings of the inverter yielding a lower overall cost of the electric drive with respect to the SyR one. All these features make the PMASyR machine an optimal solution for the automotive application in which high torque density and a wide CPSR are required [136].

The multi-objective design of such a machine has been deeply investigated in literature [137,

138]. In these works the average torque, the torque ripple and the CPSR are set as cost functions and only the transversal motor geometry is optimized. Furthermore, the number of winding turns and the motor stack length are properly adapted after the optimization to meet the rated current and voltage required by the application.

However, this is possible if the number of turns is high enough that, a relatively small modification of the number of turns or stack length, does not involve significant changes on the motor performance. Conversely, if the voltage limit and the maximum target speed yield a very low number of turns (i.e. less than 3) any modification of the number of turns or the stack length may involve completely different machine inputs or, more drastically, compromise the feasibility of the drive system.

This chapter proposes a multi-objective PMASyR motor design procedure that (i) evaluates the feasibility of the drive system in overload and flux-weakening condition and (ii) computes the optimization cost functions in the same operating condition to allow easy and direct considerations of the Pareto fronts, without any further computations and checks after the optimization [10].

The proposed procedure is used to design the motor for an actual E-Scooter application, shown in Figure 11.1, already presented by Askoll at EICMA2018 exposition in Milan. In the present case study, the selected cost functions are: (i) motor cost (ii) torque ripple and (iii) losses per outer surface in a given steady state flux-weakening condition. Finally, a prototype of the most promising design solution is manufactured and tested to prove the effectiveness of the proposed design procedure.

Figure 11.1: Render of the E-Scooter prototype.

11.2 Design requirements and data

The main design requirements and constraints are reported in Table 11.1. The current and voltage limits are imposed by the inverter and battery cells provided for the E-Scooter.

The motor has to produce the overload torque T_{OL} (taken as reference) in the speed range between 0 rpm (standstill condition) and n_{B} (base condition). The upper limit chosen for the base speed is 2000 rpm but can be omitted if all the other requirements are met. The HS torque T_{HS}, equal to one third of the overload one, has to be guarantee up to the maximum speed, n_{HS}, of 9000 rpm. The maximum axial and radial dimensions are imposed by the available space on board. The maximum motor stack length is $L_{\mathrm{stk}} = 150\,\mathrm{mm}$ while the maximum diameter is fixed and equal to $D_{\mathrm{se}} = 150\,\mathrm{mm}$. The slot number is $Q_{\mathrm{s}} = 36$ while the pole number is $2p = 6$. The PMs have to be rectangular shape and their number per pole does not have to exceed four. These constraints are imposed to ease the PMs insertion in the rotor flux-barriers and to reduce their total cost. Sintered ferrite PMs are adopted, their working temperature is assumed to be 120 °C. The motor air-gap length is set to $g = 0.4\,\mathrm{mm}$ according to the manufacturing limitations. Copper is selected for the winding and the assumed working temperature, for the Joule losses computation, is 145 °C according to the selected insulation class. No winding parallel connections are allowed to simplify the coil terminals welding and a double layer layout is preferred to get a better stator MMF and therefore to limit the torque ripple. A standard M330-35A lamination is used for the stator and rotor core. The torque ripple percentage, computed as the relative standard deviation percentage of the torque waveform, has to be lower than 5%. The total materials cost of the motor

Table 11.1: Design requirements and constraints.

Definition	Symbol	Value	Unit
Current limit (RMS)	I_{INV}	300	A
Voltage DC bus	V_{DC}	54	V
Torque (overload)	T_{OL}	1	p.u.
Torque (HS)	T_{HS}	0.33	p.u.
Base speed	n_{B}	< 2000	rpm
Maximum speed	n_{HS}	9000	rpm
External diameter	D_{se}	150	mm
Stack length	L_{stk}	<150	mm
PM pieces per pole*	-	≤ 4	-
Air-gap length	g	0.4	mm
Slot number	Q_{s}	36	-
Pole number	$2p$	6	-
No parallel connections			
Objectives			
Maximum torque ripple	$r_{\%}$	<5	%
Maximum total cost	C_{tot}	1	p.u.
Losses/$(\pi D_{\mathrm{se}} L_{\mathrm{stk}})$	k_{Loss}	< 20	kW/m^2
Materials			
Element		Name	Temperature
Lamination		M330-35A	-
Winding		Copper	145 °C
Permanent magnet		Sintered ferrite	120 °C

(*) Rectangular shape is required.

has to be lower than a reference cost C_{tot}. The coefficient k_{Loss} is the ratio between the admitted total losses and the stator stack external surface (i.e. $\pi D_{\mathrm{se}} L_{\mathrm{stk}}$). It strongly affects the design of the machine cooling. Typical values are 3 kW/m^2 for natural cooled system, 10 kW/m^2 for forced ventilation and up to 40 kW/m^2 for liquid cooling and end windings potting. A maximum limit of 20 kW/m^2 has been set preliminary.

11.3 Stator and rotor geometries

This section reports the stator and rotor geometries adopted for the design of the PMASyR motor. The parameters and relative variation ranges set for the optimization are also presented.

11.3.1 Stator

The stator slot geometry and its main parameters are reported in Figure 11.2(a). The outer diameter, D_{se}, is fixed while the ratio between the inner and outer diameter has been set between 0.5 and 0.7. The tooth width, w_{t}, and slot height, h_{s}, reference values have been selected considering a standard stator lamination with the same outer diameter. The variation range of these two parameters has been set between 0.8 and 1.2.

11.3.2 Rotor

In the present case study, the segmented flux-barrier shape, shown in Figure 11.2(b), has been selected for the simple flux-barriers geometry and the possibility of achieving a high filling with standard rectangular shaped PMs. The number of three flux-barriers per pole has been selected

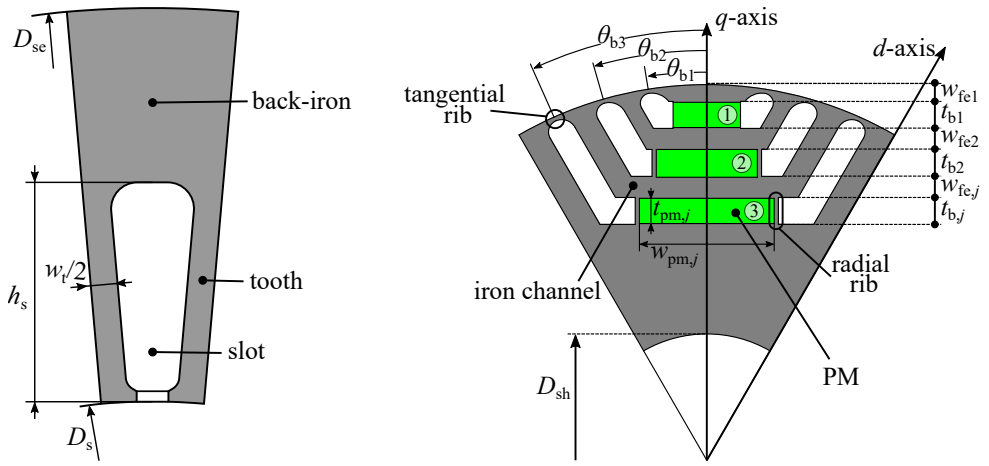

(a) *Stator parameters.* **(b)** *Rotor parameters.*

Figure 11.2: Main geometrical parameters of the PMASyR motor.

according to the results provided in the literature [63, 131]. The geometrical parameters used for the optimization are the flux-barrier thicknesses $t_{b1}, \dots t_{b3}$ and four iron channel widths $w_{fe1}, \dots, w_{fe4}$. Each flux-barrier angle, ϑ_{bj} (with $j = 1, 2, 3$), is free to move between 0.05 and 0.95 of the angle defined by the j-th outer and inner flux-barrier edges. All the three flux-barriers are filled by a magnet in the middle. The thickness of the j-th magnet, t_{pmj} is equal to the corresponding flux-barrier t_{bj}, mainly to limit the total number of free parameters and secondly to use the same matrix for the magnet production. In the optimization, the width of each magnet is free to move between 50% and 100% of the available flux-barrier space. The tangential iron ribs thicknesses are set equal to the lamination width, as usually required. The radial iron ribs have been used for all the flux-barriers and their thickness have been set equal to the tangential rib one.

11.4 Design aspects regarding the number of turns

The given current, I_{INV}, and voltage, $V_N = V_{DC}/\sqrt{(3)}$, limits yield the following constraints:

$$\begin{cases} I_{slot,OL} \leq n_{cs} I_{INV} \\ V_N \geq p\omega_{FW}\, k_w \dfrac{n_{cs} Q_s}{6}\, \phi_{FW} \end{cases} \tag{11.1}$$

where n_{cs} is the number of series conductor per slot, $I_{slot,OL}$ is the overload current in a slot, k_w is the winding factor and ϕ_{FW} is the magnetic flux in the target HS working point (HSWP). From (11.1), the upper and lower bound of n_{cs} can be found:

$$\begin{cases} n_{cs} \geq \dfrac{I_{slot,OL}}{I_{INV}} \\ n_{cs} \leq 6\, \dfrac{V_N}{p\omega_{FW} k_w Q_s \phi_{FW}} \end{cases} \tag{11.2}$$

The value of $I_{slot,OL}$ is unknown a priori but can be estimated as follows:

$$I_{slot,OL} = \frac{\hat{K}_s \pi D_{s,min}}{k_w Q_s} \tag{11.3}$$

where $\hat{K}_s$ is the electric loading, typically set between 40 kA/m and 60 kA/m, while $D_{s,min}$ is the minimum feasible stator diameter. Setting $\hat{K}_s = 60\,\text{kA/m}$ and $D_{s,min} = 85\,\text{mm}$, from the first of

(11.2), it results:

$$I_{\mathrm{slot,OL}} = 463\,\mathrm{A} \qquad n_{\mathrm{cs}} \geq 2 \tag{11.4}$$

The upper n_{cs} limit is computed assuming the geometric configurations with the minimum stator diameter and stack length so that the lowest value of magnetic flux can be estimated. In overload condition, the air-gap flux density, B_{g}, can be set between 1 T and 1.2 T. Hence, the air-gap magnetic flux is given by:

$$\phi_{\mathrm{OL}} = B_{\mathrm{g}} \frac{D_{\mathrm{s,min}} L_{\mathrm{stk,min}}}{p} \approx 2.4\,\mathrm{mWb} \tag{11.5}$$

where $L_{\mathrm{stk,min}}$ is the minimum stack length equals to 85 mm. The HS flux is then computed with the following relationship:

$$\phi_{\mathrm{FW}} = \frac{n_{\mathrm{OL}}}{n_{\mathrm{FW}}} \phi_{\mathrm{OL}} = 0.53\,\mathrm{mWb} \tag{11.6}$$

where n_{OL} is the overload speed set equal to the minimum n_{B}. Finally, according to the HSWP speed, the second of (11.2) gives $n_{\mathrm{cs}} \leq 3$. Since no parallel connections are allowed and a double layer layout is adopted, the limit is rounded to the lower even number, so that is results $n_{\mathrm{cs}} \leq 2$. The results suggest that the number of turns has to be $n_{\mathrm{cs}} = 2$.

11.5 Individual evaluation procedure

The flowchart in Figure 11.3 summarizes the main steps performed for each individual evaluation during the optimization.

11.5.1 Geometry feasibility check

At first, a set of parameters is generated by the optimizer algorithm and the geometric feasibility of the motor is evaluated. If no problems occur, the procedure goes on the next step, otherwise the individual is rejected.

11.5.2 Overload capability

In this step the overload capability, in terms of average torque and PMs demagnetization, is investigated. The current angle, $\alpha_{\mathrm{i}}^{\mathrm{e}}$, is fixed to 55° while the current amplitude is estimated in a iterative way by means of Algorithm 1. To simply the computation, the PM torque contribute is neglected so that the torque is assumed to be a quadratic function of the current only. The motor torque is evaluated with a single step static FE analysis. To reduce the estimation error due to the torque ripple, the torque is computed as follows:

$$T_{\mathrm{dq}} = \frac{3}{2} p \big(\Lambda_{\mathrm{d}} I_{\mathrm{q}} - \Lambda_{\mathrm{q}} I_{\mathrm{d}} \big) \tag{11.7}$$

In the same simulations, the minimum flux density within the PMs is checked to evaluate the demagnetization risk. If after some iterations the target torque, T_{OL}, is not reached within, because of current limitation or PMs demagnetization, the considered individual is rejected, otherwise the evaluation of the HSWP feasibility is performed.

11.5.3 High-speed working point feasibility check

In this step, the algorithm determines the feasibility of the HSWP estimating, with an iterative procedure, the current vector that yields the required torque, T_{HS}, at the given mechanical speed n_{HS} within the current and voltage limits.

If the voltage margin is very low, as in this work, it is essential to take into account the voltage drop due to resistive and end-winding inductance effects. The computation of the winding

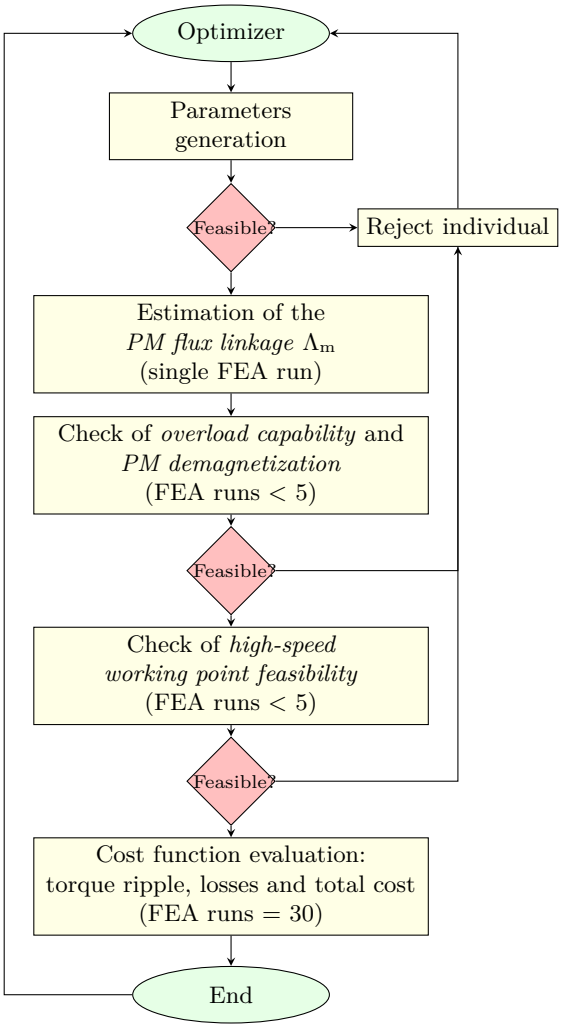

Figure 11.3: Flowchart of the evaluation procedure performed for each individual during the optimization.

resistance at the maximum admissible working temperature allows to have, in the worst case, an estimation of the maximum voltage drop. It is given by:

$$R_s = \rho_{145\,^\circ C} \frac{\left(L_{stk} + \ell_{ew}\right) n_{cs}^2 Q_s}{3 S_{slot} k_{fill}} \tag{11.8}$$

where $\rho_{145\,^\circ C}$ is the winding material resistivity at 145 °C, ℓ_{ew} is the end-winding length, S_{slot} is the slot cross-section and k_{fill} is the slot fill factor. The end-winding length can be estimated analytically as follows

$$\ell_{ew} = 2.5 \frac{D_s}{p} \tag{11.9}$$

while the relative inductance is:

$$L_{ew} = 2pq^2 \mu_0 n_{cs}^2 k_{ew} \ell_{ew} \tag{11.10}$$

where q is the number of slots per pole per phase, μ_0 is the vacuum magnetic permeability and k_{ew} is a coefficient that depends on the winding disposition (i.e. $k_{ew} = 0.35$) [117, 139].

The d- and q-axis component of the current vector can be found solving the following system

Algorithm 1 Evaluation of the overload capability and PMs demagnetization

$k = 0$
$k_{\max} = 10$
$I_1 = I_{\text{INV}}$
$\alpha_{\text{i}}^{\text{e}} = 55$
Run single step static FEA
Compute T_{FEA} by means of (11.7)
Evaluate PMs demagnetization
while $|T_{\text{FEA}} - T_{\text{OL}}| > \varepsilon_{\text{T}}$ **and** $k \leq k_{\max}$ **do**
  $k = k + 1$
  $I_k = I_{(k-1)} \cdot \sqrt{\frac{T_{\text{OL}}}{T_{\text{FEA}}}}$
  Run single step static FEA
  Compute T_{FEA} by means of (11.7)
  Evaluate PMs demagnetization
end while

of nonlinear equations:

$$\begin{cases} I_{\text{d}} = \dfrac{2}{3} \dfrac{T_{\text{HS}}}{p\left[\Lambda_{\text{m}} + \left(L_{\text{d}} - L_{\text{q}}\right) I_{\text{q}}\right]} \\ V_{\text{N}}^2 = R_{\text{s}}^2 \left(I_{\text{d}} + I_{\text{q}}\right)^2 + \omega_{\text{HS}}^2 \left[\left(L_{\text{q}} I_{\text{q}} - \Lambda_{\text{m}}\right)^2 + \left(L_{\text{d}} I_{\text{d}}\right)^2\right] \end{cases} \tag{11.11}$$

where L_{d} and L_{q} are the apparent inductances of the d- and q-axis computed as follows:

$$L_{\text{d}} = \frac{\Lambda_{\text{d}}}{I_{\text{d}}} + L_{\text{ew}} \qquad L_{\text{q}} = \frac{\Lambda_{\text{q}} + \Lambda_{\text{m}}}{I_{\text{q}}} + L_{\text{ew}} \tag{11.12}$$

Eqn. (11.11) represents the intersection between the constant torque locus, $T_{\text{HS}} = T(I_{\text{d}}, I_{\text{q}})$, and the constant voltage locus, $V_{\text{N}} = V(I_{\text{d}}, I_{\text{q}})$. The working point is not feasible if (11.11) does not have solution which means that the constant torque curve does not intersect the constant voltage locus as reported in Figure 11.4(a). Otherwise, one or two solutions may exist. In particular, the first case, shown in Figure 11.4(b), corresponds, to the MTPV condition in which the constant torque locus is tangent to the constant voltage one. In case of two solutions, shown in Figure 11.4(c), only the one with the lowest current amplitude has to be selected since it yields the same flux linkage (i.e. same iron losses) with lower joule losses. Since the inductances strongly depend on the motor

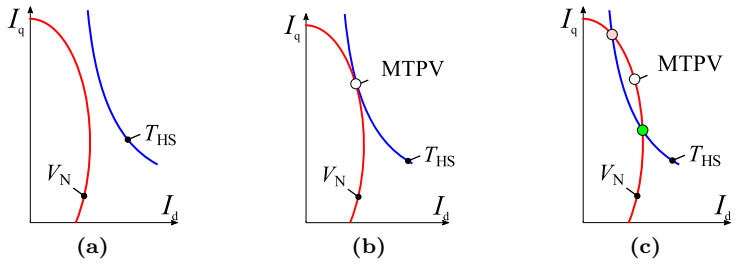

Figure 11.4: Computation of the working point feasibility: unfeasible (a), one solution (b) and two solutions.

saturation, the solution of (11.11) provides accurate results only locally. For this reason, some iterations have to be carried out to reach a proper accuracy.

Figure 11.5 shows qualitatively the procedure used to estimate the feasibility of the HSWP in the $I_{\text{d}} - I_{\text{q}}$ plane. Figure 11.5(a) shows the starting situation of the algorithm in which only the current vector, $\mathbf{I}_{\text{OL}}$, and the relative inductances, are known from the overload capability

test carried out in the previous step. The dash dotted and dashed lines represent the constant torque and constant voltage loci in (11.11), respectively. The red and blue lines are the actual constant torque and constant voltage loci (unknown a priori) obtained sampling the $I_\mathrm{d} - I_\mathrm{q}$ plane with several FE analyses. The difference between the actual and the estimated curves is due to aforementioned saturation effect. The current vector $\mathbf{I}_\mathrm{HS}$ is the result of (11.11) and represents the first estimation of the HSWP. The vector $\varepsilon_\mathbf{I}$ is the difference between the initial and the estimated current vector and it is used to stop the algorithm when its value is lower than a given tolerance $\varepsilon_{\mathbf{I},\mathrm{min}}$. In the current example, shown in Figure 11.5(a), the amplitude of ε_I is higher than $\varepsilon_{\mathbf{I},\mathrm{min}}$ (shaded circle near the estimated working point) so that a further iteration has to be performed.

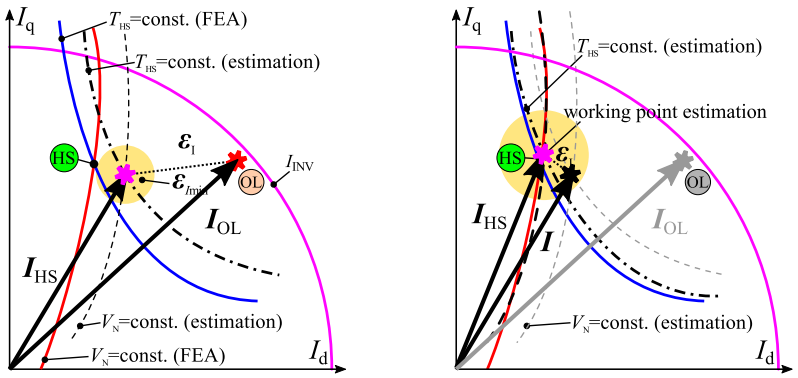

(a) *First iteration.*

(b) *Final iteration and convergence.*

Figure 11.5: Estimation of the HSWP. The *estimated* curves are computed with (11.11) while the *FEA* ones are obtained sampling the $I_\mathrm{d} - I_\mathrm{q}$ plane with several FE analyses.

In the next iteration, Figure 11.5(b), a single FE analysis is carried out with the estimated current vector $\mathbf{I}_\mathrm{HS}$ and the inductances are updated. Then, a new current vector is estimated by means of (11.11) and the relative error is computed. This procedure is repeated until $\varepsilon_{\mathbf{I},\mathrm{min}} \leq \varepsilon_\mathbf{I}$. If no convergence is achieved after a certain number of iterations, the individual is rejected. Otherwise, the procedure continues to the final step. In Figure 11.5(b), the previous and the estimated working points are within the shaded circle which means that the convergence is reached. Algorithm 2 reports the main steps need to implement such a procedure.

Algorithm 2 Estimation of the HS working point.

```
Estimation of R_s and L_ew
j = 0, j_max = 10
I = I_OL
while ε_I > ε_I,min > and j < j_max do
    if j > 0 then
        Run single step static FEA
        Inductances computation by means of (11.12)
    end if
    Estimation of I_HS by means of (11.11)
    ε_I = |I − I_HS|
    I = I_HS
    j = j + 1
end while
```

11.5.4 Evaluation of the optimization objectives

In this last step, the optimization cost functions are evaluated. The total motor cost is computed as the summation of the PMs, copper and iron costs determined by their weight and the relative specific costs.

Since k_{Loss} depends on the sum of winding and core losses, it is essential to have an accurate estimation of their individual values to allow proper design solutions. In fact, a wrong estimation of their value could yield solutions with unbalanced electric and magnetic loading [133].

Between the copper and the core losses, the second one are surely more affected by uncertainty. In general, the Steinmetz equation ($\alpha = 1$) is adopted for the estimation of the stator teeth and back-iron losses as follows:

$$P_{\text{Fet}} = \left(k_{\text{hy}} f^{\alpha} B_{\text{t}}^2 + k_{\text{ec}} f^2 B_{\text{t}}^2\right) G_{\text{t}} \tag{11.13}$$

$$P_{\text{Febi}} = \left(k_{\text{hy}} f^{\alpha} B_{\text{bi}}^2 + k_{\text{ec}} f^2 B_{\text{bi}}^2\right) G_{\text{bi}} \tag{11.14}$$

where B_{t} (B_{bi}) is the maximum flux density in the teeth (back-iron), f is the electric frequency, G_{t} (G_{bi}) is the teeth (back-iron) weight; k_{hy} and k_{ec} are the hysteresis and eddy-current losses coefficients, respectively. Usually, their values can be computed with a curve fitting of the lamination specific losses reported in the data sheets. The actual flux density behavior in the motor core contains many harmonics due to several effects (e.g. saturation, slotting, PWM supply) and their contribute is not taken into account in (11.13) and (11.14). An improved method for computing the iron losses in FE analysis is to compute the fast Fourier transform of the flux density behavior in all the mesh elements and to apply (11.13) and (11.14) for each harmonic. Recently, such a method has been implemented also in FEMM [140, 141]. In this case study, the frequency exponent, α, of the hysteresis losses term has been set in order to have a better curve fitting of the lamination data as reported in [133, 142]. Table 11.2 reports the iron losses computed by means of the simplified Steinmetz method (SM), the fast Fourier method (FFTM) and a commercial software (MagNet). In the latter, the iron losses coefficients and exponents have been set equal to the FFTM method. For the comparison, the optimal individual, selected in section 11.6, has been analyzed. The coefficients k_{hy} and k_{ec} and the BH curve have been set equal in all the approaches. Several operating points at different electric frequencies have been evaluated. The first column reports the per unit torque while the second column reports the per unit speed. The relative reference values are the overload torque, T_{OL}, and the maximum mechanical speed, n_{HS}. For the losses comparison, the FFTM losses in the HSWP are taken as reference value. No additional losses coefficients have been considered in the comparison.

It is evident the good agreement between the FFTM and MagNet results while SM underestimates the losses in all the conditions. Furthermore, the losses computed with the SM do not vary significantly with the operating point unlike the other two methods in which a losses increase of 47% is observed from the lowest to the highest speed. The good agreement between the FFTM and MagNet results induced the authors to adopt the FFTM for the iron losses computation. However, such a choice involved a longer computational time since, in general, at least one electric period has to be simulated to get a reliable harmonic analysis of the flux density harmonics. Thanks to the symmetry of the machine, only an half of the electric period has been simulated.

11.6 Optimization results

This section reports the results of the optimization carried out with the parameters and the evaluation procedures discussed previously. A multi-objective differential evolution algorithm has been used for the optimization. The total number of parameters is 11, as seen in section 11.3, while the number of objectives is 3. The maximum number of generations was set to 300 with 55 individuals each. However, the optimization has been interrupt after 266 generations since no improvements was achieved after the 245-th generation.

The objective planes of the optimization are shown in Figure 11.6. Figure 11.6(a) reports the torque ripple versus k_{Loss}. The gray markers indicate the total individuals of the optimization while the other markers represent the individuals that yield the cost functions within the required

Table 11.2: Iron losses computation: comparison between different computational approaches: Steinmetz method (SM), fast fourier transform method (FFTM) and commercial software (MagNet). The highest FFTM iron losses, n_{HS} and T_{OL} are selected as reference values.

Torque (p.u.)	Speed (p.u.)	Iron losses (p.u.)		
		SM	FFTM	MagNet
0.33	**1**	0.20	**1**	1.03
0.48	0.79	0.20	0.87	0.93
0.62	0.67	0.21	0.86	0.87
0.77	0.59	0.21	0.77	0.77
0.92	0.52	0.22	0.63	0.65
1	0.49	0.22	0.57	0.59

ranges (see Table 11.1). The red circle markers indicate the Pareto front of the considered plane (PF1) while the blue circles represent the Pareto front of the cost versus k_{Loss} plane (PF2). In the first plot, the dimension of the markers depends on the cost so that a bigger marker means a higher cost. In the second plot the size is related to the torque ripple analogously. Figure 11.6(b) reports the total cost versus k_{Loss} plane. Similarly to the previous plot, the blue markers are the PF2 individuals while the red ones refer to the PF1 front.

It can be noted that the number of the PF2 individuals (25) is higher than PF1 (9). This means that many combinations of motor geometry (i.e. motor cost) are possible but a very limited part of them satisfy the conditions to achieve a low torque ripple. The decrease of the total cost for higher value of k_{Loss} is due to the reduction of the machine volume, the stack length, in particular.

Being the cooling system unknown at the time of writing this thesis, the authors preferred to select the individual that exhibits a good compromise in terms of low k_{Loss} and torque ripple, leaving to the total cost a minor relevance for the realization of a first prototype. The selected individual is highlighted in the plots by green circle. Obviously, many other choices can be done on the basis of the two Pareto fronts.

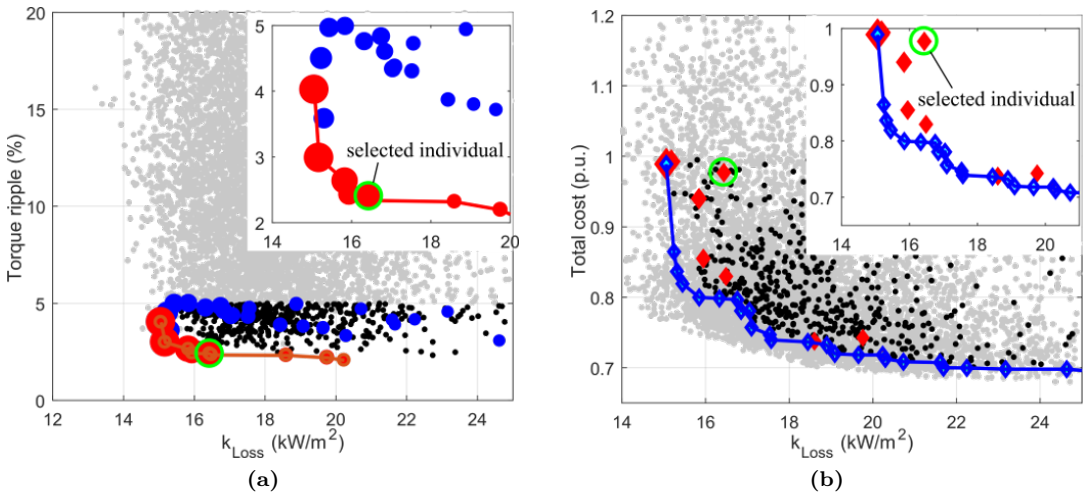

(a) (b)

Figure 11.6: Objectives planes of the optimization. The gray markers indicates all the population, the black markers are the individuals whose cost functions are within the design requirement limits, the red markers are the non-dominated individuals in the torque ripple versus k_{Loss} plane and the blue markers are the non-dominated individuals in the total cost versus k_{Loss} plane.

11.7 Experimental results

This section reports the preliminary experimental results carried out on the motor prototype whose rotor and stator are shown in Figure 11.7(a) and Figure 11.7(b), respectively.

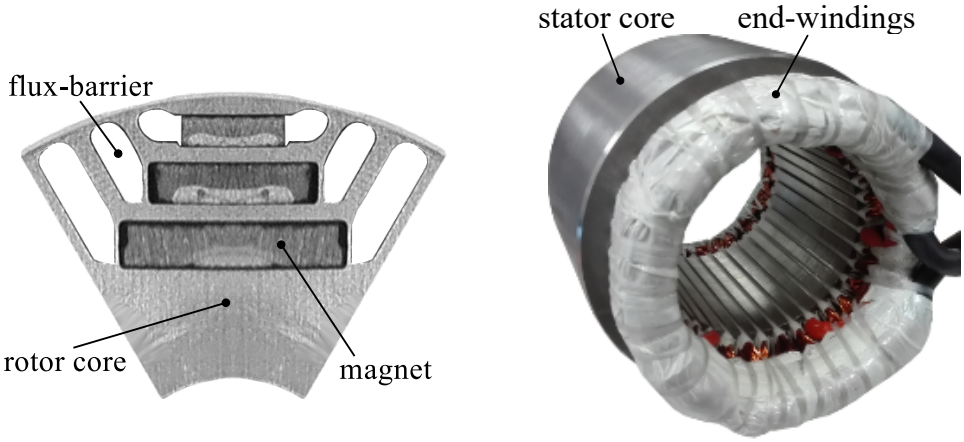

(a) *Rotor pole.* **(b)** *Stator.*

Figure 11.7: Pictures of motor prototype.

Only low speed tests are carried out for the lack of a test bench with a proper power. This means that only the torque versus rotor position behaviors and the magnetizing characteristics (i.e. $\Lambda_{\mathrm{d}}(I_{\mathrm{d}}, I_{\mathrm{q}})$ and $\Lambda_{\mathrm{q}}(I_{\mathrm{d}}, I_{\mathrm{q}})$) were actually tested. The power versus speed curves are obtained processing the available data with the same algorithm used for the FE results.

Figure 11.8(a) reports the FE and experimental torque versus rotor position behaviors, obtained with different current amplitudes in MTPA condition, the reference torque value is T_{OL}. It can be noted that there is a good agreement between the FE and experimental curves both in terms of average torque and torque ripple. In particular, the discrepancy between FE and experimental average torque is always lower than 4%. The power versus speed curves, for different current amplitudes, are reported in Figure 11.8(b). It can be noted that the HSWP, highlighted in the same figure, is always below the maximum power profile, this suggests that the motor drive is capable to deliver the rated power at the given maximum speed.

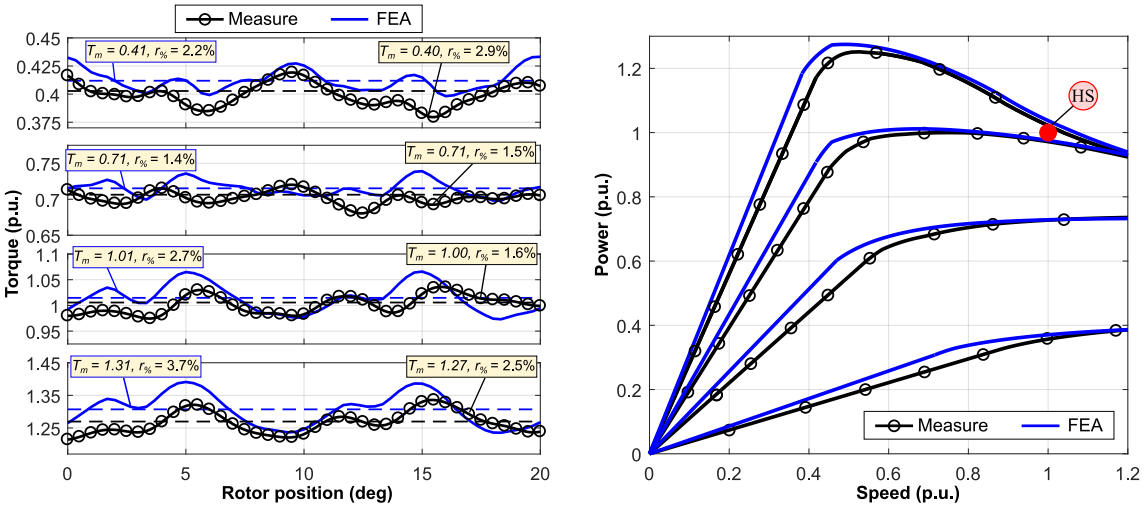

(a) *Torque versus rotor positions in MTPA condition.* **(b)** *Power versus speed. (Indirect results).*

Figure 11.8: Comparison between FEA and experimental results for different current amplitudes.

11.8 Conclusion

This chapter dealt with the design of a PMASyR motor for an E-Scooter application by means of FE-based multi-objective optimization procedure. In particular, such a procedure is able to find solutions which meet determined overload and flux-weakening capability with a given inverter Volt-Ampere rating. According to the optimization results, a prototype has been manufactured and tested to investigate the reliability of the proposed design procedure. The preliminary experimental results have shown a good agreement with the FE predictions in terms of average torque and torque ripple. Promising results are also obtained in terms of power capability.

Part IV

Bonded Magnets for PMASyR machines

Chapter 12

Bonded Magnets in PMASyR Machines

12.1 Introduction

The PMASyR machine is well known to mitigate the low power factor and power capability that characterize the SyR machine by means of a small PM flux contribute. Depending on the adopted design and economic strategies, such an excitation flux may be produced by a small amount of rare earth PMs or by low magnetic energy ferrites. Both solutions allows to keep the PMASyR cost very competitive with the classical rare-earth based PMSM however, in the recent years, the second solution is often preferred to avoid any risk related to the high rare-earth materials cost fluctuation. Thanks to its advantages, the PMASyR machine is adopted in home-appliance, spindle and automotive applications [10, 143, 144].

The main PMASyR machine design keys are the flux-barriers geometry and PM compensation [10, 145]. Even thought these two aspects are not independent from each other, the first one mainly affects the average torque and torque ripple while the second one affects the high-speed power capability [69, 146, 147].

As pointed out in chapter 11, rectangular shaped PMs are usually adopted to simplify as much as possible the rotor geometry and the overall manufacturing cost as well. However, when high PM compensation is required, such a design choice greatly limits the machine performance since, as shown in Figure 12.1(a), only a small part of the effective flux-barriers cross section area can be filled by PMs.

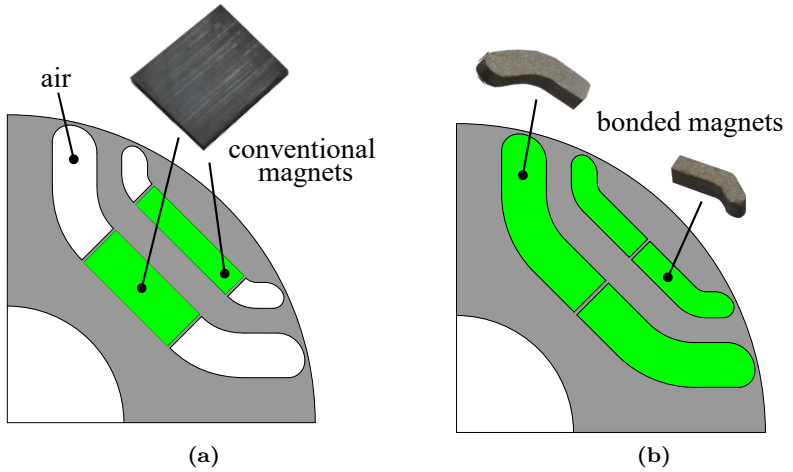

Figure 12.1: PMASyR motors with sintered magnets (a) and BMs (b).

The bonded magnets (BMs) represent a valid solution since they can be easily shaped or directly injected, at fluid state, into the final volume to fill [7, 11, 148]. Figure 12.1(b) shows how the BMs can be effectively used for the realization of a PMASyR rotor and highlights the higher amount of PM materials with respect to the classical solution in Figure 12.1(a). The BMs are constituted by a mixture of a magnetic powder and polymeric binder [149]. The magnetic powder may be hard ferrite, NdFeB, SmCo while the binders depend on the typology of the moulding process. The normally used polymeric materials are Polyamide (PA) for injection moulding and thermoset resins for compression moulding [150]. The BMs can be made in very complex shapes using both moulding technologies [151]. Finally, the magnetic characteristics of the BMs can be "tuned" through the percentage of the plastic binder. The NdFeB BMs have better magnetic characteristics with respect to ferrites, mainly for the high intrinsic coercivity.

The aims of this study is to investigate experimentally the impact of different production technologies on the BMs properties and to evaluate their suitability for PMASyR machine applications. In the first part a brief description of the motor geometry and its design is presented. Then, the steps for BMs preparation and magnetization are described. In particular, two BM typologies are tested: one prepared with compression moulding and another with injection moulding. Next, three motor prototypes, reported in Figure 12.2, are manufactured: one SyR machine and two PMASyR machines with compression and injection moulding BMs. These prototypes are tested in laboratory and their performance are finally compared.

Figure 12.2: Motor prototypes manufatured for the study: one SyR machine and two PMASyR machines.

12.2 Motor geometry

A standard geometry, whose main data are reported in Table 12.1, has been selected for the stator. The segmented flux-barriers geometry, described in section 15.2, has been preferred for the rotor because of its simplicity. The number of flux-barriers per pole has been set to two to limit the number of BMs to manufacture. It is worth noticing that these design choices are made only to simplify the BMs production in the laboratory. The rotor geometry has been optimized using the procedure described in section 4.3. The selected rotor parameters were the two flux-barrier angles and the magnetic insulation ratio. The flux-barriers and iron channel dimensions have been computed with the procedure reported in section 15.3. The optimization objectives were to maximize the average torque and to minimize the torque ripple. The optimization has been performed in 60 generation of 20 individuals each. The optimal rotor parameters are reported in Table 12.1 and the a sketch of the rotor geometry is shown in Figure 12.3(a). The FE torque behavior computed in MTPA condition is reported in Figure 12.3(b), the motor achieves an average torque and ripple of 5.3 Nm and 22 %, respectively. A rotor skewing of a slot pitch (i.e. 10°) with eight steps has been selected to reduce the main torque harmonic. With such a solution, the average torque slightly reduces to 5.1 Nm while the torque ripple decreases to 5 %, as reported in Figure 12.3(b).

Table 12.1: Main data of the SyR machine.

Number of pole pairs	2	-
Number of slots	36	
Stack length	40	mm
Stator outer diameter	150	mm
Stator inner diameter	96	mm
Rotor outer diameter	95.2	mm
Air-gap	0.4	mm
Rotor inner diameter	40	mm
Current density	6	A/mm^2
Flux-barrier angles	$\{16.05, 33.8\}$	deg
Magnetic insulation ratio	0.46	-

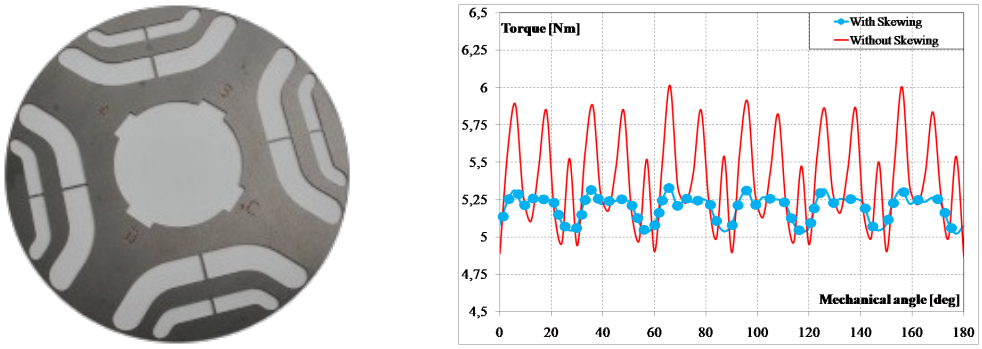

(a) **(b)**

Figure 12.3: SyR rotor geometry (*a*) and torque behavior in MTPA condition with and without skewing (*b*).

12.3 BMs preparation

12.3.1 Compression moulding

In the compression technique, the phenolic resin has been used as polymeric binder and mixed with NdFeB powder. For this process, the proper amount of binder content has to be carefully selected on the basis of the operating pressure and resin typology. In general, it ranges between 0.8% and 5% in weight (wt%). After some mechanical tests carried out in laboratory, a value of 4% has been set to ensure a proper mechanical strength[1].

For the BMs mixture a phenolic resin and MQP 14-12 NdFeB powder have been selected. The latter is a magnetic powder for high temperature applications (up to 150 °C). At first, the obtained magnetic mixture is compressed by an hydraulic press at a operating pressure of 600 MPa (Figure 12.4(a)). Then, the obtained sample is heat treated at 150 °C for 45 minutes. The processed discoid is finally machined (Figure 12.4(b)) to obtain the final samples shown in Figure 12.4(c).

12.3.2 Injection moulding

For injection moulding, the BMs are prepared using the commercial product MQIP-M260, which is NdFeB compound with polyamide 12 (PA12) in 8 wt% in pellet form as reported in Figure 12.5(a). Such value usually represents the lowest limit for the plastic part because the extrusion process with twin-screw needs a certain viscosity. The pellets are firstly heated at a temperature of about 275 °C to reach the fluid state. Once the mixture is completely fluid, the temperature is reduced to 80 °C and kept constant during the injection process. In this study the magnetic mixture has been

[1] A sample with a polymer content of 5 wt% exhibited structural problems after the thermal treatment.

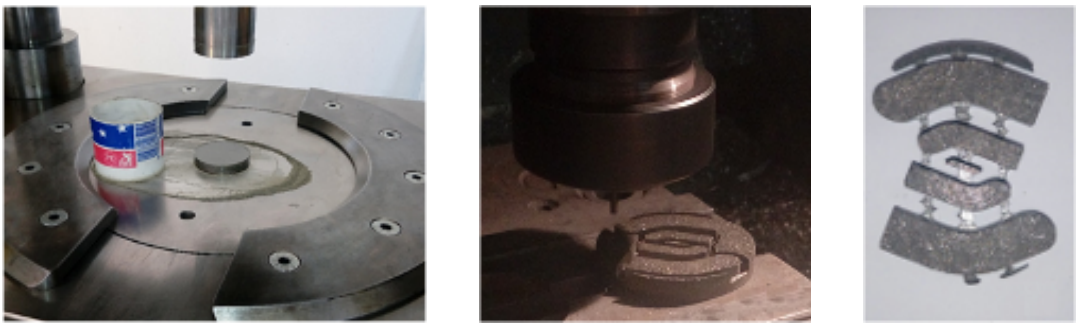

(a) (b) (c)

Figure 12.4: Discoid sample after the process moulding (a), working process of the compacted disk (b) and final product (c).

injected in shaped molds and not directly in the rotor lamination. The final product is reported in Figure 12.5(b).

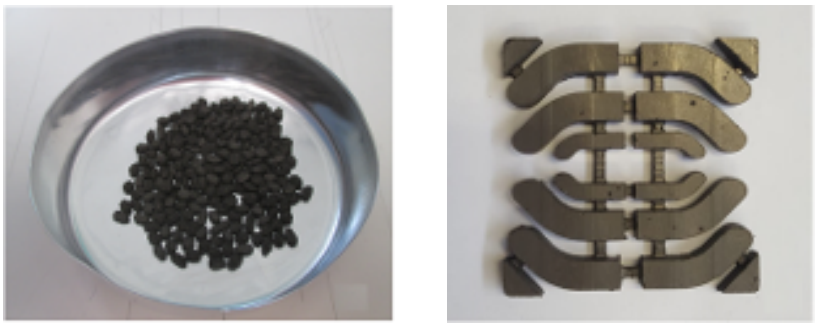

(a) (b)

Figure 12.5: MQIP-M260 pellets used for the injection moulding (a) and final BMs samples (b).

12.4 BMs magnetization and characterization

12.4.1 Magnetization

The custom magnet holder in Figure 12.6(a) has been manufactured to keep the BMs pieces in position during the magnetization impulse. Such a magnet holder has been also designed to obtain a magnetization direction as much as possible perpendicular to the flux-barrier edges with the standard magnetizer shown in Figure 12.6(b). The BMs magnetization in situ using the assembled prototype was not possible for the high current (over 50 A) required for the process. This operation has been carried out for all the BMs pieces required to fill the PMASyR rotors. In this step the magnetized BMs were organized as reported in Figure 12.6(c) in order to keep trace of their polarity. By means of the green magnetic paper test, in Figure 12.6(d), it has been observed a negligible local flux density reduction near the BMs extremities as confirmation of the effective magnet holder design.

12.4.2 Magnetic characterization

Some magnetized BM samples have been characterized by means of a hysteresisgraph as reported in [7]. The resulting averaged demagnetization curves of the compressed and injected BMs are shown in Figure 12.7(a) and Figure 12.7(b), respectively. From a comparison between the two

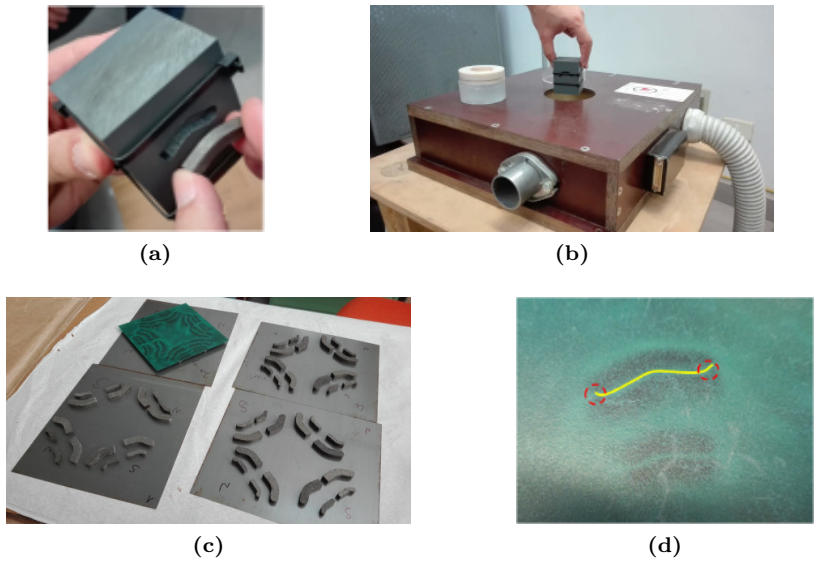

(a) (b) (c) (d)

Figure 12.6: BMs magnetization steps.

graphs it is evident that the compression moulding allows to obtain the highest remanence flux while the injection moulding yields BMs with higher coercive field. Such magnetic properties have been used in FE analysis to estimated the PMASyR machines performance.

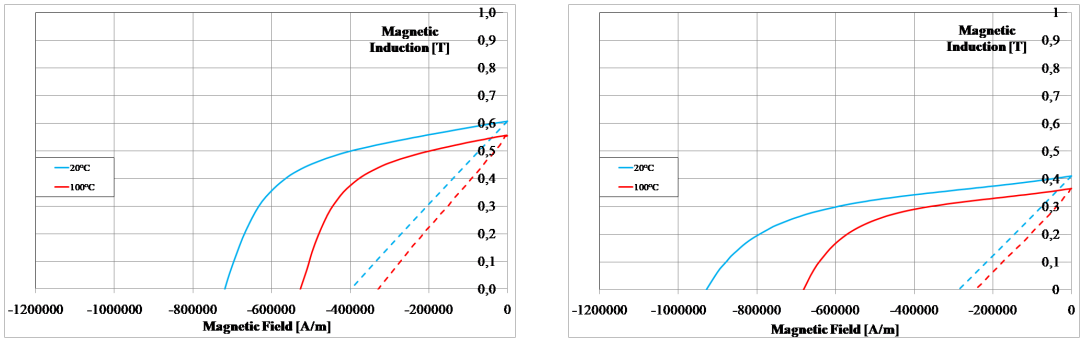

(a) (b)

Figure 12.7: Measured demagnetization curve of NdFeB BMs prepared with compresssion (a) and injection (b) moulding process.

12.5 Prototype assembling

12.5.1 SyR rotor

The main steps of the SyR rotor assembling are reported in Figure 12.8. The rotor has been assembled in laboratory manually starting from the shaft, Figure 12.8(a), and the single rotor laminations, Figure 12.8(b). The latter have been stacked one by one on the shaft as reported in Figure 12.8(c). The four different rotor keyway slots on the rotor inner diameter have been used as reference for the eight rotor steps. In fact, they have been stacked following the order:

$$A, B, C, D, \bar{D}, \bar{C}, \bar{B}, \bar{A},$$

where the bar indicates the mirrored orientation. Three of these steps are clearly visible in Figure 12.8(d) while the assembled rotor is shown in Figure 12.8(e).

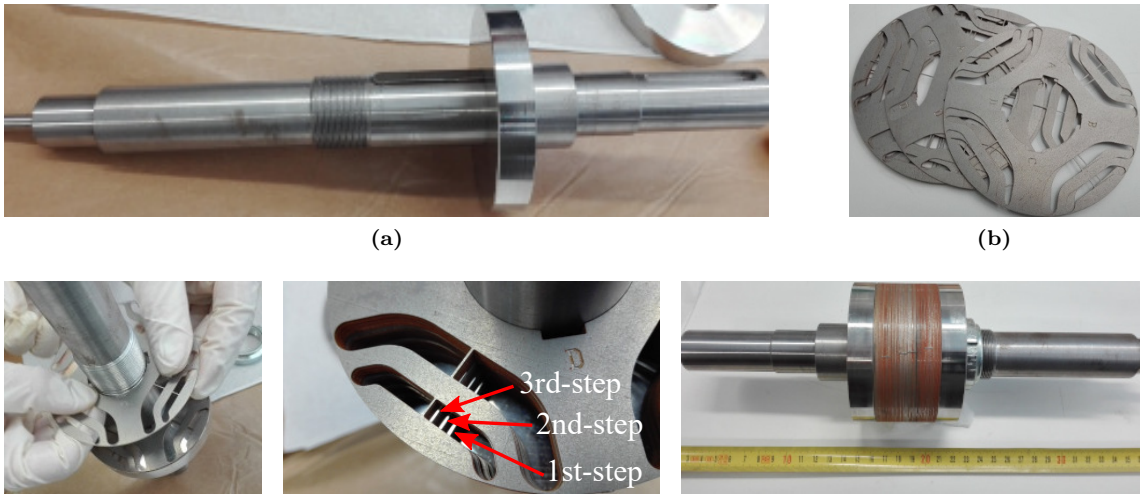

(a) **(b)** **(c)** **(d)** **(e)**

Figure 12.8: SyR rotor assembling steps.

12.5.2 PMASyR rotor

The PMASyR assembling is similar to the SyR one, the only difference is the BMs insertion into the rotor flux-barrier slots. After the completion of the first rotor step stack, Figure 12.9(a), the BMs are inserted manually one by one in the flux-barrier slots as reported in Figure 12.9(b). This operation has been carried out for each rotor step. In Figure 12.9(c) it is possible to see the effect of the rotor skewing on the complete rotor.

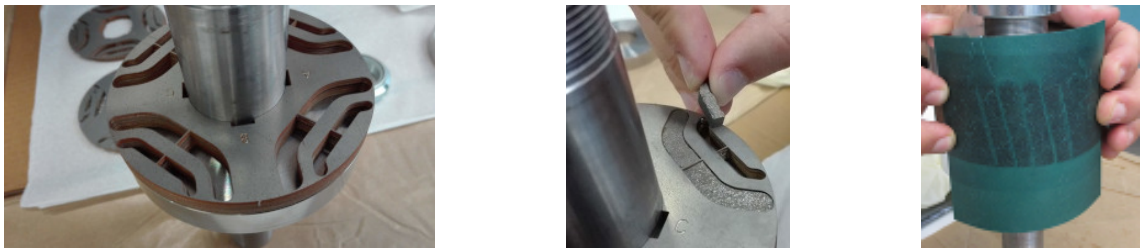

(a) **(b)** **(c)**

Figure 12.9: PMASyR rotor assembling steps.

12.6 Experimental results

The tests carried out on the three prototypes allowed to get their MTPA locus and torque behaviors for different current amplitudes.

12.6.1 Torque versus current angle

The experimental and FE average torque versus current angle curves of the three prototypes are reported in the first column of Figure 12.10. The simulation data are indicated by means of

continuous lines while the measurement values are represented by black markers. The MTPA trajectory is reported in red continuous line. In general, the measured average torque values are slightly lower than FE ones. Many aspects can explain such a difference. The most important is of course related to the non uniform magnetic characteristics in the BM samples. An other aspect is the presence of additional air-gaps between the BMs and flux-barrier surfaces determined by the BMs and lamination mechanical tolerances. This is confirmed by the fact that in some cases the BMs insertion was easy and in other cases was very hard. Also the BMs temperature plays a important role on the machine performance. In the FE analyses it was set to 80 °C while there is any indication of the temperature behavior during the tests. Finally, the actual lamination magnetic properties (i.e. BH curve) may be not completely coincident to the one used in the FE model. The latter aspect is surely present since a certain error is present in the SyR machine results as well.

With respect to the SyR machine, the average torque increases of 55% and 39% for the PMASyR motor with the compression and injection moulding BMs, respectively. This difference is due to the higher remanence of the BMs obtained by compression.

12.6.2 Torque behaviors

The second column of Figure 12.10 reports the FE and experimental torque behaviors of the three motors obtained in MTPA condition with the rated current. From Figure 12.10(b) it can be noted that the SyR motor has the best matching between measurement and simulation data. In fact the average torque error is about 3% while for the ripple it is about 6%. For the PMASyR motor with BMs made through compression moulding, Figure 12.10(c), the average torque difference is higher, i.e. 7%, while the ripple one is 1%. Similar average torque error but higher torque ripple difference, i.e. 9%, has been found for the PMASyR motor with BMs prepared by injection moulding, Figure 12.10(e). The use of BMs increases the ripple respectively of 145% for the PMASyR motor with compression moulded BMs and of 80% for PMASyR motor with injection moulded BMs.

12.6.3 Power factor

For all prototypes, the power factor has been computed on the basis of the experimental dq flux linkages and the winding resistance at the rated speed of 1000 rpm, the results are reported in Table 12.2. It can be noted that the highest power factor, 0.93, is achieved by the PMASyR machines equipped with compression moulded BMs. Sightly lower value, i.e. 0.87, is achieved by the other PMASyR machine. Both motors exhibit yield a quite good power factor improvement with respect to the SyR one (0.71).

Table 12.2: Power factor of the prototypes at the rated current (3 A) in MTPA condition.

Motor Types	PF
SyR motor	0.71
PMASyR motor compression	0.93
PMASyR motor injection	0.87

12.7 Conclusion

An investigation of the BMs suitability for PMASyR machines have been carried out in this chapter. Two types of BMs based on different production technologies have been proposed: the compression one and injection one. The former allows to obtain better magnetic properties, while, the latter is more suitable for an industrial process, mainly in terms of production rates. A good matching between experimental and FE results have been obtained, in particular regarding the torque waveforms. A torque density increment up to 50% has been found for the PMASyR

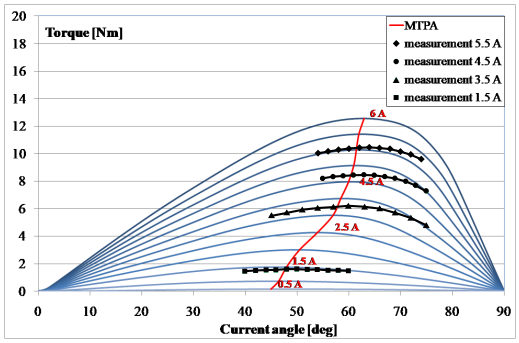

(a) *SyR machine.*

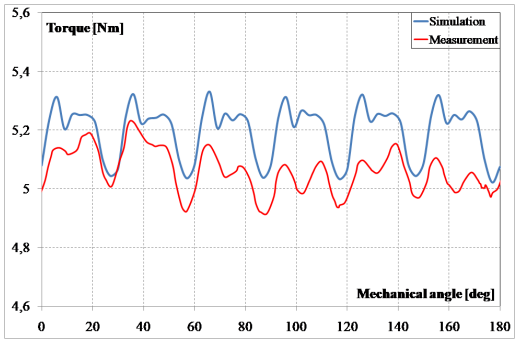

(b) *SyR machine.*

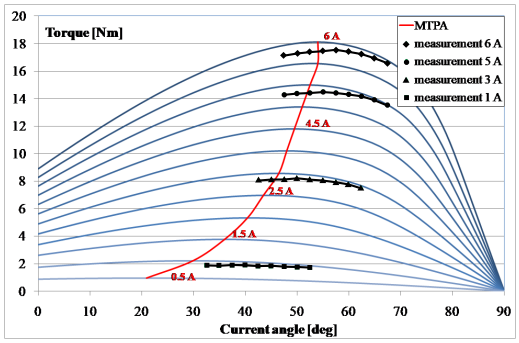

(c) *PMASyR machine with compression BM.*

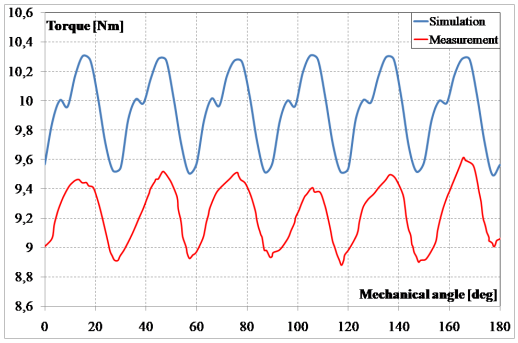

(d) *PMASyR machine with compression BM.*

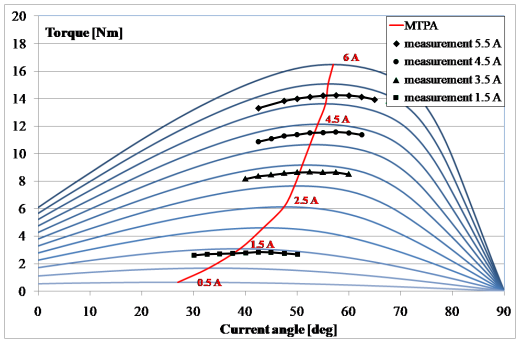

(e) *PMASyR machine with injection BM.*

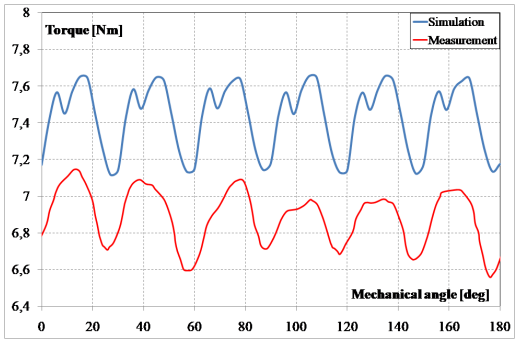

(f) *PMASyR machine with injection BM.*

Figure 12.10: Torque versus current angle (first column) and torque versus rotor position curves (second column): comparison between FE and experimental results. The torque behaviors are obtained at the rated current in MTPA condition.

machine prototype with BMs obtained by compression. The same prototype has a power factor of 0.93 at rated condition, much higher than SyR motor (0.71). In general, a noticeable torque ripple increase has been obtained in both PMASyR motors. However such an increment can be effectively reduced adopting a more complex rotor with almost three-flux barriers per pole and optimizing their parameters accordingly.

Part V

Tools

Chapter 13

Efficiency map computation

13.1 Introduction

One of the most effective graphical way to describe the performance of an electric machine is the efficiency map. The efficiency map is a constant-efficiency contour plot in the torque, or power, versus speed plane [142, 152–158]. Each point of such a map corresponds to a determined current supply condition that exhibits the maximum efficiency for a given torque and speed. An example is reported in Figure 13.1.

Numerically speaking, it is a 2D matrix with R rows and C columns; i and j are the row and column indices, respectively. The number of rows and columns depends on the size of the torque and speed arrays selected to build the evenly spaced grid. The maximum torque depends on the operating condition and current limit. In general, it can be set equal to the rated or overload torque. The maximum speed depends on the mechanical constraint of the machine. The voltage is automatically taken into account in the efficiency map computation.

Referring to Figure 13.1, the two arrays are defined as follows:

$$\tau = \begin{pmatrix} \tau^{(1)} \\ \tau^{(2)} \\ \vdots \\ \tau^{(R)} \end{pmatrix} \qquad \omega_\mathrm{m} = \left(\omega_\mathrm{m}^{(1)}, \omega_\mathrm{m}^{(2)}, \ldots, \omega_\mathrm{m}^{(C)}\right) \tag{13.1}$$

which means that the (i, j) element of the efficiency map, $\boldsymbol{\eta}$, contains the maximum efficiency achievable with the torque, $\tau^{(i)}$, at the mechanical speed, $\omega_\mathrm{m}^{(j)}$.

In general, for synchronous machine drives, there are infinite combinations of I_d and I_q currents that produce the torque $\tau^{(i)}$ at the speed $\omega_\mathrm{m}^{(j)}$ within the current and voltage limits. The hard point of the efficiency map computation is finding the best I_d and I_q combination that yields the maximum efficiency. This chapter reports a detailed description of the algorithm used to compute the efficiency map.

In the following, unless otherwise stated, all the operations performed with the arrays or matrices are *elementwise* operations. For example, let's define the matrices $\boldsymbol{A}$ and $\boldsymbol{B}$ as follows:

$$\boldsymbol{A} = \begin{pmatrix} A_{11} & A_{12} \\ A_{21} & A_{22} \end{pmatrix} \qquad \boldsymbol{B} = \begin{pmatrix} B_{11} & B_{12} \\ B_{21} & B_{22} \end{pmatrix} \tag{13.2}$$

the elementwise product is:

$$\boldsymbol{C} = \boldsymbol{A} \odot \boldsymbol{B} = \begin{pmatrix} A_{11} \cdot B_{11} & A_{11} \cdot B_{12} \\ A_{21} \cdot B_{21} & A_{22} \cdot B_{22} \end{pmatrix} \tag{13.3}$$

while, the elementwise reciprocal of $\boldsymbol{A}$ is:

$$\frac{1}{\boldsymbol{A}} = \begin{pmatrix} 1/A_{11} & 1/A_{12} \\ 1/A_{21} & 1/A_{22} \end{pmatrix} \tag{13.4}$$

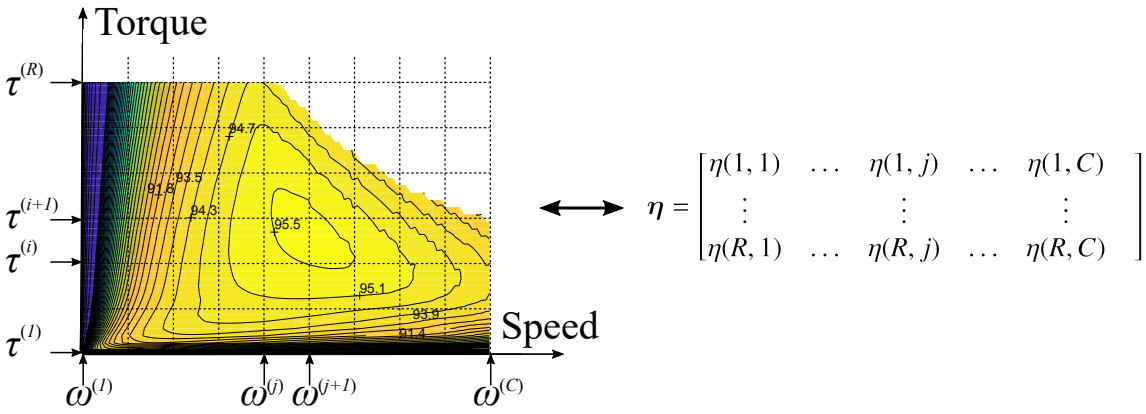

Figure 13.1: Efficiency map in the torque versus speed plane example.

$$\boldsymbol{\eta} = \begin{bmatrix} \eta(1,1) & \dots & \eta(1,j) & \dots & \eta(1,C) \\ \vdots & & \vdots & & \vdots \\ \eta(R,1) & \dots & \eta(R,j) & \dots & \eta(R,C) \end{bmatrix} \tag{13.5}$$

13.2 Input data

The main input data are the magnetizing curves and iron losses matrices obtained for an evenly spaced grid of I_q and I_q currents, as reported in Figure 13.2

The iron losses can be computed in different ways. In case of FE results, it is convenient to compute the hysteresis and eddy current losses for every grid point at a given reference speed, ω_m^* yielding the matrices P_hy^* and P_ec^*.

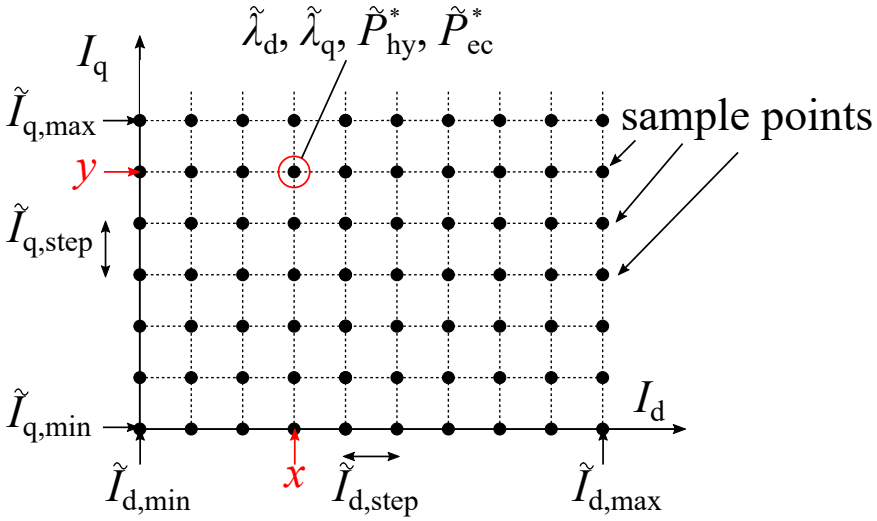

Figure 13.2: I_d–I_q evenly spaced grid. For each point of the grid, the *dq* flux linkages and the hysteresis and eddy current iron losses have to be computed. These matrices allow to describe entirely the machine behavior with a proper data processing.

13.3 Constant-torque loci current points

The next step is to find the I_d and I_q current combinations that describe the constant-torque levels of the array τ.

In the proposed method, the MATLAB® function `contourc` is adopted. For a given constant torque level $\tau^{(i)}$ (i-th element of $\boldsymbol{\tau}$), the function returns a certain number of points. Figure 13.3(a) shows qualitatively the constant torque curves relative to $\tau^{(i)}$ and $\tau^{(i+1)}$. In particular, the first and second loci are described by k (i.e. 4) and h (i.e. 10) points, respectively.

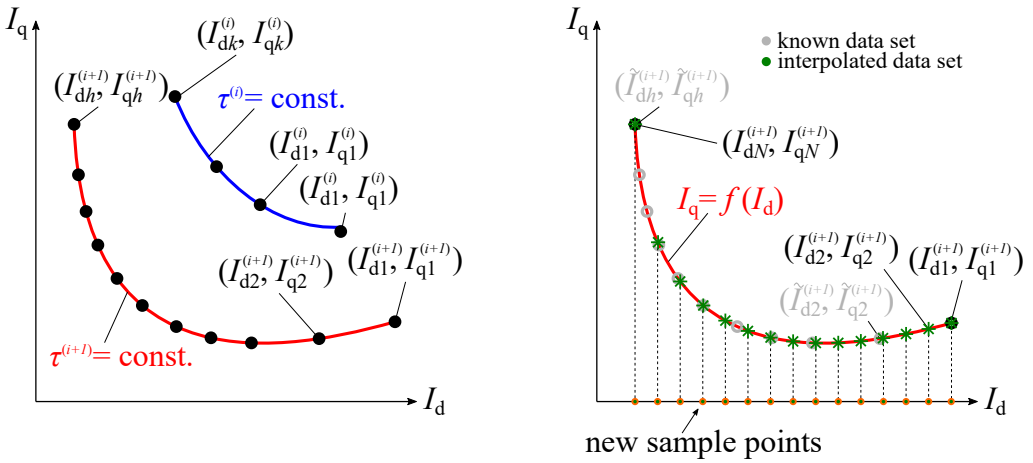

(a) *Constant-torque locus points.*

(b) *Interpolation of the $\tau^{(i)}$ constant-torque locus points.*

Figure 13.3: Computation and interpolation of the constant torque loci in the $I_q - I_q$ plane.

13.4 Constant-torque number of points homogenization

For a reason that will be clarified later on, it is necessary to describe all the constant-torque curves with the same number of points, N. To do that, a 1D interpolation has to be performed.

Firstly, a new set of N evenly spaced I_d currents is defined setting the minimum and maximum values of the initial data set as extreme values. From the new set of d-axis currents, I_d, the respective q-axis currents, I_q, are then interpolated. This step is described qualitatively in Figure 13.3(b). The filled circles on the I_d-axis represent the I_d values while the star markers are the interpolated I_q currents. The empty circles on the plot represent the initial data set obtained in section 13.3. This operation has to be performed for each element of the array $\boldsymbol{\tau}$ in (13.1). At the end of the procedure, R different I_d and I_q arrays, of size $N \times 1$, will be created, as reported in (13.6).

$$I_d{}^{(i)} = \begin{pmatrix} I_{d,1}^{(i)} \\ \vdots \\ I_{d,N}^{(i)} \end{pmatrix} \qquad I_q{}^{(i)} = \begin{pmatrix} I_{q,1}^{(i)} \\ \vdots \\ I_{q,N}^{(i)} \end{pmatrix} \qquad i = 1, 2, \dots R \tag{13.6}$$

13.5 Creation of the 3D matrices

For more clarity, let's first consider the data relative to the torque $\tau^{(i)}$. The column arrays ${I_\mathrm{d}}^{(i)}$ and ${I_\mathrm{q}}^{(i)}$ are replicated C times along the column direction yielding the following matrices:

$$\boldsymbol{I}_\mathrm{d}^{(i)} = \left[\begin{pmatrix} I_{\mathrm{d},1}^{(i)} \\ \vdots \\ I_{\mathrm{d},N}^{(i)} \end{pmatrix}_1 \quad \cdots \quad \begin{pmatrix} I_{\mathrm{d},1}^{(i)} \\ \vdots \\ I_{\mathrm{d},N}^{(i)} \end{pmatrix}_j \quad \cdots \quad \begin{pmatrix} I_{\mathrm{d},1}^{(i)} \\ \vdots \\ I_{\mathrm{d},N}^{(i)} \end{pmatrix}_C \right]_i \tag{13.7}$$

$$\boldsymbol{I}_\mathrm{q}^{(i)} = \left[\begin{pmatrix} I_{\mathrm{q},1}^{(i)} \\ \vdots \\ I_{\mathrm{q},N}^{(i)} \end{pmatrix}_1 \quad \cdots \quad \begin{pmatrix} I_{\mathrm{q},1}^{(i)} \\ \vdots \\ I_{\mathrm{q},N}^{(i)} \end{pmatrix}_j \quad \cdots \quad \begin{pmatrix} I_{\mathrm{q},1}^{(i)} \\ \vdots \\ I_{\mathrm{q},N}^{(i)} \end{pmatrix}_C \right]_i \tag{13.8}$$

After that, the speeds matrices has to be created. The construction is quite simple and consists of replicating N times the row array ω_m along the row dimension. The result is the matrix $\boldsymbol{\omega}_\mathrm{m}^{(i)}$:

$$\boldsymbol{\omega}_\mathrm{m}^{(i)} = \left[\begin{matrix} \left(\omega_\mathrm{m}^{(1)} & \dots & \omega_\mathrm{m}^{(C)} \right)_1 \\ \vdots \\ \left(\omega_\mathrm{m}^{(1)} & \dots & \omega_\mathrm{m}^{(C)} \right)_n \\ \vdots \\ \left(\omega_\mathrm{m}^{(1)} & \dots & \omega_\mathrm{m}^{(C)} \right)_N \end{matrix} \right]_i \tag{13.9}$$

Then, the matrices (13.7), (13.8) and (13.9) have to be replicated R times along the third dimension (i.e. *layer* in MATLAB® syntax) as shown schematically in Figure 13.4. The current amplitude 3D matrix is:

$$[\boldsymbol{I}] = \sqrt{[\boldsymbol{I}_\mathrm{d}]^2 + [\boldsymbol{I}_\mathrm{q}]^2} \tag{13.10}$$

while the hysteresis and eddy current losses, relative to $[\boldsymbol{I}_\mathrm{d}]$ and $[\boldsymbol{I}_\mathrm{q}]$ can be computed interpolating

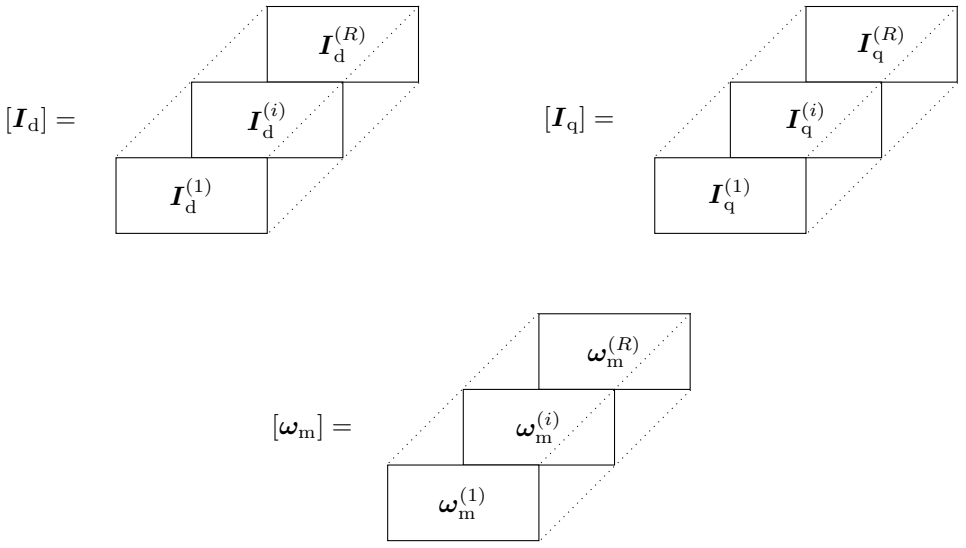

Figure 13.4: 3D current and speed matrices. Their dimension is $N \times C \times R$ where N is the number of points for each constant-torque curve while C and R are the length of ω_m and τ, respectively.

the initial data set obtaining the matrices $[\boldsymbol{P}_\mathrm{hy}^*]$ and $[\boldsymbol{P}_\mathrm{ec}^*]$.

13.6 Computation of the derived quantities

Once the current and speed 3D arrays are built, it is possible to compute all the derived quantities. The first step is computing the *dq* flux linkages for each current combination in $[\boldsymbol{I}_\mathrm{d}]$ and $[\boldsymbol{I}_\mathrm{q}]$ interpolating the initial data set discussed in section 13.2. The results are the 3D arrays $[\boldsymbol{\Lambda}_\mathrm{d}]$ and $[\boldsymbol{\Lambda}_\mathrm{q}]$ with the same size and indices meaning of $[\boldsymbol{I}_\mathrm{d}]$.

The losses values, $[\boldsymbol{P}_\mathrm{hy}]$ and $[\boldsymbol{P}_\mathrm{ec}]$, relative to the currents $[\boldsymbol{I}_\mathrm{d}]$ and $[\boldsymbol{I}_\mathrm{q}]$ are computed interpolating the initial data set. Then, they are re-scaled according to the actual speed $[\boldsymbol{\omega}_\mathrm{m}]$. Such an operation depends on the iron losses equation used for the computation of $\tilde{P_\mathrm{hy}}^*$ and $\tilde{P_\mathrm{ec}}^*$. They can be computed as follows:

$$[\boldsymbol{P}_\mathrm{hy}] = [\boldsymbol{P}^*_\mathrm{hy}] \odot \left(\frac{[\boldsymbol{\omega}_\mathrm{m}]}{\omega^*_\mathrm{m}} \right)^{\alpha} \qquad \text{and} \qquad [\boldsymbol{P}_\mathrm{ec}] = [\boldsymbol{P}^*_\mathrm{ec}] \odot \left(\frac{[\boldsymbol{\omega}_\mathrm{m}]}{\omega^*_\mathrm{m}} \right)^{2} \tag{13.11}$$

where α is an exponent used to get a better fitting of the actual lamination losses data [133, 142]. It is worth noticing that the condition $\alpha = 1$ yields the standard Steinmetz equation.

The 3D array of the Joule losses is simply computed as follows:

$$[\boldsymbol{P}_\mathrm{J}] = \frac{3}{2} R_\mathrm{w} \sqrt{[\boldsymbol{I}_\mathrm{d}]^2 + [\boldsymbol{I}_\mathrm{q}]^2} \tag{13.12}$$

where R_w is the phase winding resistance assumed to be constant for all the working points neglecting the temperature effect on its value. A rule of thumb is to compute the resistance at the maximum temperature allowed by the winding insulation class.

The 3D array of the torque presents is computed as follows:

$$[\boldsymbol{\tau}] = \frac{3}{2} \cdot p \cdot ([\boldsymbol{\Lambda}_\mathrm{d}] \odot [\boldsymbol{I}_\mathrm{q}] - [\boldsymbol{\Lambda}_\mathrm{q}] \odot [\boldsymbol{I}_\mathrm{d}]) \tag{13.13}$$

it is worth noticing that, according to the adopted indices meaning, the i-th layer of $[\boldsymbol{\tau}]$ presents all the elements equal to $\tau^{(i)}$.

The mechanical power is given by:

$$[\boldsymbol{P}_\mathrm{m}] = [\boldsymbol{\tau}] \odot [\boldsymbol{\omega}_\mathrm{m}] \tag{13.14}$$

while the efficiency is:

$$[\boldsymbol{\eta}] = \frac{[\boldsymbol{P}_\mathrm{m}]}{[\boldsymbol{P}_\mathrm{m}] + [\boldsymbol{P}_\mathrm{J}] + [\boldsymbol{P}_\mathrm{Fe}]} \tag{13.15}$$

The terminal voltage components and the total current have to be computed. Their computation depends on how the iron losses equivalent resistance is connected to the standard *dq* electric model of the machine. In general, the iron losses resistance can be connected in parallel with the machine terminals or in series with the machine impedance as reported in Figure 13.5(a) and Figure 13.5(b), respectively.

For parallel and series connection, the equations are:

$$\text{parallel:} \begin{cases} U_\mathrm{d} = U'_\mathrm{d} \\ U_\mathrm{q} = U'_\mathrm{q} \\ I_\mathrm{Fe} = \frac{P_\mathrm{Fe}}{\sqrt{U_\mathrm{d}^2 + U_\mathrm{q}^2}} \\ I_\mathrm{d} = I'_\mathrm{d} + I_\mathrm{Fe} \\ I_\mathrm{q} = I'_\mathrm{q} + I_\mathrm{Fe} \end{cases} \qquad \text{series:} \begin{cases} I_\mathrm{d} = I'_\mathrm{d} \\ I_\mathrm{q} = I'_\mathrm{q} \\ U_\mathrm{Fe} = \frac{P_\mathrm{Fe}}{\sqrt{I_\mathrm{d}^2 + I_\mathrm{q}^2}} \\ U_\mathrm{d} = U'_\mathrm{d} + U_\mathrm{Fe} \\ U_\mathrm{q} = U'_\mathrm{q} + U_\mathrm{Fe} \end{cases} \tag{13.16}$$

where U'_d and U'_q are the inner voltage *dq* components given by:

$$\begin{cases} U_\mathrm{d} = R_\mathrm{w} I_\mathrm{d} - p \omega_\mathrm{m} \Lambda_\mathrm{q} \\ U_\mathrm{q} = R_\mathrm{w} I_\mathrm{q} + p \omega_\mathrm{m} \Lambda_\mathrm{d} \end{cases} \tag{13.17}$$

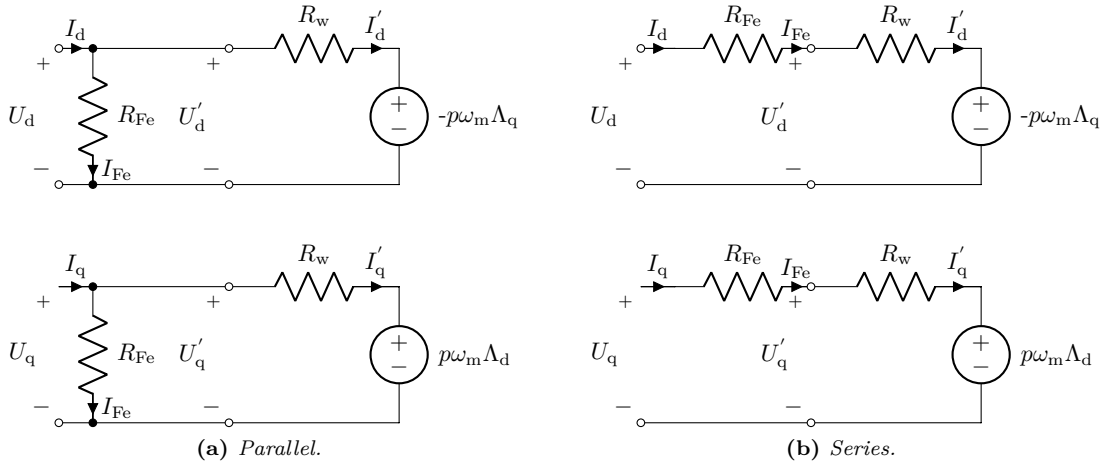

(a) *Parallel.* **(b)** *Series.*

Figure 13.5: *dq* electric model of the machine with different connection of the iron losses resistance.

Setting $[\boldsymbol{I}_\mathrm{d}]$, $[\boldsymbol{I}_\mathrm{q}]$, $[\boldsymbol{P}_\mathrm{hy}]$ and $[\boldsymbol{P}_\mathrm{ec}]$ in (13.16), it results the 3D arrays $[\boldsymbol{U}_\mathrm{d}]$ and $[\boldsymbol{U}_\mathrm{q}]$ while the voltage amplitude is given by:

$$[\boldsymbol{U}] = \sqrt{[\boldsymbol{U}_\mathrm{d}]^2 + [\boldsymbol{U}_\mathrm{q}]^2} \tag{13.18}$$

At this point, the element indices of $[\boldsymbol{U}]$ and $[\boldsymbol{I}]$ that are not compatible with the voltage and current limits are found. Then, the corresponding elements in all the previously computed matrices are replaced by `NaN` in order to exclude these elements from the maximum efficiency computation.

13.7 Maximum efficiency computation

Thanks to the matrix indexing order adopted, it is possible to observe that the j-th column of the i-th layer of $[\boldsymbol{\eta}]$ contains the efficiencies computed for all the current combinations relative to $\tau^{(i)}$ at the speed $\omega_\mathrm{m}^{(j)}$. This means that, the maximum efficiency of the j-th column and i-th layer represents a point of the efficiency map, in the torque versus speed plane, whose coordinates are $\omega_\mathrm{m}^{(j)}$ and $\tau^{(i)}$. Furthermore, the set of column maximum efficiencies of the i-th layer is a row of the efficiency map corresponding to the torque $\tau^{(i)}$. So, applying the function **maxcol** for each layer of $[\boldsymbol{\eta}]$ it results the complete efficiency map, $\widehat{\boldsymbol{\eta}}$, as shown in Figure 13.6.

All the other quantities, indicated with the hat symbol, can be obtained selecting the elements which corresponds to the maximum efficiency position. For example, the i-th row and j-th column of the matrix $\widehat{\boldsymbol{P}_\mathrm{J}}$ will contain the joule losses computed at the speed $\omega_\mathrm{m}^{(j)}$ and torque $\tau^{(i)}$ obtained with the current-voltage combination which yield the maximum efficiency $\widehat{\boldsymbol{\eta}}(i,j)$.

The same approach can be carried out for the IM with the addition of the rotor slip and joule losses. Their computation is beyond the target of the present thesis but it is described in detail in [159, 160].

13.8 Efficiency map including thermal limit

The proposed efficiency map algorithm can be further improved taking into account the thermal limit and resistance variation with the temperature. As usual, the performance are computed at steady state condition.

It is worth noticing that the resistance dependence on the temperature affects the joule losses computation as well as the terminal voltage computation by means of (13.12) and (13.17), respectively. The influence of the core temperature on the eddy current losses is not considered. Also the temperature effect on the PMs is neglected.

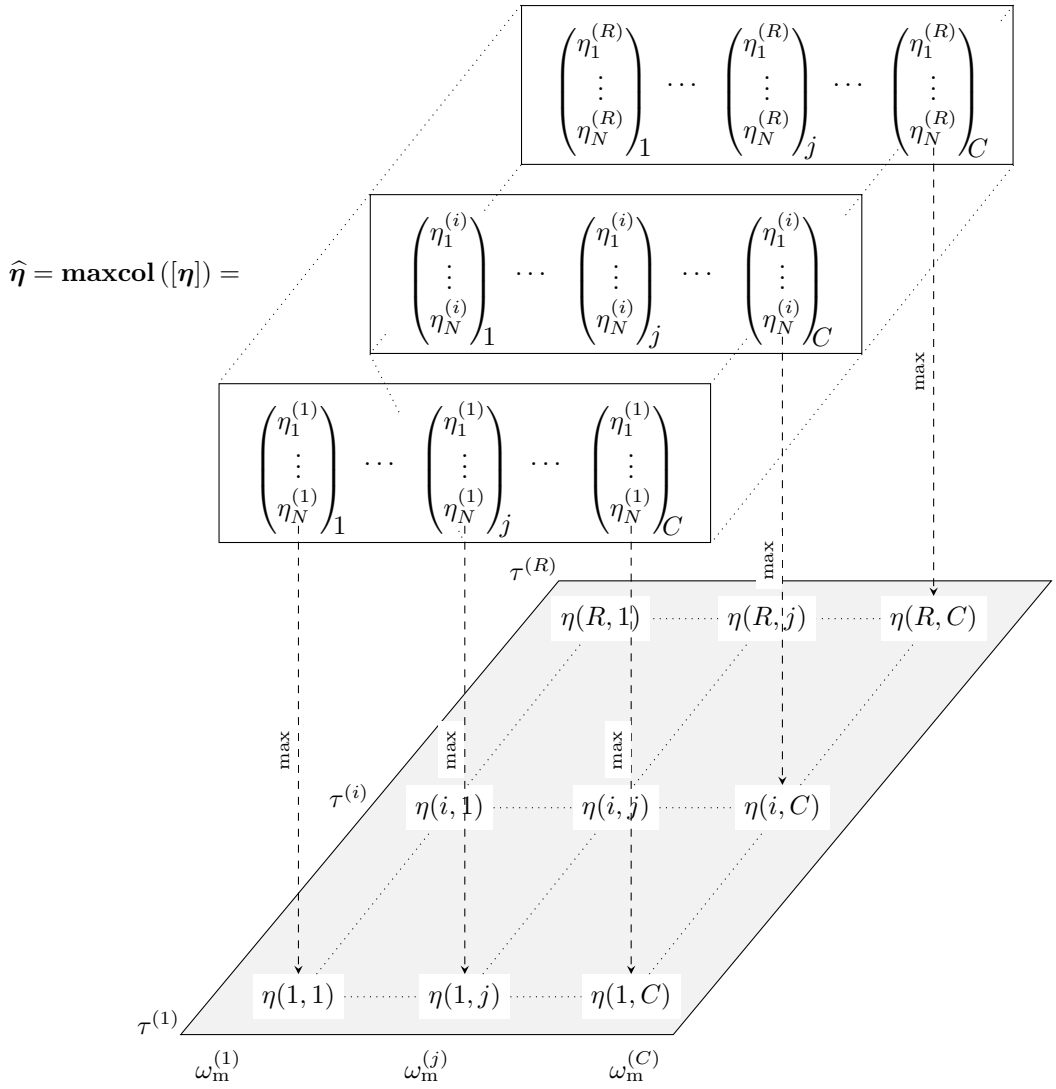

Figure 13.6: Scheme for the computation of the maximum efficiency from the 3D array $[\boldsymbol{\eta}]$. The function **maxcol** returns the maximum of each column.

13.8.1 Efficiency map at different temperature

On the basis of the iron and joule losses maps computed in (13.11) and (13.12) it is possible to estimate the actual winding temperature by means of a thermal analysis. Such analysis can be carried out by means of a lumped parameters network [161] or FE analysis. In any cases, the actual winding temperature, T_{w}, is described by the following relationship:

$$T_{\mathrm{w}} = T_{\mathrm{w}}\left(P_{\mathrm{J}}(\widetilde{T_{\mathrm{w}}}), P_{\mathrm{hy}}(\omega_{\mathrm{m}}), P_{\mathrm{ec}}(\omega_{\mathrm{m}}^2)\right) \tag{13.19}$$

where $\widetilde{T}$ is the assumed winding temperature used for the resistance computation.

Let's first define the assumed winding temperature vector:

$$\widetilde{T_{\mathrm{w}}} = \left(\widetilde{T_{\mathrm{w}}}^{(1)}, \widetilde{T_{\mathrm{w}}}^{(2)}, \ldots, \widetilde{T_{\mathrm{w}}}^{(M)}\right) \tag{13.20}$$

where $\widetilde{T_{\mathrm{w}}}^{(1)}$ and $\widetilde{T_{\mathrm{w}}}^{(M)}$ can be set equal to the environment temperature (i.e. 20 °C) and the maximum insulation class temperature, respectively.

For each element of $\widetilde{T_{\mathrm{w}}}$ it is possible to compute the joule losses and efficiency maps by means of (13.12) and (13.15) obtaining the 3D arrays reported in Figure 13.7. Since the iron losses do not depend on the temperature, the matrices $\widehat{\boldsymbol{P}_{\mathrm{hy}}}$ and $\widehat{\boldsymbol{P}_{\mathrm{ec}}}$ can be replicated M times along the third dimension obtaining $[\widehat{\boldsymbol{P}_{\mathrm{hy}}}]$ and $[\widehat{\boldsymbol{P}_{\mathrm{ec}}}]$.

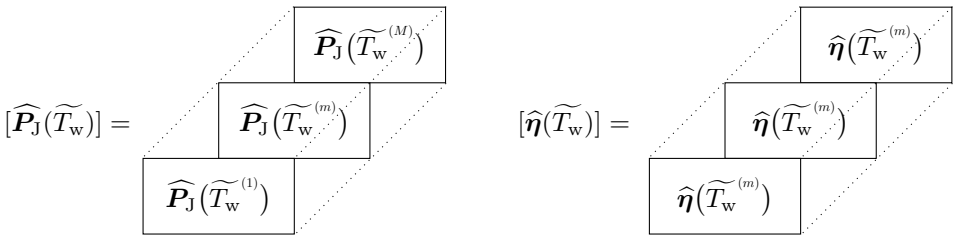

Figure 13.7: Efficiency and joule losses 3D maps computed for different winding temperature.

13.8.2 Thermal analysis

Once the losses maps are know, it is possible to perform a thermal analysis for each of their element. In particular, the joule and iron losses are set as heat source in the thermal model. This computation provides M different winding temperature matrices as shown in Figure 13.8. In particular, the i-th row, j-th column and m-th layer of the matrix $[\widehat{\boldsymbol{T}_{\mathrm{w}}}]$ contains the winding temperature obtained at the speed $\omega_{\mathrm{m}}^{(j)}$ and torque $\tau^{(i)}$ with an assumed winding temperature of $\widetilde{T_{\mathrm{w}}}^{(m)}$. All the elements that presents a value higher than the maximum allowed temperature are replaced by a NaN value since they do no represent a valid steady state solution.

It is worth noticing that, after a preliminary estimation of the maximum iron and joule losses, it is possible to carry out the thermal analyses separately from the electromagnetic ones so that their computational time is not altered. Furthermore, for a given electromagnetic map, it is possible to couple different thermal analyses with different material properties (e.g. material conductivity), boundary conditions (e.g. heat exchange), computational accuracy (2D or 3D FE analysis or CFD analysis) and other settings.

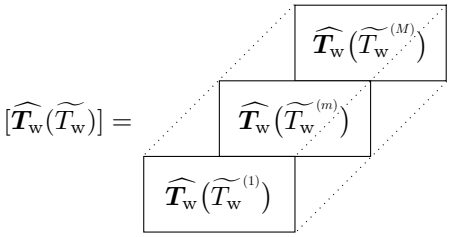

Figure 13.8: Winding losses 3D matrix obtained from the thermal analysis.

The m-th layer of the $[\widehat{\boldsymbol{T}_{\mathrm{w}}}(\widetilde{T_{\mathrm{w}}})]$ is shown qualitatively in the bottom right $\omega_{\mathrm{m}} - \tau$ plane in Figure 13.9. Among the map elements, only the ones that belongs to the constant winding temperature locus $\widehat{T_{\mathrm{w}}}^{(m)}$ are computed correctly since the actual winding temperature is equal to the assumed one $\widetilde{T_{\mathrm{w}}}^{(m)}$. The efficiency of each of this nodes is then computed interpolating the relative efficiency map layer $\widehat{\boldsymbol{\eta}}(\widetilde{T_{\mathrm{w}}}^{(m)})$ and finally, only these nodes are stored for the final efficiency map assembling. The M-th layer of the matrix $[\widehat{\boldsymbol{T}_{\mathrm{w}}}(\widetilde{T_{\mathrm{w}}})]$ refers to the maximum allowed temperature. The nodes that belongs to the constant winding temperature locus $\widehat{T_{\mathrm{w}}}^{(M)}$ describes the maximum thermal limit hence it delimits the actual $\omega_{\mathrm{m}} - \tau$ plane that can be effectively used at steady state condition.

Repeating such a procedure for each layer of $[\widehat{\boldsymbol{T}_{\mathrm{w}}}(\widetilde{T_{\mathrm{w}}})]$, it results the correct efficiency map $\widehat{\boldsymbol{\eta}^*}$ shows qualitatively on the right of Figure 13.9. It is possible to see that the efficiency maps is

different from the estimated one and the actual maximum torque is lower than the one provided by the voltage and current limits.

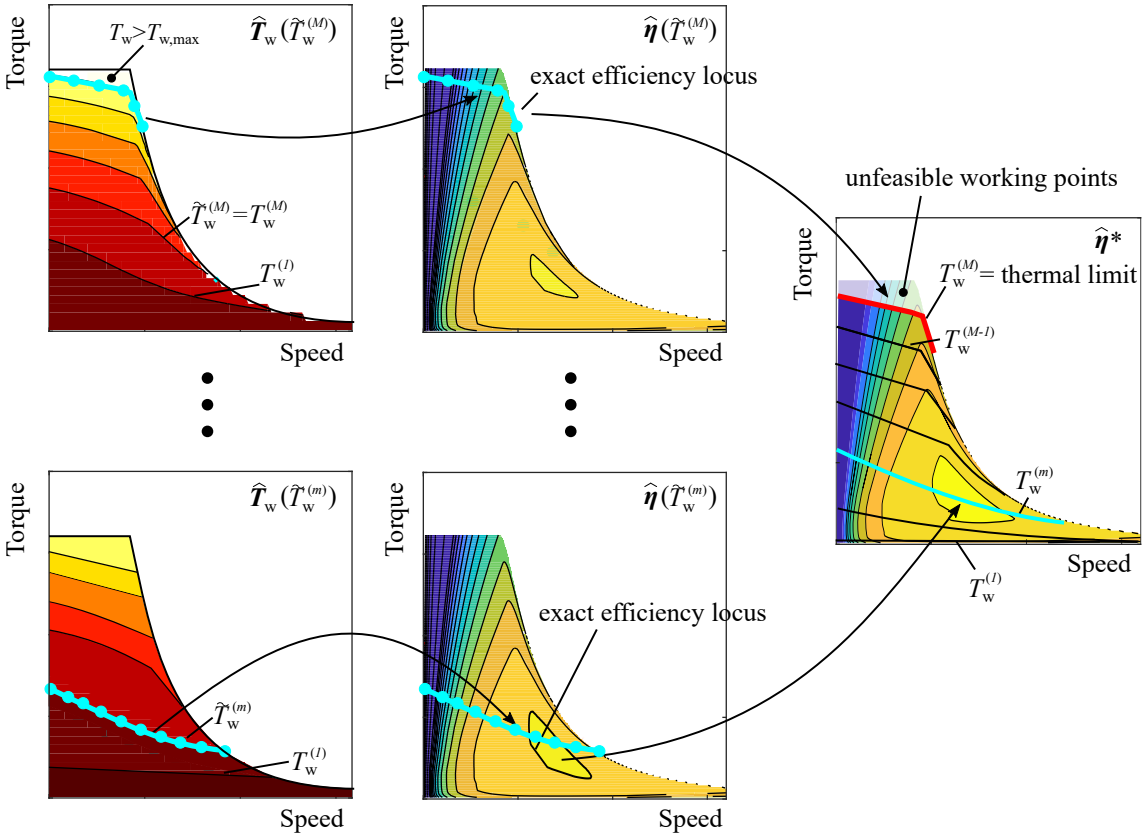

Figure 13.9: Proposed procedure for the identification of the thermal limits.

Chapter 14

Structural analysis with GetDP

14.1 Brief presentation of GetDP

GetDP is a free open-source scientific software for the numerical solution of integro-differential equations [162, 163]. Its name is the acronym of *General environment for the treatment of Discrete Problems*. The main features of GetDP are:

- It can deal with one-dimensional models (1D), two-dimensional models (2D), plane and axisymmetric three-dimensional models (3D)
- It deals with different problem time states such as static, transient, harmonic and eigenvalue value
- It allows to select several numerical methods for the problem solutions (e.g. finite element, boundary element and volume integral methods)
- It allows to solve coupled physical models involving electromagnetic phenomena (e.g. magnetostatics, magnetodynamics, wave propagation, lumped electric circuits), acoustic phenomena, thermal phenomena and mechanical phenomena (elasticity, rigid body movement)
- It can be controlled by command prompt and can run dedicated script written in ASCII data file
- The problem definition syntax is very close to the symbolic mathematical expressions

Figure 14.1 shows some examples of the problems that GetDP can handle.

14.2 Mathematical formulation for structural analysis

The structural analysis of a body is based on the linear elasticity model. The latter, describes the deformation and inner stress that occurs in a solid body when a determined load condition is applied. The adjective *linear* specifies that the deformation (or strain) are infinitesimal and there is a linear relationship between the stress components and strain. A further assumption adopted in the following is that the body is *isotropic* which means that its constitutive laws are independent from the reference frame used to indicate the stress components. Such analysis is selected since it suits with the characteristic of a SyR lamination.

14.2.1 Basic equations

The basic equations that describe a linear elasticity model are: the equation of motion, the strain displacement equations and the constitutive equations [164, 165].

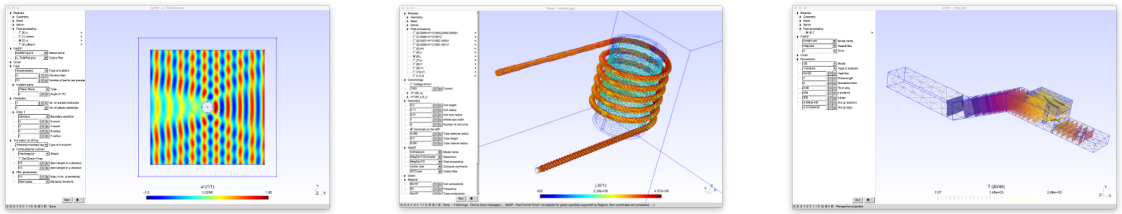

(a) *Acustic scattering.* **(b)** *Magneto-thermal model.* **(c)** *Thermal conduction.*

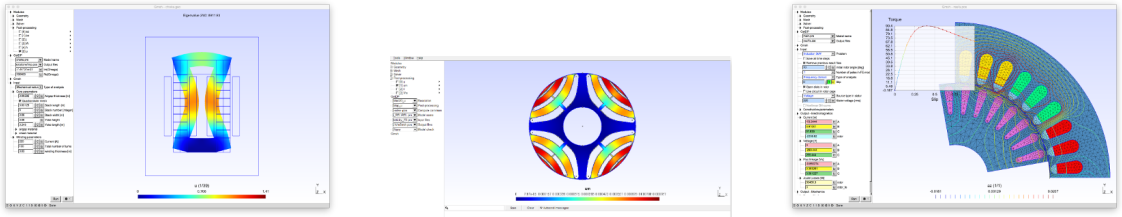

(d) *Magnetostriction.* **(e)** *Structural analysis.* **(f)** *Electric machines.*

Figure 14.1: Examples of geometries and problems that can be analyzed with GetDP.

Equation of motion

The equation of motion represents the dynamic equilibrium of the body and is expressed as follows:

$$\nabla \cdot \boldsymbol{\sigma} + \boldsymbol{F} = \rho \frac{\mathrm{d}^2 \boldsymbol{u}}{\mathrm{d}t^2} \tag{14.1}$$

where $\boldsymbol{\sigma}$ is the Cauchy stress tensor, $\boldsymbol{F}$ is the body force per unit, ρ is the mass density, $\boldsymbol{u}$ is the displacement vector and t is the time. The last term is null since the structural problem are time independent. $\boldsymbol{\sigma}$ is a tensor which contains the nine components of the state stress classified as *normal*, σ, and *tangential*, τ:

$$\boldsymbol{\sigma} = \begin{bmatrix} \sigma_{11} & \sigma_{12} & \sigma_{13} \\ \sigma_{21} & \sigma_{22} & \sigma_{23} \\ \sigma_{31} & \sigma_{32} & \sigma_{33} \end{bmatrix} = \begin{bmatrix} \sigma_x & \tau_{xy} & \tau_{xz} \\ \tau_{yx} & \sigma_y & \tau_{yz} \\ \tau_{zx} & \tau_{zy} & \sigma_z \end{bmatrix} \tag{14.2}$$

thanks to the symmetry property, $\boldsymbol{\sigma} = \boldsymbol{\sigma}^{\mathrm{T}}$, the number of distinct stress components is six. The SI unit is $\mathrm{N/m^2}$ however, the MPa is usually adopted in engineering.

Strain-displacement equation

As the name suggests, this equation relates the infinitesimal strain tensor, $\boldsymbol{\varepsilon}$ to the displacement vector, $\boldsymbol{u}$. The expression of $\boldsymbol{\varepsilon}$ is:

$$\boldsymbol{\varepsilon} = \begin{bmatrix} \varepsilon_{11} & \varepsilon_{12} & \varepsilon_{13} \\ \varepsilon_{21} & \varepsilon_{22} & \varepsilon_{23} \\ \varepsilon_{31} & \varepsilon_{32} & \varepsilon_{33} \end{bmatrix} \qquad \text{with} \qquad \varepsilon_{ij} = \frac{1}{2}\left(\frac{\mathrm{d}u_i}{\mathrm{d}x_j} + \frac{\mathrm{d}u_j}{\mathrm{d}x_i}\right) \qquad i,j = 1,2,3 \tag{14.3}$$

the diagonal contains the *normal* strains while the left elements are the *shear* strains. By definition, $\boldsymbol{\varepsilon}$ is symmetric so that there are only six distinct share components. The (14.3) can be written in the following differential form:

$$\boldsymbol{\varepsilon} = \frac{1}{2}\left[\nabla \boldsymbol{u} + (\nabla \boldsymbol{u})^{\mathrm{T}}\right] \tag{14.4}$$

Constitutive law

The constitutive law that relates the stresses and strains of a continuous elastic material is the Hooke's law expressed as follows:

$$\begin{bmatrix}\sigma_{11}\\ \sigma_{22}\\ \sigma_{33}\\ \sigma_{23}\\ \sigma_{13}\\ \sigma_{12}\end{bmatrix} = \frac{E}{(1+\nu)(1-2\nu)} \begin{bmatrix}1-\nu & \nu & \nu & 0 & 0 & 0\\ \nu & 1-\nu & \nu & 0 & 0 & 0\\ \nu & \nu & 1-\nu & 0 & 0 & 0\\ 0 & 0 & 0 & \frac{1-2\nu}{2} & 0 & 0\\ 0 & 0 & 0 & 0 & \frac{1-2\nu}{2} & 0\\ 0 & 0 & 0 & 0 & 0 & \frac{1-2\nu}{2}\end{bmatrix} \begin{bmatrix}\varepsilon_{11}\\ \varepsilon_{22}\\ \varepsilon_{33}\\ 2\varepsilon_{23}\\ 2\varepsilon_{13}\\ 2\varepsilon_{12}\end{bmatrix} \tag{14.5}$$

where E is the Young's modulus and ν is the Poisson's ratio. In case of plane stress conditions, it is verified that:

$$\sigma_{31} = \sigma_{13} = \sigma_{32} = \sigma_{23} = \sigma_{33} = 0 \tag{14.6}$$

so that, it results:

$$\begin{bmatrix}\sigma_{11}\\ \sigma_{22}\\ \sigma_{12}\end{bmatrix} = \frac{E}{1-\nu^2} \begin{bmatrix}1 & \nu & 0\\ \nu & 1 & 0\\ 0 & 0 & \frac{1-\nu}{2}\end{bmatrix} \begin{bmatrix}\varepsilon_{11}\\ \varepsilon_{22}\\ 2\varepsilon_{12}\end{bmatrix} \tag{14.7}$$

Some basic applications of the linear elasticity model are solved with GetDP in the following. The results reliability is confirmed by the analytical solutions. Finally, a complete example of the procedure adopted to analyze a SyR rotor is presented.

14.3 Cantilever beam with single load at the end

The cantilever beam represents one of the simplest body to test the linear elasticity equations. In this case, it is clamped at one end while a force, $\boldsymbol{F} = 100\,\mathrm{N}$, is applied to the other extreme, as shown in Figure 14.2. The beam dimensions and the material properties are reported in Table 14.1.

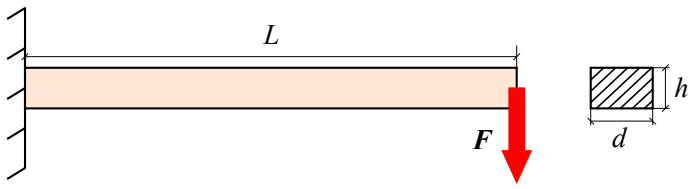

Figure 14.2: Cantilever beam with single load at the end.

14.3.1 Analytical solution

The beam moment of inertia is [166]:

$$J = \frac{1}{12}\, w\, d = \frac{10^6}{12}\mathrm{mm}^4 \tag{14.8}$$

the the maximum deflection at the loaded extreme is:

$$u_{\max} = \frac{1}{3}\,\frac{F\,L^3}{E\,J} = 1.9\,\mu\mathrm{m} \tag{14.9}$$

the maximum bending stress is given by:

$$\sigma_x = \frac{6\,F\,L}{d\,h} = 6 \times 10^5\,\mathrm{Pa} \tag{14.10}$$

while the maximum shear stress is:

$$\tau_{xy} = \frac{3}{2}\,\frac{F}{d\,h} = 1.5 \times 10^4\,\mathrm{Pa} \tag{14.11}$$

finally, the Von Mises stress is:

$$\sigma_{\text{vm}} = \sqrt{\sigma_x^2 + 3\tau_{xy}^2} \approx 6 \times 10^5 \,\text{Pa} \tag{14.12}$$

Table 14.1: Beam dimensione and material properties.

NAME	SYMBOL	VALUE
Beam length	L	100 mm
Beam height	h	10 mm
Beam deep	d	1000 mm
Young's modulus	E	210 MPa
Poisson's ratio	ν	0.3

14.3.2 GetDP solution

Problem data

The file `data.pro` contains the model dimensions, the physical group labels, the material properties and the force amplitude and. It is called both in pre- and post-processing by Gmsh and GetDP, respectively. Its content is reported in Listing 14.1.

Listing 14.1: File `data.pro`.

```
// beam dimensions
unit = 1e-3;
L = 100*unit; // length (m)
h = 10*unit; // height (m)
lc = 1*unit; // characteristic length (m)
// physical labels
beam = 100;
left = 10;
bottom = 20;
right = 30;
top = 40;
// material properties
E = 210e9; // Young's modulus (Pa)
v = 0.3; // Poisson's ratio (-)
// force amplitude
Load = 100/h; // (N)
```

Model creation

The geometry creation and the assignation of the physical groups (necessary to GetDP) have been done with Gmsh [167]. Then physical group names are reported in Figure 14.3. The left segment, labeled as `'left'`, is used to assign the boundary conditions $u_x = 0$ and $u_y = 0$, the right segment, labeled as `'right'` is used to assign the concentrated force F while the beam area is used to set the material properties E and ν and to define the region in which apply (14.7). The Gmsh code (saved in a `.geo` text file) to draw the beam geometry is reported in Listing 14.2.

Listing 14.2: Gmsh code (`.geo`) to draw the beam geometry and assign the physical groups.

```
Include "data.pro";

// add points
Point(1) = {0,0,0,lc};
Point(2) = {L,0,0,lc};
```

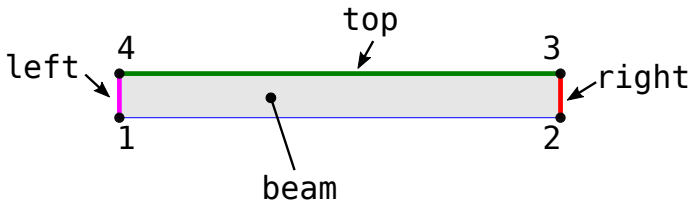

Figure 14.3: Beam geometry and physical group names.

```
Point(3) = {L,h,0,lc};
Point(4) = {0,h,0,lc};
Line(1) = {1, 2};
Line(2) = {2, 3};
Line(3) = {3, 4};
Line(4) = {4, 1};

// create beam surface
Line Loop(5) = {3, 4, 1, 2};
Plane Surface(6) = {5};

// assign physical groups
Physical Surface(beam) = {6};
Physical Line("left", left) = {4};
Physical Line("bottom", bottom) = {1};
Physical Line("right", right) = {2};
Physical Line("top", top) = {3};
```

Groups, materials and boundary condition properties

The GetDP code (saved in a `.pro` text file) to define the group, the material properties and the boundary conditions is reported in Listing 14.3.

After the creation of the geometry is necessary to define the material properties, the boundary conditions and assign them to the proper physical group. Firstly, the group relatives to the beam area, the clamped segment and the load segment are declared. It is worth noticing that the force is distributed along the right segment. For this reason it is defined as F/h in the file `data.pro`.

Then, the beam material is described by (14.7) and it is assigned to the group `beam` while the force is defined with only the y component and it is applied to the group `load`.

After that, the boundary conditions `DeplacementX` and `DeplacementY` are declared within the `Constraint` field. They are assigned to the groups `fixed` with the value `0`.

Finally, the formulation file `Elasticity_2D.pro`, reported in Appendix 15.3.5, is invoked and the problem is solved. Some post-processing operations on the resulting $\boldsymbol{u}$ field are performed to get the Force field and the Von Mises stress.

Listing 14.3: GetDP code (`.pro`) to set the model groups, the material properties and the boundary conditions to the cantilever beam model.

```
Include "data.pro"; // load physical group labels

// define the model groups
Group{
  beam = Region[{beam}]; // beam region
  fixed = Region[{left}]; // clamped side
  load = Region[{right}]; // loaded side

  Domain_Force_Sur = Region[ { } ];
  Domain_Force_Lin = Region[ {load} ];
  Domain_Force     = Region[ {Domain_Force_Sur , Domain_Force_Lin}];
  Domain_Disp      = Region[ {beam} ];
```

```
}

Function{
  // set the beam material function property
  C_m[ beam ] = E/(1-v^2)*TensorSym[ 1,   v,    0,
  1,    0,
  (1-v)/2 ];

  // apply Force on group 'load'
  F[load] = Load*Vector[0,-1,0];
}

// Define boundary conditions
Constraint{
  // d ux = 0
  { Name DeplacementX ; Type Assign ;
    Case {
      { Region fixed; Value 0 ; }
    }
  }
  // d uy = 0
  { Name DeplacementY ; Type Assign ;
    Case {
      { Region fixed; Value 0 ; }
    }
  }
}

// load the formulation
Include "Elasticity_2D.pro"

// post processing operations
PostOperation Map_u UsingPost Mec2D_u {
  Print [ u,  OnElementsOf Domain_Disp, File "u.pos"] ; // displacement
  Print [ um, OnElementsOf Domain_Disp,  File "um.pos"] ; // displacement amplitude
  Print [ F,  OnElementsOf Domain_Force,  File "F.pos"] ; // load
  Print [ Vm , OnElementsOf Domain_Disp, File "Vm.pos"] ; // Von Mises stress
}
```

Remark on the GetDP formulation

The GetDP code relative to the elasticity model formulation is reported in Listing 14.4. Without describing in detail the GetDP syntax, it is possible to see that the (14.1) is applied to the group `Domain_disp` (i.e. the beam area) without the term $\boldsymbol{F}$. The latter is imposed to the group `Domain_force` that, in this example, is the left side of the beam.

Listing 14.4: GetDP formulation of the 2D elasticity problem.

```
Formulation{
  { Name Mec2D_u ; Type FemEquation ;
    Quantity {
      { Name u ; Type Local ; NameOfSpace H_u_Mec2D ; }
    }
    Equation {
      Galerkin { [ C_m[] * Dof{D1 u}, {D1 u} ] ;
        In Domain_Disp ; Jacobian Vol ; Integration GradGrad ; }
      Galerkin { [ -F[] , {u} ] ;
        In Domain_Force; Jacobian SurLinVol; Integration GradGrad; }
    }
  }
```

```
}
```

14.3.3 Results

The displacement plot and of the beam is shown in Figure 14.4(a). It is possible to see that the maximum deflection occurs on the right side and its amplitude is equal to the analytical one computed in (14.9). The Von Mises stress plot in Figure 14.4(b) shows that the maximum value is in good agreement with the analytical one and is near the clamped side of the beam. In fact, in that region the bending stress is higher and reach the maximum at the clamped side.

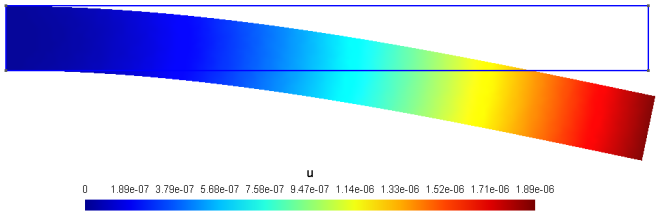

(a) *Displacement plot.*

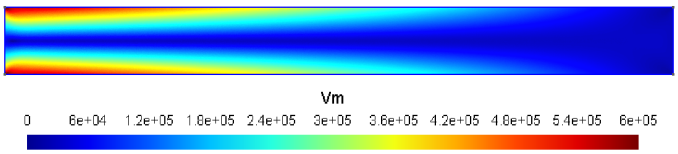

(b) *Von Mises plot.*

Figure 14.4: Resulting plots of the beam with single load at the end (the graphical displacement is amplified).

14.4 Cantilever beam with distributed load

In this case, the beam it is clamped at one end while a uniform distributed load, $\boldsymbol{q} = 1\,\mathrm{N/mm}$, is applied in vertical direction on top side as illustrated in Figure 14.2. The beam dimensions and the material properties are reported in Table 14.1.

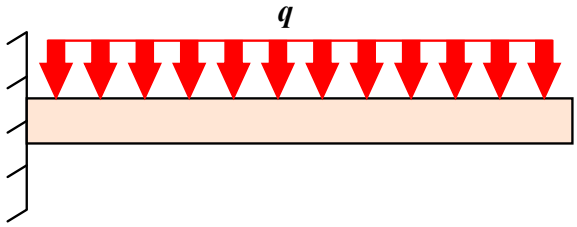

Figure 14.5: Cantilever beam with distributed load.

14.4.1 Analytical solution

The moment of inertia has been computed in (14.8). The maximum deflection is:

$$u_{\max} = \frac{1}{8}\frac{q\,L^4}{E\,J} = 0.71\,\mu\mathrm{m} \tag{14.13}$$

The maximum bending moment is:

$$M_{\max} = \frac{q\,L^2}{2} = 5\,\mathrm{Nmm} \tag{14.14}$$

hence, the relative stress is:

$$\sigma_x = \frac{6M_{\max}}{d\,h^2} = 3 \times 10^5\,\text{Pa} \tag{14.15}$$

the maximum shear is:

$$T_{\max} = q\,L = 100\,\text{N} \tag{14.16}$$

so, the relative stress has been already computed in (14.11). Finally, with (14.12), the Von Mises stress is $\sigma_{\text{vm}} \approx \sigma_x = 3 \times 10^5$ Pa.

14.4.2 GetDP solution

Code changes

Only few changes on the GetDP code of the previous example allows to solve the current one. The Gmsh code does not require any modification since the geometry is the same.

Firstly, the `Load` variable in the file `data.pro` has to be set to 1. Then, the region assigned to the group `load` has to be set to `top` to indicate that the load is applied on the top side (Figure 14.3) of the beam.

Listing 14.5: Setting of the group `load`.

```
// continue ...
load = Region[{top}]; // loaded side
// continue ...
```

Results

The displacement plot of the beam with uniform distributed load is shown in Figure 14.6(a). It can be see that the maximum deflection is 0.71 µm as predicted analytically by (14.13). Also the Von Mises plot in Figure 14.6(b) confirms the analytical results achieving a maximum stress value of 3×10^5 Pa.

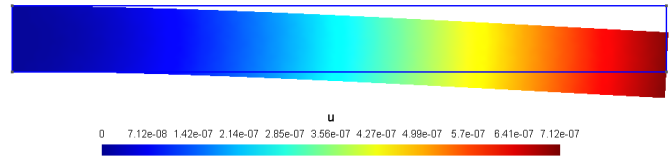

(a) *Displacement plot.*

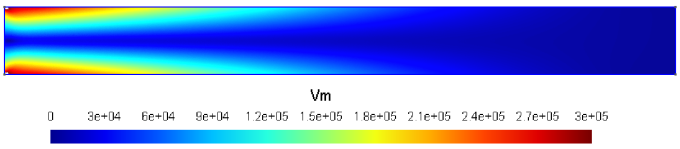

(b) *Von Mises plot.*

Figure 14.6: Resulting plots of the beam with distributed load on top (the graphical displacement is amplified).

14.5 Rotating hollow disk

The rotating hollow disk is a very simple structural problem whose behavior is similar to the more complex SyR rotor geometries. Furthermore, the displacement and stress can be computed analytically and so, it is possible to verify the GetDP results reliability.

The hollow disk, shown in Figure 14.7, rotates at speed n and presents a mass density ρ. The inner and outer diameter are free to move. The unique load is the centrifugal force due to the rotating disk mass. The main problem data are reported in Table 14.2.

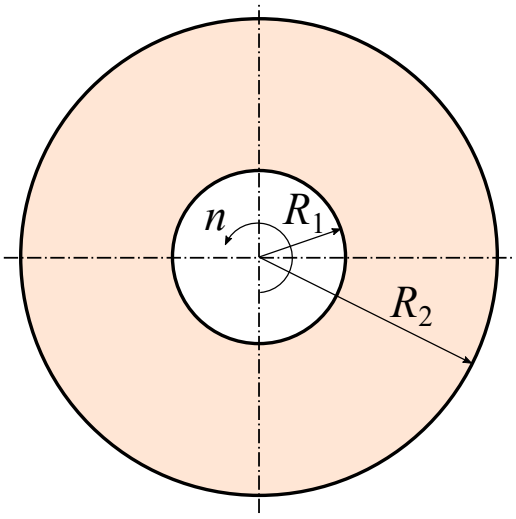

Figure 14.7: Hollow disk geometry.

Table 14.2: Hollow disk problem data.

Name	Symbol	Value
Beam length	L	100 mm
Outer radius	R_1	250 mm
Inner radius	R_2	100 mm
2 Angular speed	n	3000 rpm
Mass density	ρ	7800 kg/m^3
Young's modulus	E	210 MPa
Poisson's ratio	ν	0.3

14.5.1 Analytical solution

Since the geometry is axial symmetric, it is convenient to use the polar reference frame. In this way, the stress components are *radial*, σ_r and *tangential*, σ_t.

The analytical formulation of the stress components and displacement are [168, 169]:

$$\sigma_r(r) = \frac{3+\nu}{8}\,\rho\omega^2\left[R_1^2 + R_2^2 - r^2 - \left(\frac{R_1 R_2}{r}\right)^2\right] \tag{14.17}$$

$$\sigma_t(r) = \frac{3+\nu}{8}\,\rho\omega^2\left[R_1^2 + R_2^2 - \frac{1+3\nu}{3+\nu}\,r^2 + \left(\frac{R_1 R_2}{r}\right)^2\right] \tag{14.18}$$

$$u(r) = \frac{3+\nu}{8}\,\rho\omega^2\,\frac{1-\nu}{E}\,r\left[R_1^2 + R_2^2 - \frac{1+\nu}{3+\nu}\,r^2 + \frac{1+\nu}{1-\nu}\left(\frac{R_1 R_2}{r}\right)^2\right] \tag{14.19}$$

The radial stress is null for $r = R_1$ and $r = R_2$ and is maximum for $r^* = \sqrt{\frac{R_1}{R_2}}R_2 = 158.1\,\text{mm}$, which yields:

$$\sigma_{r,\max} = \sigma_r(r^*) = 7.15\,\text{MPa} \tag{14.20}$$

the maximum tangential stress occurs in the inner radius $r = R_1$:

$$\sigma_{t,\max} = \sigma_t(R_1) = 41.05\,\text{MPa} \tag{14.21}$$

while is minimum for $r = R_2$:

$$\sigma_{t,\min} = \sigma_t(R_2) = 14.77\,\text{MPa} \tag{14.22}$$

The maximum displacement occurs for $r = R_1$ and is:

$$u_{\max} = u(R_1) = 19.54\,\text{mm} \tag{14.23}$$

while is minimum for $r = R_2$:

$$u_{\min} = u(R_2) = 17.6\,\text{mm} \tag{14.24}$$

14.5.2 GetDP solution

Problem data

The main data of the problem are declared in the text file `data.pro` reported in Listing 14.6. In particular, it contains the models dimensions, the physical groups number, the material properties and the input angular speed.

Listing 14.6: File `data.pro` of the hollow disk problem.

```
// beam dimensions
unit = 1e-3;
R = 250*unit; // outer radius (m)
r = 100*unit; // inner radius (m)
cl = 2.5*unit; // characteristic length (m)
// physical labels
body = 100;
ux0 = 1001;
uy0 = 1002;
// material properties
MassDensity = 7800; // mass density (kg/m3)
E = 210e9; // Young's modulus (Pa)
v = 0.3; // Poisson's ratio (-)
// input
MechSpeedRPM = 3000; // angular speed (rpm)
```

Model creation

The Gmsh code to draw the model in Figure 14.8 is reported in Listing 14.7. The physical lines labeled as `ux0` and `uy0` are necessary to set the constraints $u_x = 0$ and $u_y = 0$, respectively. The physical surface of the model is labeled as `body`.

Listing 14.7: Gmsh code (`.geo`) to draw the hollow disk and assign the physical groups.

```
Include "data.pro";

Point(1) = {0, 0, 0, cl}; // disk center

// add outer circle points
Point(2) = {R, 0, 0, cl};
Point(3) = {0, R, 0, cl};
Point(4) = {-R, 0, 0, cl};
Point(5) = {0, -R, 0, cl};
// add outer circle arcs
Circle(1) = {2, 1, 3};
Circle(2) = {3, 1, 4};
Circle(3) = {4, 1, 5};
Circle(4) = {5, 1, 2};
// add inner circle points
Point(6) = {r, 0, 0, cl};
Point(7) = {0, r, 0, cl};
Point(8) = {-r, 0, 0, cl};
Point(9) = {0, -r, 0, cl};
// add inner circle arcs
```

```
Circle(5) = {6, 1, 7};
Circle(6) = {7, 1, 8};
Circle(7) = {8, 1, 9};
Circle(8) = {9, 1, 6};
// add lines for boundary conditions
Line(9) = {6, 2};
Line(10) = {7, 3};
Line(11) = {8, 4};
Line(12) = {9, 5};

// add disk surfaces
Line Loop(1) = {9, 1, -10, -5};
Plane Surface(1) = {1};
Line Loop(2) = {2, -11, -6, 10};
Plane Surface(2) = {2};
Line Loop(3) = {3, -12, -7, 11};
Plane Surface(3) = {3};
Line Loop(4) = {4, -9, -8, 12};
Plane Surface(4) = {4};

// assign physical groups
Physical Surface("body", body) = {1, 2, 3, 4};
Physical Line("uy=0", uy0) = {9, 11};
Physical Line("ux=0", ux0) = {12, 10};
```

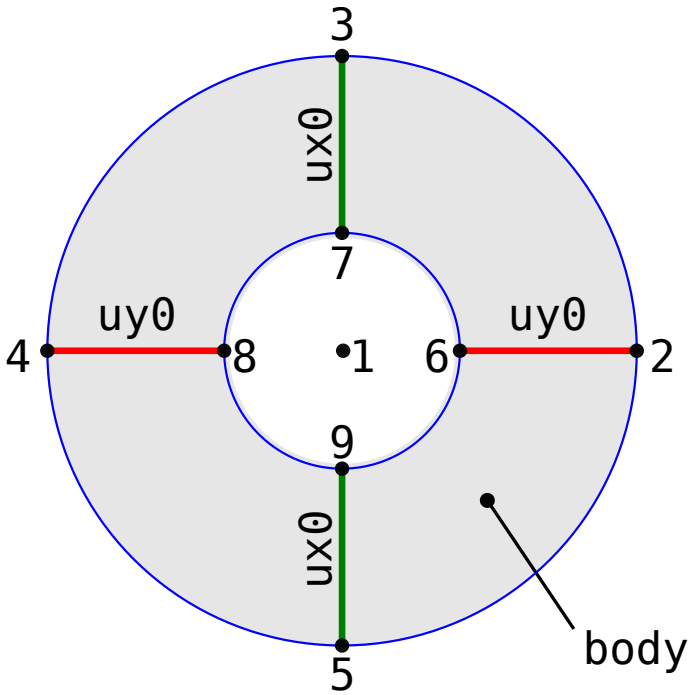

Figure 14.8: Hollow disk geometry and physical group names.

Groups, Functions and Constraints

In the first part of the GetDP code in Listing 14.8, the model groups, functions and constraints are defined. In particular, the disk region is assigned to the group `body` while the physical lines `ux0` and `uy0` are assigned to the homonym groups.

After that, the material behavior, described by (14.7) and the centrifugal force density are defined in the function model field. The centrifugal density force of the j-th mesh element is

computed as follows:

$$f = \omega^2 \, r_j \, \rho \tag{14.25}$$

where r_j is the radius of the j-th mesh element center of gravity, automatically computed by GetDP with the function `XYZ[]`.

A null horizontal displacement constraint is then assigned to the group `ux0`. Similarly, the null vertical displacement is set to the group `uy0`.

Then, the GetDP formulation is invoked and the problem is solved. It is worth noticing that the formulation code is that used for the cantilever beam problem.

At the end, some post-processing computation on the displacement field are performed to get the additional outputs.

Listing 14.8: GetDP code (`.pro`) to set the model groups, the material properties and the boundary conditions to the hollow disk model.

```
Include "data.pro";

// define the model groups
Group {
  body = Region[body];
  ux0 = Region[ux0];
  uy0 = Region[uy0];

  Domain_Force_Sur = Region[ {body } ];
  Domain_Force_Lin = Region[ {} ];
  Domain_Force     = Region[ {Domain_Force_Sur , Domain_Force_Lin}];
  Domain_Disp      = Region[ {body} ] ;
}

Function {
  // set the material behavior
  C_m[ disk ] = E/(1-v^2)*TensorSym[ 1,   v,    0,
  1,    0,
  (1-v)/2 ];
  // compute the speed
  omega  = 2*Pi*MechSpeedRPM/60; // angular speed (rad/s)
  rho[]  = MassDensity; // mass density (kg/m^3)
  // assign a radial centrifugal force for each element
  // its amplitude depends on the speed and element mass and distance from the center
  F[body] = omega^2 * XYZ[] * rho[] ; // centrifugal density force (N/m^3)
}

// set the constraints
Constraint{
  { Name DeplacementX ; Type Assign ;
    Case {
      { Region ux0; Value 0 ; }
    }
  }
  { Name DeplacementY ; Type Assign ;
    Case {
      { Region uy0; Value 0 ; }
    }
  }
}

// load the formulation
Include "Elasticity_2D.pro"

// post processing operations
PostOperation Map_u UsingPost Mec2D_u {
```

```
  Print [ u,  OnElementsOf Domain_Disp, File "u.pos"] ; // displacement
  Print [ um, OnElementsOf Domain_Disp,  File "um.pos"] ; // displacement amplitude
  Print [ F,  OnElementsOf Domain_Force,  File "F.pos"] ; // load
  Print [ Vm , OnElementsOf Domain_Disp, File "Vm.pos"] ; // Von Mises stress
}
```

Results

The displacement plot of the problem is reported in Figure 14.9(a). The displacement distribution and amplitude confirm the analytical results. In fact, at the inner and outer radius, the displacement is 19.5 mm and 17.6 mm, respectively.

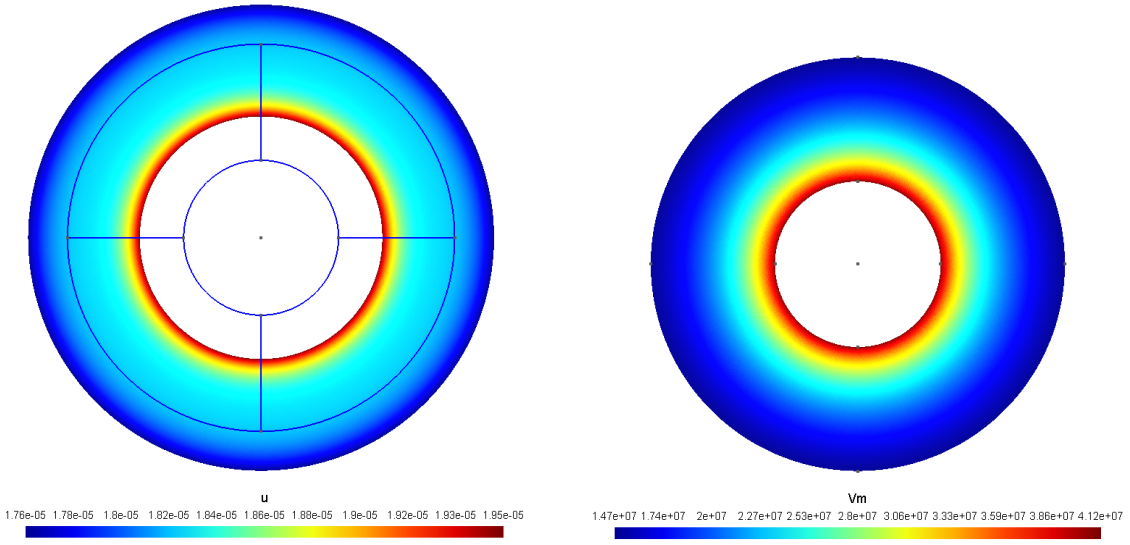

(a) *Displacement plot.* **(b)** *Von Mises plot.*

Figure 14.9: Resulting plots of the rotating hollow disk (the graphical displacement is amplified).

14.6 Rotating SyR rotor geometry

The FE structural analysis of a SyR rotor is similar to the hollow disk problem, the presence of the flux-barriers represents the only change. In this case, an exact analytical solution does not exist but, as described in Part I, only an estimation of the average stress in the radial rib regions is possible.

For these reason this section reports only few steps of the problem definition while the results validation and discussion are carried out in Part I.

The complete four poles SyR rotor geometry is reported in Figure 14.10(a). For simplicity, only the reduced one pole model is analyzed in the following. This reduces the model complexity and does not require any changes on the GetDP code in Listing 14.8. The main problem data are reported in chapter 6.

14.6.1 Model geometry

The rotor geometry is not drawn directly with the Gmsh code because of its complexity but is imported from a `dxf` file. The Gmsh model and the physical group names are reported in Figure 14.10(c).

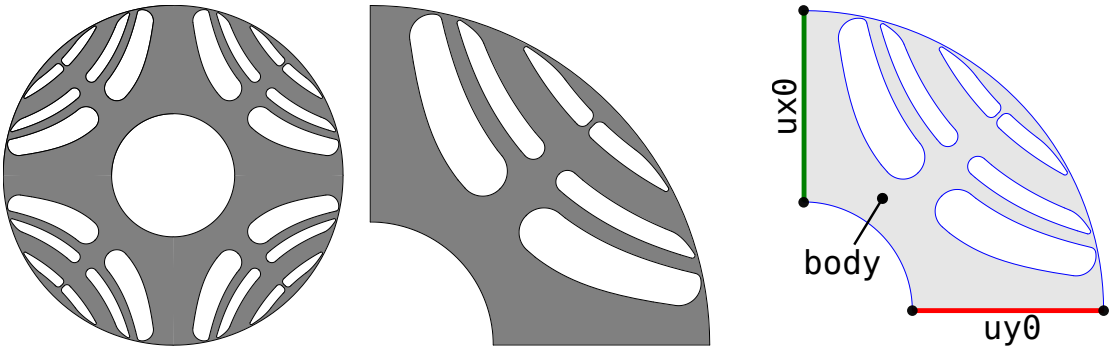

(a) *Complete model.* **(b)** *One-pole model.* **(c)** *Gmsh model.*

Figure 14.10: SyR rotor geometry sketches (a) and (b) and physical group names.

14.6.2 Results

The displacement and Von Mises plots of the SyR rotor structural analysis are shown in Figure 14.11(a) and Figure 14.11(b), respectively. As will be discussed in Part I, the maximum Von Mises stress within the radial ribs are in good agreement with the analytical estimation.

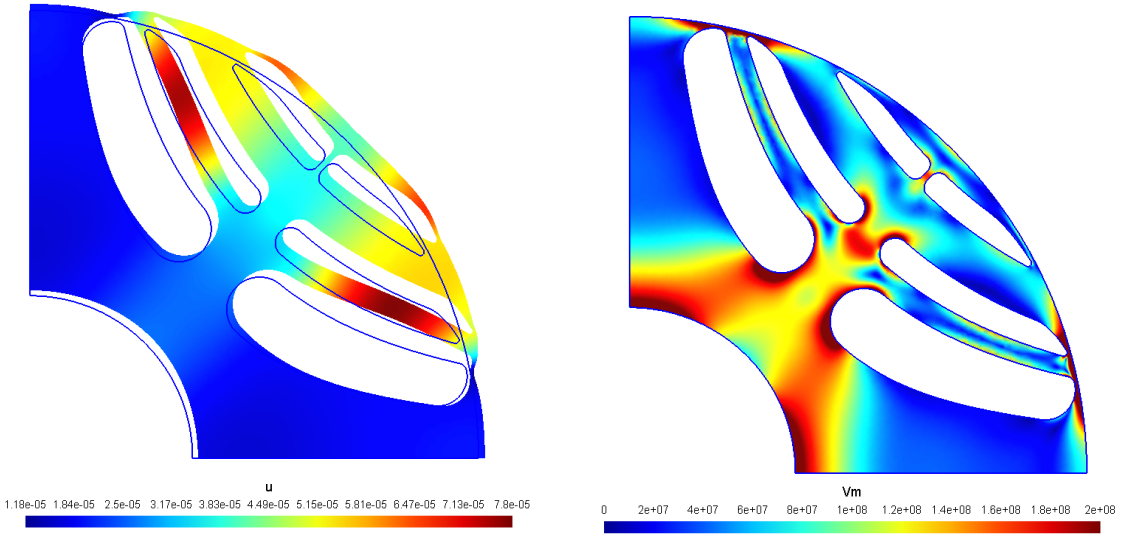

(a) *Displacement plot.* **(b)** *Von Mises plot.*

Figure 14.11: Resulting plots of the rotating SyR rotor (the graphical displacement is amplified).

Chapter 15

SyR rotor geometries

This chapter reports the design rules adopted to draw the different SyR rotor geometries of the present thesis.

At first, the *fluid* and *segmented* shaped flux-barriers rotor drawings are described. Then, a design methodology to choose the proper SyR rotor parameters is presented.

15.1 Fluid flux-barriers rotor

The criteria to draw the fluid flux-barriers is to align their edges to determined flux lines that would appear in the case of a d-axis magnetization of a solid rotor geometry [57]. The concept is clearly explained in Figure 15.1 which shows how the flux-barrier edges overlap the flux lines obtained with a solid rotor. This design strategy allows to minimize the d-axis flux lines distortion and effectively block the q-axis ones with beneficial effect on the rotor anisotropy.

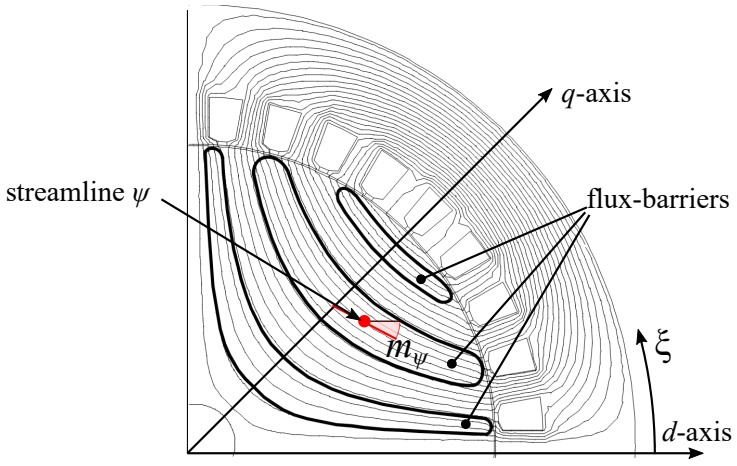

Figure 15.1: d-axis flux lines and relative flux-barriers geometry.

15.1.1 Streamline functions

Without considering iron saturation, a flux line trajectory of a generic solid rotor with $2p$ poles, also called *stream function* ψ, can be described analytically in polar coordinates by:

$$\psi(r,\xi) = \left(\frac{r^{2p} - R_{\text{sh}}^{2p}}{r^p R_{\text{sh}}^p} \right) \sin(p\xi) \tag{15.1}$$

where R_{sh} is the shaft radius and ξ is the angular coordinate from the d-axis [57, 170].

Alternatively, the radius, r, and the angular coordinate, ξ can be computed with the following equations:

$$r(\xi,\psi) = R_{\text{sh}} \sqrt[p]{\frac{\psi + \sqrt{\psi^2 + 4\sin^2(p\xi)}}{2\sin(p\xi)}} \tag{15.2}$$

$$\xi(r,\psi) = \frac{1}{p}\arcsin\left(\frac{\psi r^p R_{\text{sh}}^p}{r^{2p} - R_{\text{sh}}^{2p}}\right) \tag{15.3}$$

The components of the "speed" vector, tangential to streamline function ψ, are given by:

$$v_r(r,\xi) = p\left(r^{p-1} - \frac{R_{\text{sh}}^{2p}}{r^{p+1}}\right)\cos(p\xi) \tag{15.4}$$

$$v_\xi(r,\xi) = -p\left(r^{p-1} + \frac{R_{\text{sh}}^{2p}}{r^{p+1}}\right)\sin(p\xi) \tag{15.5}$$

which can be easily transformed in cartesian components as follows:

$$v_x = v_r\cos(\xi) - v_\xi\sin(\xi) \tag{15.6}$$

$$v_y = v_r\sin(\xi) + v_\xi\cos(\xi) \tag{15.7}$$

Finally, it is possible to compute the slope of a streamline in the point (x, y) by:

$$m_\psi(x,y) = \arctan\left(\frac{v_y}{v_x}\right) \tag{15.8}$$

15.1.2 Streamlines identification

As reported in Figure 15.2, the j-th flux-barrier is described by the streamline functions ψ_{Oj} and ψ_{Ij} which are the outer and inner flux-barrier edges, respectively. The value of these streamlines functions can be computed through (15.1) setting as radial coordinate the radii R_{Oj} and R_{Ij} and as angular coordinate the angle $\pi/(2p)$. A method to compute the midpoint flux-barrier radii is described in section 15.3 .

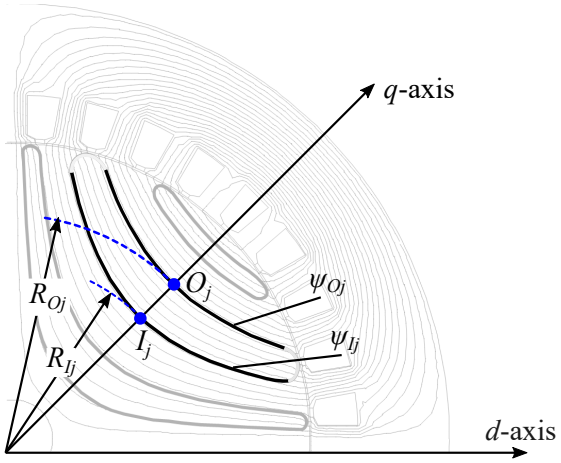

Figure 15.2: *d*-axis flux lines and relative flux-barriers geometry.

15.1.3 Flux-barrier end fillet

The coordinates of the point B_j in Figure 15.3 are given by:

$$\begin{cases} x_{Bj} &= \left(\frac{D_r}{2} - t_{\text{rib.t}}\right)\cos\left(\frac{\pi}{2p} - \xi\right) \\ y_{Bj} &= \left(\frac{D_r}{2} - t_{\text{rib.t}}\right)\sin\left(\frac{\pi}{2p} - \xi\right) \end{cases} \tag{15.9}$$

where $t_{\text{rib.t}}$ is the tangential rib thickness.

At this point, it possible to compute the center of the arc fillets which joint tangentially the flux-barrier edges to the point B_j. Figure 15.3 shows the computation of the outer fillet of the j-th flux-barrier. To draw the arc fillet it is necessary to know the flux-barrier joint point, A_{Oj} and the arc fillet center, C_{Oj}. To do that the following system of nonlinear equations has to be solved:

$$\begin{cases} x_{Aj} - r_{Aj}(\xi, \psi_{Oj})\cos(\xi_{Aj}) = 0 & \text{(15.10a)} \\ y_{Aj} - r_{Aj}(\xi, \psi_{Oj})\sin(\xi_{Aj}) = 0 & \text{(15.10b)} \\ \left(x_{Aj} - x_{C_{Oj}}\right)^2 + \left(y_{Aj} - y_{C_{Oj}}\right)^2 - r_{\text{f}}^2 = 0 & \text{(15.10c)} \\ \left(x_{Bj} - x_{C_{Oj}}\right)^2 + \left(y_{Bj} - y_{C_{Oj}}\right)^2 - r_{\text{f}}^2 = 0 & \text{(15.10d)} \\ \dfrac{y_{A_j} - y_{C_{Oj}}}{x_{A_j} - x_{C_{Oj}}} + \dfrac{1}{m_{\psi_{Oj}}} = 0 & \text{(15.10e)} \\ y_{COj} - \dfrac{y_{Bj}}{x_{Bj}} = 0 & \text{(15.10f)} \end{cases}$$

Eqns. (15.10a) and (15.10b) impose that the point A_j belong to the streamline ψ_{Oj}. Eqns. (15.10c) and (15.10d) set the distances between the joint points and the arc fillet center to be equal. Eqn. (15.10e) fixes the point C_{Oj} to lie on the straight line perpendicular to ψ_{Oj} honoring the point x_{Aj}. Eqn. (15.10f) fixes the point C_{Oj} to lie on the straight line which connect the origin to point B_j.

The same procedure applies for the computation of the arc fillet which joints the inner flux-barrier to the point B_j.

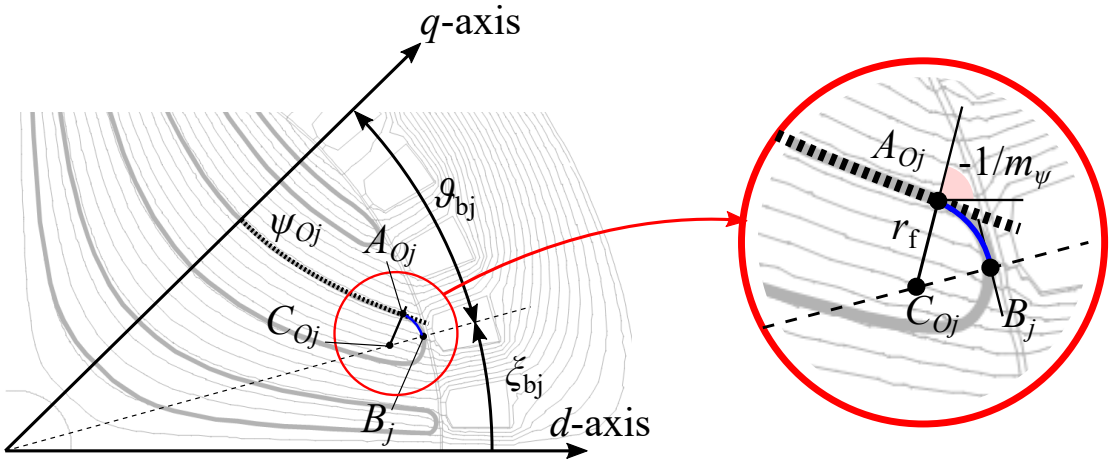

Figure 15.3: Computation of the fillet point of the j-th flux-barrier outer edge.

15.1.4 Radial ribs

The radial rib lateral sides lie on the straight line distant $t_{\text{rib}j}/2$ from the q-axis. The points M_j and N_j, in Figure 15.4, are the intersection between such a straight line and the two flux-barrier edges.

The point M_j, can be computed with the following system of equations:

$$\begin{cases} y_{Mj} - \tan\left(\dfrac{\pi}{2p}\right) x_{Mj} - \dfrac{t_{\mathrm{rib}j}}{2\cos\frac{\pi}{2p}} = 0 & \text{(15.11a)} \\ x_{Mj} - r_{Mj}(\xi, \psi_{Oj})\cos(\xi) = 0 & \text{(15.11b)} \\ y_{Mj} - r_{Mj}(\xi, \psi_{Oj})\sin(\xi) = 0 & \text{(15.11c)} \end{cases}$$

It is worth noticing that the space created for the radial ribs can be also used to draw a rectangular PM slot. This computation is not reported since it has not been used in the thesis.

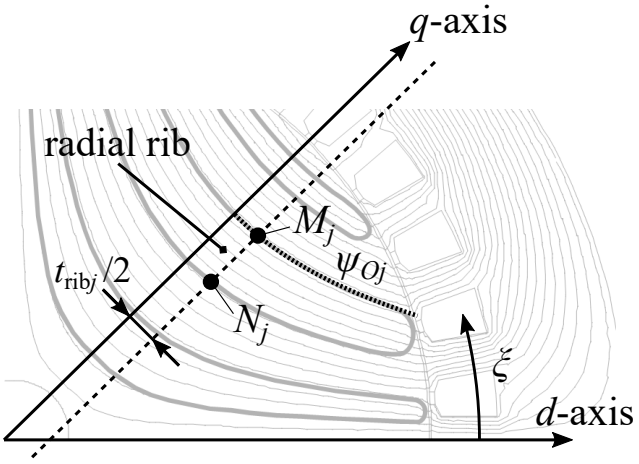

Figure 15.4: Computation of the radial rib of the j-th flux-barrier.

15.1.5 Automatic fluid flux-barrier drawing algorithm

The Algorithm 3 reports the pseudocode to draw a fluid flux-barriers rotor.

Algorithm 3 Fluid flux-barriers automatic drawing

Input: Rotor and shaft diameters: D_{r}, D_{sh}
Input: Tangential rib thickness: $t_{\mathrm{rib.t}}$
Input: Radial rib thicknesses: $t_{\mathrm{rib}1}, \ldots, t_{\mathrm{rib}N_{\mathrm{b}}}$
Input: Flux-barrier angles: $\vartheta_{\mathrm{b}1}, \ldots, \vartheta_{\mathrm{b}N_{\mathrm{b}}}$
Input: Middle flux-barrier outer radii: $R_{O1}, \ldots, R_{ON_{\mathrm{b}}}$
Input: Middle flux-barrier inner radii: $R_{I1}, \ldots, R_{IN_{\mathrm{b}}}$
  for $j = 1$ **To** N_{b} **do**
    Compute point B_j with (15.9)
    Compute outer streamline, $\psi_{Oj}(R_{Oj}, \frac{\pi}{2p})$ with (15.1)
    Compute inner streamline, $\psi_{Ij}(R_{OIj}, \frac{\pi}{2p})$ with (15.1)
    Compute inner and outer fillet joint points with system (15.10)
    Compute radial ribs joint points, M_j and N_j, with system (15.11)
  end for

15.1.6 Examples

Figure 15.5 sketches four different fluid flux-barriers rotor geometries obtained with the drawing procedure. Figure 15.5(a) and Figure 15.5(b) present the same flux-barrier inner and outer middle radii but different number of poles. Figure 15.5(b) and Figure 15.5(c) have the same number of poles but the second one presents larger radial ribs and thicker flux-barriers. Figure 15.5(d) shows an eight-poles rotor with a bigger rotor shaft diameter and thin flux-barriers.

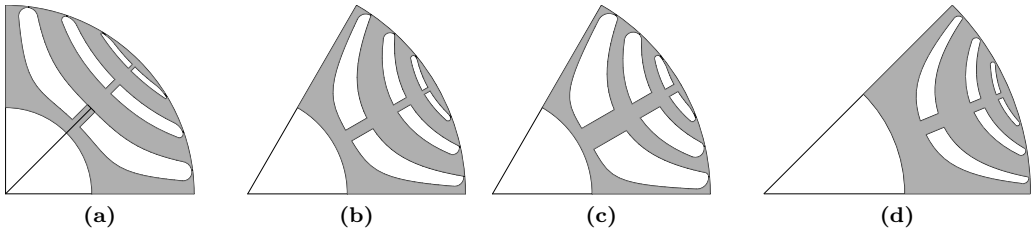

Figure 15.5: Fluid flux-barrier rotors with different number of poles, flux-barrier geometry and radial ribs size.

15.2 Segmented flux-barrier rotor

The segmented flux-barriers rotor presents a simple geometry and, for this reason, it is often preferred to the fluid flux-barriers one even though it yields a lower rotor anisotropy. A further advantage of this geometry is that it allows to achieve a high flux-barriers filling with the common sintered PM without affecting the rotor geometry.

A sketch of a segmented flux-barriers rotor is shown in Figure 15.6. As can be noted, the simplicity of the present rotor geometry is due to the fact that, except the fillets, the flux-barriers edges are mainly straight lines. In particular, all the lateral flux-barriers sides are parallel to the d-axis. Moreover, the flux-barrier thicknesses are constant while the iron channel are not. It is worth noticing that an alternative rotor geometry with constant iron channel thickness and variable flux-barrier thicknesses can be drawn as well. However, it is not here described since it has not been used in this thesis studies.

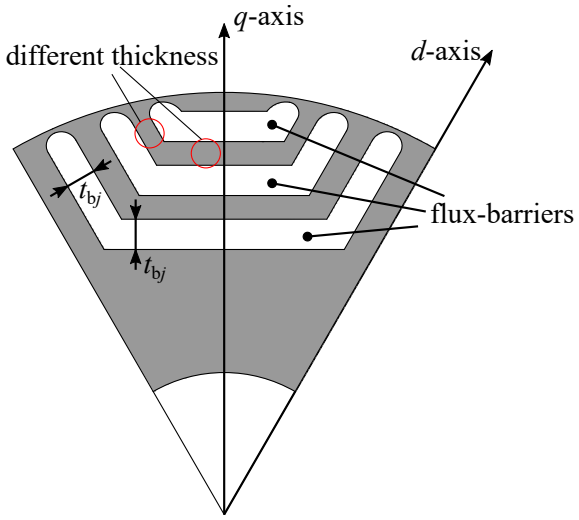

Figure 15.6: Sketch of segmented flux-barriers rotor.

15.2.1 Flux-barrier edges identification

The computation of the j-th flux-barrier starts from the points B_j, O_j and I_j reported in Figure 15.7(a). The first one is given by:

$$\begin{cases} x_{Bj} = -\left(\frac{D_\mathrm{r}}{2} - t_\mathrm{rib.t}\right)\sin\vartheta_{\mathrm{b}j} \\ y_{Bj} = \left(\frac{D_\mathrm{r}}{2} - t_\mathrm{rib.t}\right)\cos\vartheta_{\mathrm{b}j} \end{cases} \tag{15.12}$$

the slope of line which connect B_j to the origin is:

$$m_{Bj} = \tan\frac{y_{Bj}}{x_{Bj}} \tag{15.13}$$

The points O_j and I_j lie on the vertical q-axis at height R_{Oj} and R_{Ij}, respectively.

Then the straight lines r, s, t, v and w, reported in Figure 15.7(b), are determined. The slope and intercept of the first one are:

$$m_r = \tan\left(\frac{\pi}{2p} + \frac{\pi}{2}\right) \tag{15.14}$$

$$q_r = y_{Bj} - m_r x_{Bj} \tag{15.15}$$

the straight lines s and t are distant from r of $+t_{\mathrm{b}j}/2$ and $-t_{\mathrm{b}j}/2$, respectively. Their intercepts are given by:

$$q_s = q_r + \frac{t_{\mathrm{b}j}}{2\cos\frac{\pi}{2p}} \tag{15.16}$$

$$q_t = q_r - \frac{t_{\mathrm{b}j}}{2\cos\frac{\pi}{2p}} \tag{15.17}$$

The straight lines v and w are simply defined by their intercepts which are $q_v = R_{Oj}$ and $q_w = R_{Ij}$, respectively. Finally, the flux-barrier edge equations are:

$$s: \quad y = m_r x + q_s \tag{15.18}$$

$$t: \quad y = m_r x + q_t \tag{15.19}$$

$$v: \quad y = q_v \tag{15.20}$$

$$w: \quad y = q_w \tag{15.21}$$

The point coordinates of H_j, intersection between s and v, are:

$$\begin{cases} x_{Hj} = \frac{q_v - q_s}{m_r} \\ y_{Hj} = q_v \end{cases} \tag{15.22}$$

similarly, the point K_j is given by:

$$\begin{cases} x_{Kj} = \frac{q_w - q_t}{m_r} \\ y_{Kj} = q_w \end{cases} \tag{15.23}$$

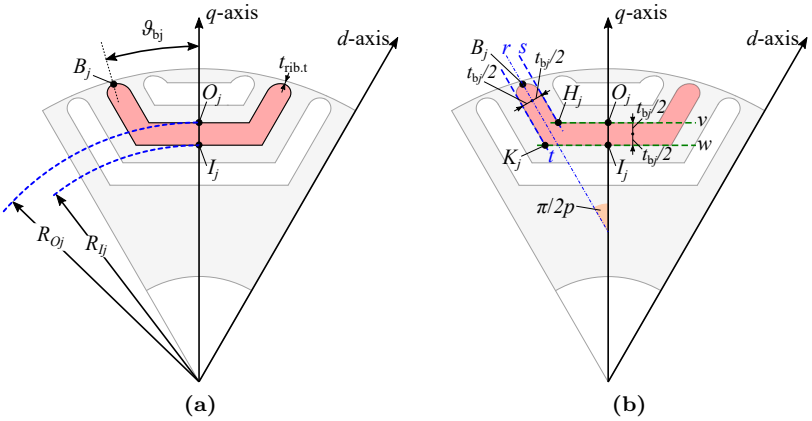

Figure 15.7: Identification of the j-th flux-barrier edges.

15.2.2 Flux-barrier end fillet

The procedure to compute a circular fillet which joints the tangentially the flux-barrier edges to the point B_j is similar to the one described in subsection 15.1.3. Regarding the fillet of the j-th

outer flux-barrier edge reported in Figure 15.8, the following condition have to honored:

$$\begin{cases} y_{CO_j} = \tan\left(\frac{\pi}{2} + \vartheta_{\mathrm{b}j}\right) x_{CO_j} & \text{(15.24a)} \\ y_{CO_j} = -\frac{1}{m_r} x_{CO_j} + q & \text{(15.24b)} \\ y_{A_j} = -\frac{1}{m_r} x_{A_j} + q & \text{(15.24c)} \\ y_{Aj} = m_r x_{Aj} + q_{Aj} & \text{(15.24d)} \\ \left(x_{Aj} - x_{C_{Oj}}\right)^2 + \left(y_{Aj} - y_{C_{Oj}}\right)^2 - r_{\mathrm{f}}^2 = 0 & \text{(15.24e)} \\ \left(x_{Bj} - x_{C_{Oj}}\right)^2 + \left(y_{Bj} - y_{C_{Oj}}\right)^2 - r_{\mathrm{f}}^2 = 0 & \text{(15.24f)} \end{cases}$$

Eqn. (15.24a) fix the point x_{CO_j} on the straight line which connects the origin to point B_j. Eqn. (15.24b) and (15.24c) impose that the point C_{Oj} must lie on the straight line, perpendicular to r, that pass honored the point A_j. Eqn. (15.24d) fix the point A_j on the straight line r. (15.24e) and (15.24f) set the same distance $\overline{AC_j}$ and $\overline{BC_j}$ to be equal. Unlike the flux-barrier geometry, the system (15.24) can be solved directly. After some equation manipulation and substitutions it results:

$$\begin{aligned} &(1 + 2k_3 + m_r^2 + 2k_5 m_r) x_{Aj}^2 + \\ &\quad (-2k_2 + 2m_r q_r - 2k_4 m_r + 2k_5 q_r - 2x_{Bj} k3 - 2y_{Bj} k_5) x_{Aj} \\ &\quad\quad (q_r^2 - 2q_r k_4 - x_{Bj}^2 + 2x_{Bj} k2 - y_{Bj}^2 + 2y_{Bj} k_4) = 0 \end{aligned} \quad \text{(15.25)}$$

where:

$$\begin{cases} k_1 = m_r + \frac{1}{m_r} \\ k_2 = \frac{q_r}{\frac{1}{m_r} + m_{B_j}} \\ k_3 = -\frac{k_1}{\frac{1}{m_r} + m_{B_j}} \\ k_4 = k_2 m_{Bj} \\ k_5 = k_3 m_{Bj} \end{cases} \quad \text{(15.26)}$$

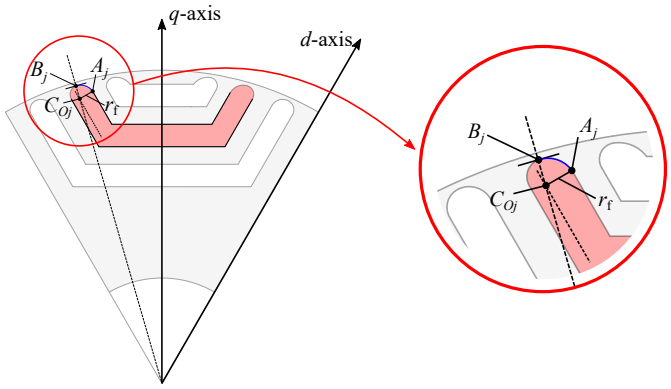

Figure 15.8: Computation of the fillet in a segmented flux-barrier rotor.

The (15.25) provides two solutions, but only the one which meets the following constraint is selected:

$$\sqrt{x_{Aj}^2 + y_{Aj}^2} < \frac{D_{\mathrm{r}}}{2} \quad \text{(15.27)}$$

which means that the joint point must be within the rotor diameter. The other joint point, D_j, on the inner flux-barrier edge can be found with the same computation with the obvious substitutions.

15.2.3 Radial ribs

As shows Figure 15.9, the computation of the radial rib points is quite simple. In particular their coordinates are:

$$\begin{cases} x_{Mj} = -t_{\mathrm{rib}j}/2 \\ y_{Mj} = R_{Oj} \end{cases} \quad \text{and} \quad \begin{cases} x_{Nj} = -t_{\mathrm{rib}j}/2 \\ y_{Nj} = R_{Ij} \end{cases} \tag{15.28}$$

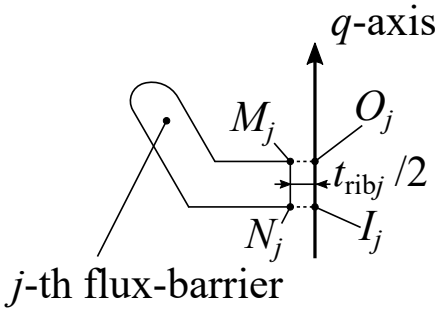

Figure 15.9: Computation of the radial rib nodes of the j-th flux-barrier.

15.2.4 Middle PM slot

A PM rectangular slot can be also added in the middle of the flux-barrier as reported in Figure 15.10. In this case, the radial rib points are:

$$\begin{cases} x_{Mj} = -t_{\mathrm{rib}j} - w_{\mathrm{pm}j}/2 \\ y_{Mj} = R_{Oj} \end{cases} \quad \text{and} \quad \begin{cases} x_{Nj} = -t_{\mathrm{rib}j}/2 - w_{\mathrm{pm}j}/2 \\ y_{Nj} = R_{Ij} \end{cases} \tag{15.29}$$

while the PM points are:

$$P_{j1}: \begin{cases} x_{Pj1} = 0 \\ y_{Pj1} = R_{\mathrm{m}j} + h_{\mathrm{pm}j}/2 \end{cases} \quad \text{and} \quad P_{j2}: \begin{cases} x_{Pj2} = -w_{\mathrm{pm}j}/2 \\ y_{Pj2} = R_{\mathrm{m}j} + h_{\mathrm{pm}j}/2 \end{cases} \tag{15.30}$$

$$P_{j3}: \begin{cases} x_{Pj3} = -w_{\mathrm{pm}j}/2 \\ y_{Pj3} = R_{\mathrm{m}j} - h_{\mathrm{pm}j}/2 \end{cases} \quad \text{and} \quad P_{j4}: \begin{cases} x_{Pj4} = 0 \\ y_{Pj4} = R_{\mathrm{m}j} - h_{\mathrm{pm}j}/2 \end{cases} \tag{15.31}$$

where $R_{\mathrm{m}j} = (R_{Oj} + R_{Ij})/2$.

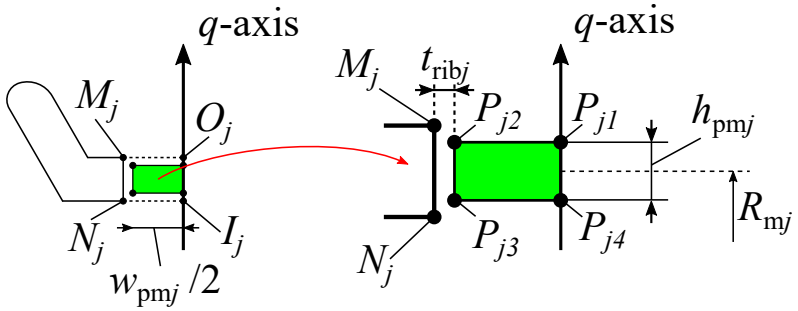

Figure 15.10: Computation of the PM nodes of the j-th flux-barrier.

15.2.5 Flux-barrier edges fillet

The flux-barrier edges can be finally smoothed with a fillet, of radius $R_{\mathrm{fb}j}$, between the horizontal and inclined edges as reported in Figure 15.11. In order to keep the flux-barrier thickness constant along the fillet, the same center is adopted for the outer flux-barrier fillet.

At first, the center of the arc fillet can be computed as follows:

$$\begin{cases} y_{C_{fbj}} = R_{Oj} + R_{\mathrm{fb}j} \\ y_{C_{fbj}} = m_r x_{C_{fbj}} + q_s + \dfrac{R_{\mathrm{fb}j}}{\cos\frac{\pi}{2p}} = m_r x_{C_{fbj}} + q_{C_{fbj}} \end{cases} \tag{15.32}$$

then, the points F_{j1} and F_{j4}, are easily determined by:

$$F_{j1}: \begin{cases} x_{F_{j1}} = x_{C_{fbj}} \\ y_{F_{j1}} = R_{Oj} \end{cases} \quad \text{and} \quad F_{j4}: \begin{cases} x_{F_{j4}} = x_{C_{fbj}} \\ y_{F_{j4}} = R_{Ij} \end{cases} \tag{15.33}$$

while the other two points require some few steps more.

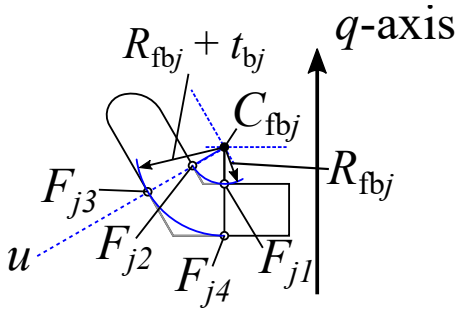

Figure 15.11: Computation of the PM nodes of the j-th flux-barrier.

The intercept of the straight line u, perpendicular to r and passing through C_{fbj}, is:

$$q_{fbj} = y_{C_{fbj}} + \frac{1}{m_r} x_{C_{fbj}} \tag{15.34}$$

so, the fillet joint point F_{j2} is the intersection between s and u, which results:

$$\begin{cases} x_{F_{j2}} = \dfrac{q_{C_{fbj}} - q_s}{m_r + \frac{1}{m_r}} \\ y_{F_{j2}} = m_r x_{F_{j2}} + q_s \end{cases} \tag{15.35}$$

while the point, F_{j3} is given by:

$$\begin{cases} x_{F_{j3}} = \dfrac{q_{C_{fbj}} - q_t}{m_r + \frac{1}{m_r}} \\ y_{F_{j3}} = m_r x_{F_{j3}} + q_t \end{cases} \tag{15.36}$$

15.2.6 Automatic segmented flux-barrier drawing algorithm

The Algorithm 4 reports the pseudocode to draw a segmented flux-barriers rotor.

15.2.7 Examples

Figure 15.12 shows some segmented flux-barrier rotor pole sketches. All the rotors presents the same flux-barrier and iron channel thicknesses. The difference between Figure 15.12(a) and Figure 15.12(b) is the number of poles: four and six, respectively. The rotor in Figure 15.12(c) is the smoothed version of the one in Figure 15.12(b). The rotor in Figure 15.12(d) presents both radial ribs and PMs in the middle of the flux-barriers.

Algorithm 4 Segmented flux-barriers automatic drawing

Input: Tangential rib thickness: $t_{\mathrm{rib.t}}$
Input: Radial rib thicknesses: $t_{\mathrm{rib}1}, \dots, t_{\mathrm{rib}N_\mathrm{b}}$
Input: Flux-barrier angles: $\vartheta_{\mathrm{b}1}, \dots, \vartheta_{\mathrm{b}N_\mathrm{b}}$
Input: Magnet thicknesses: $h_{\mathrm{pm}1}, \dots, h_{\mathrm{pm}N_\mathrm{b}}$
Input: Magnet widths: $w_{\mathrm{pm}1}, \dots, w_{\mathrm{pm}N_\mathrm{b}}$
Input: Flux-barrier fillet radii: $R_{\mathrm{fb}1}, \dots, R_{\mathrm{fb}N_\mathrm{b}}$
Input: Middle flux-barrier outer radii: $R_{O1}, \dots, R_{ON_\mathrm{b}}$
Input: Middle flux-barrier inner radii: $R_{I1}, \dots, R_{IN_\mathrm{b}}$
  for $j = 1$ **To** N_b **do**
    Compute point B_j with (15.12)
    Compute points H_j and K_j with (15.22) and (15.23)
    Compute joint point fillets A_j and D_j system (15.24)
    if $w_{\mathrm{pm}j} > 0$ **then**
      Compute radial rib with (15.29)
      Compute PM points with (15.31)
    else
      Compute radial rib with (15.28)
    end if
    if $R_{\mathrm{fb}j} > 0$ **then**
      Compute flux-barrier fillet with (15.33), (15.35) and (15.36)
    end if
  end for

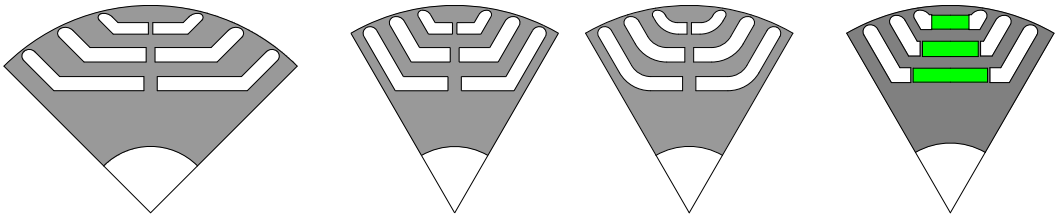

Figure 15.12: Segmented flux-barrier rotors with different number of poles and fillets.

15.3 Flux-barriers and iron channels design

Both the drawing procedures seen in the previous sections requires, at least, the knowledge of the intercept points between the flux-barriers and q-axis and the flux-barrier angles.

The rotor diameter, the shaft diameter and the flux-barriers middle radii define in turn N_b flux-barrier thicknesses, $t_{\mathrm{b}j}, \dots, t_{\mathrm{b}N_\mathrm{b}}$ and $N_\mathrm{b}+1$ iron channel widths, $w_{\mathrm{fe}j}, \dots, w_{\mathrm{fe}N_\mathrm{b}+1}$, as reported in Figure 15.13.

In the following, a SyR machine design methodology to reduce the number of parameters on the basis of analytical considerations is presented [3, 132].

15.3.1 Magnetic insulation ratio k_{air}

On the basis of the flux-barrier thicknesses and iron channel widths, it is possible to define the magnetic insulation ratio, k_{air}, as:

$$k_{\mathrm{air}} = \frac{\sum_{j=1}^{N_\mathrm{b}} \sum t_{\mathrm{b}j}}{\frac{D_\mathrm{r}-D_\mathrm{sh}}{2}} = \frac{\sum_{j=1}^{N_\mathrm{b}} \sum t_{\mathrm{b}j}}{\sum_{j=1}^{N_\mathrm{b}} t_{\mathrm{b}j} + \sum_{j=1}^{N_\mathrm{b}+1} w_{\mathrm{fe}j}} = \frac{l_{\mathrm{air}}}{l_{\mathrm{air}} + l_{\mathrm{fe}}} \tag{15.37}$$

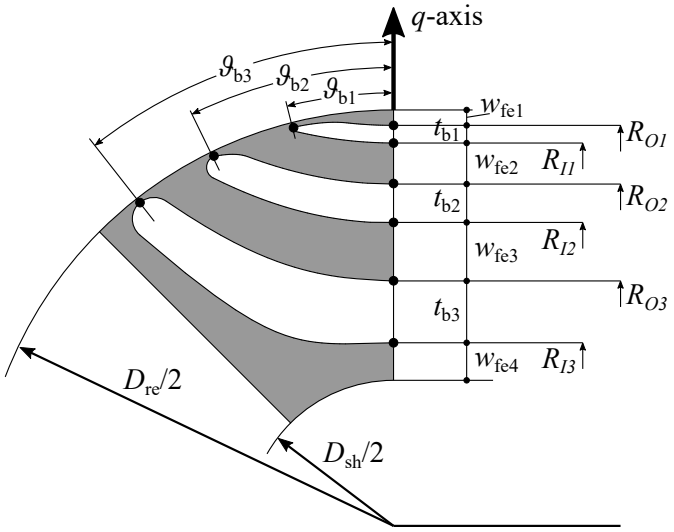

Figure 15.13: Sketch of a SyR rotor with three flux-barriers per pole with relative quotes.

which gives and indication of the amount of magnetic insulation (i.e. air) along the q-axis. This is clearly shown in Figure 15.14 where SyR rotors with different values of k_{air} and the same flux-barrier angles are reported. It can be noted that, for $k_{\text{air}} = 0.2$, the flux-barriers are quite thin while the iron channel are large. For $k_{\text{air}} = 0.5$ the amount of air and iron along the q-axis is the same. For $k_{\text{air}} = 0.8$ there are large flux-barriers with thin iron channels.

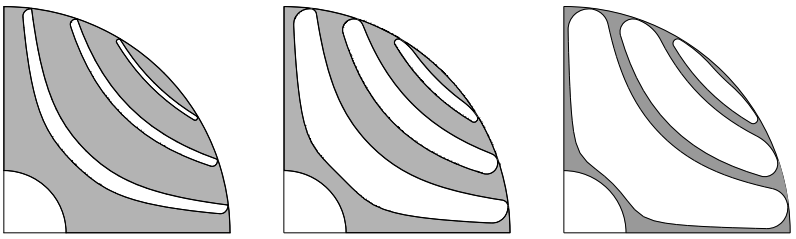

(a) $k_{\text{air}} = 0.2$. **(b)** $k_{\text{air}} = 0.5$. **(c)** $k_{\text{air}} = 0.8$.

Figure 15.14: SyR rotors with different values of k_{air}.

15.3.2 Iron channel widths design

The aim of the criteria to select the optimal iron channel widths is to maximize the d-axis flux linkage by assigning to each iron channel a width proportional to the MMF at the air-gap [57].

The main assumptions that allow to get an analytical design criteria are: linear magnetic behavior of the iron and sinusoidal distribution of the stator scalar magnetic, potential within the air-gap. The latter can be expressed in per unit (p.u.) by:

$$U_{\text{s}}(\theta^e) = \sin(p\theta_{\text{m}}) \tag{15.38}$$

where θ_{m} is the mechanical rotor coordinated whose origin lies on the q-axis. The average value

of the MMF in front of the j-th iron channel, f_j, can be computed as follows:

$$\begin{cases} f_1 = \dfrac{1}{\vartheta_{\mathrm{b}1}} \displaystyle\int_0^{\vartheta_{\mathrm{b}1}} U_{\mathrm{s}} \sin(p\theta_{\mathrm{m}})\, d\theta_{\mathrm{m}} \\ \quad \vdots \\ f_j = \dfrac{1}{\vartheta_{\mathrm{b}j} - \vartheta_{\mathrm{b}(j-1)}} \displaystyle\int_{\vartheta_{\mathrm{b}(j-1)}}^{\vartheta_{\mathrm{b}j}} U_{\mathrm{s}} \sin(p\theta_{\mathrm{m}})\, d\theta_{\mathrm{m}} \\ \quad \vdots \\ f_{N_{\mathrm{b}}+1} = \dfrac{2}{\frac{\pi}{2p} - \vartheta_{\mathrm{b}N_{\mathrm{b}}}} \displaystyle\int_{\vartheta_{\mathrm{b}N_{\mathrm{b}}}}^{\frac{\pi}{2p}} U_{\mathrm{s}} \sin(p\theta_{\mathrm{m}})\, d\theta_{\mathrm{m}} \end{cases} \tag{15.39}$$

this operation is shown qualitatively in Figure 15.15.

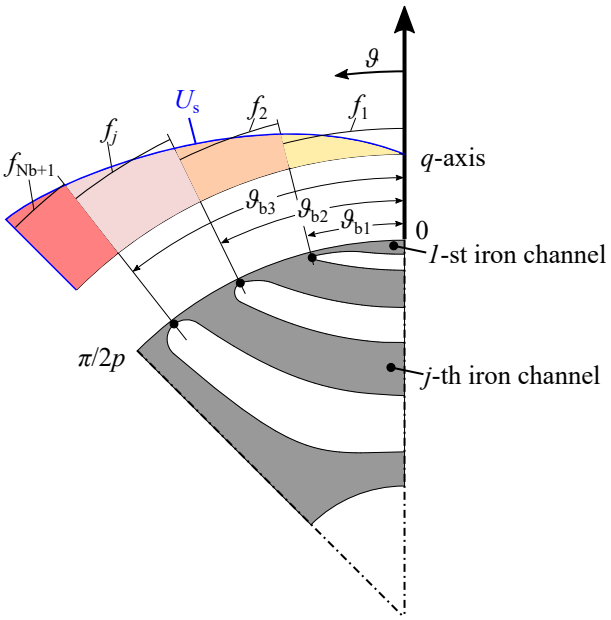

Figure 15.15: Computation of the average MMF in front of each iron channel.

Then, the iron channel widths can be computed solving the following system:

$$\begin{cases} \displaystyle\sum_{j=1}^{N_{\mathrm{b}}+1} w_{\mathrm{fe}j} = (1 - k_{\mathrm{air}}) \frac{D_{\mathrm{r}} - D_{\mathrm{sh}}}{2} \\ \dfrac{w_{\mathrm{fe}k}}{w_{\mathrm{fe}h}} = \dfrac{f_k}{f_h} \end{cases} \tag{15.40}$$

after some arrangements it results:

$$\begin{cases} w_{\mathrm{fe}1} = \dfrac{l_{\mathrm{fe}}}{\sum_{j=1}^{N_{\mathrm{b}}+1} \frac{f_j}{f_1}} \\ w_{\mathrm{fe}j} = w_{\mathrm{fe}1} \frac{f_j}{f_1} \end{cases} \tag{15.41}$$

finally, in order to consider the tangential rib contribute, the first iron channel width has to be adjusted as follows:

$$w'_{\mathrm{fe}1} = w_{\mathrm{fe}1} - t_{\mathrm{rib.t}} \tag{15.42}$$

15.3.3 Flux-barrier thicknesses design

The aim of the flux-barrier thicknesses design is to minimize the q-axis flux linkage [57, 73]. The p.u. behavior of the MMF within the air-gap with a q-axis magnetization is expressed by:

$$U_{\mathrm{s}} = \cos(p\theta_{\mathrm{m}}) \tag{15.43}$$

from which it is possible to compute the average stator scalar magnetic potential, f_j, in front of the j-th flux-barrier:

$$\begin{cases} f_1 = \dfrac{1}{\vartheta_{\mathrm{b}1}} \displaystyle\int_0^{\vartheta_{\mathrm{b}1}} U_{\mathrm{s}} \cos(p\theta_{\mathrm{m}})\, d\theta_{\mathrm{m}} \\ f_j = \dfrac{1}{\vartheta_{\mathrm{b}j} - \vartheta_{\mathrm{b}(j-1)}} \displaystyle\int_{\vartheta_{\mathrm{b}(j-1)}}^{\vartheta_{\mathrm{b}j}} U_{\mathrm{s}} \cos(p\theta_{\mathrm{m}})\, d\theta_{\mathrm{m}} \end{cases} \tag{15.44}$$

from which it is possible to compute the voltage drops across each flux-barrier, Δf_j:

$$\begin{cases} \Delta f_j = f_j - f_{(j+1)} & j = 1, \ldots, N_{\mathrm{b}} - 1 \\ \Delta f_{N_{\mathrm{b}}} = f_{N_{\mathrm{b}}} \end{cases} \tag{15.45}$$

this computation is described qualitatively in Figure 15.16.

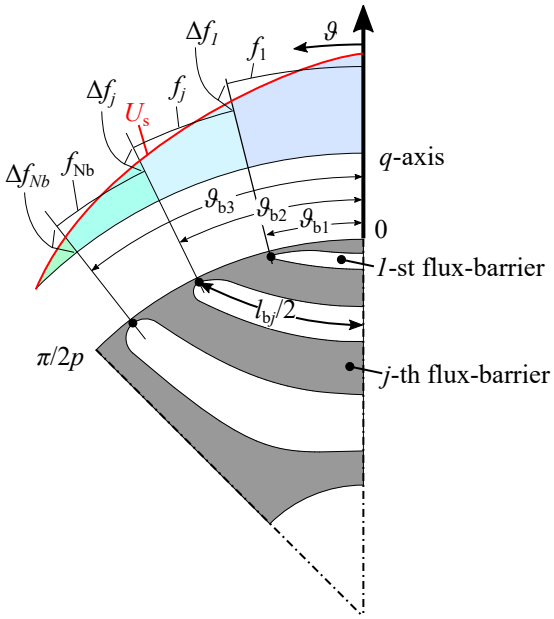

Figure 15.16: Computation of the average MMF in front of each flux-barrier.

From the derivations given in [73], the relationship which yields the minimum q-axis flux linkage is:

$$\frac{t_{\mathrm{b}j}}{t_{\mathrm{b}k}} = \frac{\Delta f_h}{\Delta f_k} \sqrt{\frac{l_{\mathrm{b}h}}{l_{\mathrm{b}k}}} \tag{15.46}$$

where $l_{\mathrm{b}j}$ is the length of the j-th flux-barrier. The constraint:

$$\sum_{j=1}^{N_{\mathrm{b}}} t_{\mathrm{b}j} = k_{\mathrm{air}} \frac{D_{\mathrm{r}} - D_{\mathrm{sh}}}{2} \tag{15.47}$$

and the simplification $l_{\mathrm{b}j} = D_{\mathrm{r}}\vartheta_{\mathrm{b}j}$, allows to express all the flux-barrier thicknesses as follows:

$$\begin{cases} \dfrac{t_{\mathrm{b}2}}{t_{\mathrm{b}1}} = \dfrac{\Delta f_2}{\Delta f_1}\sqrt{\dfrac{\vartheta_{\mathrm{b}2}}{\vartheta_{\mathrm{b}1}}} \\ \quad \vdots \\ \dfrac{t_{\mathrm{b}j}}{t_{\mathrm{b}1}} = \dfrac{\Delta f_j}{\Delta f_1}\sqrt{\dfrac{\vartheta_{\mathrm{b}j}}{\vartheta_{\mathrm{b}1}}} \\ \quad \vdots \\ \dfrac{t_{\mathrm{b}N_{\mathrm{b}}}}{t_{\mathrm{b}1}} = \dfrac{\Delta f_{N_{\mathrm{b}}}}{\Delta f_1}\sqrt{\dfrac{\vartheta_{\mathrm{b}N_{\mathrm{b}}}}{\vartheta_{\mathrm{b}1}}} \end{cases} \tag{15.48}$$

and, after some arrangements, it results:

$$t_{\mathrm{b}1} = \frac{l_{\mathrm{air}}}{\sum_{j=1}^{N_{\mathrm{b}}} \frac{\Delta f_j}{\Delta f_1}\sqrt{\frac{\vartheta_{\mathrm{b}j}}{\vartheta_{\mathrm{b}1}}}} t_{\mathrm{b}j} = \frac{\Delta f_j}{\Delta f_1}\sqrt{\frac{\vartheta_{\mathrm{b}j}}{\vartheta_{\mathrm{b}1}}} t_{\mathrm{b}1} \qquad j = 2, \ldots, N_{\mathrm{b}} \tag{15.49}$$

15.3.4 Flux-barrier inner and outer middle radii

Once all the flux-barrier and iron channel dimensions are known, it is possible to compute the j-th inner and outer flux-barrier radii as follows:

$$R_{Oj} = D_{\mathrm{r}}/2 - \sum_{i=1}^{j} w_{\mathrm{fe}i} - \sum_{i=1}^{j-1} t_{\mathrm{b}i} \tag{15.50}$$

$$R_{Ij} = R_{Oj} - t_{\mathrm{b}j} \tag{15.51}$$

15.3.5 Automatic drawing algorithm

The Algorithm 4 reports the pseudocode to draw a SyR rotor with optimal flux-barrier and iron channel dimensions.

Algorithm 5 Complete rotor parameters computation.

Input: Rotor and shaft diameters: D_{r} and D_{sh}
Input: Tangential rib thickness: $t_{\mathrm{rib.t}}$
Input: Flux-barrier angles: $\vartheta_{\mathrm{b}1}, \ldots, \vartheta_{\mathrm{b}N_{\mathrm{b}}}$
Input: Magnetic insulation ratio: k_{air}
  Compute iron channel widths with (15.41)
  Compute flux-barrier thicknesses with (15.49)
  Compute middle inner and outer radii with (15.50) and (15.51)
  if Rotor topology = *fluid* **then**
    Run Algorithm 3
  else if Rotor topology = *segmented* **then**
    Run Algorithm 4
  end if

Conclusion

This thesis mainly dealt with the design and analysis of SyR machine for high-speed and fault-tolerant applications, the design of a PMASyR machine for an electric scooter application and the possibility to use bonded magnets in such a machine topology.

High-speed SyR machine

At first, an analytical procedure to mechanically design the SyR rotor radial ribs has been proposed and its reliability has been verified by means of finite element structural analyses. Then, a simple analytical model has been developed to study the effect of the radial ribs design on the machine performance. From such an analysis, it has been found that (i) the SyR rotor anisotropy worsens as the mechanical speed limit increases because of the large q-axis flux that flows through them, (ii) for a given rotor diameter, a theoretical maximum output power exists, (iii) the SyR rotor saturation is higher in the iron channels and lower within the radial ribs as the mechanical speed limit increases and (iv) the SyR machine performance can be predicted with accuracy in a wide speed range only by means of a detailed nonlinear reluctance network of the stator and rotor or by means of FE analysis. After that, two alternative design methodologies have been proposed for an HS SyR machine: one supported by both analytical computation and FE analysis, one entirely based on a multi-objective differential evolution optimization algorithm. A comparison between the two methods has shown that only the second one is suitable for the design of HS SyR machine since it takes into account the rotor saturation and select the SyR rotor parameters accordingly. On the basis of this observation several SyR rotor geometries have been optimized for different mechanical speed limits to investigate the impact of the mechanical design on the SyR rotor parameters. The results have shown that the optimal SyR rotor flux-barrier angles and magnetic insulation ratio change with the mechanical speed limit. In particular, it has been observed that at high mechanical speed limits it is more convenient to design a SyR rotor with a high amount of magnetic insulation material per pole to reduce the rotating iron mass, the related centrifugal force and therefore the radial rib sizes. Finally, a comparison between a surface mounted permanent magnet machine and a SyR machine, both designed for an high-speed application, is carried out. The study has shown that the SyR machine cost is about one third of the PM machine one and its efficiency is only 1% lower. On the other hand, a very poor power factor has been obtained from the SyR machine, i.e. 0.55, unlike the SPM machine one (about 0.87). In conclusion, even thought the SyR machine yields a good efficiency at very low cost, its poor power factor may compromises its suitability for HS application.

Fault-Tolerant SyR machine

The aim of this study was twofold. Firstly, the impact of different dual three-phase winding arrangements on the SyR machine average torque, torque ripple, unbalanced radial force on the rotor and mutual coupling has been evaluated. Secondly, different design strategies have been investigated to improve the fault-tolerant performance of a SyR machine. Concerning the first point, three different winding arrangements have been proposed: two dual three-phase windings and an actual six phase winding. The analyses have shown that only one, called W-12-12, is suitable

for the low mutual mutual coupling between the phases, negligible unbalanced radial force and quite good average torque in OC-HWM. However, also a quite high torque ripple has been observed in OC-HWM. On the basis of this observation, several optimization strategies have been investigated to mitigate or to overcome such a drawback. The results of all the optimizations revealed that (i) it is recommended to optimize the FWM and OC-HWM performance concurrently and (ii) it is sufficient to optimize the geometry of a classical stator with evenly spaced slots. According to the optimization results, a prototype has been manufactured and then tested in laboratory. Good agreement between finite element and experimental results has been found both in terms of torque behavior and mutual coupling. Moreover, the test in short circuit condition of one of the two winding revealed a quite low amplitude of short circuit currents (below the rated value). However, despite all the design precautions, a low power factor, i.e. 0.45, has been found in OC-HWM. This aspect was essentially due to the higher q-axis flux that occurs when the machine operate in such an operating condition. In conclusion, a proper winding arrangement choice and geometry optimization allow to improve the SyR machine performance in OC-HWM but, on the other hand, a very poor factor still remains the main drawback.

PMASyR machine design for an Electric Scooter

This work dealt with the design of a PMASyR motor for an E-Scooter application by means of a FE-based multi-objective optimization procedure. The main key points of such a procedure were (i) to meet a determined overload capability, (ii) to evaluate the feasibility of the high-speed working according to a very low voltage constraint and (iii) to evaluate all the individuals of the optimization in the same operating conditions to allow an easy results interpretation. The procedure has been applied for the design of PMASyR motor which has been manufactured accordingly. The preliminary experimental results have shown a good agreement with the FE predictions in terms of average torque and torque ripple. Promising results are also obtained in terms of power capability.

Bonded magnets for PMASyR machine

The study has investigated the suitability of two different bonded magnet production technologies for PMASyR machines. In particular, the compression and injection moulding processes are considered. The study has been presented in all its main parts: (i) preparation of the bonded magnets from the raw materials, (ii) magnetic characterization, (iii) prototype assembling, (iv) FE analysis and (v) experimental results. In particular, three prototypes have been manufactured: one SyR machine and two PMASyR machines (one for each magnet typology). The magnetic characterizations have shown that the compression moulding process yields better magnetic properties, while, the injection one is more suitable for an industrial process, mainly in terms of production rates. The experimental tests carried out on the final motor prototypes have shown a good matching with FE results, in particular regarding the torque waveforms. A torque density increment up to 50% has been found for the PMASyR machine prototype with BMs obtained by compression. The same prototype has a power factor of 0.93 at rated condition, much higher than SyR motor (0.71). On the other hand, a torque ripple increase has been obtained in both PMASyR motors. However such an increment can be effectively reduced adopting a more complex rotor geometry with almost three-flux barriers per pole and optimizing their parameters accordingly.

Appendices

HS-SyR analytical model constants

The constants used in the analytical model presented in chapter 2 are here reported. The coefficients ρ_1, ρ_2, ρ_3, b, e, f, r, s, z and other missing variables can be found in [65].

$$X = AI_{\mathrm{d}}I_{\mathrm{q}} + (B + C + D + E)I_{\mathrm{d}} \tag{52}$$

$$A = \frac{9}{2\pi} p\mu_0 \left(\frac{k_w N_{\mathrm{s}}}{2p}\right)^2 \frac{D_{\mathrm{s}} L_{\mathrm{stk}}}{g''} \tag{53}$$

$$B = \frac{3}{16} k_{\mathrm{w}} N_{\mathrm{s}} \mu_0 L_{\mathrm{stk}} \frac{D_{\mathrm{s}}^2 \hat{K}_{\mathrm{s}}}{p g''} \left(\sin(\pi - \alpha_{\mathrm{i}}^{\mathrm{e}}) - \sin(-\alpha_{\mathrm{i}}^{\mathrm{e}})\right) \tag{54}$$

$$C = -\frac{3}{4} k_{\mathrm{w}} N_{\mathrm{s}} \mu_0 L_{\mathrm{stk}} \frac{D_{\mathrm{s}}^2}{g''} \left[\frac{\hat{K}_{\mathrm{sq}}}{p} \rho_1\right] \left[\vartheta_{\mathrm{b3}} - \vartheta_{\mathrm{b2}}\right] \tag{55}$$

$$D = -\frac{3}{4} k_{\mathrm{w}} N_{\mathrm{s}} \mu_0 L_{\mathrm{stk}} \frac{D_{\mathrm{s}}^2}{g''} \left[\frac{\hat{K}_{\mathrm{sq}}}{p} \rho_2\right] \left[\vartheta_{\mathrm{b2}} - \vartheta_{\mathrm{b1}}\right] \tag{56}$$

$$E = -\frac{3}{4} k_{\mathrm{w}} N_{\mathrm{s}} \mu_0 L_{\mathrm{stk}} \frac{D_{\mathrm{s}}^2}{g''} \left[\frac{\hat{K}_{\mathrm{sq}}}{p} \rho_1\right] \vartheta_{\mathrm{b1}} \tag{57}$$

$$Y = (F + G + M)I_{\mathrm{d}} \tag{58}$$

$$F = \frac{3}{4} p k_{\mathrm{w}} N_{\mathrm{s}} \mu_0 L_{\mathrm{stk}}^2 \frac{D_{\mathrm{s}}}{g''} \frac{D_{\mathrm{r}}^3}{8} B_{\mathrm{sat}} \frac{\nu_\sigma \gamma_{\mathrm{Lam}}}{\sigma_{\mathrm{r}}} \left[\vartheta_{\mathrm{b3}} - \vartheta_{\mathrm{b2}}\right] \cdot \tag{59}$$

$$\cdot \Big\{ s\mathcal{R}_{\mathrm{b1}}(2\vartheta_{\mathrm{b1}} - \sin 2\vartheta_{\mathrm{b1}}) + y\mathcal{R}_{\mathrm{b2}} k_2 (2\vartheta_{\mathrm{b2}} - \sin 2\vartheta_{\mathrm{b2}}) - r\mathcal{R}_{\mathrm{b3}} k_3 (2\vartheta_{\mathrm{b3}} - \sin 2\vartheta_{\mathrm{b3}}) \Big\} \tag{60}$$

$$G = \frac{3}{8} p k_{\mathrm{w}} N_{\mathrm{s}} \mu_0 L_{\mathrm{stk}}^2 \frac{D_{\mathrm{r}}^3}{8} B_{\mathrm{sat}} \frac{D_{\mathrm{s}}}{g''} \frac{\nu_\sigma \gamma_{\mathrm{Lam}}}{\sigma_{\mathrm{r}}} \left[\vartheta_{\mathrm{b2}} - \vartheta_{\mathrm{b1}} \right] \cdot \Big\{ (2\vartheta_{\mathrm{b1}} - \sin 2\vartheta_{\mathrm{b1}}) \big[\mathcal{R}_{\mathrm{b1}} (zs + e) \big] + \\ + (2\vartheta_{\mathrm{b2}} - \sin 2\vartheta_{\mathrm{b2}}) \big[\mathcal{R}_{\mathrm{b2}} k_2 (y - z) \big] + \\ + (2\vartheta_{\mathrm{b3}} - \sin 2\vartheta_{\mathrm{b3}}) (r \mathcal{R}_{\mathrm{b3}} k_3) \Big\}$$

$$M = \frac{3}{8} p k_{\mathrm{w}} N_{\mathrm{s}} \mu_0 L_{\mathrm{stk}}^2 \frac{D_{\mathrm{r}}^3}{8} B_{\mathrm{sat}} \frac{D_{\mathrm{s}}}{g''} \frac{\nu_\sigma \gamma_{\mathrm{Lam}}}{\sigma_{\mathrm{r}}} \left[2\vartheta_{\mathrm{b1}} \right] \cdot \\ \cdot \Big\{ (2\vartheta_{\mathrm{b1}} - \sin 2\vartheta_{\mathrm{b1}}) \big[b \mathcal{R}_{\mathrm{b1}} (zs + e - 1) \big] + \\ + (2\vartheta_{\mathrm{b2}} - \sin 2\vartheta_{\mathrm{b2}}) b z \mathcal{R}_{\mathrm{b2}} k_2 (y - 1) + \\ - (2\vartheta_{\mathrm{b3}} - \sin 2\vartheta_{\mathrm{b3}}) r \mathcal{R}_{\mathrm{b3}} k_3 \Big\} \tag{61}$$

$$f_{\mathrm{r1}} = b \Big[z \left(s U_{\mathrm{sat1}} + y U_{\mathrm{sat2}} - r U_{\mathrm{sat3}} \right) + \big[(e - 1) U_{\mathrm{sat1}} - z U_{\mathrm{sat2}} \big] \Big] \tag{62}$$

$$f_{\mathrm{r2}} = z \Big[(s + e/z) U_{\mathrm{sat1}} + (y - 1) U_{\mathrm{sat2}} - r U_{\mathrm{sat3}} \Big] \tag{63}$$

$$f_{\mathrm{r3}} = s U_{\mathrm{sat1}} + y U_{\mathrm{sat2}} - r U_{\mathrm{sat3}} \tag{64}$$

$$g_{\mathrm{r1}} = b \Big(r z U_{\mathrm{sat3}} - (zs + e - 1) U_{\mathrm{sat1}} - z (y - 1) U_{\mathrm{sat2}} \Big) \tag{65}$$

$$g_{\mathrm{r2}} = z \Big(r U_{\mathrm{sat3}} - (s + e/z) U_{\mathrm{sat1}} - (y - 1) U_{\mathrm{sat2}} \Big) \tag{66}$$

$$g_{\mathrm{r3}} = r U_{\mathrm{sat3}} - s U_{\mathrm{sat1}} - y U_{\mathrm{sat2}} \tag{67}$$

GetDP elasticity formulation

The GetDP formulation code (content in the file `Elasticity_2D.pro`) used to solve the 2D elasticity problems in chapter 14 and in all the FE structural analyses of the present thesis is here reported. For more details see [162, 163].

```
Group{
  DefineGroup[Domain_Disp, Domain_Force, Domain_Force_Sur, Domain_Force_Lin] ;
  DomainTot = Region[ {Domain_Disp, Domain_Force} ];
}


Group{
  DefineGroup[ DomainInf ] ;
  DefineVariable[ Val_Rint, Val_Rext ] ;
}


Jacobian{
  { Name Vol ;
    Case {
      { Region DomainInf ; Jacobian VolSphShell {Val_Rint, Val_Rext} ; }
      { Region All ; Jacobian Vol ; }
    }
  }
  { Name Sur ;
    Case { { Region All ; Jacobian Sur ; }
    }
  }
  { Name Lin ;
    Case { { Region All ; Jacobian Lin ; }
    }
  }
  { Name SurLinVol ;
    Case {
      { Region Domain_Force_Sur ; Jacobian Sur ; }
      { Region Domain_Force_Lin ; Jacobian Lin ; }
      { Region All ; Jacobian Vol ; }
    }
  }
}

Integration{
  { Name GradGrad ;
    Case {
      { Type Gauss ;
        Case {
          { GeoElement Point       ; NumberOfPoints  1 ; }
          { GeoElement Line        ; NumberOfPoints  2 ; }
          //          { GeoElement Line2       ; NumberOfPoints  2 ; }
```

```
        { GeoElement Triangle    ; NumberOfPoints  4 ; }
        //          { GeoElement Triangle2    ; NumberOfPoints  6 ; }
        { GeoElement Quadrangle  ; NumberOfPoints  4 ; }
      }
    }
  }
}

FunctionSpace{
  { Name H_u_Mec2D ; Type Vector ;
    BasisFunction {
      { Name sxn ; NameOfCoef uxn ; Function BF_NodeX ;
        dFunction {BF_NodeX_D12, BF_Zero} ;
        Support DomainTot ; Entity NodesOf[ All ] ; }
      { Name syn ; NameOfCoef uyn ; Function BF_NodeY ;
        dFunction {BF_NodeY_D12, BF_Zero} ;
        Support DomainTot ; Entity NodesOf[ All ] ; }
    }
    Constraint{
      { NameOfCoef uxn ;
        EntityType NodesOf ; NameOfConstraint DeplacementX ; }
      { NameOfCoef uyn ;
        EntityType NodesOf ; NameOfConstraint DeplacementY ; }
    }
  }
}

Formulation{
  { Name Mec2D_u ; Type FemEquation ;
    Quantity {
      { Name u ; Type Local ; NameOfSpace H_u_Mec2D ; }
    }
    Equation {
      Galerkin { [ C_m[] * Dof{D1 u}, {D1 u} ] ;
        In Domain_Disp ; Jacobian Vol ; Integration GradGrad ; }
      Galerkin { [ -F[] , {u} ] ;
        In Domain_Force; Jacobian SurLinVol; Integration GradGrad; }
    }
  }
}

Resolution{
  { Name Mec2D_u ;
    System {
      { Name Sys_Mec ; NameOfFormulation Mec2D_u ; }
    }
    Operation{ Generate Sys_Mec ; Solve Sys_Mec ; SaveSolution Sys_Mec ; }
  }
}

PostProcessing{
  { Name Mec2D_u ; NameOfFormulation Mec2D_u ;
    PostQuantity {
      { Name u ; Value { Term { [ {u} ]    ; In Domain_Disp ; } } }
      { Name um ; Value { Term { [Norm[{u}]] ; In Domain_Disp ; } } }
      { Name F ; Value { Term { [F[]]    ; In Domain_Force ; } } }
      { Name Vm ; Value { Term {
            [Sqrt[ CompX[C_m[]*{D1 u}]#1^2 + CompY[C_m[]*{D1 u}]#2^2 - #1*#2
```

```
            +  3*(CompZ[C_m[]*{D1 u}])^2   ] ] ; In Domain_Disp ; } } }
    }
  }
}
```

Bibliography

[1] C. Babetto, G. Bacco, and N. Bianchi. "Analytical Power Limits Curves of High-Speed Synchronous Reluctance Machines". In: *IEEE Transactions on Industry Applications* (2018), p. 1. ISSN: 0093-9994.

[2] C. Babetto, G. Bacco, and N. Bianchi. "Synchronous Reluctance Machine Optimization for High Speed Applications". In: *IEEE Transactions on Energy Conversion* 8969.c (2018), pp. 1–1. ISSN: 0885-8969.

[3] C. Babetto, G. Bacco, and N. Bianchi. "Design methodology for high-speed synchronous reluctance machines". In: *IET Electric Power Applications* 12.8 (2018), pp. 1110–1116. ISSN: 1751-8660.

[4] C. Babetto, G. Bacco, and N. Bianchi. "Analytical approach to determine the power limit of high-speed synchronous reluctance machines". In: *2017 IEEE International Electric Machines and Drives Conference, IEMDC 2017*. 2017. ISBN: 9781509042814.

[5] C. Babetto et al. "High speed motors: A comparison between synchronous PM and reluctance machines". In: *2017 IEEE Energy Conversion Congress and Exposition (ECCE)*. Cincinnati, 2017, pp. 3927–3934.

[6] C. Babetto and N. Bianchi. "Synchronous Reluctance Motor with Dual Three-Phase Winding for Fault-Tolerant Applications". In: *2018 XIII International Conference on Electrical Machines (ICEM)*. 2018, pp. 2297–2303.

[7] E. Poskovic et al. "The study of permanent magnet assisted reluctance machine with the adoption of NdFeB bonded magnets". In: *2018 International Symposium on Power Electronics, Electrical Drives, Automation and Motion (SPEEDAM)*. 2018, pp. 274–279.

[8] C. Babetto et al. "High-Speed Synchronous Reluctance Motors: Computation of the Power Limits by Means of Reluctance Networks". In: *2018 IEEE 18th International Power Electronics and Motion Control Conference (PEMC)*. 2018, pp. 556–561.

[9] C. Babetto et al. "Design Optimization and Analysis of a Synchronous Reluctance Machine for Fault-Tolerant Applications". In: *2019 IEEE International Electric Machines Drives Conference (IEMDC)*. 2019, pp. 1784–1791.

[10] C. Babetto, N. Bianchi, and G. Benedetti. "Design and Optimization of a PMASR Motor for Low-Voltage E-Scooter Applications". In: *2019 IEEE International Electric Machines Drives Conference (IEMDC)*. May 2019, pp. 1016–1023.

[11] E. Pošković et al. "Bonded Magnets in PM-Assisted Synchronous Reluctance Machines: Performance Dependence on the Production Technology". In: *2019 IEEE International Electric Machines Drives Conference (IEMDC)*. 2019, pp. 442–448.

[12] J. Park, C. Babetto, and N. Bianchi. "Fault Analysis for Dual Three-Phase Synchronous Reluctance Motor". In: *2019 IEEE International Electric Machines Drives Conference (IEMDC)*. 2019, pp. 1–6.

[13] A. Bellini et al. "Stator fault diagnosis by reactive power in dual three-phase reluctance motors". In: *12th IEEE International Symposium on Diagnostics for Electric Machines, Power Electronics and Drives, 2019. SDEMPED 2019.* 2019.

[14] C. Babetto et al. “Design and Optimization of Synchronous Motors for Low-Voltage Electric Vehicles”. In: *2019 IEEE Energy Conversion Congress and Exposition (ECCE)*. Baltimore, 2019.

[15] G. Bacco et al. “Efficiency Maps Computation and Comparison Including Thermal Limits”. In: *2019 IEEE Energy Conversion Congress and Exposition (ECCE)*. Baltimore, 2019.

[16] C. Babetto et al. “Optimal Design and Experimental Validation of a Synchronous Reluctance Machine for Fault-Tolerant Applications”. In: *2019 IEEE Energy Conversion Congress and Exposition (ECCE)*. Baltimore, 2019.

[17] J. Park et al. “Comparison of Fault Characteristics for Dual Three-Phase Synchronous Reluctance Motor”. In: *2019 IEEE Energy Conversion Congress and Exposition (ECCE)*. Baltimore, 2019.

[18] D. Gerada et al. “High-Speed Electrical Machines: Technologies, Trends, and Developments”. In: *IEEE Transactions on Industrial Electronics* 61.6 (June 2014), pp. 2946–2959. ISSN: 0278-0046.

[19] R. Abebe et al. “High speed drives review: Machines, converters and applications”. In: *IECON 2016 - 42nd Annual Conference of the IEEE Industrial Electronics Society*. 2016, pp. 1675–1679.

[20] N. Fernando et al. “Impact of Soft Magnetic Material on Design of High-Speed Permanent-Magnet Machines”. In: *IEEE Transactions on Industrial Electronics* 64.3 (2017), pp. 2415–2423.

[21] R. Kolano et al. “Amorphous Soft Magnetic Core for the Stator of the High-Speed PMBLDC Motor With Half-Open Slots”. In: *IEEE Transactions on Magnetics* 52.6 (2016), pp. 1–5.

[22] Y. Zhang et al. “Anisotropic Magnetostriction of Nonoriented Silicon Steel Sheet and Its Frequency Dependence”. In: *IEEE Transactions on Magnetics* 51.11 (Nov. 2015), pp. 1–4.

[23] D. Golovanov et al. “The Influence of Stator Material on the Power Density and Iron Loss of a High-Performace Starter-Generator for More Electric Aircraft”. In: *2018 21st International Conference on Electrical Machines and Systems (ICEMS)*. 2018, pp. 169–173.

[24] Y. Li et al. “Sensorless control method for the high speed permanent magnet synchronous starter-generator used in microturbine generation system”. In: *2011 International Conference on Electrical and Control Engineering*. 2011, pp. 2545–2549.

[25] R. M. Kennel. “Ultra high speed drive with permanent magnet synchronous motors and hardware based field oriented control”. In: *2007 International Aegean Conference on Electrical Machines and Power Electronics*. 2007, pp. 116–124.

[26] J. Cao and J. Zhang. “Trajectory tracking control method for high-speed and high-acceleration machine tool”. In: *The 27th Chinese Control and Decision Conference (2015 CCDC)*. 2015, pp. 5398–5403.

[27] A. Borisavljevic, M. Brands, and E. Lomonova. “Vector control of very-high-speed PM machines”. In: *2012 XXth International Conference on Electrical Machines*. 2012, pp. 2462–2468.

[28] R. Leuzzi et al. “High-Speed Machines: Typologies, Standards, and Operation Under PWM Supply”. In: *2018 AEIT International Annual Conference*. 2018, pp. 1–6.

[29] H. Lahne and D. Gerling. “Comparison of state-of-the-art high-speed high-power machines: Research study including a design example of a 50000 rpm induction machine”. In: *IECON 2015 - 41st Annual Conference of the IEEE Industrial Electronics Society*. Nov. 2015, pp. 3519–3524.

[30] M. V. Terzic, D. S. Mihic, and S. N. Vukosavić. “Design of High-Speed, Low-Inertia Induction Machines With Drag-Cup Rotor”. In: *IEEE Transactions on Energy Conversion* 29.1 (2014), pp. 169–177. ISSN: 0885-8969.

[31] M. Larsson et al. “Design and evaluation of high-speed induction machine”. In: *IEEE International Electric Machines and Drives Conference, 2003. IEMDC'03.* Vol. 1. 2003, 77–82 vol.1.

[32] Z. Hao and W. Fengxiang. “Comparative study on high speed induction machine with different rotor structures”. In: *2007 International Conference on Electrical Machines and Systems (ICEMS).* 2007, pp. 1009–1012.

[33] D. Gerada et al. “Design Aspects of High-Speed High-Power-Density Laminated-Rotor Induction Machines”. In: *IEEE Transactions on Industrial Electronics* 58.9 (2011), pp. 4039–4047. ISSN: 0278-0046.

[34] J. Klima and O. Vitek. “The influence of the rotor slits on the performance of high-speed solid-rotor induction machine”. In: *2016 17th International Conference on Mechatronics - Mechatronika (ME).* 2016, pp. 1–5.

[35] R. Lateb, J. Enon, and L. Durantay. “High speed, high power electrical induction motor technologies for integrated compressors”. In: *2009 International Conference on Electrical Machines and Systems.* Nov. 2009, pp. 1–5.

[36] N. Boules. “Impact Of Slot Harmonics On Losses Of High-Speed Permanent Magnet Machines With A Magnet Retaining Ring”. In: *Electric Machines & Power Systems* 6.6 (1981), pp. 527–539.

[37] Z. Q. Zhu, K. Ng, and D. Howe. “Design and analysis of high-speed brushless permanent magnet motors”. In: *1997 Eighth International Conference on Electrical Machines and Drives (Conf. Publ. No. 444).* Cambridge, UK, 1997, pp. 381–385.

[38] A. Binder, T. Schneider, and M. Klohr. “Fixation of buried and surface-mounted magnets in high-speed permanent-magnet synchronous machines”. In: *IEEE Transactions on Industry Applications* 42.4 (July 2006), pp. 1031–1037. ISSN: 0093-9994.

[39] F. Zhang et al. “Rotor Retaining Sleeve Design for a 1.12-MW High-Speed PM Machine”. In: *IEEE Transactions on Industry Applications* 51.5 (Sept. 2015), pp. 3675–3685. ISSN: 0093-9994.

[40] L. Alberti et al. “Impact of Rotor Losses in a 12-Slot 10-Pole Axial Flux PM Machine”. In: *2008 IEEE Industry Applications Society Annual Meeting.* Oct. 2008, pp. 1–8.

[41] G. Berardi and N. Bianchi. “Rotor losses reduction in high speed PM generators for organic rankine cycle systems”. In: *2017 IEEE Energy Conversion Congress and Exposition (ECCE).* 2017, pp. 5396–5402.

[42] N. Bianchi, S. Bolognani, and F. Luise. “Potentials and limits of high-speed PM motors”. In: *IEEE Transactions on Industry Applications* 40.6 (2004), pp. 1570–1578. ISSN: 00939994.

[43] J. Xing et al. “Study on Anti-Demagnetization of Magnet for High Speed Permanent Magnet Machine”. In: *IEEE Transactions on Applied Superconductivity* 20.3 (2010), pp. 856–860. ISSN: 1051-8223.

[44] G. Berardi, N. Bianchi, and D. Gasperini. “A high speed PM generator for an Organic Rankine Cycle system”. In: *2017 IEEE International Electric Machines and Drives Conference (IEMDC).* May 2017, pp. 1–8.

[45] A. Knauf and R. Vollmerr. “Rotor for a permanent magnet synchronous machine”. US2003173853 (A1), 2003.

[46] Jinyun Gan et al. “A new surface-inset, permanent-magnet, brushless DC motor drive for electric vehicles”. In: *IEEE Transactions on Magnetics* 36.5 (2000), pp. 3810–3818.

[47] M. Marino. “Analytical modeling and optimization of a radial permanent magnets synchronous machine”. In: (Sept. 2009).

[48] J. Kolehmainen. “Dovetail rotor poles in synchronous permanent magnet and reluctance machines”. PhD Thesis. Aalto University, 2011.

[49] A. Vagati, G. Pellegrino, and P. Guglielmi. "Comparison between SPM and IPM motor drives for EV application". In: *The XIX International Conference on Electrical Machines - ICEM 2010*. 2010, pp. 1–6.

[50] E. W. Fairall, B. Bilgin, and A. Emadi. "State-of-the-art high-speed switched reluctance machines". In: *2015 IEEE International Electric Machines Drives Conference (IEMDC)*. 2015, pp. 1621–1627.

[51] T. Raminosoa et al. "Design and Optimization of a Switched Reluctance Motor Driving a Compressor for a PEM Fuel-Cell System for Automotive Applications". In: *IEEE Transactions on Industrial Electronics* 57.9 (2010), pp. 2988–2997. ISSN: 0278-0046.

[52] Sung Hong Won et al. "Performance Prediction of Switched Reluctance Motor Considering Windage Loss for High Speed Application". In: *2006 12th Biennial IEEE Conference on Electromagnetic Field Computation*. Apr. 2006, p. 417.

[53] R. E. Doherty and C. A. Nickle. "Synchronous machines: An extension of Blondel's two-reaction theory". In: *Journal of the A.I.E.E.* 45.10 (1926), pp. 974–987. ISSN: 0095-9804.

[54] M. Hofer and M. Schroedl. "Comparison of a flux barrier and a salient pole synchronous reluctance machine for high rotational speeds in electric traction applications". In: *2017 20th International Conference on Electrical Machines and Systems (ICEMS)*. 2017, pp. 1–6.

[55] M. E. Hadi Zaim. "High-Speed Solid Rotor Synchronous Reluctance Machine Design and Optimization". In: *IEEE Transactions on Magnetics* 45.3 (2009), pp. 1796–1799.

[56] J. Ikäheimo and J. Kolehmainen and T. Känsäkangas and V. Kivelä and R. R. Moghaddam. "Synchronous High-Speed Reluctance Machine With Novel Rotor Construction". In: *IEEE Transactions on Industrial Electronics* 61.6 (2014), pp. 2969–2975. ISSN: 0278-0046.

[57] R. R. Moghaddam. "Synchronous Reluctance Machine for VSD application". PhD Thesis. KTH School of Electrical Engineering, 2011.

[58] F. Cupertino, M. Palmieri, and G. Pellegrino. "Design of high-speed synchronous reluctance machines". In: *2015 IEEE Energy Conversion Congress and Exposition (ECCE)*. 2015, pp. 4828–4834.

[59] M. Di Nardo et al. "Multi-physics optimization strategies for high speed synchronous reluctance machines". In: *2015 IEEE Energy Conversion Congress and Exposition (ECCE)*. 2015, pp. 2813–2820.

[60] M. Di Nardo et al. "Structural design optimization of a high speed synchronous reluctance machine". In: *2016 XXII International Conference on Electrical Machines (ICEM)*. 2016, pp. 2073–2079.

[61] M. Barcaro, G. Meneghetti, and N. Bianchi. "Structural analysis of the interior PM rotor considering both static and fatigue loading". In: *IEEE Transactions on Industry Applications* 50.1 (2014), pp. 253–260. ISSN: 00939994.

[62] S. Ferrari and G. Pellegrino. "FEA-Augmented Design Equations for Synchronous Reluctance Machines". In: *2018 IEEE Energy Conversion Congress and Exposition (ECCE)*. 2018, pp. 5395–5402.

[63] T. A. Lipo et al. *Synchronous Reluctance Motors and Drives - A New Alternative*. Denver: IEEE Industry Applications Society, 1994.

[64] M. Barcaro and N. Bianchi. "Interior PM machines using ferrite to replace rare-earth surface PM machines". In: *IEEE Transactions on Industry Applications* 50.2 (2014), pp. 979–985. ISSN: 00939994.

[65] M. Barcaro. "Design and Analysis of Interior Permanent Magnet Synchronous Machines for Electric Vehicles". PhD Thesis. University of Padova, 2011.

[66] C. López et al. "Rotor of synchronous reluctance motor optimization by means reluctance network and genetic algorithm". In: *2016 XXII International Conference on Electrical Machines (ICEM)*. 2016, pp. 2052–2058.

[67] C. López Torres et al. “Fast optimization of the magnetic model by means of reluctance network for PMa-SynRM”. In: *IECON 2016 - 42nd Annual Conference of the IEEE Industrial Electronics Society*. 2016, pp. 1642–1647.

[68] C. López-Torres et al. “Design and Optimization for Vehicle Driving Cycle of Rare-Earth-Free SynRM Based on Coupled Lumped Thermal and Magnetic Networks”. In: *IEEE Transactions on Vehicular Technology* 67.1 (2018), pp. 196–205. ISSN: 0018-9545.

[69] G. Bacco and N. Bianchi. “Choice of flux-barriers position in synchronous reluctance machines”. In: *2017 IEEE Energy Conversion Congress and Exposition (ECCE)*. Cincinnati, 2017, pp. 1872–1879.

[70] N. Bianchi et al. “Rotor flux-barrier design for torque ripple reduction in synchronous reluctance and PM-assisted synchronous reluctance motors”. In: *IEEE Transactions on Industry Applications* 45.3 (2009), pp. 921–928. ISSN: 00939994.

[71] T. M. Jahns and W. L. Soong. “Pulsating torque minimization techniques for permanent magnet AC motor drives - A review”. In: *IEEE Transactions on Industrial Electronics* 43.2 (1996), pp. 321–330. ISSN: 02780046.

[72] A. Vagati et al. “Design of low-torque-ripple synchronous reluctance motors”. In: *IEEE Transactions on Industry Applications* 34.4 (July 1998), pp. 758–765. ISSN: 0093-9994.

[73] A. Vagati et al. “Design criteria of high performance synchronous reluctance motors”. In: *Conference Record of the 1992 IEEE Industry Applications Society Annual Meeting*. 1992, 66–73 vol.1.

[74] G. Pellegrino, F. Cupertino, and C. Gerada. “Automatic Design of Synchronous Reluctance Motors Focusing on Barrier Shape Optimization”. In: *IEEE Transactions on Industry Applications* 51.2 (2015), pp. 1465–1474. ISSN: 0093-9994.

[75] N. Bianchi, M. Degano, and E. Fornasiero. “Sensitivity Analysis of Torque Ripple Reduction of Synchronous Reluctance and Interior PM Motors”. In: *IEEE Transactions on Industry Applications* 51.1 (2015), pp. 187–195. ISSN: 0093-9994.

[76] G. Berardi and N. Bianchi. “High Speed PM Generators for Organic Rankine Cycle Systems: Reduction of Eddy Current Rotor Losses”. In: *IEEE Transactions on Industry Applications* (2019), p. 1.

[77] G. Berardi, N. Bianchi, and D. Gasperini. “A High Speed PM Generator for an Organic Rankine Cycle System”. In: *IEEE Transactions on Industry Applications* 55.5 (2019), pp. 4633–4642.

[78] D. Borg-Bartolo et al. “Thermal modelling and selection of a high speed permanent magnet surface mount electrical machine”. In: *6th IET International Conference on Power Electronics, Machines and Drives (PEMD 2012)*. 2012, pp. 1–6.

[79] M. A. H. Rasid et al. “Thermal model of stator slot for small synchronous reluctance machine”. In: *2014 International Conference on Electrical Machines (ICEM)*. 2014, pp. 2199–2204.

[80] P. S. Ghahfarokhi et al. “Steady-State Thermal Model of a Synchronous Reluctance Motor”. In: *2018 IEEE 59th International Scientific Conference on Power and Electrical Engineering of Riga Technical University (RTUCON)*. Nov. 2018, pp. 1–5.

[81] A. Consoli. “Special Section on Robust Operation of Electrical Drives”. In: *IEEE Transactions on Power Electronics* 27.2 (Feb. 2012), pp. 476–478.

[82] I. Bolvashenkov et al. *Fault-Tolerant Traction Electric Drives: Reliability, Topologies and Components Design*. SpringerBriefs in Electrical and Computer Engineering Series. SPRINGER VERLAG, SINGAPOR, 2019. ISBN: 9789811392757.

[83] M. Ruba and L. Szabo. “Fault Tolerant Electrical Machines. State of the Art and Future Directions”. In: *Journal of Computer Science and Control Systems* 1 (May 2008).

[84] H. Toliyat et al. *Electric Machines: Modeling, Condition Monitoring, and Fault Diagnosis*. CRC Press, 2017. ISBN: 9781420006285.

[85] M. El Hachemi Benbouzid. "A review of induction motors signature analysis as a medium for faults detection". In: *IEEE Transactions on Industrial Electronics* 47.5 (2000), pp. 984–993.

[86] A. G. Jack, B. C. Mecrow, and J. A. Haylock. "A comparative study of permanent magnet and switched reluctance motors for high-performance fault-tolerant applications". In: *IEEE Transactions on Industry Applications* 32.4 (July 1996), pp. 889–895. ISSN: 0093-9994.

[87] D. Fodorean et al. "Comparison of the main types of fault-tolerant electrical drives used in vehicle applications". In: *2008 International Symposium on Power Electronics, Electrical Drives, Automation and Motion*. 2008, pp. 895–900.

[88] S. Williamson, S. Smith, and C. Hodge. "Fault tolerance in multiphase propulsion motors". In: *Proceedings of IMarEST - Part A - Journal of Marine Engineering and Technology* 2004 (Mar. 2004), pp. 3–7.

[89] J. M. Apsley et al. "Induction motor performance as a function of phase number". In: *IEE Proceedings - Electric Power Applications* 153.6 (2006).

[90] F. Jawad, G. Vahid, and J. Gojko. *Fault Diagnosis of Induction Motors*. Energy Engineering. Institution of Engineering and Technology, 2017.

[91] T. Elch-Heb and J. P. Hautier. "Remedial strategy for inverter-induction machine system faults using two-phase operation". In: *1993 Fifth European Conference on Power Electronics and Applications*. 1993, 151–156 vol.5.

[92] Tian-Hua Liu, Jen-Ren Fu, and T. A. Lipo. "A strategy for improving reliability of field-oriented controlled induction motor drives". In: *IEEE Transactions on Industry Applications* 29.5 (1993), pp. 910–918.

[93] M. Beltrao de Rossiter Correa et al. "An induction motor drive system with improved fault tolerance". In: *IEEE Transactions on Industry Applications* 37.3 (2001), pp. 873–879.

[94] A. M. S. Mendes and A. J. Marques Cardoso. "Fault-Tolerant Operating Strategies Applied to Three-Phase Induction-Motor Drives". In: *IEEE Transactions on Industrial Electronics* 53.6 (2006), pp. 1807–1817.

[95] D. Kastha and B. K. Bose. "Fault mode single-phase operation of a variable frequency induction motor drive and improvement of pulsating torque characteristics". In: *IEEE Transactions on Industrial Electronics* 41.4 (1994), pp. 426–433.

[96] L. Alberti and N. Bianchi. "Impact of winding arrangement in dual 3-phase induction motor for fault tolerant applications". In: *The XIX International Conference on Electrical Machines - ICEM 2010*. Sept. 2010, pp. 1–6.

[97] Zhong Peng et al. "Fault-tolerant control of multiphase induction machine drives based on virtual winding method". In: *2017 IEEE Transportation Electrification Conference and Expo (ITEC)*. 2017, pp. 252–256.

[98] Q. Chen et al. "A New Fault-Tolerant Permanent-Magnet Machine for Electric Vehicle Applications". In: *IEEE Transactions on Magnetics* 47.10 (2011), pp. 4183–4186. ISSN: 0018-9464.

[99] L. Parsa and H. A. Toliyat. "Five-phase permanent-magnet motor drives". In: *IEEE Transactions on Industry Applications* 41.1 (2005), pp. 30–37.

[100] L. Alberti and N. Bianchi. "Experimental Tests of Dual Three-Phase Induction Motor Under Faulty Operating Condition". In: *IEEE Transactions on Industrial Electronics* 59.5 (May 2012), pp. 2041–2048. ISSN: 0278-0046.

[101] M. Ruba. "Fault-Tolerant Electrical Machines and Drives". In: *Fault Diagnosis and Detection*. Ed. by M. Demetgul and M. Ünal. Rijeka: IntechOpen, 2017. Chap. 8.

[102] M. Hassan. "Switched reluctance machine having unbalance forces compensation coils". US5422525A. 1994.

[103] B. C. Mecrow et al. "Segmental rotor switched reluctance motors with single-tooth windings". In: *IEE Proceedings - Electric Power Applications* 150.5 (2003), pp. 591–599.

[104] Z. Xu, D. Lee, and J. Ahn. "Design of a novel 6/5 segmental rotor type switched reluctance motor". In: *2014 IEEE Industry Application Society Annual Meeting*. 2014, pp. 1–7.

[105] B. A. Welchko et al. "IPM synchronous machine drive response to symmetrical and asymmetrical short circuit faults". In: *IEEE Transactions on Energy Conversion* 18.2 (2003), pp. 291–298. ISSN: 08858969.

[106] N. Bianchi, S. Bolognani, and M. D. Pr. "Design of a fault-tolerant IPM motor for electric power steering". In: *IEEE Transactions on Vehicular Technology* 55.4 (2006), pp. 2873–2880.

[107] T. M. Jahns. "Improved Reliability in Solid-State AC Drives by Means of Multiple Independent Phase Drive Units". In: *IEEE Transactions on Industry Applications* IA-16.3 (1980), pp. 321–331.

[108] N. Bianchi et al. "Design considerations on fractional-slot fault-tolerant synchronous motors". In: *IEEE International Conference on Electric Machines and Drives, 2005.* 2005, pp. 902–909.

[109] N. Bianchi, M. D. Prè, and L. Alberti. *Theory and Design of Fractional-slot Pm Machines*. IEEE IAS Tutorial Course Notes. CLEUP, 2007. ISBN: 9788861291225.

[110] L. Parsa and H. A. Toliyat. "Fault-tolerant five-phase permanent magnet motor drives". In: *Conference Record of the 2004 IEEE Industry Applications Conference, 2004. 39th IAS Annual Meeting.* Vol. 2. 2004, 1048–1054 vol.2.

[111] N. Bianchi, S. Bolognani, and M. Dai Pré. "Design and tests of a fault-tolerant five-phase permanent magnet motor". In: *2006 37th IEEE Power Electronics Specialists Conference*. 2006, pp. 1–8.

[112] N. Bianchi, S. Bolognani, and M. Dai Pre. "Strategies for the Fault-Tolerant Current Control of a Five-Phase Permanent-Magnet Motor". In: *IEEE Transactions on Industry Applications* 43.4 (2007), pp. 960–970.

[113] M. Barcaro, N. Bianchi, and F. Magnussen. "Analysis and Tests of a Dual Three-Phase 12-Slot 10-Pole Permanent-Magnet Motor". In: *IEEE Transactions on Industry Applications* 46.6 (Nov. 2010), pp. 2355–2362.

[114] M. Barcaro, N. Bianchi, and F. Magnussen. "Faulty Operations of a PM Fractional-Slot Machine With a Dual Three-Phase Winding". In: *IEEE Transactions on Industrial Electronics* 58.9 (2011), pp. 3825–3832.

[115] D. Qin, X. Luo, and T. Lipo. "Reluctance motor control for fault-tolerant capability". In: June 1997, WA1/1.1–WA1/1.6.

[116] D. B. Matos, J. O. Estima, and A. J. M. Cardoso. "Performance of a synchronous reluctance motor drive with a fault-tolerant three-level neutral point clamped inverter". In: *2016 XXII International Conference on Electrical Machines (ICEM)*. 2016, pp. 1152–1159.

[117] M. Liwschitz-Garik and C. Whipple. *Electric machinery*. Electric Machinery v. 2. D. Van Nostrand company, inc., 1947.

[118] N. Bianchi and M. Dai Pré. "Use of the star of slots in designing fractional-slot single-layer synchronous motors". In: *IEE Proceedings - Electric Power Applications* 153.3 (2006), pp. 459–466. ISSN: 1350-2352.

[119] G. D'Amato et al. "Urban air pollution and climate change as environmental risk factors of respiratory allergy: an update". In: *Journal of Investigational Allergology and Clinical Immunology* 20.2 (2010), pp. 95–102.

[120] L. B. Lave and E. P. Seskin. *Air pollution and human health*. RFF Press, 2013.

[121] B. Gurjar et al. "Human health risks in megacities due to air pollution". In: *Atmospheric Environment* 44.36 (2010), pp. 4606–4613.

[122] X. Zhang et al. “Policy incentives for the adoption of electric vehicles across countries”. In: *Sustainability* 6.11 (2014), pp. 8056–8078.

[123] J. de Santiago et al. “Electrical Motor Drivelines in Commercial All-Electric Vehicles: A Review”. In: *IEEE Transactions on Vehicular Technology* 61.2 (Feb. 2012), pp. 475–484. ISSN: 0018-9545.

[124] B. Frieske, M. Kloetzke, and F. Mauser. “Trends in vehicle concept and key technology development for hybrid and battery electric vehicles”. In: *2013 World Electric Vehicle Symposium and Exhibition (EVS27)*. Barcelona, Spain, Nov. 2013, pp. 1–12.

[125] N. Bianchi, S. Bolognani, and M. Zigliotto. “High-performance PM synchronous motor drive for an electrical scooter”. In: *IEEE Transactions on Industry Applications* 37.5 (Sept. 2001), pp. 1348–1355. ISSN: 0093-9994.

[126] N. Ravi, S. Ekram, and D. Mahajan. “Design and Development of a In-Wheel Brushless D.C. Motor Drive for an Electric Scooter”. In: *2006 International Conference on Power Electronic, Drives and Energy Systems*. New Delhi, India, Dec. 2006, pp. 1–4.

[127] B. Song, K. Chang, and J. Choi. “Design of an outer-rotor-type permanent magnet motor for electric scooter propulsion systems”. In: *The 2010 International Power Electronics Conference - ECCE ASIA -*. Sapporo, Japan, June 2010, pp. 2763–2742.

[128] W. Gruber, W. Bäck, and W. Amrhein. “Design and implementation of a wheel hub motor for an electric scooter”. In: *2011 IEEE Vehicle Power and Propulsion Conference*. Chicago, IL, USA, Sept. 2011, pp. 1–6.

[129] D. Fodorean, L. Idoumghar, and L. Szabo. “Motorization for an Electric Scooter by Using Permanent-Magnet Machines Optimized Based on a Hybrid Metaheuristic Algorithm”. In: *IEEE Transactions on Vehicular Technology* 62.1 (Jan. 2013), pp. 39–49. ISSN: 0018-9545.

[130] A. M. Omekanda. “Switched reluctance machines for EV and HEV propulsion: State-of-the-art”. In: *2013 IEEE Workshop on Electrical Machines Design, Control and Diagnosis (WEMDCD)*. Paris, France, Mar. 2013, pp. 70–74.

[131] R. R. Moghaddam, F. Magnussen, and C. Sadarangani. “Novel rotor design optimization of synchronous reluctance machine for high torque density”. In: *6th IET International Conference on Power Electronics, Machines and Drives (PEMD 2012)*. 2012, B32–B32. ISBN: 978-1-84919-616-1.

[132] Y. Wang, G. Bacco, and N. Bianchi. “Geometry Analysis and Optimization of PM-Assisted Reluctance Motors”. In: *IEEE Transactions on Industry Applications* 53.5 (2017), pp. 4338–4347. ISSN: 0093-9994.

[133] G. Pellegrino et al. *The rediscovery of synchronous reluctance and ferrite permanent magnet motors: tutorial course notes*. Springer, 2016.

[134] H. Cai, B. Guan, and L. Xu. “Low-Cost Ferrite PM-Assisted Synchronous Reluctance Machine for Electric Vehicles”. In: *IEEE Transactions on Industrial Electronics* 61.10 (2014), pp. 5741–5748. ISSN: 0278-0046.

[135] M. Obata et al. “Performance of PMASynRM With Ferrite Magnets for EV/HEV Applications Considering Productivity”. In: *IEEE Transactions on Industry Applications* 50.4 (July 2014), pp. 2427–2435. ISSN: 0093-9994.

[136] M. Ehsani et al. *Modern electric, hybrid electric, and fuel cell vehicles*. CRC press, 2018.

[137] G. Pellegrino and F. Cupertino. “FEA-based multi-objective optimization of IPM motor design including rotor losses”. In: *2010 IEEE Energy Conversion Congress and Exposition*. Atlanta, GA, USA, Sept. 2010, pp. 3659–3666.

[138] S. Ooi et al. “Performance Evaluation of a High-Power-Density PMASynRM With Ferrite Magnets”. In: *IEEE Transactions on Industry Applications* 49.3 (May 2013), pp. 1308–1315. ISSN: 0093-9994.

[139] J. Pyrhonen, T. Jokinen, and V. Hrabovcova. *Design of rotating electrical machines*. John Wiley & Sons, 2013.

[140] D. Meeker. *Finite Element Method Magnetics*. 2009.

[141] *Rotating Losses in a Surface Mount Permanent Magnet Motor*. `http://www.femm.info/wiki/SPMLoss`.

[142] A. Mahmoudi et al. "Efficiency maps of electrical machines". In: *2015 IEEE Energy Conversion Congress and Exposition (ECCE)*. 2015, pp. 2791–2799.

[143] E. Carraro, M. Morandin, and N. Bianchi. "Traction PMASR Motor Optimization According to a Given Driving Cycle". In: *IEEE Transactions on Industry Applications* 52.1 (2016), pp. 209–216.

[144] P. Guglielmi et al. "An IPM-PMASR motor for home appliance washing machines". In: *IECON 2013 - 39th Annual Conference of the IEEE Industrial Electronics Society*. Nov. 2013, pp. 2608–2613.

[145] P. Guglielmi et al. "Magnet minimization in IPM-PMASR motor design for wide speed range application". In: *2011 IEEE Energy Conversion Congress and Exposition*. 2011, pp. 4201–4207.

[146] N. Bianchi and S. Bolognani. "Design Procedure of a Synchronous Motor for Flux-Weakening Applications". In: *Proceedings of EPE Symposium*. Nancy, France, June Nancy, France, 1996, pp. 235–240.

[147] N. Bianchi, E. Fornasiero, and W. Soong. "Selection of PM Flux Linkage for Maximum Low-Speed Torque Rating in a PM-Assisted Synchronous Reluctance Machine". In: *IEEE Transactions on Industry Applications* 51.5 (2015), pp. 3600–3608. ISSN: 0093-9994.

[148] G. Hadjipanayis. *Bonded Magnets: Proceedings of the NATO Advanced Research Workshop on Science and Technology of Bonded Magnets Newark, U.S.A. 22–25 August 2002*. Nato Science Series II: Springer Netherlands, 2012. ISBN: 9789400710900.

[149] S.-x. BAI et al. "Progress of Research on Bonded Nd-Fe-B Magnets". In: *Journal of Iron and Steel Research, International* 13 (2006), pp. 489–493. ISSN: 1006-706X.

[150] L. Ferraris et al. "Theoretic and Experimental Approach to the Adoption of Bonded Magnets in Fractional Machines for Automotive Applications". In: *IEEE Transactions on Industrial Electronics* 59.5 (2012), pp. 2309–2318. ISSN: 0278-0046.

[151] L. Ferraris and E. Poškovic. "Bonded magnets for brushless fractional machines: Process parameters effects evaluation". In: *IECON 2013 - 39th Annual Conference of the IEEE Industrial Electronics Society*. Nov. 2013, pp. 2632–2637.

[152] C. López et al. "New SynRM design approach based on behaviour maps analysis". In: *2016 XXII International Conference on Electrical Machines (ICEM)*. 2016, pp. 1915–1921.

[153] J. Goss et al. "A comparison between maximum torque/ampere and maximum efficiency control strategies in IPM synchronous machines". In: *2014 IEEE Energy Conversion Congress and Exposition (ECCE)*. 2014, pp. 2403–2410.

[154] A. Mahmoudi et al. "Loss Function Modeling of Efficiency Maps of Electrical Machines". In: *IEEE Transactions on Industry Applications* 53.5 (2017), pp. 4221–4231. ISSN: 0093-9994.

[155] S. B. Shah and A. Arkkio. "Efficiency map prediction of flux switching machine". In: *2015 18th International Conference on Electrical Machines and Systems (ICEMS)*. 2015, pp. 1490–1493.

[156] R. Bojoi et al. "Efficiency and loss mapping of AC motors using advanced testing tools". In: *2016 XXII International Conference on Electrical Machines (ICEM)*. 2016, pp. 1043–1049.

[157] S. Stipetic et al. "Calculation of Efficiency Maps Using a Scalable Saturated Model of Synchronous Permanent Magnet Machines". In: *IEEE Transactions on Industry Applications* 54.5 (2018), pp. 4257–4267. ISSN: 0093-9994.

[158] G. Pellegrino et al. "Performance Comparison Between Surface-Mounted and Interior PM Motor Drives for Electric Vehicle Application". In: *IEEE Transactions on Industrial Electronics* 59.2 (Feb. 2012), pp. 803–811. ISSN: 0278-0046.

[159] M. Carbonieri, N. Bianchi, and L. Alberti. "Direct Analysis of Induction Motor Using Finite Element". In: *2018 IEEE Energy Conversion Congress and Exposition (ECCE)*. 2018, pp. 277–283.

[160] M. Carbonieri, N. Bianchi, and L. Alberti. "A Fast and Direct Analysis of Three-Phase Induction Motors Using Finite Element". In: *2018 XIII International Conference on Electrical Machines (ICEM)*. 2018, pp. 18–24.

[161] A. Boglietti et al. "A simplified thermal model for variable-speed self-cooled industrial induction motor". In: *IEEE Transactions on Industry Applications* 39.4 (2003), pp. 945–952. ISSN: 0093-9994.

[162] P. Dular and C. Geuzaine. *GetDP reference manual: the documentation for GetDP, a general environment for the treatment of discrete problems*.

[163] P. Dular et al. "A general environment for the treatment of discrete problems and its application to the finite element method". In: *IEEE Transactions on Magnetics* 34.5 (1998), pp. 3395–3398. ISSN: 0018-9464.

[164] W. S. Slaughter. *The Linearized Theory of Elasticity*. Birkhäuser Boston, 2012. ISBN: 9781461200932.

[165] L. C. Dell'Acqua. *Meccanica delle strutture*. Collana di Istruzione Scientifica.Serie di Ingegneria Civile, 3 voll v. 1. McGraw-Hill Companies, 1992. ISBN: 9788838606656.

[166] G. Meneghetti, M. Manzolaro, and M. Quaresimin. *Introduction to the Structural Analysis with ANSYS Numerical Code*. Progetto Libreria, 2014. ISBN: 9788896477595.

[167] C. Geuzaine and J. Remacle. "Gmsh: a three-dimensional finite element mesh generator with built-in pre- and post-processing facilities". In: *International Journal for Numerical Methods in Engineering* 79 (2009), pp. 1309–1331.

[168] P. R. Lancaster and D. Mitchell. *Advanced Solid Mechanics: Theory, Worked Examples and Problems*. Macmillan, 1980. ISBN: 9780333240137.

[169] P. Lazzarin. *Esercizi di costruzione di macchine*. CUSL Nuova vita, 1995.

[170] K. Binns, P. Lawrenson, and C. Trowbridge. *The Analytical and Numerical Solution of Electric and Magnetic Fields*. Wiley, 1993. ISBN: 9780471924609.